THE EFFECTS OF TITANIUM NITRIDE PARTICLES AND
FREE NITROGEN ON THE HEAT-AFFECTED ZONE
TOUGHNESS OF API 2Y-TYPE PLATE STEELS

by

Matthew J. Merwin

ProQuest Number: 10796708

ProQuest 10796708

A thesis submitted to the Faculty and the Board of Trustees of the Colorado School

of Mines in partial fulfillment of the requirements for the degree of Doctor of Philosophy

(Metallurgical and Materials Engineering)

Golden, CO

Date _1/17/97_

Signed: _____
Matthew J. Merwin

Approved: _____
Dr. Steven W. Thompson

Golden, CO

Date _1/17/97_

_____
Dr. John J. Moore
Department Chairman
Department of Metallurgical and
Materials Engineering
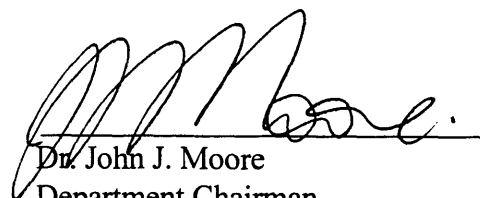
ii

ABSTRACT

Four alloys based on the API 2Y specification (containing, in wt. pct., 0.08C, 1.5Mn, 0.2Si, 0.2Ni, 0.025Al, and various levels of titanium and nitrogen) were designed to examine the effects of excess or free nitrogen (0.004%, 0.008%, or 0.012%) and titanium nitride volume fraction (either 1.2×10^{-4} or 2.6×10^{-4}) on the impact toughness of the coarse-grained-heat-affected zone in high-heat-input welds. A Gleeble 1500 thermomechanical test system was used to simulate welds with 4 kJ/mm and 8 kJ/mm heat inputs on 50-mm-thick plate. For both heat inputs, thermal cycles utilized a 1350°C peak temperature to simulate the coarse-grained-heat-affected zones. Additional thermal cycles based on the 4 kJ/mm heat input cycle with peak temperatures of 1250°C and 1400°C were also investigated.

Comparatively small titanium nitride precipitates (those smaller than 1 µm in size) were analyzed via carbon extraction replicas in a scanning-transmission electron microscope. Precipitate sizes were quantified from specimens obtained from the as-quenched-and-tempered plate and from Gleeble-welding-simulation blanks. Measured average precipitate sizes compared favorably with those predicted from a model based on the standard Wagner particle-coarsening model. A major modification associated with the present approach was to incorporate the non-isothermal nature of the welding simulations.

iii

The present work showed that the average size of the comparatively fine titanium nitride precipitates (< 100 nm) was influenced largely by coarsening during cooling of the original ingot, and the temperature of titanium nitride formation played a secondary role in the relative sizes of the precipitates for the alloys examined. Coarsening of these precipitates was minimized with high free nitrogen levels and correspondingly low free titanium levels.

Comparatively coarse titanium nitride inclusions (those larger than 1 μm in size) and other coarse microstructural features were characterized *via* standard quantitative metallography techniques in association with the light microscope. Standard Charpy V-notch testing was conducted on specimens machined from Gleeble-welding-simulation blanks. Impact toughness was measured based on 100-J transition temperatures from Charpy V-notch testing, and measured values ranged from approximately 20°C to -55°C. However, for a specific thermal cycle (defined by peak temperature and heat input), the difference in 100-J transition temperature for the alloys studied was small, typically less than about 10°C.

During austenite decomposition in welding-simulation specimens, the comparatively coarse titanium nitride inclusions (under some conditions) provided nucleation sites for primary ferrite formation. While these titanium nitride inclusions had a direct negative effect on the 100-J transition temperature, these particles had an indirect positive effect *via* the nucleation of primary ferrite. Specifically, for the limited range of microstructural conditions examined, the presence of primary ferrite had a beneficial effect

on the 100-J transition temperature. The presence of free nitrogen had a direct negative effect on the 100-J transition temperature. This effect was most evident in fine microstructures, *i.e.*, those generated from thermal simulations with a 1250°C peak temperature, where an increase of approximately 2°C in 100-J transition temperature was observed for an increase of 0.001 wt. % free nitrogen. In coarse microstructures it was hypothesized that differences in other microstructural features tended to mask the contribution from free nitrogen. In general, microstructural refinement provided a beneficial effect on the 100-J transition temperature, although the grain-size effect was confounded by other contributions and, therefore, was not as dominant as expected.

Because of the presence of several competing factors which influence the 100-J transition temperature, there is no one alloy which out-performs the other alloys at all peak temperatures with a heat input of 4 kJ/mm. Specifically, at a peak temperature of 1250°C, alloy LNLV provides the best performance because of the comparatively low free nitrogen level and low volume fraction of coarse titanium nitride particles; at 1350°C, alloy LNHV benefits significantly from primary ferrite which is nucleated at large titanium nitride particles; and at 1400°C, all of the low-volume-fraction alloys (HNLV, INLV, LNLV) perform similarly.

TABLE OF CONTENTS

LIST OF FIGURES

xvii

LIST OF TABLES

ACKNOWLEDGMENTS

I would like to take this opportunity to thank a few of the many people that provided help during my time at CSM doing this research, and made the overall experience of graduate school so enjoyable.

First, many thanks go to my thesis committee for their helpful insights and conversations. I truly learned a lot from you all. While I am grateful to all of my committee members, there are a few members that merit special attention.

I would like to thank Dr. George Krauss, current President of ASM International and former director of the Advanced Steel Processing and Products Research Center, for selecting me to participate in the ASPPRC at CSM. This has been an excellent opportunity for me to learn many aspects of physical and mechanical metallurgy, as well as gaining a new respect and enthusiasm for steel.

Dr. Steven Thompson, my advisor, certainly deserves thanks for many aspects of my learning experience at CSM. Clearly there is not enough room here to fully describe all of the things that an advisor does for a student. Really all I can do is say thank you, knowing that it somehow lacks the full appreciation I feel.

I thank Dr. Chester Van Tyne for our frequent discussions, both technical and social. Dr. Van Tyne has been very helpful in the areas that I still don't fully understand,

allowing me to complete this document. Also, it has been nice to see a faculty member take an active interest in the students. Graduate students will complain, and it is good to have a faculty member listen without holding it against you.

I would also like to thank the sponsors of the Advanced Steel Processing and Products Research Center for funding this project. Specifically, the sponsors of the Plate Group deserve extra thanks for not only monetary, but also technical, support.

The sponsors from U.S. Steel and Bethlehem Steel, Drs. Joe Defilippi and Steve Hansen, were particularly active in their support of this project. These individuals were instrumental in the definition of this project and U.S. Steel provided the alloys. Also, the interactions during the SRC semiannual meetings were always helpful in keeping research on track.

In addition to the above, Dr. Defilippi also gave me the opportunity to work on this project at the US Steel Tech Center for a summer. I hope that others can have the same chance. It was a great learning experience and I am sure that it played an instrumental part in my employment there in the near future. Thanks again.

Lastly, I would like to thank all of the friends that I have made during my time at CSM. Andy Perry, Eric Gallo, Sean Peterson, and Matt Johnson, just to name a few, not only were there for enlightening discussions on technical matters but also made my work a fun place to be.

1.0 INTRODUCTION

In the interest of increased productivity and economy, high-heat-input welding (≥ 4 kJ/mm, or 100 kJ/in.) of steel plates has become more commonplace (1,2,3). The main benefit of using high-heat input welding is economy (4). With a higher weld heat input, more material is deposited in a given weld pass. As a result, less time is consumed in welding a given component. There are, however, some concerns associated with the mechanical properties of the welded joint, specifically in the heat-affected zone (HAZ). The area in which most loss of strength and toughness has been encountered is the coarse-grained heat-affected zone (CGHAZ). With the very high temperatures found adjacent to the weld fusion line ($\geq 1300°C$) and the long times at these temperatures, as shown in Figure 1.1, significant energy becomes available for austenite grain growth (2-5). This grain growth has been shown to negatively affect the toughness of the CGHAZ, either from coarse microstructures resulting on cooling or enhanced hardenability and transformation to hard microstructures (6). As a result it would be beneficial if the grain size of the HAZ could be controlled such that the very large austenite grains would not be present. The following sections will discuss the mechanisms responsible for the negative effect of large grain size on toughness and techniques for possible grain size control.
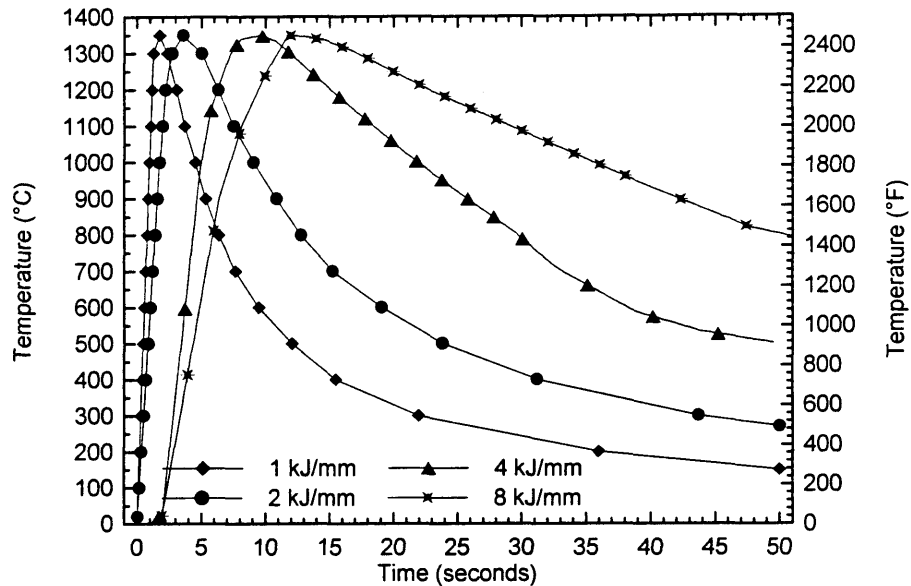
Figure 1.1.   Typical thermal cycles experienced in the coarse-grained heat affected zone
for various heat input welds.

1.1   Purpose for This Study

As previously stated, control of the austenite grain size in the heat-affected zone

during the welding process would be beneficial to the toughness of the welded joint. For

many years, "microalloying" has been used to control grain size in as-rolled steel products

as well as welded structrures. Microalloying is the practice of adding small amounts of

carbide- and/or nitride-forming elements, usually titanium, aluminum, niobium, vanadium,

or combinations of these, to steel so that a dispersion of fine nitride/carbide precipitates

form. These precipitates can strengthen the steel and can also help maintain fine grain size

by grain-boundary pinning. Figure 1.2 shows the relative temperature ranges over which

the above mentioned microalloying elements are effective in controlling austenite grain

size.
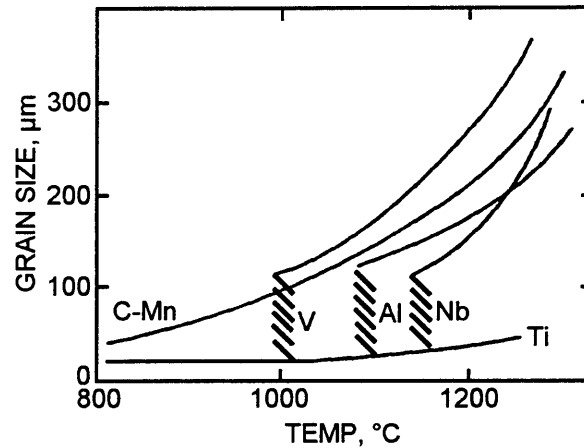
Figure 1.2.   Austenite grain growth in steel with different microalloying elements (7).

As shown in Figure 1.2, alloying with aluminum, niobium, or titanium is an

effective method to prevent austenite grain growth over a wide range of temperatures.

Figure 1.2 also shows that titanium additions are effective up to temperatures exceeding

1200°C. This feature is due to the highly stable titanium nitride precipitates that form is

steels. Therefore titanium is most commonly used to prevent austenite grain growth at high

temperatures experienced in the weld HAZ (5,8,9).

While it is known that titanium nitride is the most effective grain growth inhibitor of

the common microalloy precipitates, there are some issues associated with controlling the

precipitate size and subsequent grain size control that have yet to be answered. It is widely

accepted that a relatively high volume fraction of small second phase precipitates is most

effective at grain boundary pinning (10, 11). A schematic diagram of the relationship

between particle size, volume fraction, and grain size is shown in Figure 1.3.
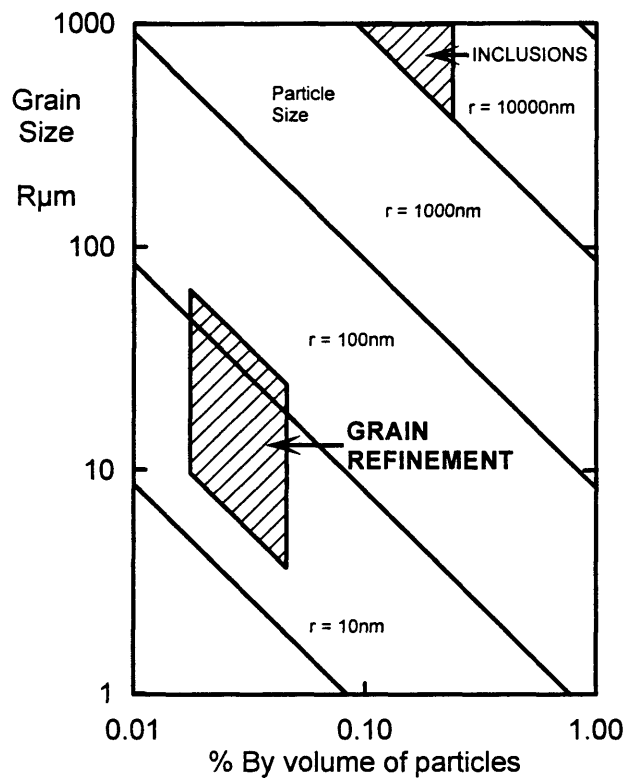
Figure 1.3.   Relationship of precipitate size and volume fraction with grain size (12).

To keep the titanium nitride precipitates small, titanium and nitrogen should be

added in hypostoichiometric ratios, or [Ti]/[N] < 3.42 by weight (9), thereby resulting in

excess nitrogen. The question is how much extra nitrogen should be present. While excess

nitrogen helps keep the titanium nitride precipitates small through the heating cycle, excess

nitrogen also decreases the impact toughness in steels (13). Increased free nitrogen content

may also lead to increased hardenability, resulting in bainitic or martensitic microstructures

upon transformation, thereby reducing impact toughness and increasing sensitivity to cold

cracking.

As shown in Figure 1.3, a large volume fraction of precipitates is helpful in

controlling grain size. However, large volume fractions may result in large precipitate

sizes. These large particle sizes may serve as nucleation of sites for cleavage fracture,

reducing the impact toughness.

These conflicting effects on impact toughness associated with titanium nitride

precipitates motivated the current research. It was hoped that a better understanding of

these effects would lead to a microalloyed steel that was capable of acceptable impact

toughness in a high-heat-input weld CGHAZ. This understanding was achieved through

Charpy V-notch testing of specially designed alloys. Four alloys were be designed with

various free nitrogen contents and different volume fractions of titanium nitride in the

temperature regime experienced in the CGHAZ. A Gleeble HAZ 1500 was used to

simulate high-heat-input weld CGHAZ's. After the material experienced the thermal cycle,

the resulting microstructure and titanium nitride size distribution were fully evaluated.

These components of the material microstructure were then elated to the impact toughness.

A more thorough discussion of the theoretical basis of this study, such as

microstructural and chemistry effects on impact toughness, grain boundary pinning theory,

particle precipitation, and coarsening will be presented in the following sections.

1.2 Microstructures Formed in Heat-Affected Zones

Since this study is primarily concerned with phenomena associated with the

microstructure and properties of coarse-grained heat-affected zones, it is appropriate to

briefly discuss what a heat-affected zone is and what microstructures might be expected to

be present. When low-carbon steel is welded, the area adjacent to the weld bead

experiences sufficiently high temperatures that major changes in microstructure occur.

Depending on the temperature achieved, different resulting microstructures can form. As

there is a gradient in temperature that the material experiences from the weld deposit to

some distance into the baseplate, there is a gradient of microstructures as well. This

gradient of microstructures is clearly described with Easterling's classic diagram showing

the correlation of distance from the weld deposit, temperature experienced at that distance,

and the corresponding microstructural changes with relation to the iron-carbon phase

diagram, as shown in Figure 1.4 (14).
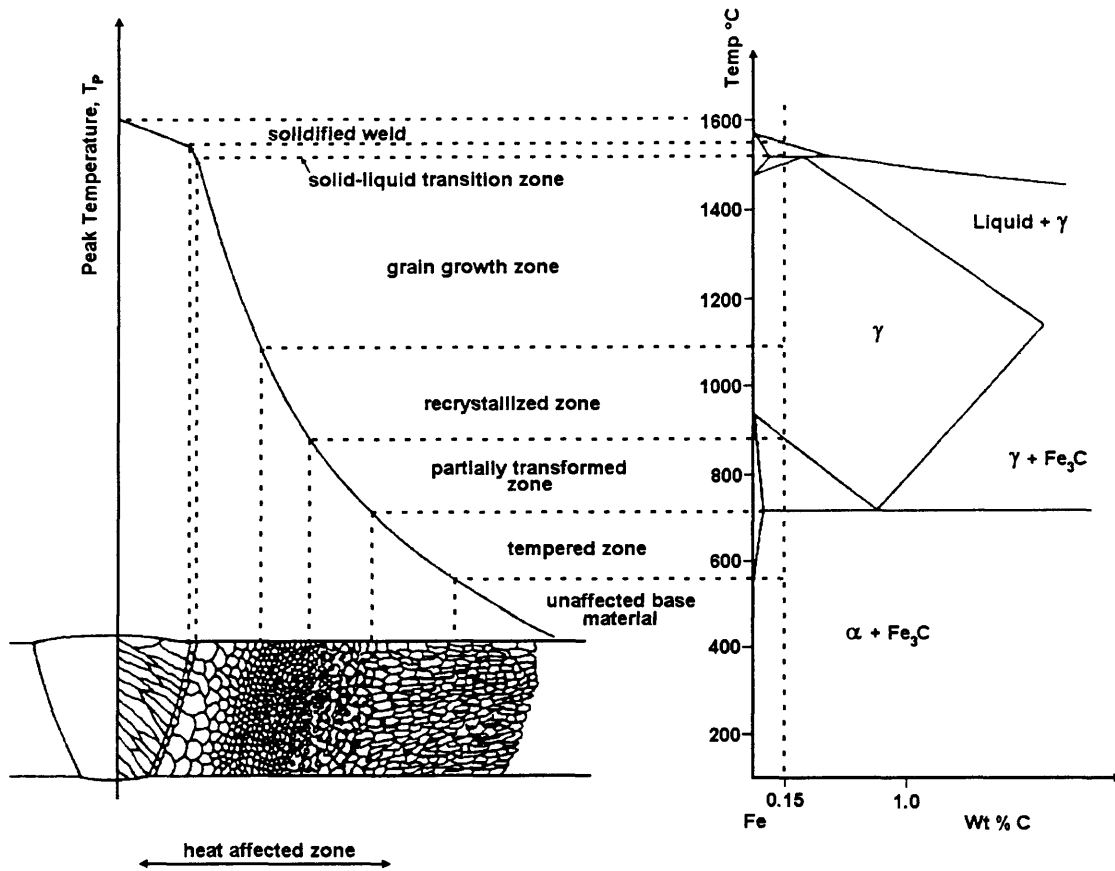
Figure 1.4   Schematic diagram of a heat-affected zone in a typical 0.15%C structural steel showing characteristic sub-zones (14).

1.2.1 Grain Growth Zone

The grain growth zone, or coarse-grained heat-affected zone, is typified by large prior-austenite grains, usually greater than $100\mu m$ in diameter (15), and is present where the material experiences temperatures between $1100°C$ and $1450°C$. The actual temperatures

that produce the coarse-grained heat-affected zone are highly dependent on the particular grade of steel. In microalloyed steels the precipitates present have a large effect on inhibition of austenite grain growth. Hence temperatures in excess of 1100°C are commonly required in these steels to produce significant grain growth. The large austenite grain size is generally attributed to continuous grain growth of the austenite (16). Due to the high temperatures experienced adjacent to the weld, nearly all precipitates dissolve. This precipitate dissolution, combined with the increased austenite grain size, provide the increased hardenability required to allow the formation of low-temperature transformation products (15). These low-temperature transformation products and/or coarse ferritic microstructure which result from the coarse austenite grains, contribute to inferior toughness (6). Consequently there has been much interest in controlling austenite grain growth in this zone to minimize the effects that contribute to decreased toughness. More-detailed descriptions of some of the microstructural features that can occur in the coarse-grained heat-affected zone will be addressed in a subsequent section.

1.2.2 Recrystallized Zone

The recrystallized zone, or fine-grained heat-affected zone, is found in the region of the material that experiences temperatures between approximately 850°C and 1100°C, depending on the steel grade. Microalloyed steels generally produce wide fine-grained

heat-affected zones due to the presence of carbonitride precipitates that impede grain

growth (15). As a result of these precipitates, the range of temperatures that yield small

austenite grains is increased. In this region, ferrite nucleation is enhanced by the large grain

boundary area inherent from the small grain size. Austenite that does not transform to

ferrite may transform to pearlite or other ferrite-carbide aggregates, depending on carbon

content and the material's hardenability. This region generally has strength and ductility

values that are improved over the base material (16).

1.2.3 Partially-Transformed Zone

This zone occurs where the material is reheated to temperatures between the Ac_1 and

Ac_3. It is also known as the intercritical heat-affected zone. Only carbon-rich components

and the regions immediately adjacent to them transform into austenite. Precipitates that do

not dissolve may coarsen during reheating and the dislocation density of the ferrite that does

not transform to austentite can decrease (15). Since it is largely the carbide-containing

microconstituents that transform to austenite, and since the austenite formation is limited,

the resulting austenite can be highly enriched in carbon. Depending upon the cooling rate,

the entire range of transformation products can be formed (16).

1.2.4 Tempered Zone

The tempered zone is also know as the subcritical zone. Between approximately 700°C and 750°C spheroidization of cementite in pearlite may occur. Beyond this, there is comparatively little change in the microstructure (14,15)

1.3 Microstructures Formed From Austenite During Cooling

In the low-carbon steels generally used for structural applications, the microstructure of the coarse-grained heat affected zone is predominantly comprised of ferritic components, usually a mixture of several forms of ferrite with bainite and/or martensite (15). This mixture is comprised of constituents that can be described as the following (in descending order of transformation temperature) (17):

a. grain boundary (allotriomorphic) ferrite
b. polygonal (equiaxed) ferrite
c. Widmanstätten ferrite
d. acicular ferrite
e. upper bainite
f. lower bainite
g. martensite

When the material of interest has a low carbon equivalent, proeutectoid ferrite may form networks about the prior-austenite grain boundaries. With higher carbon equivalents,

Widmanstätten sideplates commonly are nucleated upon the allotriomorphic proeutectoid

ferrite. Depending on the material and the cooling rate, the interior of the prior-austenite

grain may be comprised of any of the lower transformation products (14). However, the

proeutectoid phase may not be present and the microstructure can be predominantly bainitic

(15). The overall microstructure of course depends on the hardenability of the material and

its thermal history.

The preceding list of microstructural components provides a general idea of what

can be present in a microstructure corresponding to the coarse-grained heat-affected zone.

The terms provided in the above list by Grong are subject to some debate. Most of this

debate centers upon the microstructures previously termed as acicular ferrite and upper

bainite. What some researchers would term upper bainite, others would term acicular

ferrite. Since different researchers have different terms for microstructural constituents, it is

instructive to provide a brief overview of some of the more common classification systems.

1.4 Ferrite and Bainite

Krauss and Thompson (18) have recently published work on the debate of the

classification of ferritic and bainitic microstructures found in low-carbon steels. They have

not been alone in the attempt to provide a system for the identification of these sometimes

complex microstructures. The International Institute for Welding has recognized a need for

classification in low carbon weld metals (19), and many others have ventured into the

debate on bainite (20,21,22). This overview will begin with bainite.

1.4.1 Traditional Bainite

Bhadesia and Christian (23) describe bainites, upper and lower, as "aggregates of

platelets or laths of ferrite separated by regions of residual phases." In their definition, the

residual phase may consist of retained austenite, martensite, or cementite. In upper bainite,

the ferrite laths do not contain carbides. Rather, carbides precipitate from enriched retained

austenite between the ferrite laths. If cementite precipitation between laths sufficiently

reduces the carbon concentration of the remaining austenite, it may then transform to ferrite.

In lower bainite, there is also precipitation of cementite between the ferrite laths, however,

additional carbides (epsilon or cementite) also are found in the interior of the ferrite laths.

These intragranular carbides have a specific orientation with the ferrite, approximately 60°

to the major axis of the lath. Due to the interior carbides in lower bainite, there is less

carbon enrichment to retained austenite, and therefore, the volume fraction of the retained

austenite is less than in upper bainite. These ferrite-carbide aggregates describe the classical

forms of bainite.

1.4.2 Classification of Ohmori, *et al.*

Ohmori, *et al.* (21,24) provided an extension to the traditional definitions such as those described above. They defined four types of bainite, three morphologies of upper bainite and lower bainite. The three upper bainite morphologies are termed Bainite I (BI), Bainite II (BII), and Bainite III (BIII) and are shown in Figure 1.5 a), b), and c), respectively. Bainite I is the novel morphology here as it accounts for non-carbide containing microstructures. Bainite II and Bainite III, correspond to the classical upper and lower bainite in constituents and morphology.

Although not explained in the papers, presumably the difference between Bainite III and lower bainite is the observed transformation temperature. The temperature separating the two original bainites, upper and lower, was thought to be approximately 350°C. In the experimental work BIII was observed to occur at approximately 500°C. The temperature ranges where the different bainite morphologies were observed is shown in Figure 1.6.

Interestingly, in the original work by Ohmori, *et al.*(21), the BI structure was termed as carbide free. In later work (24) a table is presented for the types of bainites oberved. It is reproduced in Table 1.1. As shown in this table, BI now has carbide present in the interlath region, and the component without carbide is termed acicular ferrite.
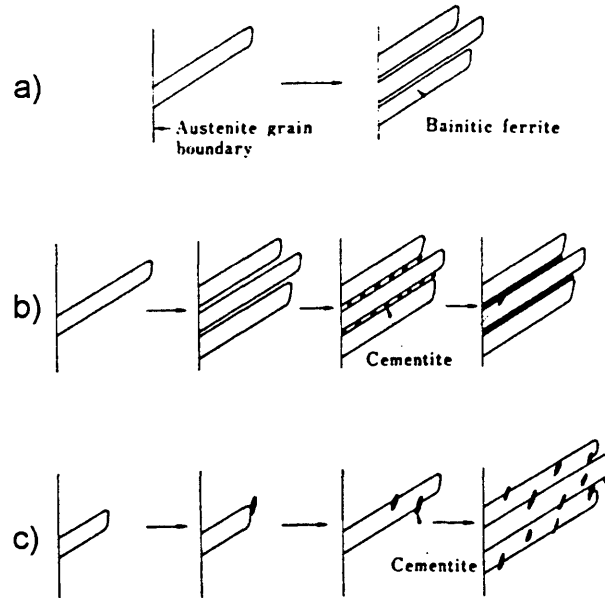
Figure 1.5. Morphology of types of upper bainite (after Ohmori, *et al.* (21)).
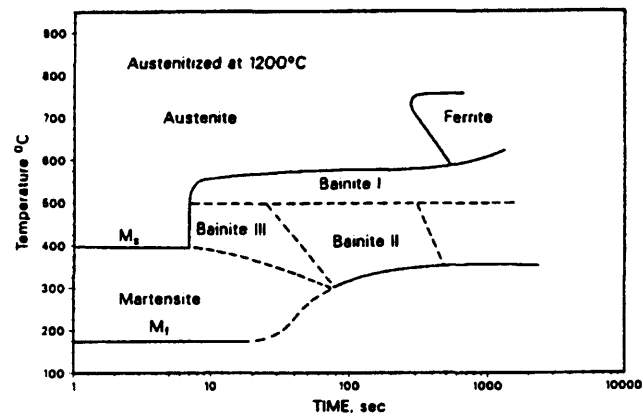
Figure 1.6. Schematic CCT diagram showing where the three bainite forms were observed to occur (after Ohmori, *et al.* (21)).

Table 1.1. Ohmori, *et al.*, system of bainite morphology (After Ohtani, *et al.* (24)).

Phase	Criteria	
	Ferrite Morphology	Carbide Distribution
Ferrite	lathlike	acicular ferrite (carbide free)
Upper bainite	BI	lath interface
	BII	
	BIII	
Lower bainite	platelike	within grain

1.4.3 Classification of Aaronson, *et al.*

The works of Bhadesia and Christian and Ohmori, *et al.* previously outlined only account for acicular ferritic crystals, either with or without carbides present. Aaronson and his coworkers (25) incorporated ferritic crystals that are not acicular in nature, as shown in Figure 1.7. In this system, bainite is defined as "the product of the diffusional nucleation and the competitive ledgewise diffusional growth of the two phases comprising the products of a eutectoid reaction" (20). In case of low carbon steels, those products are ferrite and cementite. Consequently, no allowance is made for microstructures that contain components other than those two, such as retained austenite or martensite/austentite constituent.
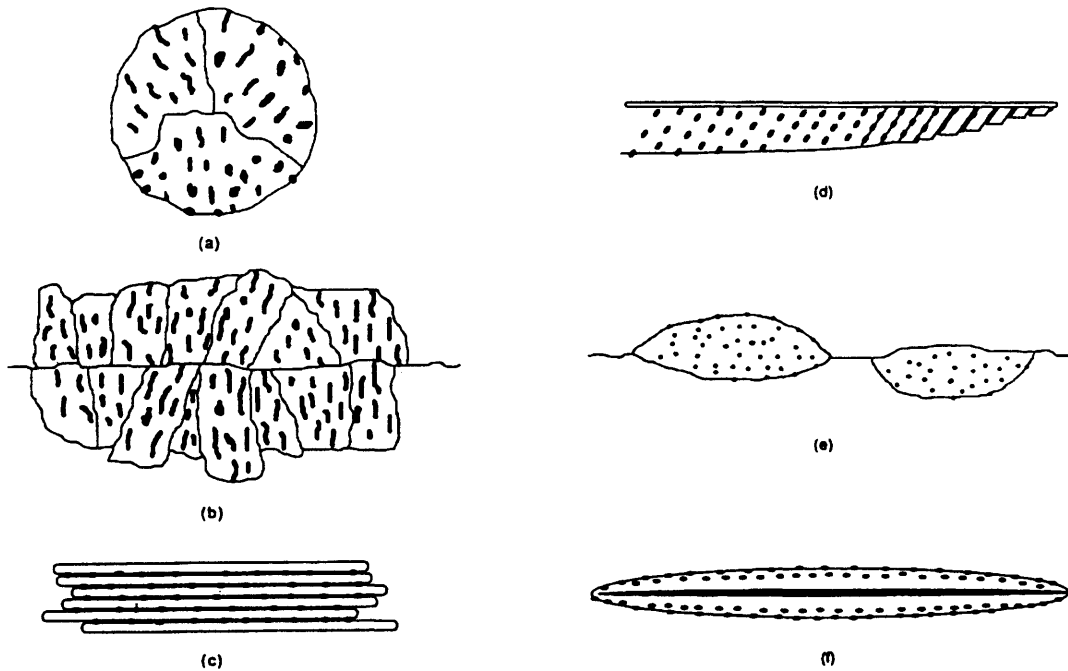
Figure 1.7. Bainitic microstructures under the system of Aaronson, *et al.* (20,25). Dark is cementite, white is ferrite. (a) Nodular bainite, (b) columnar bainite, (c) upper bainite, (d) lower bainite, (e) grain boundary allotriomorphic bainite, and (f) inverse bainite.

1.4.4 Classification of Habraken and Economopoulos

Habraken and Economopoulos (26) introduced a class of microstructures that "consisted of ferrite and carbon-rich zones, partly transformed into martensite, that did not necessarily contain carbides". These microstructures were produced by continuous cooling. While microstructures consistent with classic upper and lower bainite were observed, non-traditional structures, containing martensite/austenite islands in a matrix of what appeared to

be massive ferrite, were common. These martensite/austenite islands were equiaxed and the

ferrite crystals did not have the traditional acicular morphology. The authors termed this

microstructure "granular bainite". A schematic CCT diagram showing the types of cooling

rates that could lead to the granular bainite structure, as well as the standard upper and

lower bainite, is reproduced in Figure 1.8.
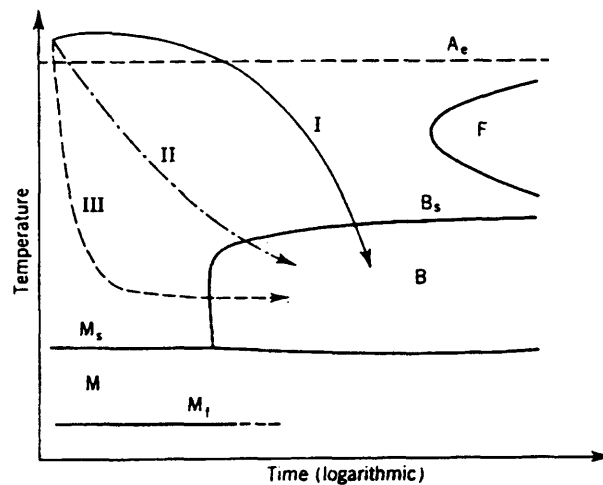
Figure 1.8.   Schematic CCT diagram from Habraken and Economopoulos (26).
              Granular, upper, and lower bainite are produced from paths I, II, and III,
              respectively.

1.4.5 Classification of Bramfitt and Speer

Bramfitt and Speer (22) have written a excellent review of bainitic and acicular

ferritic microstructures. They also provide a classification system that accommodates

various second phases is association with acicular ferrite laths. In this system ferrite present

in allotriomorphic or polygonal morphology would be excluded from the bainite class.

Three classes of bainite are proposed based upon the relationship between the ferrite laths

and the secondary constituents. There is no attempt made to differentiate between platelike

and lathlike morphologies in the Bramfitt and Speer system. Below is a listing of the three

classes of bainite (the Arabic numerals are used to avoid confusion with the Ohmori

system).

Table 1.2. Bainite classes in the Bramfitt and Speer classification.

Bainite Class	Abbreviation	Second Phase
1	B_1	Intralath constituents
2	B_2	Interlath films or particles
3	B_3	Discrete regions of retained parent phase (or secondary transformation product)

Along with the three classes of bainite, the other corresponding transformation

products are denoted with a superscript. The notation for these constituents are the first

letter of the constituents name (except for epsilon carbide): a - austenite, c - cementite, m -

martensite, p - pearlite, and ε - epsilon carbide. The classification system is shown

schematically in Figure 1.9.

Austenite

Martensite   Pearlite

Polygonal Ferrite

Bainite

B_1	B_2	B_3
acicular ferrite with intralath (plate) precipitation	acicular ferrite with interlath particles or films	acicular ferrite with "discrete-island" constituent
cementite (B_1^c)	cementite (B_2^c)	austenite (B_3^a)
epsilon carbide (B_1^ε)	austenite (B_2^a)	martensite (B_3^m)
	martensite (B_2^m)	pearlite (B_3^p)
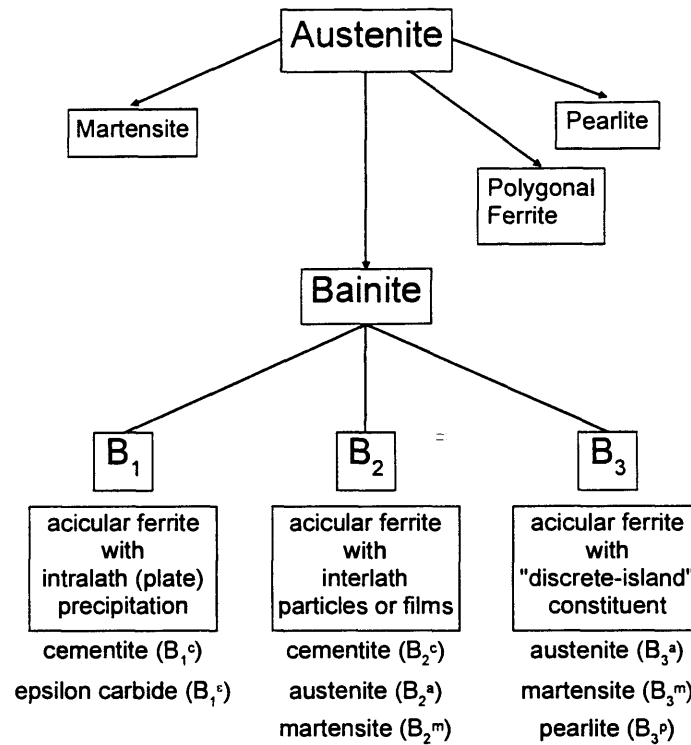
Figure 1.9. Schematic diagram for the Bramfitt and Speer bainite classification system (22).

Based on the Bramfitt-Speer system, traditional lower bainite would be classified as B_1^c (or B_1^ε). Correspondingly, traditional upper bainite would be B_2^c. Most granular bainites, a term that does not appeal to Bramfitt and Speer, would fall under the third bainite class as $B_3^{m,a}$. As shown in the last example, combinations of constituents can be implemented effectively so long as the user is careful. Microstructures such as $B_1^c + B_2^c$ are quite different from $B_{1,2}^c$. In the first case, the two different constituents exist in completely different packets, while in the latter designation, adjacent laths demonstrate attributes of B_1 and B_2.

1.4.6 Classification of International Institute for Welding

The last classification system to be discussed here is from the International Institute for Welding (IIW) (19). This classification is aimed directly at identifying microstructures with light microscopy. While this classification was intended for use with weld metals, many of the microstructural constituents are common to continuously cooled specimens and heat-affected zones. This specification is for major microstructural constituents and not "microphases".

The first defined constituent is primary ferrite (PF). It is subdivided into grain boundary ferrite (PF(G)) and intragranular polygonal ferrite (PF(I)). The subdivision obviously refers to the of nucleation of the proeutectoid ferrite.

Acicular ferrite is defined as adjacent needle-like or plate-like crystals of ferrite that are not aligned, are relatively small, and are found in the interior of the austenite grains. Note the difference in terminology here between previous references to acicular ferrite in baseplate microstructures. When discussing bainites in the baseplate classifications, acicular ferrite is lathlike ferrite cystals separated within packets by low angle boundaries or second phases. The differences between the weld metal and baseplate references to acicular ferrite are also extended to the regions were the constituents form. In weld metal, acicular ferrite is nucleated intragranularly, while the acicular ferrite referenced in baseplate studies is typically first formed at austenite grain boundaries. Bhadesia and Christian (23) assert

that this is the only difference between what is termed acicular ferrite in the welding

community and what is defined as bainite (bainitic ferrite) in the baseplate community.

They suggest that the relatively high density of oxide inclusions found in a weld deposit

causes independent nucleation of ferrite laths in close proximity. These laths then impinge

upon each other, preventing the traditional sheaf morphology. In fact, the authors report

that both acicular ferrite (welding connotation) and bainite can form under the same

isothermal transformation conditions, provided that the steel has high inclusion content

(23). The difference is simply a matter of austenite grain size. For bainite to form, the

austenite grain size must be small so that grain boundary nucleation is dominant over the

inclusion nucleation. Conversely, if the austenite grain size is large, then the inclusion

nucleation mechanism can operate effectively and acicular ferrite can form.

The bainites discussed in the previous sections fall under the designation of "ferrite

with second phase" in the IIW specification. This designation is subdivided into two forms:

ferrite with aligned second phase (FS(A)) and ferrite with non-aligned second phase

(FS(NA)). This designation applies when the area of interest consists of two or more

parallel ferrite laths. If there are only two laths, the aspect ratio of the laths becomes the

determining factor. For aspect ratios greater than 4:1 the constituent is FS, otherwise it is

classified as acicular or primary ferrite. Ferrite with non-aligned second phase is applied

when ferrite completely surrounds equiaxed microphases or isolated acicular ferrite laths. It

is left to the person examining the microstructure to determine if more precise definition can

be applied. In the case of aligned second phases the possibilities are sideplates (FS(SP)), bainite (FS(B)), upper bainite (FS(UB)), and lower bainite (FS(LB)). It is unlikely that these latter, very specific microconstituents can be identified with the light microscope.

Another classification is ferrite/carbide aggregate (FC). This designation applies to fine ferrite/carbide structures such as pearlite. If it is possible to identify the structure as pearlite, then it is reflected in the abbreviation FC(P). This term is used only if the structure is larger than adjacent ferrite grains. If this is not the case the structure is considered a microphase. The IIW specification does not account for microphases. If in point counting the crosshairs intersect at a microphase, then the surrounding microstructure is identified and reported.

The last constituent specified is martensite, M. The same rules apply to martensite as to the ferrite/carbide aggregate. The martensite colony must be larger than the adjacent ferrite grains or it is considered a microphase.

To aid in the identification of microstructures, the IIW specification includes schematic diagrams for the various microconstituents. These diagrams are shown in Figure 1.10. The IIW also provides a flow chart for phase identification which is reproduced in Figure 1.11.
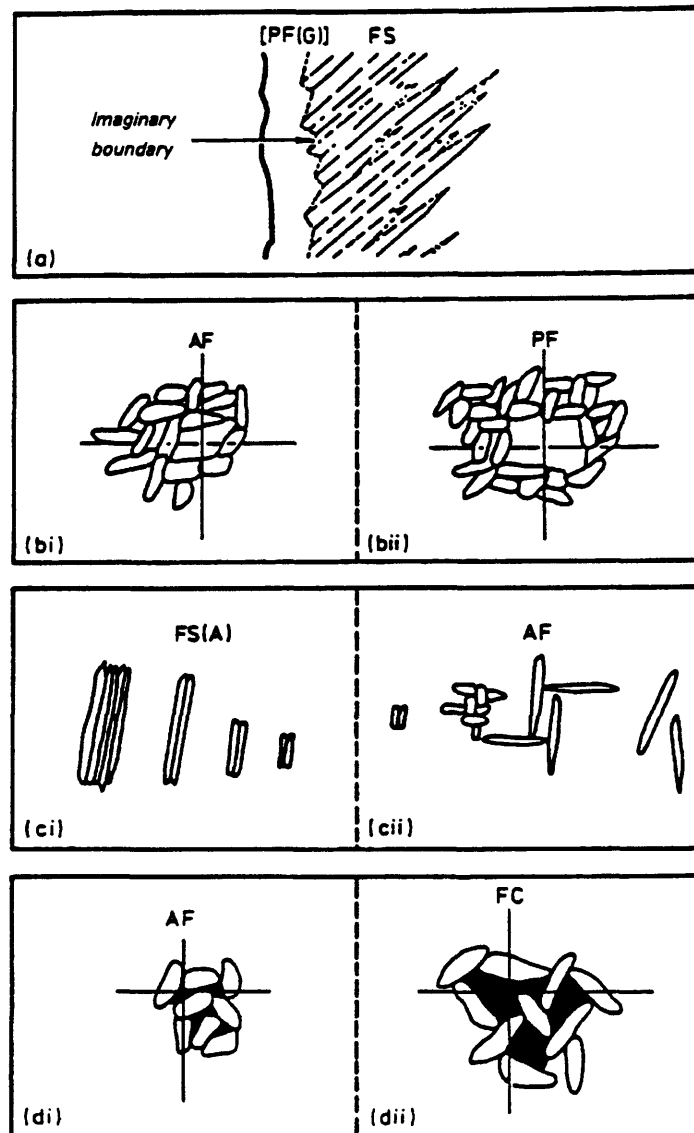
a) Imaginary boundary joining ends of second phases (indicated by dotted line);

bi) Ferrite under crosswire < 3 X average lath width;

bii) Ferrite under crosswire > 3 X average lath width;

ci) Two or more parallel laths and aspect ratio > 4:1;

cii) Two parallel laths with aspect ratio < 4:1 or non-aligned laths or isolated high aspect ratio laths;

di) Area of FC colony under crosswire < individual ferrite lath area;

dii) Area of FC colony under crosswire > individual ferrite lath area

Figure 1.10. Schematic diagram for identification of microstructural constituents in the IIW classification (19).

Examine the microstructural constituent at the grid point

Is it ferrite? — Yes

No

Is it a non-metallic inclusion? — Yes

Is the colony size larger than the intra-granular ferrite (FS or AF) lath size? — Yes — Is it martensite? — Yes — (M)

No — (FC)

Inclusion

Micro-phase — No

Examine the surrounding (or the nearest) ferrite

Does it surround either micro-phases or laths of AF? — Yes — (FS)

No

Does it lie on a prior austenite grain boundary or sub-boundary? — Yes — (PF(G))

No or don't know

Is the length to width ratio > 4:1? — Yes — Is there an immediately adjacent parallel lath? — Yes — (FS)

No — No

Is the ferrite grain size > 3× the average width of laths within prior austenite grains? — Yes — (PF)

No

(AF)

Main category	Sub-category	Abbreviation
Primary ferrite		PF
	Grain boundary ferrite	PF (G)
	Intragranular polygonal ferrite	PF (I)
Ferrite with second phase		FS
	Ferrite with non-aligned second phase	FS (NA)
	Ferrite with aligned second phase	FS (A)
	Ferrite side plates	FS (SP)
	Bainite	FS (B)
	Upper bainite	FS (UB)
	Lower bainite	FS (LB)
Acicular ferrite		AF
Ferrite-carbide aggregate		FC
	Pearlite	FC (P)
Martensite		M
	Lath martensite	M (L)
	Twin martensite	M (T)

Figure 1.11. Flowchart for phase identification in the IIW system (19).

1.5 Fundamental Issues Related to Toughness of Low-Carbon Ferritic Steels

Toughness is the measure of a material's ability to absorb energy by plastic deformation (27). Toughness can be considered as the area under a stress-strain curve and is thus a property that is a function of both strength and ductility. This area quantifies the work per unit volume that a material can absorb before rupture. In comparing two steels, one may have a lower strength than the other but still demonstrate greater toughness, due to superior elongation to failure. This feature is shown schematically in Figure 1.12.
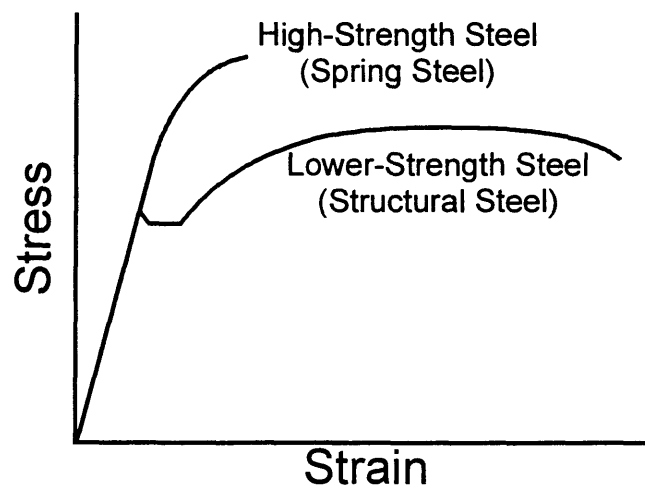
Figure 1.12. Schematic diagram depicting difference in toughness of high-strength and lower-strength steels (After Dieter (27)).

When a material fractures in a brittle manner, little energy is absorbed, and thus the material is not "tough" (28). Consequently, it is beneficial to design materials that fracture

in a ductile manner so that energy can be consumed via plastic flow. For the material to undergo plastic flow prior to failure it is important to eliminate the factors that promote brittle fracture, or cleavage, as much as possible. To effectively eliminate these factors, it is important to have an understanding of brittle fracture. The following section will address some of the fundamentals of brittle fracture.

1.5.1 Brittle Fracture

Most works on brittle fracture begin with, or are derived from in some fashion from, the work of Griffith (29). Griffith's work was concerned with the discrepancy between the theoretical fracture strength of materials, associated with the stress required to break the bonds of adjacent planes of atoms, and the maximum strength observed in materials. The theoretical fracture strength of materials, derived from atomic bond cohesive strength versus atomic separation, is commonly estimated to be one tenth of the elastic modulus of the material, E/10 (30). However, the observed fracture stresses of engineering materials are 10 to 1000 times lower than this theoretical value.

Griffith deduced that flaws must be present in all materials and that these flaws provide stress concentrations such that local stresses in the material exceed the theoretical fracture stress, even if the nominal stress is well below the theoretical strength. Griffith's theory is essentially an energy balance between the stored energy from elastic strain and

energy required to create new surfaces when the material separates. Consider the schematic

diagram depicted in Figure 1.13. This diagram shows a semi-infinite plate of negligible
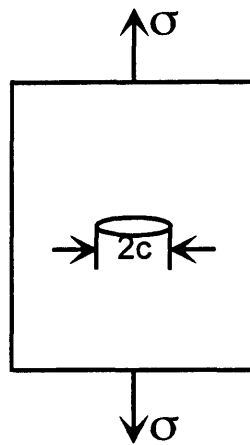
Figure 1.13. Schematic diagram of semi-infinite plate for Griffith crack model.

thickness, with an elliptical crack in its center, of length 2c. Without going through

exhaustive derivation here (see Ref. 30 for details), the energy balance yields the following

relation:

$$\sigma = \left(\frac{2E\gamma_s}{\pi c}\right)^{\frac{1}{2}}$$

Eqn. 1.1

where σ is the critical stress above which the crack will propagate, E is the elastic modulus,

γ_s is the surface energy of the material, and c is one-half the crack length. As mentioned

above, equation 1.1 is for a plate of negligible thickness, or a plane stress condition. There

is a similar relation for a thick plate, or a plane strain condition:

$$\sigma = \left(\frac{2E\gamma_s}{(1-v^2)\pi c} \right)^{\frac{1}{2}}$$
Eqn. 1.2

where v is Poisson's ratio.

Griffith's analysis was performed using a perfectly brittle, glasslike model material. Consequently, no plastic deformation takes place. However, in metals, even if they fail in a completely brittle fashion, some work of plastic deformation is done near the crack tip (30). To account for this work of plastic deformation, Orowan (31) suggested the surface energy term in Griffith's equation be substituted with an effective surface energy term, $\gamma_s + \gamma_p$, where γ_p reflects the work of plastic flow during crack extension. The value of γ_p has been estimated as 10^2 to 10^3 J/m^2, while γ_s is approximately 1 to 2 J/m^2. Consequently, equation 1.1 can be rewritten as (30):

$$\sigma_f = \left(\frac{2E(\gamma_s + \gamma_p)}{\pi c} \right)^{\frac{1}{2}} \approx \left(\frac{E\gamma_p}{c} \right)^{\frac{1}{2}}$$
Eqn. 1.3

Now that there is a way to account for the decreased fracture strength of materials, due to the presence of flaws, the question remains what causes these flaws.

In steels there are several sources for internal flaws, or microcracks. Fracture of second phase particles, such as carbides and nitrides will result in microcracks (see following section on microstructural components and toughness). Dislocation pile-ups at barriers can cause microcracks as well. A good discussion of this process is provided by

Dieter (32) and readers are directed there for an in-depth presentation. A brief discussion here will provide a basic understanding of the process.

When a material is loaded sufficiently, dislocations glide along active slip planes until a barrier is reached. A barrier could consist of a second-phase particle or a grain boundary. The barrier prevents further dislocation glide and, if cross-slip is negligible, subsequent dislocations pile-up behind the barrier. As the stress builds, the dislocations are forced closer together until some critical value is reached where the dislocations coalesce into a wedge crack. It is possible that the stored strain energy is sufficient to grow the microcrack without more dislocation motion to the pile-up, causing complete fracture. However this is not common in metals, which generally exhibit a growth stage where the applied stress must be increased to grow the microcrack. It is therefore the stress to propagate the microcracks that is the material's fracture stress.

Brittle fracture should be avoided if at all possible. The catastrophic manner in which brittle fracture occurs makes it very dangerous in structures. In steels, the service temperature can be critical in preventing cleavage fracture. The following section will discuss why this is so.

1.5.2 Ductile-to-Brittle Fracture Transition

Another interesting phenomenon observed in body-centered-cubic (BCC) metals is

the ductile-to-brittle fracture mode transition. At low temperatures BCC metals fail in a

brittle manner, while at high temperatures failure occurs in a ductile manner by void

nucleation, growth, and coalescence. The work of Cottrell (33) provides a theoretical basis

for the transition based upon the dislocation model for microcrack formation previously

discussed. He provides an equation to show the important parameters involved in brittle

fracture:

$$\left(\tau_i D^{\frac{1}{2}} + k'\right)k' = G\gamma_s \beta \qquad \text{Eqn. 1.4}$$

where τ_i is the resistance of the lattice to dislocation movement, D is the grain size, k' is a

parameter related to the release of dislocations from a pile-up, γ_s is the effective surface

energy (including the energy of plastic deformation), and β is a term which expresses the

ratio of shear stress to normal stress (in torsion: $\beta=1$, in tension: $\beta=1/2$, for a notch: $\beta=1/3$).

This relation describes the propagation of a microcrack; if the left side is greater than the

right side a propagating brittle crack can occur at a shear stress equal to the yield stress.

Dieter provides a good explanation of the significance of these parameters to

microstructures (34). If the left side of the equation is smaller than the right side, a

microcrack will not grow. k' determines the number of dislocations released into a pile-up

when the source is unlocked. Materials with a high k' (such as iron and molybdenum) are more likely fail in a brittle fashion than materials with lower k' (such as niobium and tantalum). Strengthening mechanisms that rely upon locking of dislocations are likely to cause brittleness. The temperature dependence of fracture mode comes from the τ_i term. In BCC metals the frictional resistance increases rapidly as the temperature falls below room temperature leading to the transition phenomenon.

1.5.3 Microstructural Effects

So far the theoretical background of cleavage fracture and toughness has been presented. It is important to have this understanding; however the application to observed phenomena in structural materials is equally important. The following sections will help provide the link between observed microstructural features and toughness properties in steel grades similar to those of interest in this study.

1.5.3.1 Ferrite Morphology

It is generally accepted that ferrite grain size is a critical issue regarding impact toughness of ferritic materials (35). However, in heat-affected zone microstructures the ferrite morphology can be quite complex. The microstructures of coarse-grained heat-

affected zones are frequently comprised of combinations of polygonal and bainitic ferrites. The bainitc ferrites can span Widmanstätten ferrite to upper and lower bainite. While the specific nature of the microconstituents and the austenite decomposition mechanisms may vary greatly when considering Widmanstätten ferrite, acicular ferrite, and the bainites, a common feature of these structures is that similarly oriented crystals of ferrite lie adjacent to one another within a packet. A key question is what is the ferrite grain size?

Tian, *et al.* (36), have provided an analysis of the relationship between the types of interface found in granular bainite microstructures and the features observed in a fractured specimen. Based upon the observed features of fracture surfaces, the authors were able to determine the types of interfaces that can improve toughness. The authors concluded that prior-austenite grain boundaries and ferrite lath packet boundaries were beneficial to toughness while interfaces between MA constituent and ferrite laths were detrimental to toughness.

1.5.3.2 Titanium Nitride Precipitates

Fairchild, *et al.*, found that the presence of large titanium nitride inclusions promoted cleavage fracture in steels with similar microstructures and chemistries to those in this study (37). They define the titanium nitride inclusions as large particles ($\geq 1\mu m$) that precipitate from the liquid steel. In comparison to a steel with lower titanium content and

significantly less inclusions, the material with the large titanium nitride precipitates consistently performed more poorly. Also, fractured titanium nitride inclusions were frequently found at cleavage initiation sites in the higher-titanium-containing steel. The overall microstructure of the two alloys was similar for both baseplate and in the weld heat-affected zone, leading to the conclusion that large titanium nitride inclusions were not numerous enough to significantly affect the microstructure. However, the higher-titanium-content steel was observed to have approximately seven times the areal density of titanium nitride inclusions, resulting in the conclusion that these large precipitates were the cause of the observed decreased toughness.

Other researchers have also found large titanium nitride particles promote brittle fracture (38). While this work was associated with higher carbon content steels, the findings are consistent with those of Fairchild, *et al.*

In his dissertation, Fairchild (39) provides a model for how titanium nitrides promote cleavage in steels. Due to differences in thermal expansion of titanium nitride and steel, stresses are generated in and around the titanium nitride particle upon cooling from either primary steel processing or welding. There is radial compression in the matrix and particle and circumferential tension in the matrix. In his model, a large titanium nitride inclusion is present in the interior of a coarse prior-austenite grain that has subsequently transformed into ferrite packets. Upon loading, a dislocation source activates upon a slip plane such that the titanium nitride inclusion serves as a barrier causing a dislocation pile-

up. Fairchild suggests that the "critical" titanium nitride precipitate, the particle that

initiates the catastrophic cleavage failure, is oriented such that the dislocation pile-up

impinges on an imperfection in the particle.

At low nominal stresses there is little effect on the inclusion due to the compressive

residual stresses that resulted from the thermal history. However, as stress increases, the

compressive shielding stress is overcome and the effect from the dislocation pile-up

becomes significant. When a critical stress is achieved the titanium nitride fractures. This

crack transfers to the surrounding ferrite matrix, in what Fairchild reports to be a rotating

fashion around the titanium nitride inclusion.

1.5.3.3 Martensite/Austenite Constituent

Bernasovsky, *et al.* (40) reported that the presence of martensite-austenite (MA)

constituent can significantly decrease the notch toughness of HSLA steels. It was found

that the morphology of the MA constituent was what determined the fracture properties.

Two forms of MA constituent were observed, elongated and equiaxed, or "massive". While

the elongated MA islands (aspect ratio > 5:1) were not found to be much of a factor on

toughness, the equiaxed islands were very deleterious.

There are several mechanisms advanced for the reasons that the MA constituent is deleterious to toughness. Some of these mechanisms are outlined nicely in the work of Davis and King (41) and are shown schematically in Figure 1.14. In the first model, the
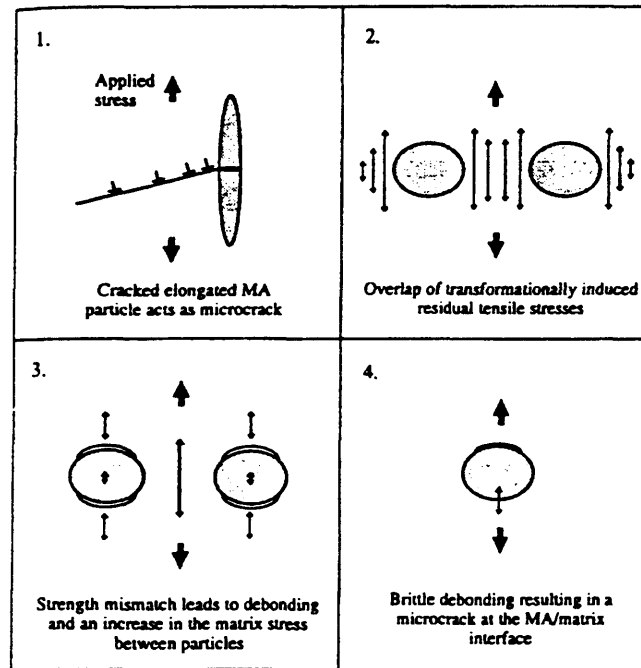
Figure 1.14. Models for mechanisms how MA constituent leads to decreased toughness (after Davis and King (41)).

MA constituent is a brittle phase that is prone to cracking. The microcracks from the MA failure initiate fracture in the ferrite matrix. Davis and King also report the occurrence of the two MA morphologies: blocky particles approximately 4 μm in diameter and elongated islands occurring between ferrite laths approximately 0.5 μm wide and several micrometers long. Davis and King observed the blocky MA to form at prior-austenite grain boundaries

during a intercritical reheat of coarse-grained heat-affected zones. In their study, the elongated MA readily cracked providing no barrier to cleavage crack propagation. The blocky particles were not observed to crack. Krauss (42) dislikes the assertion that the MA constituent is "brittle", and notes that unless embrittled, martensites will fail in a ductile mode. Perhaps the limited ductility of the martensite due to its high dislocation density is the reason it is called brittle, when actually it is not a brittle phase like cementite.

Another model is based on the residual stress field in ferrite associated with the volume expansion of the austenite to martensite transformation. The volume expansion results in a residual tensile stress in the ferrite matrix surrounding the MA particles, assisting in cleavage fracture. If there are other MA particles in close proximity the residual stress is correspondingly increased.

In the third model, the difference in strength level of the MA and ferrite matrix results in debonding. When the applied load is such that the softer ferrite matrix plastically deforms while the MA is still elastically deforming, the strain mismatch causes large stresses across the MA/matrix interface. This debonding causes stress concentrations in the matrix, particularly when the particles are closely spaced, promoting matrix failure.

A fourth model described a brittle decohesion at the MA-ferrite interface. However, no details are described as to how this decohesion occurs.

The work of Davis and King was associated with the intercritically-reheated coarse-grained heat-affected zone (IRCGHAZ). Microstructures in steels that experience this

thermal history can contain networks of blocky MA constituent along prior-austenite grain boundaries due to the second thermal cycle heating the specimen to the ferrite + austenite phase field. Correspondingly, these microstructures have MA islands in close proximity where the second proposed model may be dominant. These networks will not be present in single pass welds or simulations. In another work Davis and King (43) report that isolated blocky MA islands, as would be present in single pass weld studies, will not have detrimental effects on toughness at room temperature. However, the high aspect ratio MA particles that would be found between ferrite laths can be detrimental to toughness as these particles have a propensity to crack.

Akselsen, *et al.* (44), propose that the residual stress associated with the volume expansion of the austenite-to-martensite reaction, combined with the strain partitioning, increase stresses in the ferrite matrix near the islands. Consequently the fracture stress of the ferrite is reached much easier, resulting in cleavage fracture.

1.5.3.4 Quantitative Analysis

The work of Pickering (13) provides a quantitative correlation among some of the microstructural and compositional factors with strength and toughness of low-carbon steels. Using multiple linear regression he was able to determine equations accounting for the effect of manganese, silicon, free nitrogen, pearlite content, and ferrite grain size on the

yield strength and impact-transition temperature of low-carbon, ferrite-pearlite steels. His

equations are shown below.

Yield Stress:

$$Y.S. \ (\frac{kg}{mm^2}) = [3.5 + 2.1(\%Mn) + 5.4(\%Si)$$
$$+ 23(\sqrt{\%N_f}) + 1.13d^{-\frac{1}{2}}] \times 1.57$$

Eqn. 1.5

Impact Trans. Temp.:

$$ITT \ (^\circ C) = -19 + 44(\%Si) + 700(\sqrt{\%N_f})$$
$$- 11.5d^{-\frac{1}{2}} + 2.2(\%pearlite)$$

Eqn. 1.6

where N_f is the amount of nitrogen free in the matrix, i.e. not combined as nitrides, and d is

the ferrite grain size. As shown in the above equations, decreasing the ferrite grain size is

the only method by which both yield strength and toughness can be improved. Also shown

in the impact-transition relation is the extremely detrimental effect that free nitrogen has on

the toughness.

Pickering also provided a graphical representation of the interrelationships between

strength and toughness for the various microstructural features and steel composition.

These plots are shown in Figure 1.15. One can infer how the various strengthening

mechanisms and alloying additions affect the fundamental quantities shown in equation 1.4.

Grain size refinement is the most beneficial strengthener because toughness is not impaired.

The improvement of impact properties by manganese additions is attributed to a decrease in

k' and also a decrease in grain size (34), possibly due to a decrease in transformation

Microstructural factors

Compositional factors

Phosphorus ~ 34

Nitrogen + 19

Tin ~ 11

Carbon + 6·4

Silicon + 5·1

Manganese ~ 3·2

Aluminum ~ 17

Dislocation
strengthening

20% Pearlite
+ 44°C

+ 6

+ 4

Dispersion
strengthening

3·2

50°C

Yield
stress (kg/mm²)

Impact-
transition
temperature
(°C)

Grain
size

− 10
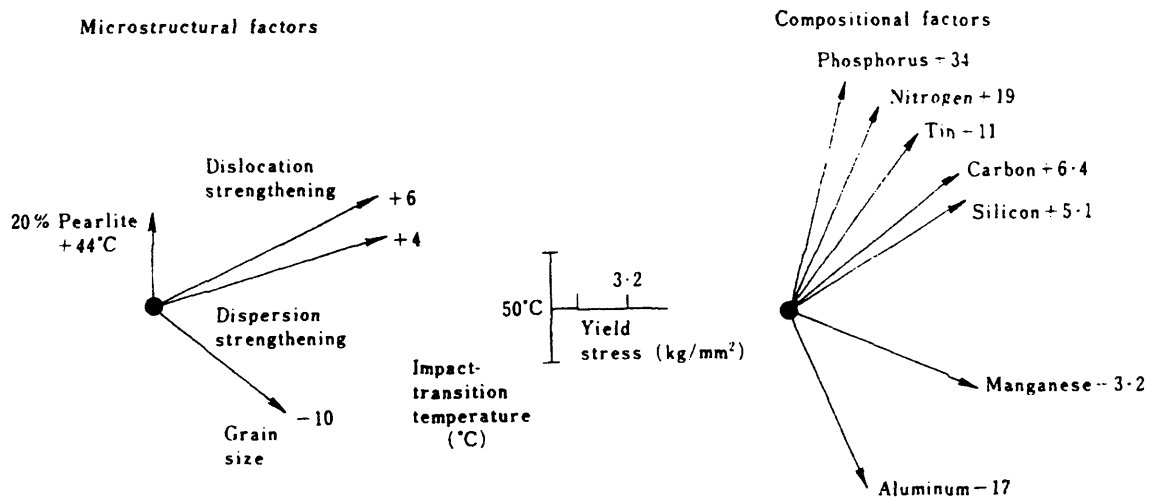
Figure 1.15. Factors affecting yield strength and impact-transition temperature (13).

temperature. The large effect of aluminum is primarily due to the gettering of nitrogen (13).

Aluminum nitrides can also be effective in grain size control, for reasons that will be

discussed later in the text. As titanium has an even greater affinity for nitrogen than

aluminum, one can propose that similar effects would be true for titanium additions as well.

The grain size referred to in the previously presented equations and discussions is

the ferrite grain size resultant from austenite decomposition. While it is clear that the ferrite

grain size is significant to the mechanical properties, the size of the prior-austenite grains is

also important. A large austenite grain size can result in transformation to coarse ferrite

grains. Clearly this is not desirable. There is another aspect of austenite grain size that is

significant to mechanical properties: the effect of grain size on hardenability. As austenite

grain size increases hardenability increases, or the likelihood of transformation to polygonal

ferrite is decreased. This can result in the formation of phases that are more likely to fail in a brittle fashion, such as untempered martensite or bainite. Obviously the austenite grain size should be kept small if at all possible. Control of austenite grain growth will be addressed in the next section.

1.6 Grain Size Control

Grain size control in the heat-affected zone of a weld is done utilizing second-phase precipitates to pin austenite grain boundaries, thereby impeding their growth. These precipitates effectively reduce the amount of grain boundary area and, therefore, the energy associated with the boundary. Consequently, an increase in grain boundary area, or energy in the system, is required for the grain boundary to migrate around the particle.

Zener first proposed a relation between the pinning particles and grain size (10), as shown below:

$$R_g = \frac{4}{3} \cdot \frac{r}{f} \qquad \qquad \text{Eqn. 1.7}$$

where R_g is the radius of the matrix grains, r is the radius of the pinning particles, and f is the volume fraction of the pinning particles. From this equation it is easily seen that the smallest grain size will result from a minimum pinning particle radius and a maximum volume fraction of particles. George and Irani (45) estimated the volume fraction of TiN

particles in a typical steel to be approximately 7.5×10^{-5}. This value matches fairly well

with Matsuda and Okumura (46), as their estimate is on the order of 10^{-4}. The former

volume fraction combined with an austenite grain size of 20 μm predicts a maximum

particle size of approximately 1.1 nm.

The Zener model is based on an isolated shrinking, spherical grain. Subsequent

analyses have shown that the Zener model overestimates the driving force of the shrinking

spherical grain. Gladman derived an equation based on another model to determine the

critical radius of pinning particles. For particles larger than this size, grain growth would

occur (11). Gladman used a model of growing tetrakaidecahedral (fourteen sided) grains, of

radius R_g, in a matrix of tetrakaidecahedral grains of radius R_0. His final equation is shown

below.

$$r_c = \frac{6R_g f}{\pi} \left(\frac{3}{2} - \frac{2}{z} \right)^{-1}$$

Eqn. 1.8

where R_g and f are the same as previously described, and r_c is the critical particle radius for

grain boundary pinning. A grain size heterogeneity factor, z, is defined as $z = R_g/R_0$, which is

between 0.2 and 2 (12). Hillert (47) deduced that the z factor would be at least 1.5 during

the grain growth process. For the same values of grain size and volume fraction of particles

used above, the critical particle size ranges from 17.1 nm at z = 1.5 to 5.7 nm at z = 2.

Figure 1.3 graphically shows the variation of particle size and grain size for z=1.5. A

critical particle radius of 13.5 nm was observed by Leduc and Sellars (48). McCutcheon, *et*

al. (49), as well as Sage, *et al.* (4), have reported particle sizes below 100 nm are effective in impeding grain boundary motion. However, values ranging from 10 to 50 nm are more commonly noted as the requisite particle size for effective grain boundary pinning (2,50,51).

It is clear from the previous discussion that the size of the second phase precipitates is of great importance when considering grain size control. The following sections will focus on how to achieve an effective particle size distribution based on particle coarsening and precipitation.

1.7 Precipitate Coarsening

At elevated temperature precipitates will grow due to Ostwald ripening. The growth may cause the particles to exceed the critical size necessary to effectively pin grain boundaries. This process is governed by the Gibbs-Thompson effect (52). In a system containing precipitates there will be a range of particle sizes resulting from different nucleation times and rates of growth. It is this variation in particle size that causes precipitate coarsening.

With two precipitates of different size, the Gibbs-Thompson effect results in two different equilibrium solute concentrations adjacent to the precipitates. The concentration adjacent to the small particle will be higher than the concentration adjacent to the large

particle. The concentration gradient will cause diffusion of the solute to the area near the large particle, resulting in the shrinking of the small particle and the growing of the large particle. This process can be extended to the entire particle distribution, where the large particles grow at the expense of the small particles, which is termed Ostwald ripening.

Wagner (53) provided an extension of Ostwald ripening to observed phenomena and determined the important parameters involved in precipitate coarsening. This work is reflected in the well-known Wagner equation, shown below:

$$r_t^3 - r_0^3 = \frac{8\sigma \, D[M]V}{9RT} \cdot t \qquad\qquad \text{Eqn. 1.9}$$

where r_t is the particle radius at time t, r_0 is the inital particle radius, σ is the surface energy of the particle-matrix interface, D is the diffusivity of the relevant atomic species, [M] is the concentration (solubility) of the relevant atomic species in the matrix, V is the particle molar volume, R is the gas constant, t is time, and T is temperature. Equation 1.9 assumes a spherical particle and is valid only for an isothermal system.

In microalloyed steels, the relevant atomic species generally refers to the microalloying element: niobium, aluminum, vanadium, or titanium. For the purposes of this study titanium will be relevant atomic species.

One may combine the Gladman equation (equation 1.8) and the Wagner equation (equation 1.9) to determine a temperature for a given time (or time for a given temperature)

at which the precipitates will grow to a size that is no longer effective. By letting $r_c = r_t$,

combining the Gladman and Wagner equations results in the following relation:

$$\left(\frac{6R_g f}{\pi}\left(\frac{3}{2}-\frac{2}{z}\right)^{-1}\right)^3 - r_0^3 = \frac{8\sigma\, D[M]V}{9RT}\cdot t \qquad\qquad \text{Eqn. 1.10}$$

One can solve either for time, or temperature, to find a critical value where precipitates are

no longer effective at pinning grains.

There are several features of the above models that are worth mentioning. First, the

grain coarsening temperature will always be below the solvus temperature of the pinning

precipitates (9). Fortunately, TiN has a very low solubility in austenite, as will be seen

later, and thus has a high solvus temperature. This feature creates a high grain coarsening

temperature that allows steel processing at relatively high temperatures while maintaining

comparatively fine austenite grain size.

Second, it is shown in the formulae that the grain coarsening temperature will be

maximized with a maximum volume fraction of pinning particles. However, these particles

must be sufficiently small to remain effective in the pinning of the grain boundaries.

Finally, the concentration of the relevant atomic species (titanium) dissolved in the

matrix is very significant to particle coarsening. Therefore it is important to have as little

dissolved titanium in the matrix as possible. Titanium is the critical species because it has a

lower diffusivity than nitrogen (13, 54). One can assume that all the nitrogen necessary to

contribute to the titanium nitride precipitate growth will be present, due to its high diffusivity in the matrix.

1.8 Titanium Nitride Precipitates

In the previous sections we have seen the importance of the precipitate size on grain size control. It is clear that small precipitates are most beneficial. How the precipitates initially form is largely responsible for their subsequent size, as nothing short of dissolving and reprecipitating the particles can reduce their size. In considering titanium nitride, extreme temperatures would be required for such a process. Consequently, great effort has been expended to determine the best way to achieve a small initial titanium nitride size distribution during steel processing. These efforts have provided much information that has been extended to subsequent steel processing and welding.

It is shown in Figure 1.16 that titanium nitride has the lowest solubility of the common microalloy precipitates. This low solubility results in very high precipitation temperatures, possibly in the liquid. It is therefore necessary to consider solubility products of the liquid steel.

It is difficult to determine the exact solubility product of TiN in steel due to the rather complex alloys that are used commercially. Many different solubility products have been proposed. Three solubility products for TiN in liquid steel are given below.
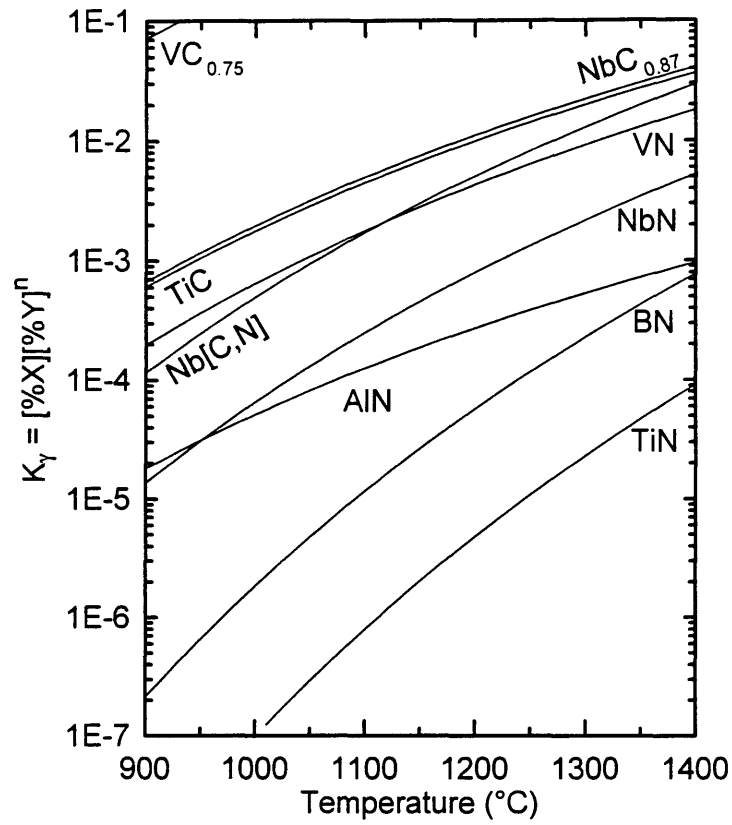
Figure 1.16. Solubility of various microalloying elements in austenite (55).

$$\log[\text{Ti}][\text{N}] = -\frac{15790}{T} + 5.40 \qquad\qquad \text{Eqn. 1.11}$$

$$\log[\text{Ti}][\text{N}] = -\frac{16130}{T} + 5.97 \qquad\qquad \text{Eqn. 1.12}$$

$$\log[\text{Ti}][\text{N}] = -\frac{17040}{T} + 6.40 \qquad\qquad \text{Eqn. 1.13}$$

The first product is from Narita (56), and the latter two are from Turkdogan (55).

For the solubility of TiN in the solid phase, there are also differences in the various

solubility products. However, the relationship put forward by Matsuda and Okumura (46)

appears to be used most frequently. This relationship is shown below:

$$\log[Ti][N] = -\frac{8000}{T} + 0.32 \qquad\qquad \text{Eqn. 1.14}$$

Another product, due to Turkdogan (55), is as follows:

$$\log[Ti][N] = -\frac{16586}{T} + 5.90 \qquad\qquad \text{Eqn. 1.15}$$

A graphical representation of Matsuda and Okumura's equation is shown in Figure

1.17. If we use the equation from Matsuda and Okumura for the solid phase (austenite), it

is clear that TiN is considerably more soluble in liquid iron than in solid. Hence,

significantly more free titanium will be present in the melt for TiN particles to grow if

precipitation occurs in the liquid steel. This precipitation would be detrimental to fracture

and the grain boundary pinning effect would be lost because the particles would be too large

to effectively restrain grain boundary migration. Indeed, particles precipitating in the melt

have been found that were approximately 15μm in diameter (57). These are roughly three

orders of magnitude too large to be effective at grain boundary pinning. It is clear that

precipitation of TiN from the melt is unwanted.
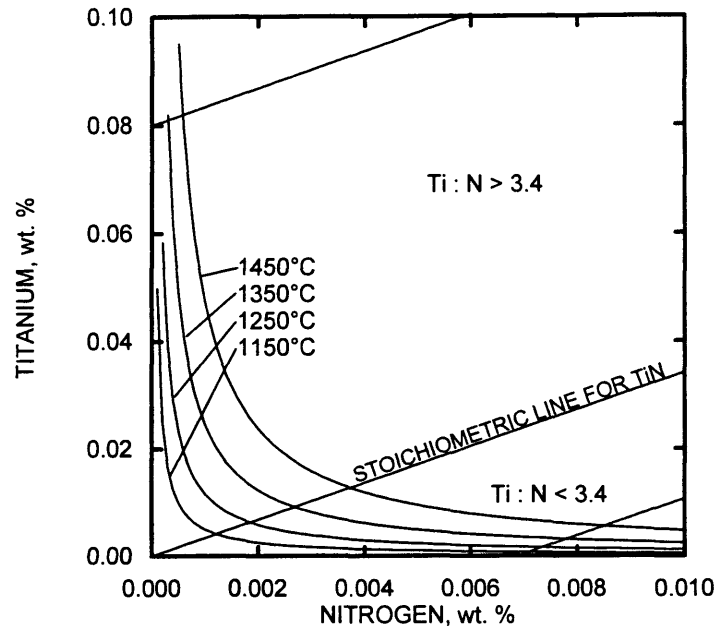
Figure 1.17. Solubility of titanium nitride in austenite as a function of nitrogen and
titanium content. After Sellars and Benyon (57). From the solubility
product of Matsuda and Okumura (46).

Precipitation in the solid may also be deleterious if it occurs at significantly high

temperatures, such as the delta ferrite range or high in the austenite range. Particles of 1 μm

diameter have been found in such cases (57). It is clear that precipitation at lower

temperatures is required to create the critical-sized particles for grain boundary pinning.

Now that the requirements for effective grain size control are known, the factors that

promote these requirements may be addressed. As mentioned earlier, relatively small

particles are required to pin grain boundaries. Fine particles are achieved by precipitation at

relatively low temperatures. One way to suppress the precipitation of TiN particles is to

keep the titanium and nitrogen contents low. It has been suggested that the titanium content

should be kept below 0.02 wt. % (9,58). Roberts has suggested that when titanium is

present in less than 0.02 wt. % , precipitation of TiN occurs below 1400°C, or in the solid

phase (59). Further, it has been reported that additions of over 0.01 wt. % do not

significantly increase the amount of precipitates which effectively restrain grain growth, but

only increase the amount of large TiN particles (60). Another benefit of low titanium

content (0.01 to 0.02 wt. %) is that the amount of free titanium left in the matrix is reduced,

which prevents coarsening of the pinning particles, and, therefore, grain growth is

minimized.

The issue of the amount of nitrogen to add is also important. If nitrogen is added in

the stoichiometric amount (Ti:N = 3.4 by weight), the grain coarsening temperature is

maximized (48). The precipitation of the TiN particles occurs at the lowest temperature for

stoichiometric additions. This temperature is naturally associated with the finest particle

sizes (61). As shown in Figure 1.18, these fine-sized particles yield a grain coarsening

temperature up to 50°C higher than for hypostoichiometric additions of nitrogen(Ti:N<3.4).

However, hypostoichiometric additions appear to have some advantages. For a

fixed titanium level in a hypostoichiometric steel, an increase in the nitrogen content causes

an increase in austenite grain size stability. Specifically, an increase in nitrogen forces more

titanium out of solution to provide a greater volume fraction of the pinning particles. As a

consequence, the titanium that has been removed from solution cannot contribute to
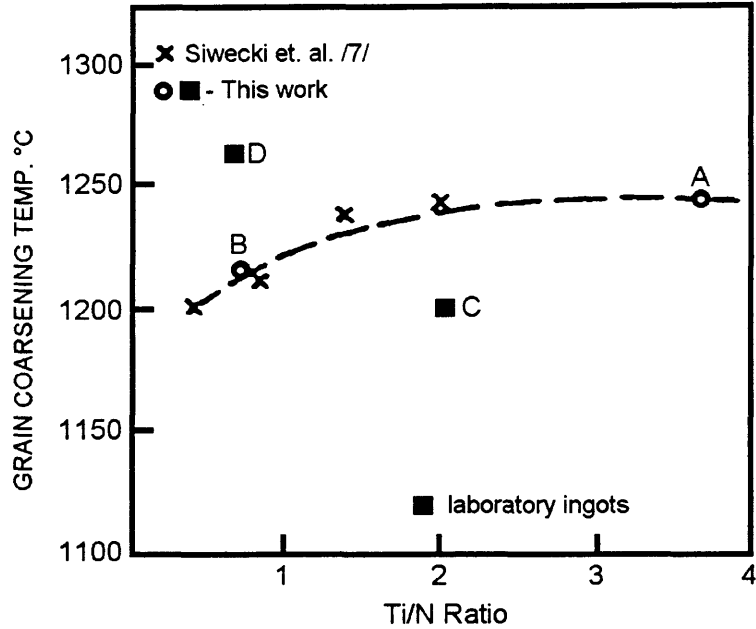
Figure 1.18. Effect of Ti:N ratio on the grain coarsening temperature (61).

coarsening of the particles to sizes beyond effectiveness (9,61,62). Some researchers have

found that even though the grain coarsening temperature may be higher for steels with

stoichiometric additions, the austenite grain size is smaller for hypostoichiometric steels

below the grain coarsening temperature (9,61). This feature is shown schematically in

Figure 1.19.

In one study it has been found that hypostoichiometric additions of nitrogen

suppress grain growth in heat-affected zones of Ti-V steels (63). Also, maintaining the

specimen at a peak temperature of 1350°C did not cause significant grain growth with

hypostoichiometric nitrogen additions. The critical radius for dissolution was calculated to
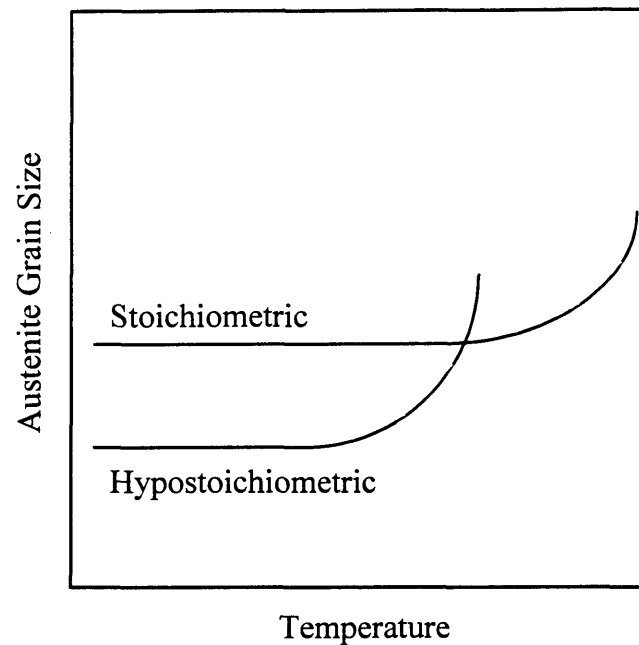
Figure 1.19. Schematic diagram showing grain coarsening characteristics for stoichiometric and non-stoichiometric alloys.

be only 17.1 nm for a hypostoichiometric steel, while for the stoichiometric steel the critical radius was 37.9 nm. 90% of the TiN particles would dissolve when the critical radius was 37.9 nm.

In contrast, other researchers have found best results with stoichiometric additions of titanium and nitrogen (64). The finest austenite grain size in the HAZ was observed with stoichiometric additions.

Another way to depress the precipitation temperature is to cool the material rapidly, as in continuously-cast steel. Figure 1.20 shows the TiN particle distribution obtained for a continuously-cast steel which contained 0.015 wt. % titanium and 0.05 wt. % nitrogen.
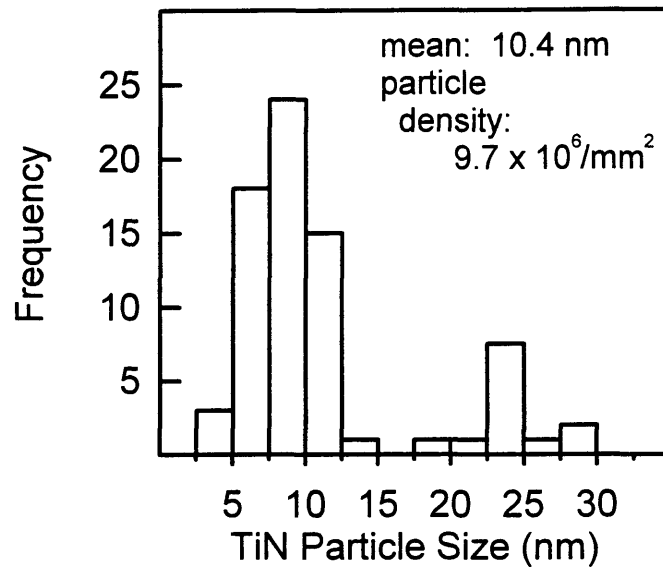
Figure 1.20. Typical TiN particle size distribution in a continuously-cast slab (56).

Rapid cooling creates the small particle sizes required to effectively pin austenite grain boundaries. The depressed precipitation temperature associated with rapid solidification would benefit hypostoichiometric alloys. Specifically, the combination of small particle sizes and high volume fraction would have beneficial effects on grain size.

In a comparison of commercial-sized ingots (10 tons) and continuously-cast blooms (220 mm square), particle size differences are striking. The average diameter of particles in a continuously-cast material was 8 nm, while the particles in an ingot were 62 nm. The resulting grain coarsening temperature was some 200°C higher for the continuously-cast material (9). It appears that grain size control by TiN particles would be most effective in continuously-cast material. Problems inherent to large ingots, such as variable cooling rates and partitioning of alloying elements, could cause considerable variation in grain growth

characteristics. However, cooling rates in small ingots (150kg) have been found to have similar cooling rates as 200-mm continuously cast blooms, thereby resulting in precipitates sufficiently small to prevent significant grain boundary migration (9,61).

The effect of carbon content should not be overlooked. As carbon content increases, the liquidus temperature of the steel decreases. With higher carbon levels, more precipitation of TiN will occur in the liquid phase. This precipitation in the liquid causes a higher percentage of large particles that are ineffective at pinning grain boundaries (9). To keep the particle size small, low carbon contents should be implemented, if possible.

1.9   Influence of Microalloying Elements on Titanium
        Nitride Precipitates

Since it is common for multiple alloying elements to be combined in a steel to achieve the desired final properties it is appropriate to discuss how these elements may interact. It has been suggested that titanium additions will only be effective in steel if the material is aluminum killed. If the steel is not aluminum killed, titanium will be lost to oxygen. Reynolds (65) reports that at least 0.01% aluminum must be added to allow titanium nitrides to effectively reduce grain growth in a 0.35C-1Cr steel in the 1100-1300°C range.

Given that the titanium is appropriately protected from loss to oxygen, the other microalloying become significant. Vanadium, for example, is added as a precipitation

hardening agent for ferrite. Vanadium nitride and carbonitride precipitate at relatively low temperature, approximately 750°C. Niobium carbonitride particles are primarily used to prevent recrystallization during controlled rolling to create deformed austenite grains with a high surface-area-to-volume ratio, ultimately leading to a fine ferrite grain size. Niobium carbonitride precipitates on austenite sub-boundaries at approximately 1000°C (7).

Regarding steels with multiple microalloying element additions, the carbonitrides of titanium, vanadium, and niobium are mutually soluble in each other (66,67,68,69). The crystal structure of vanadium and titanium nitride is the NaCl type with lattice parameters of a_0=0.4106 to 0.4130 nm and a_0=0.4230 to 0.4236 nm, respectively. Niobium nitride has a hexagonal structure with a_0=0.2960 to 0.2968 nm and c_0=0.1125 to 0.1128 nm (56). Since TiN precipitates first, it is common to find niobium and vanadium occurring in the TiN particle. This effect may have significant implications regarding coarsening of TiN particles and, therefore, grain size control in the steel. It appears that niobium increases the coarsening of the TiN particles, while the vanadium does not. This result is due to the relatively high precipitation temperature of niobium carbonitride which may allow the niobium to be incorporated into the TiN lattice. When reheating occurs, the effectively higher solubility of (Ti,Nb)(C,N) results in the liberation of titanium and niobium, and hence, the amount of free titanium in the matrix increases. This increase has already been shown to lead to coarsening of TiN particles. Since vanadium nitride forms at lower temperatures, it is more likely to form "shells" on the TiN particles, or independent

precipitates. As the vanadium nitride dissolves on reheating, the TiN is unaffected and the particle coarsening characteristics are likewise unaffected (9). It has also been reported that niobium minimizes precipitation of TiN during solidification and thereby decreases the particle size of carbonitrides (63). This may be attributable to a decrease in activity of carbonitrides when of mixed composition (Ti,Nb)(C,N) as opposed to pure TiN. This causes a decrease in precipitation temperature due to an increased solubility (70).

1.10 Hardenability

Any study that addresses transformation products in steels must consider hardenability. Hardenability is a steel's ability to delay diffusion-controlled transformation from austenite to ferrite, pearlite, or bainite (71). If a steel has good hardenability, the austenite decomposition to ferrite and pearlite will be retarded, allowing for other transformation products to form at lower temperatures. There are two ways that the austenite decomposition can be retarded. Either the growth, or the nucleation, of ferrite and pearlite must be reduced. How alloying elements affect hardenability will be discussed first.

1.10.1 Alloying Elements

The transformation from austenite to ferrite and pearlite is a diffusional process. Alloying elements can be added that must diffuse across the transformation boundary for the reaction to continue. If the diffusion of the alloying element is sluggish, the transformation can be slowed, thereby increasing hardenability. For the alloying elements to be slow diffusers, they must occupy substitutional sites in the lattice. Interstitial alloying elements, such as carbon or nitrogen, will diffuse rapidly and not hinder the transformation. Also, austenite stabilizing elements, such as manganese, nickel, and copper, will depress the A_1 temperature (71,72). This depression of the transformation temperature has the effect of reducing the diffusion of all elemental species in the steel. Consequently, hardenability is increased.

While nitrogen may not be considered a traditional alloying element in terms of increasing a steels hardenability, Shams has shown that nitrogen also reduces the austenite decomposition temperature in steels (73), which would indeed increase hardenability. Although Shams investigated five alloys, two are of interest to this study. The base material had a composition of 0.075C-1.44Mn-0.25Si-0.002N while an increased nitrogen material had a composition of 0.070C-1.57Mn-0.24Si-0.019N. The increased nitrogen material also had increased aluminum content, 0.011 wt. % compared to 0.005 wt. %. Specimens were heated to temperatures that would produce the same austenite grain size, 960°C for the low

nitrogen steel and 1000°C for the high nitrogen steel, and then cooled at rates of 360, 120, 36, and 12°C/min. For the base material it was found that the transformation start temperature, Ar_3, decreased with increasing cooling rate from 829°C to 792°C. The transformation finish temperature also decreased with increasing cooling rate, from 708°C to 645°C. With the increased nitrogen the transformation temperatures were reduced substantially. At the fastest cooling rate the transformation start and finish temperatures were 728°C and 562°C, respectively. At a cooling rate of 12°C/min, the transformation start temperature was 780°C while the transformation finish temperature was 668°C. The lowering of the Ar_3 observed is greater than would be expected by a similar addition of carbon. Shams concludes that "Nitrogen is thus more effective in delaying transformation than carbon" (73).

1.10.2 Austenite Grain Size

It was mentioned previously that hardenability can be increased by decreasing the nucleation of ferrite and pearlite. It is in this vein that the austenite grain size has an effect on hardenability. Austenite grain boundaries provide preferred nucleation sites for the nucleation of the austenite decomposition reaction. When the grain size is small there is a large amount of grain boundary area, and consequently there is a large number of nucleation sites. Conversely when the austenite grain size is large, the number of nucleation sites is

decreased along with the grain boundary area. As a result hardenability is enhanced with an increase in austenite grain size (74). Clearly this is an important consideration when the properties of the coarse-grained heat-affected zone are at issue.

2.0 ALLOY DESIGN

A set of four alloys was designed to help elucidate the effects of free nitrogen content and volume fraction of titanium nitride on the heat-affected zone toughness of API 2Y-type plate steels. To this end, the alloys have various quantities of free nitrogen and titanium nitride volume fraction at a temperature experienced in the coarse-grained heat-affected zone. Three alloys were made with a constant volume fraction of titanium nitride and different levels of free nitrogen. A fourth alloy had the same free nitrogen content as the lowest of the above-mentioned three alloys, but approximately double the titanium nitride volume fraction. As has been previously discussed, the presence of additional microalloying elements can significantly increase the complexity of precipitation in steels. To avoid these complications, it was decided not to add niobium or vanadium.

2.1 Phase Diagram and Solubility Calculations

To determine the correct total titanium and nitrogen additions, some analysis of titanium nitride solubility was undertaken. The solubility product can be used to create a phase diagram for a given temperature. It was decided that the temperature of interest

would be 1350°C, which is commonly used in reference to the coarse-grained heat-affected

zone of steels. A portion of the relevant phase diagram is shown in Figure 2.1.
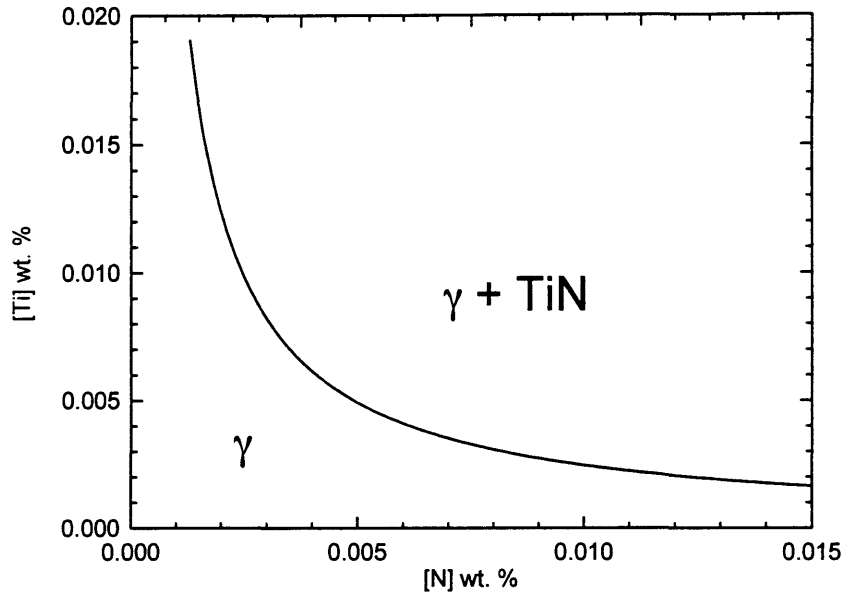
Figure 2.1. Solubility of titanium nitride in austenite as a function of nitrogen and
titanium content at 1350°C. From the solubility product of Matsuda and
Okumura (46).

Given a phase diagram for the system, the lever rule can be applied to determine the

proper titanium and nitrogen contents for the alloys. From the lever rule:

$$F_m = \frac{[Ti]_{TOT} - [Ti]_{SOLN}}{[Ti]_{TiN} - [Ti]_{SOLN}}$$ Eqn. 2.1

In the above equation F_m is the mass fraction of titanium nitride, $[Ti]_{TOT}$ is the total amount

of titanium in the alloy, $[Ti]_{SOLN}$ is the amount of titanium in solid solution in the austenite,

and $[Ti]_{TiN}$ is the amount of titanium present in the titanium nitride particles. Manipulating

the expression for the solubility product of Matsuda and Okumura, the following function

for $[Ti]_{SOLN}$ is:

$$[Ti]_{SOLN} = \frac{10^{\frac{-8000}{T}+0.32}}{[N]_{SOLN}}$$

Eqn. 2.2

where $[N]_{SOLN}$ is the amount of free nitrogen in the matrix. Recall that the temperature of

interest is 1350°C. Therefore,

$$[Ti]_{SOLN} = \frac{2.46 \times 10^{-5}}{[N]_{SOLN}}$$

Eqn. 2.3

Since the amount of titanium in titanium nitride is 77.4 wt. %, then combining equations 2.1

and 2.3 yields:

$$F_m \left[77.4 - \frac{2.46 \times 10^{-5}}{[N]_{SOLN}} \right] = [Ti]_{TOT} - \frac{2.46 \times 10^{-5}}{[N]_{SOLN}}$$

Eqn. 2.4

Assuming the titanium nitride precipitate is stoichiometric, the ratio of titanium to nitrogen

in the precipitate is (by weight):

$$\frac{[Ti]_{PPT}}{[N]_{PPT}} = 3.42$$

Eqn. 2.5

where the PPT subscript denotes weight percent of the element in the precipitate. Mass

balances for titanium and nitrogen show that:

$$[N]_{PPT} = [N]_{TOT} - [N]_{SOLN} \qquad \text{Eqn. 2.6}$$

$$[Ti]_{PPT} = [Ti]_{TOT} - [Ti]_{SOLN} \qquad \text{Eqn. 2.7}$$

Combining the last three equations:

$$\left([N]_{TOT} - [N]_{SOLN}\right) 3.42 = [Ti]_{TOT} - [Ti]_{SOLN} \qquad \text{Eqn. 2.8}$$

With the amount of nitrogen in solution ($[N]_{SOLN}$) and the mass fraction of

precipitate (F_m), equations 2.3 and 2.4 can be used to determine the total amount of titanium

($[Ti]_{TOT}$) and the amount of titanium in solution ($[Ti]_{SOLN}$) in the alloy. Equation 2.8 can

then be used to find the total nitrogen in the alloy ($[N]_{TOT}$).

In this section, the mass fraction has been discussed. However, volume fraction is

the quantity that is of more interest. This issue is easily remedied since the volume fraction

of the precipitate can be determined through the mass fraction:

$$F_V = \frac{V_{TiN}}{V_{TiN} + V_{Steel}} \qquad \text{Eqn. 2.9}$$

where F_V is the volume fraction of titanium nitride, V_{TiN} and V_{Steel} are the volume of

titanium nitride particles and steel, respectively. Considering that

$$V_{TiN} << V_{Steel} \qquad \text{Eqn. 2.10}$$

Therefore,

$$F_V \approx \frac{V_{TiN}}{V_{Steel}}$$
Eqn. 2.11

Using the function for density,

$$D = \frac{m}{V}, \quad or \quad V = \frac{m}{D}$$
Eqn. 2.12

where D, m, and V are density, mass and volume, respectively. Combining equations 2.11

and 2.12 yields:

$$F_V = \frac{\dfrac{m_{TiN}}{D_{TiN}}}{\dfrac{m_{Steel}}{D_{Steel}}} = \frac{m_{TiN}}{m_{Steel}} \cdot \frac{D_{Steel}}{D_{TiN}}$$
Eqn. 2.13

Therefore,

$$F_V = F_m \cdot \frac{D_{Steel}}{D_{TiN}}$$
Eqn. 2.14

The densities of steel and titanium nitride were taken to be 7.86 g/cm^3 and 5.22 g/cm^3,

respectively (75). Therefore,

$$F_V = F_m \cdot 1.51$$
Eqn. 2.15

It is through manipulations of the above equations that the overall alloy chemisty

can be determined by defining free nitrogen level and titanium nitride volume fraction.

2.2 Recommended Alloy Compositions

Through consultation with the sponsors of this project, it was decided that the three levels of free nitrogen should be 0.004 wt. %, 0.008 wt. %, and 0.012 wt. %. It has been previously mentioned that other researchers reported titanium nitride volume fractions of approximately 10^{-4}. For this study, a titanium nitride volume fraction of 1.1×10^{-4} was implemented for the constant volume fraction alloys, and 2.6×10^{-4} was used for the increased-volume-fraction alloy. Based on these values, recommended total nitrogen and titanium additions were calculated. These compositions are shown in Table 2.1.

Table 2.1. Recommended Alloy Compositions.

Alloy	Total [Ti] in alloy (wt. %)	Total [N] in alloy (wt. %)	Free [N] at 1350°C (wt. %)	Volume fraction of TiN at 1350°
HNLV	0.008	0.0135	0.012	1.1×10^{-4}
INLV	0.009	0.0100	0.008	1.1×10^{-4}
LNLV	0.012	0.0055	0.004	1.1×10^{-4}
LNHV	0.020	0.0080	0.004	2.6×10^{-4}

The alloy designations (HNLV, INLV, LNLV, LNHV) are used to describe the alloy. The first two letters correspond to the free nitrogen level: HN for high nitrogen, IN for intermediate nitrogen, and LN for low nitrogen. The last two letters correspond to the

volume fraction of titanium nitride: LV for low volume fraction and HV for high volume

fraction.

3.0 EXPERIMENTAL MATERIALS

The companies sponsoring this research identified API 2Y-type plate steels as materials of interest to them. API 2Y is an intermediate strength, quenched-and-tempered steel for use in welded construction of offshore structures. It is intended to be resistant to impact, plastic fatigue loading, and lamellar tearing (76). The grade selected was API 2Y-50T, where the 50 indicates the minimum yield strength in ksi, (345 Mpa), and T indicates that the material is over 38 mm (1½ inches) thick. In this study, the plates were 50 mm, or two inches, thick.

Four 225 kg (500 lb.) laboratory heats were melted based on the API 2Y specification and the suggested titanium and nitrogen contents outlined in the previous section. After casting, the ingots were rolled immediately from 180 mm (7 in.) to 100 mm (4in.). Then the ingots were sectioned into three plates 330 mm (13 in.) in length, discarding the hot top and ingot bottom. The plates were then reheated to approximately 1250°C (2280°F) and cross-rolled 90° from the ingot axis to a thickness of 50 mm (2 in.). Final dimensions of the plates were 50 x 280 x 560 mm (2 x 11 x 22 in.).

After rolling, the plates were heat treated by austenitizing at 900°C (1650°F) for 1.5 hours followed by an immersion water quench. The plates were then tempered at 610°C (1125°F) for 1.5 hours. The resulting steel chemistries are shown below in Table 3.1.

Table 3.1. Composition of Experimental Steels. All values in wt. %.

Alloy	C	Mn	P	S	Si	Ni	Al	Ti	N
HNLV	0.084	1.48	0.009	0.0039	0.22	0.20	0.024	**0.008**	**0.015**
INLV	0.081	1.48	0.009	0.0041	0.21	0.20	0.027	**0.009**	**0.011**
LNLV	0.084	1.51	0.010	0.0040	0.22	0.20	0.025	**0.012**	**0.005**
LNHV	0.080	1.43	0.009	0.0040	0.20	0.19	0.036	**0.019**	**0.007**

With a similar analysis as described in the Alloy Design section, the values for free

nitrogen and volume fraction of titanium nitride were calculated for the actual alloy

compositions and were compared with recommendations. These values are shown in Table

3.2.

Table 3.2. Comparison of Requested and Actual Free Nitrogen and Titanium Nitride
Volume Fraction at 1350°C. Values calculated from Matsuda and Okumura
solubility product.

Alloy	Requested Free [N] (wt. %)	Free [N] Based on Actual Alloy (wt. %)	Requested V_F TiN	V_F TiN Based on Actual Alloy
HNLV	0.012	0.013	1.1×10^{-4}	1.2×10^{-4}
INLV	0.008	0.009	1.1×10^{-4}	1.2×10^{-4}
LNLV	0.004	0.004	1.1×10^{-4}	1.1×10^{-4}
LNHV	0.004	0.005	2.6×10^{-4}	2.6×10^{-4}

As shown in the above two tables, the set of alloys used in this study are well suited for the comparison. With the exclusion of titanium and nitrogen additions, all four alloys have similar compositions. Also, there is relatively good agreement between the requested free nitrogen and volume fraction titanium nitride and the estimated values based on the actual alloy composition.

4.0 EXPERIMENTAL PROCEDURE

The experimental work for this project began with a characterization of the baseplate, or as-quenched-and-tempered, materials. This analysis was important because the study would only be relevant if the four alloys were similar in baseplate properties. Once the base materials were fully characterized then thermal cycles could be created to simulate welding. The characterization was accomplished by first performing actual submerged-arc welds on the baseplate to create a standard that the subsequent simulations would match. Lastly, the material that had been thermally cycled to simulate the welds was analyzed.

4.1 Metallography and Carbon Extraction Replicas

4.1.1 Specimen Preparation

Standard metallographic techniques were used almost exclusively for the metallography that was done in this study. Grinding consisted of papers with grits of 120, 240, 320, 400, and 600, cleaning the specimen between steps. In all cases water was used as a lubricant. After the 600 grit step, a 6μm diamond suspension on nylon cloth was used.

Water-alumina slurries were avoided where possible, as significant pitting occurred with their use. Rather, commercially available diamond suspensions were used during specimen preparation. Again the specimens were cleaned, and then polished with ¼-μm-diamond suspension on a flocked twill cloth. If a sample required repolishing after an etching procedure, a 0.03-μm-alumina water based slurry was used on flocked twill. Time was kept to a minimum, usually less than 20 seconds, to prevent pitting.

The standard etchant used in this study was 2% nital. With the exception of prior-austenite grain boundary analysis, nital was used exclusively.

A saturated-aqueous-picric-acid reagent was used for the prior-austenite grain boundary etching. This reagent contains the wetting agent dodeclybenzenesulfonic acid, sodium salt. By weight the mixture is 90:16:3 of distilled water : wetting agent : picric acid. The etchant was heated to between 60°C and 70°C prior to use. Specimens were immersed in the etchant such that the polished surface was perpendicular to the container bottom, and no agitation was used during the etching process. The time required for suitable results varied. It was observed that if ferrite is present on the prior-austenite grain boundaries, an increased etching time, sometimes over ten minutes, was required. In other cases the prior-austenite grain structure was revealed in times as short as 30 seconds. Generally, a specimen was placed in the etchant for 15-second intervals to determine if short etching times were appropriate. If after one minute of etching time the specimens did not adequately reveal the grain structure, 30-second intervals were used. Once the suitable total

etching time was determined for the specimen condition, the samples could be placed in the etchant for the duration of the etch without removal. Apparently the periodic removal and cleaning of the specimen for inspection had little effect on etching response.

Invariably a dark film would appear on the specimen surface during etching. No attempt was made to disturb this film while the specimen was immersed in the solution. The film was readily removed with liquid hand soap and water.

The specimens were etched in the untempered condition, *i.e.,* they were not tempered after the weld simulation thermal cycles. Some researchers have found that a tempering treatment at approximately 450°C for one to three days was helpful for prior-austenite grain boundary attack (77,78) due to segregation of tramp elements to the grain boundaries; however, this was not necessary in the present study.

4.1.2 Light Microscopy

In most cases it was found that light microscopy was suitable for microstructural evaluation of these materials. Darkfield illumination was particularly helpful when studying prior-austenite grain boundaries. In all other cases, brightfield illumination was used.

4.1.3 Carbon Extraction Replicas

Titanium nitride precipitates were studied with carbon extraction replicas in a scanning-transmission electron microscope (STEM) in the transmission mode. Specimens were prepared as above for standard analysis. Once etched, the specimens were cleaned ultrasonically in an acetone bath. Carbon was then evaporated onto the surface. A knife edge was used to section the carbon layer into approximately 3-mm-square segments. The specimens were then immersed in 2% nital to lift the carbon film from the surface. Standard 3-mm-copper grids were then used to "fish" out the pieces of carbon from the etchant. Frequently the replicas rolled tightly into tubes. When this occured, they were placed in a dilute solution of deionized water in ethanol, with the replica detaching from the copper grid. This solution had the effect of flattening the replica so that it could be effectively placed on the copper grid.

With the carbon extraction replica in the TEM, a suitable field was found to photograph, hopefully with a large number of titanium nitride precipitates. Several fields from each specimen were photographed. Using the photograph negatives, the titanium nitride precipitates were measured for size. Since the transmitted images of these precipitates often appear as squares or rectangles, the two edge lengths were measured and arithmetically averaged to determine the particle size. More than one hundred precipitates

were measured for each condition. For the purposes of this study, titanium nitride particles

smaller than 1 μm in size are termed "precipitates".

4.2 Baseplate Characterization

Upon receipt of the experimental materials, specimens were removed from the

plates for metallographic analysis. Standard metallographic techniques were employed to

study the microstructure of the four alloys throughout the thickness of the plate. Carbon

extraction replicas were used to determine the titanium nitride size distribution. Tensile and

Charpy V-notch (CVN) testing was performed to determine the mechanical properties of

the base materials. Tensile specimens were taken from the plate centerline, ¼-thickness,

and near-surface positions to study the difference in properties through the thickness of the

plate associated with the lack of through-hardenability. Charpy specimens were extracted

exclusively from the ¼-thickness position.

4.3 Submerged Arc Welds

Bead-on-plate submerged arc welds were applied to one plate of each alloy with the

intent of creating a baseline of characteristics to match with welding simulations.

Subsequent simulations with a Gleeble HAZ 1500 thermomechanical test system was used

to accurately represent the coarse-grained heat affected zone of the actual welds. Two heat

inputs were examined, 4 kJ/mm (100 kJ/in.) and 8 kJ/mm (200 kJ/in.). All welds were done

in a single pass, with parameters shown in Table 4.1.

Table 4.1. Parameters Used in Submerged Arc Welds.

Parameter	4 kJ/mm Heat Input[†]	8 kJ/mm Heat Input[†]
Current (Amps)	650	650
Potential (Volts)	32	32
Travel Speed (mm/s)	5.3	5.3

[†] 4 kJ/mm heat input is a single wire weld. 8 kJ/mm heat input is a double wire weld with 19-mm (0.75 in.) wire spacing, lead wire DC reverse, trailing wire AC.

Thermocouples were welded to the plate surface at the expected fusion line to

record the thermal history experienced by the plate. After welding, the plates were

sectioned, thereby removing the weld bead and the heat-affected zone. The welded region

was then sectioned further for metallographic analysis. Microhardness was also used to

characterize the coarse-grained heat-affected zone.

4.4 Thermal Cycles

Several different thermal cycles were implemented in this study. It was necessary to

make modifications to the original two thermal cycles to determine austenite grain size, as

well as provide insight on chemistry effects on properties. These thermal cycles are presented in the following sections.

4.4.1 Submerged Arc Weld CGHAZ Simulation

Based on the recorded thermal history from the submerged arc welds, and some slight modifications to make effective correlation with the actual heat-affected zone, thermal cycles were programmed into the Gleeble 1500 thermomechanical test system. These cycles are shown in Figure 4.1. A peak temperature of 1350°C was used with cooling times between 800°C and 500°C of 19 and 52 seconds for the 4 kJ/mm heat input and the 8 kJ/mm heat input, respectively. The heating current was removed at 300°C, which is reflected by the inflection point in the thermal cycle.These simulations were performed on specimens that measured 11mm x 11mm x ~100mm. This increased specimen cross section allowed full-sized Charpy V-notch specimens to be machined without the possible effects of oxidation and decarburization becoming an issue in the study.
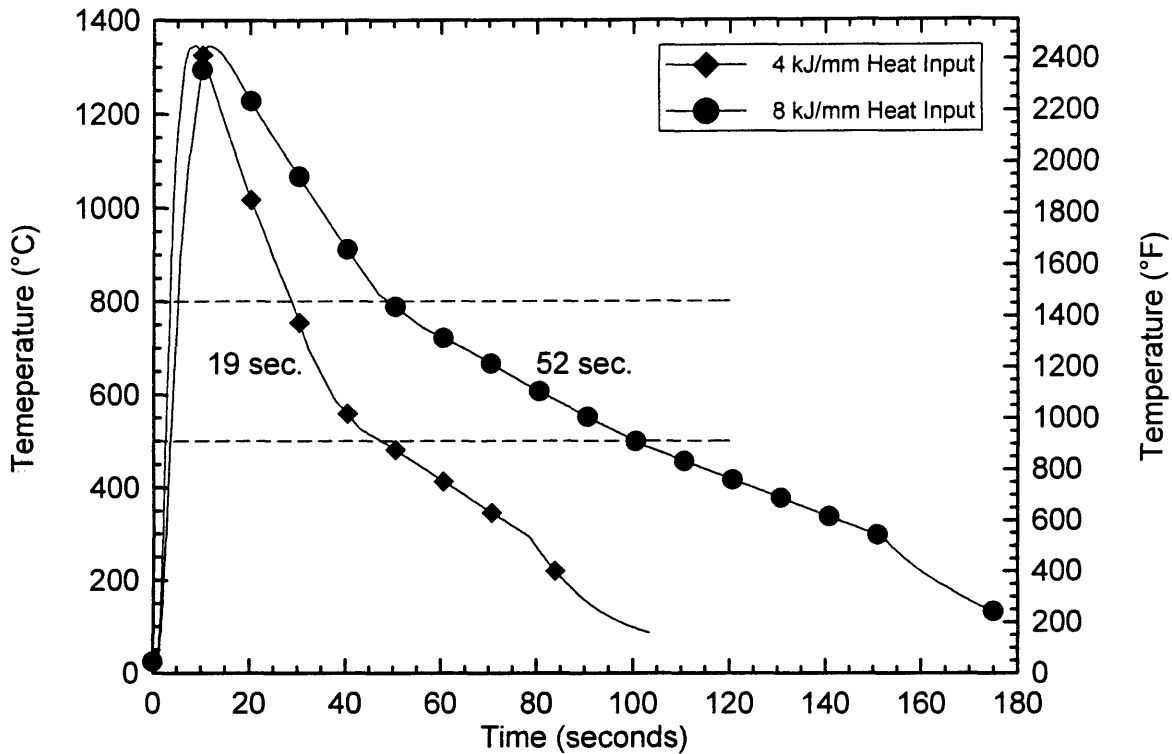
Figure 4.1.   Thermal cycles used for coarse-grained heat-afffected zone simulation.

Because the Gleeble uses resistance heating to create the programmed thermal

cycle, there is a longitudinal temperature gradient, and therefore a microstructural gradient,

in the test specimen. By increasing the separation of the Gleeble jaws the work zone, or the

volume of material that experiences the programmed thermal sequence, is expanded. In this

study, unless otherwise noted, the jaw separation was defined to be 25 mm (1 in.). This

separation provided a work zone estimated to be 5 mm long. To provide an adequate

contact area between the specimens and the Gleeble jaws, so that the required heating and

cooling rates could be achieved, the test specimens were required to be longer than the standard Charpy V-notch specimen length of 55 mm, hence the approximate 100 mm length.

4.4.2 Alternate Peak Temperatures

After some analysis of specimens thermally cycled with the programs depicted in Figure 4.1, it was decided that thermal cycles with different peak temperatures might reveal some interesting phenomena. With this in mind, thermal cycles with two other peak temperatures were examined, 1250°C and 1400°C. These cycles were constrained to simulations associated with the 4 kJ/mm heat input. The cycles with the 1250°C and 1400°C peak temperatures are shown in comparison to the 4 kJ/mm heat input, 1350°C peak temperature cycle in Figure 4.2.

4.4.3 Thermal Cycles for Austenite Grain Size

Unfortunately, due to these material's insufficient hardenability, the austenite grain size could not be determined using specimens thermally treated with the cycles shown in Figure 4.1 or Figure 4.2. As the austenite grain size is a significant issue in this study, the
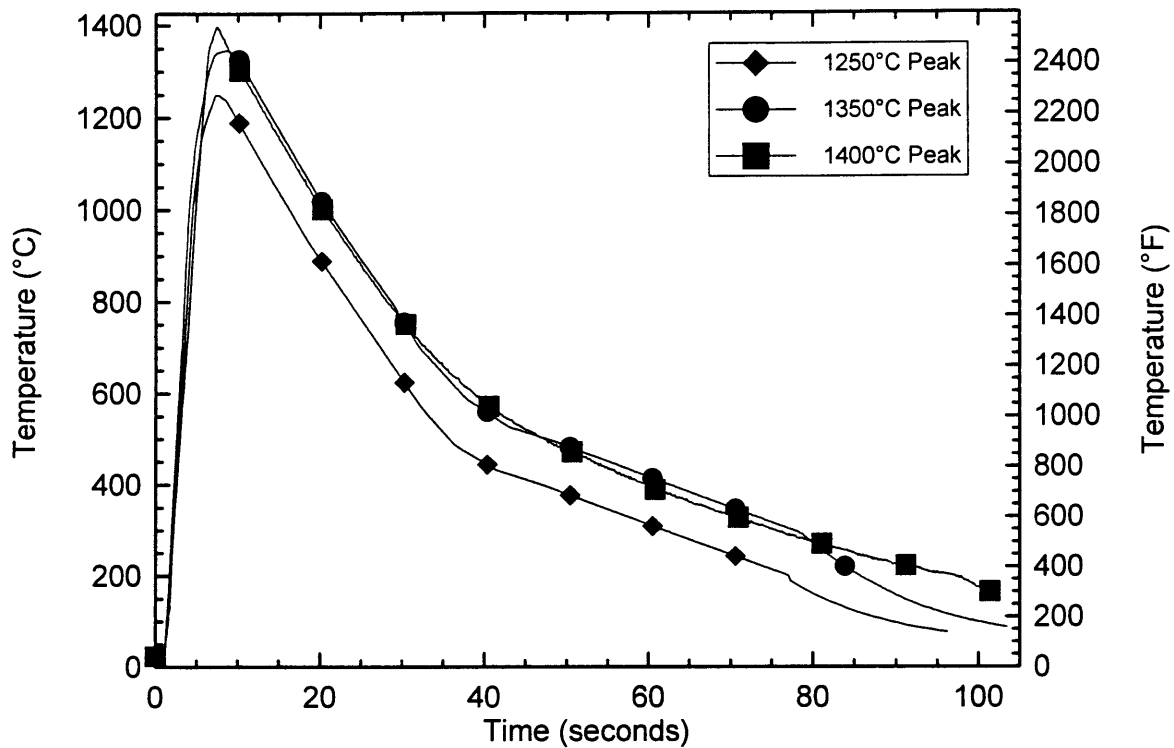
Figure 4.2. Thermal cycles for the 4 kJ/mm heat input with 1250°C, 1350°C, and 1400°C peak temperatures.

thermal cycles had to be modified to have the highest cooling rate possible to provide a

martensitic microstructure. This modification was achieved by removing the electrical

current at a high temperature and applying a helium quench. This temperature was 1250°C

for the 1350°C and 1400°C peak temperature cycles and 1200°C for the 1250°C peak

temperature cycle. Also, Gleeble jaw separation was decreased to 13 mm (0.5 in.) to

enhance cooling. The combination of helium quenching and decreased jaw separation

resulted in cooling rates high enough to achieve the martensitic microstructures required to

reveal the prior-austenite grain size upon etching. Typical thermal cycles for grain size

analysis are shown in Figure 4.3.
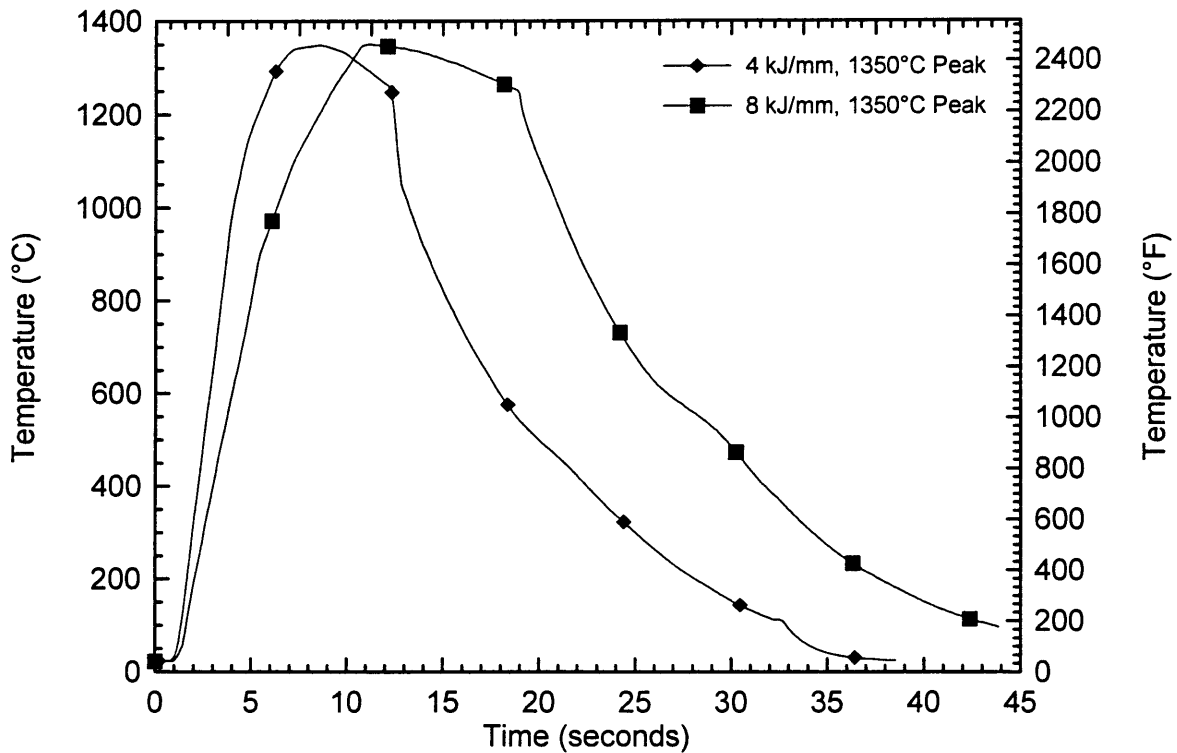
Figure 4.3.   Thermal history for specimens cycled with the grain size method,
implementing a quench at high temperature.

4.4.4 Continuous Cooling Cycles

To help explain any microstructural differences between the alloys and thermal

conditions of interest in this study, some continuous-cooling-transformation testing was

done. Two peak temperatures were investigated, 1250°C and 1400°C. The initial portion

of the 4 kJ/mm heat input thermal cycle was used and, at a temperature 50°C below the

peak, a controlled cooling schedule was implemented. The controlled cooling was based

upon Newton's law of cooling, where the plot of log[T] vs. time is linear. A defined

cooling time between 800°C and 500°C (Δt_{8-5}) determines the magnitude of the cooling rate.

Three cooling rates were chosen to provide a broad range of microstructures with

corresponding Δt_{8-5} times of 3, 30, and 300 seconds. These cycles are shown in Figure 4.4.
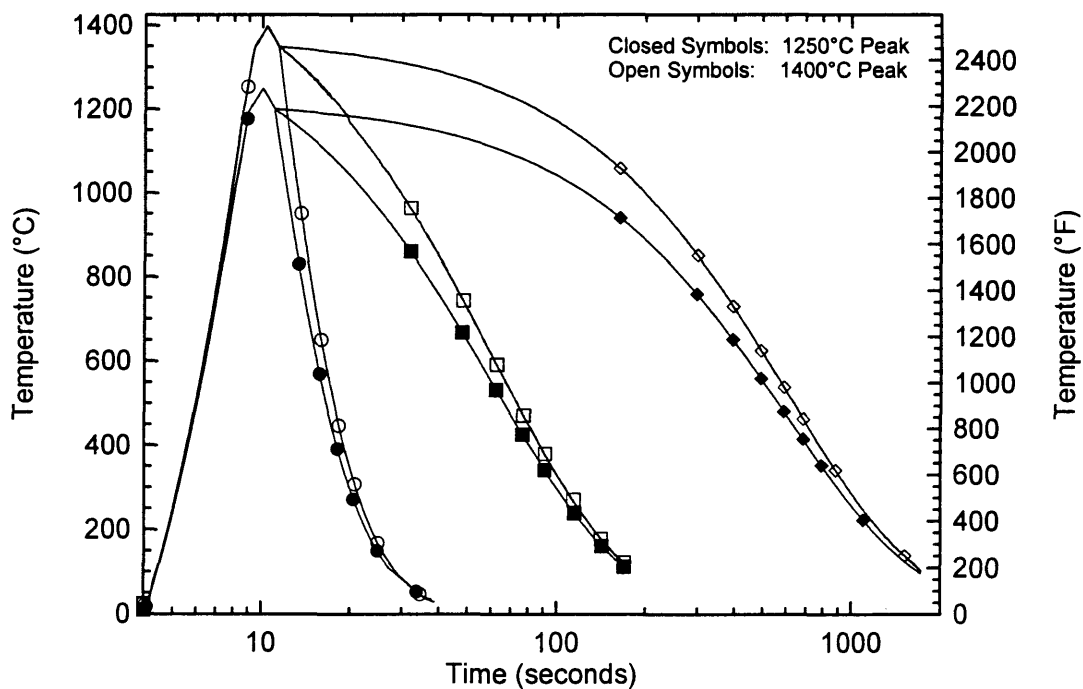
Figure 4.4. Thermal cycles for CCT testing.

4.5 Heat-Affected Zone Characterization

Once the suitable thermal cycles were determined, the materials subjected to simulated coarse-grained heat affected zones could be evaluated. This section outlines the procedures implemented to evaluate the thermally cycled materials.

4.5.1 Mechanical Properties of HAZ

The mechanical properties of the thermally cycled materials were evaluated by microhardness and Charpy V-notch testing. The microhardness testing was done with a 500 gram load and a Vicker's indenter. In all cases a minimum of ten indentations were used to determine the average hardness value.

In an attempt to account for the variability observed in the Charpy V-notch testing, three curves were drawn manually through the data to provide a lower bound, an upper bound, and an "average" of the data. A 100 J criteria was used to identify the transition temperature. The transition temperature was taken to be that point where the "average" curve intersected the 100 J energy absorbed value. The range of data was determined by the intersection of the upper bound and the lower bound curves with the 100 J value.

4.5.2 Quantitative Analysis of Microstructure

Quantitative analysis of the microstructure was performed by point counting to determine the relative quantities of microstructural components. Six categories were defined and used during the analysis of microstructure. The categories used are a modification of the previously presented IIW classification (see Figure 1.10). These categories are shown in Table 4.2.

Table 4.2. Categories used in point counting of HAZ microstructures.

Abbreviation	Description
PF	Polygonal, or primary, ferrite with no second phases
FS(A)	Ferrite with aligned second phases
FS(NA)	Ferrite with non-aligned second phases
MA(A)	Martensite/Austenite constituent with a high aspect ratio
MA(B)	Martensite/Austenite constituent with a blocky, or equiaxed, morphology
NR	Not-resolvable: second phase constituents that are not resolvable at the magnification of the light microscope

The photomicrograph provided in Figure 4.5 shows examples for each of the above microstructural constituents.

A 10 x 10 grid was used for the point counting. Ten fields of view were examined with the light microscope at a magnification of 1000x. Two specimens of each alloy and
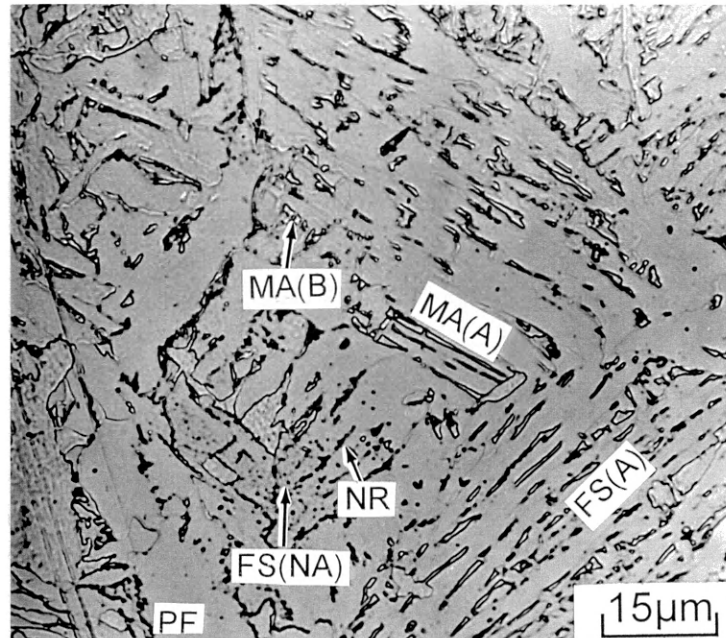
Figure 4.5.   Photomicrograph showing examples of microstructural constituents
identified during point counting.

thermal condition were examined. If the crosshairs of the grid intersected a second phase

component, that component was counted as well as the surrounding microstructure. For

example, if the crosshairs landed upon an equiaxed MA island, the likely tally would be a

count for MA(B) and FS(NA), or possibly FS(A). As a result of this procedure, the total

number of counts usually exceeds 100. However, all of the data are recorded in terms of

percent of the counted features, so the increased total counts is accommodated.

In addition to the point counting, an attempt was made to determine the size of these

microstructural constituents by using a lineal intercept method. This method provides a

"mean free path" between microstructural constituents. A pattern consisting of five,

horizontal, 10 cm long lines was placed on top of the specimen image and the number of

times that a boundary intersected a line was recorded. In a similar fashion to the point

counting, several categories of boundaries were chosen in hopes of finding a critical

microstructural feature that may be correlated to impact transition temperature. These

categories are shown in Table 4.3.

Carbon extraction replicas were used to determine the size distribution of titanium

nitride precipitates for the 1350°C peak temperature thermal cycles, both 4 kJ/mm and 8

kJ/mm heat input.

Large titanium nitride inclusions were evaluated by light microscopy. An area of

approximately 1 mm^2 was investigated at 1000x and the longest dimension of the inclusion

was measured with a 10x scale lupe. The average size of titanium nitride inclusions and

Table 4.3. Boundary categories used in lineal intercept analysis.

Abbreviation	Description
FHAB	Ferrite high-angle boundary
MA(A)	Boundary between ferrite and high-aspect-ratio MA constituent
MA(B)	Boundary between ferrite and blocky MA constituent
NR	Boundary between ferrite and a non-resolvable second phase particle

their number density was calculated for all alloys and peak temperatures with the 4 kJ/mm

heat input. For the purpose of this study, titanium nitride particles that are larger than 1 μm

in size are termed "inclusions", as opposed to the finer precipitates that are smaller than 1

μm.

4.6 Continuous Cooling Transformation (CCT) Testing

As mentioned previously, CCT testing consisting of two peak temperatures and

three cooling rates was done on the alloys in this study. This testing was done using

specimens with different geometry than the standard Gleeble blanks. Kloberdanz (79)

showed that a reduced section in the specimen was required to achieve the rapid cooling

rates necessary in CCT testing. A comparison of these samples with the standard Gleeble

samples are shown is Figure 4.6. Duplicate specimens were tested and hardness and

microstructure were evaluated. Dilatometry was used to determine transformation

temperatures.

a. Standard Specimen Blank for Gleeble Testing.
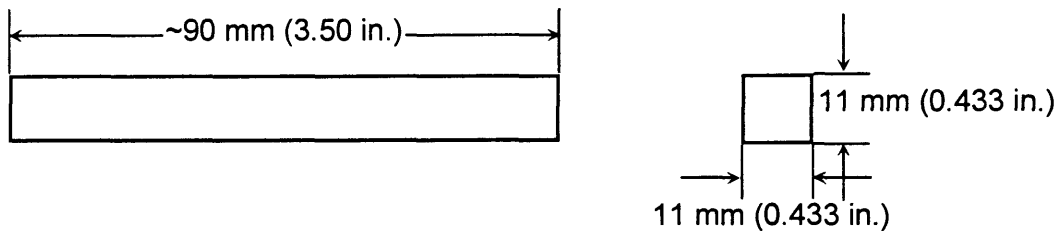
b. Specimen Blank for CCT Testing.
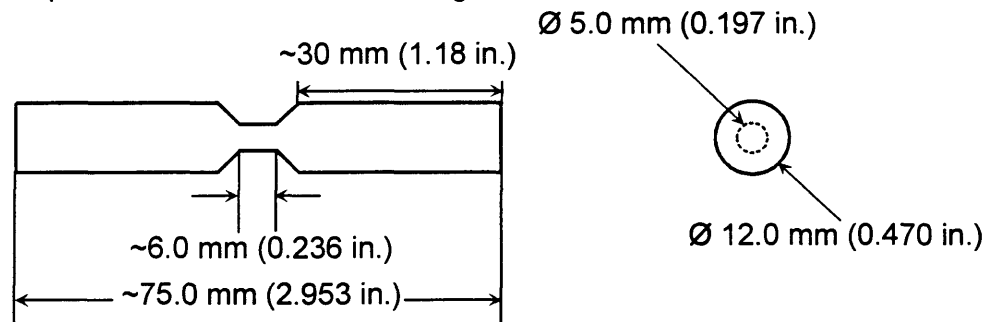
Figure 4.6. Specimen geometry for (a) standard Gleeble specimens and (b) CCT testing specimens.

5.0 RESULTS

5.1 As-Quenched-and-Tempered Baseplate Characterization

5.1.1 Microstructure and Hardness

Photomicrographs of alloy HNLV in the as-quenched-and-tempered condition are shown in Figure 5.1. Micrographs for the other three alloys are shown in Appendix A. Apparent in these micrographs is the variation in microstructure through the thickness of the plate. In the center of the plate the microstructure is comprised of predominantly polygonal ferrite with fine ferrite-cementite aggregates as well as some grain boundary cementite. The polygonal ferrite becomes increasingly finer and somewhat more acicular closer to the plate surface. This variation in microstructure results in a corresponding variation in hardness through the plate thickness, as shown in Figure 5.2.

Evident from both the micrographs and the hardness data is the fact that while there is significant variation throughout the thickness of these plates, there is very little difference

a)

b)

c)

30μm
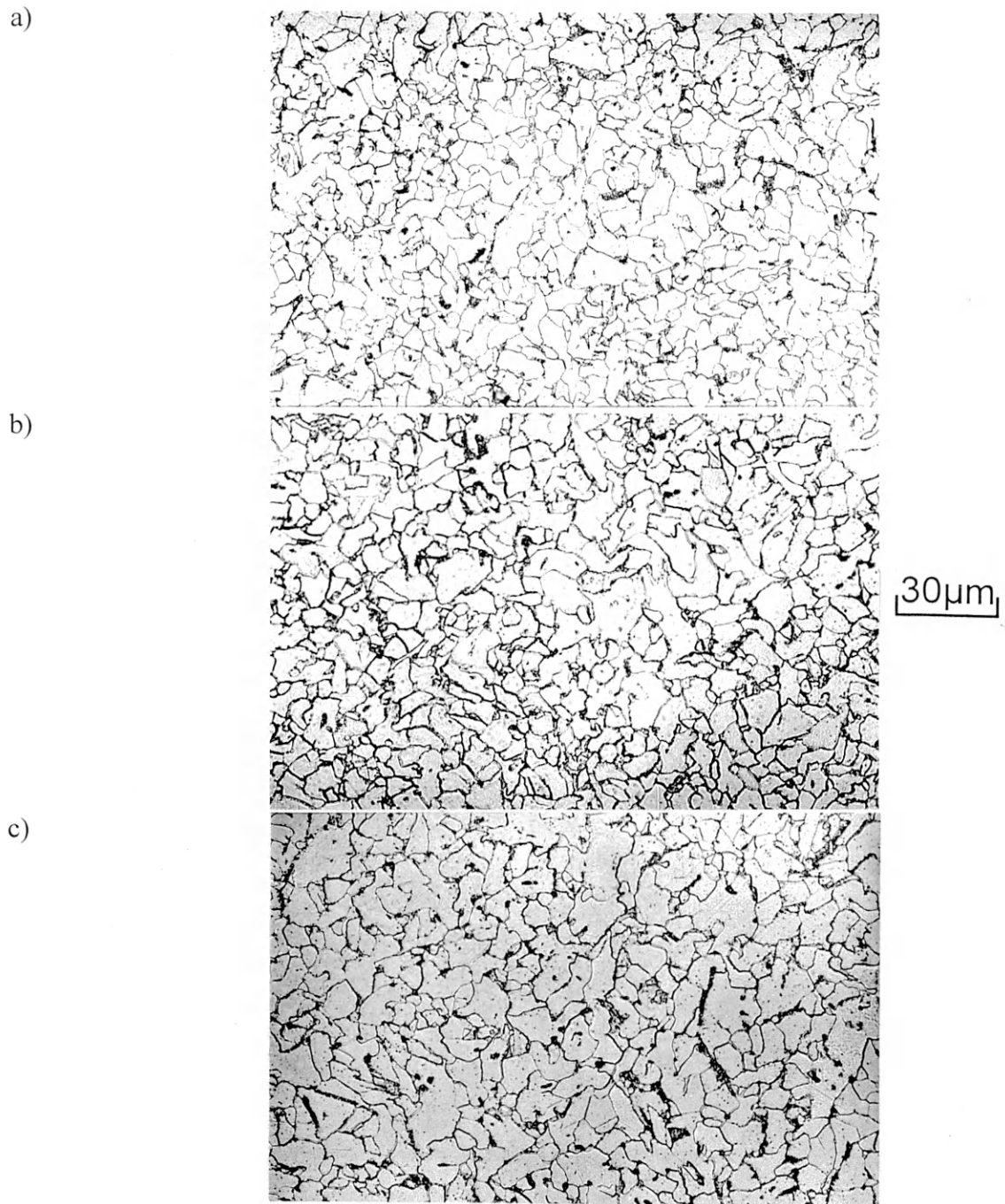
Figure 5.1.   Photomicrographs of as-quenched-and-tempered material. Alloy HNLV a)
Near surface. b) 1/4-thickness. c) Mid-thickness. 500x. Nital etch.
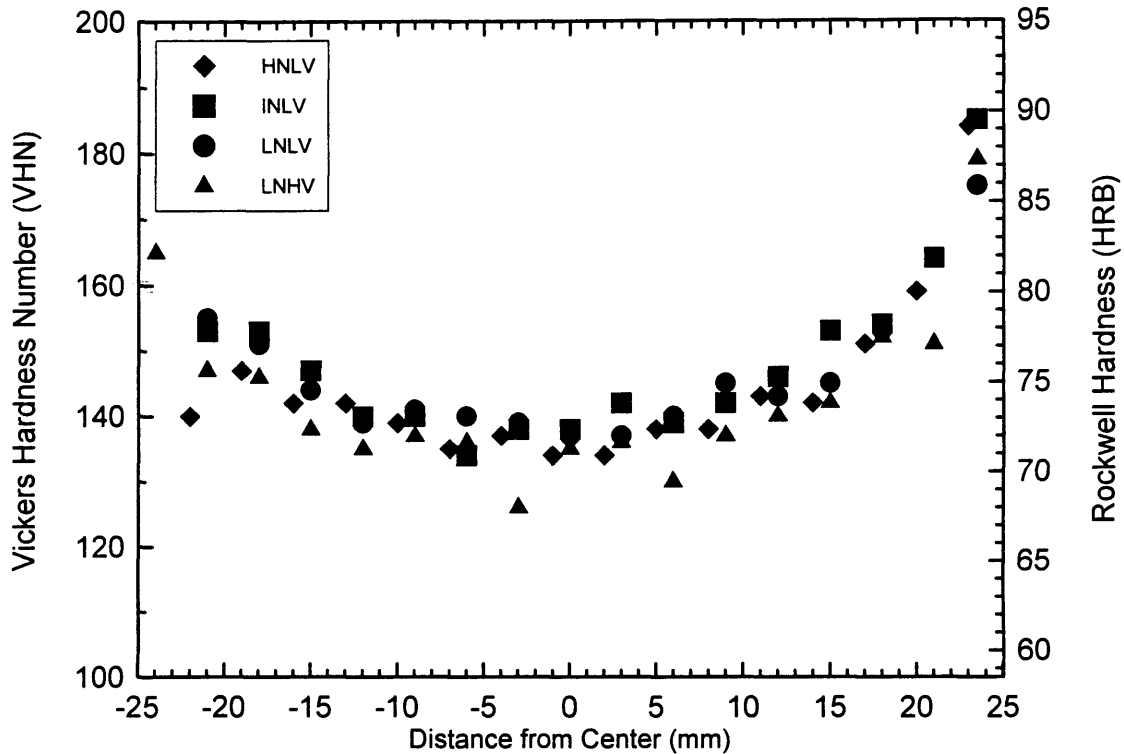
Figure 5.2.   Hardness profile through the thickness of the as-quenched-and-tempered plates.

between the alloys. To ensure further that these alloys were similar in the as-quenched-and-tempered condition, tensile and Charpy V-notch testing was done.

5.1.2 Tensile and Charpy V-Notch Testing

Based on the variation in microstructure described in the previous section, tensile testing was done from three positions in the plate: near-surface, ¼-thickness, and mid-thickness. The results of this testing are shown in Figure 5.3. Nominal yield and tensile
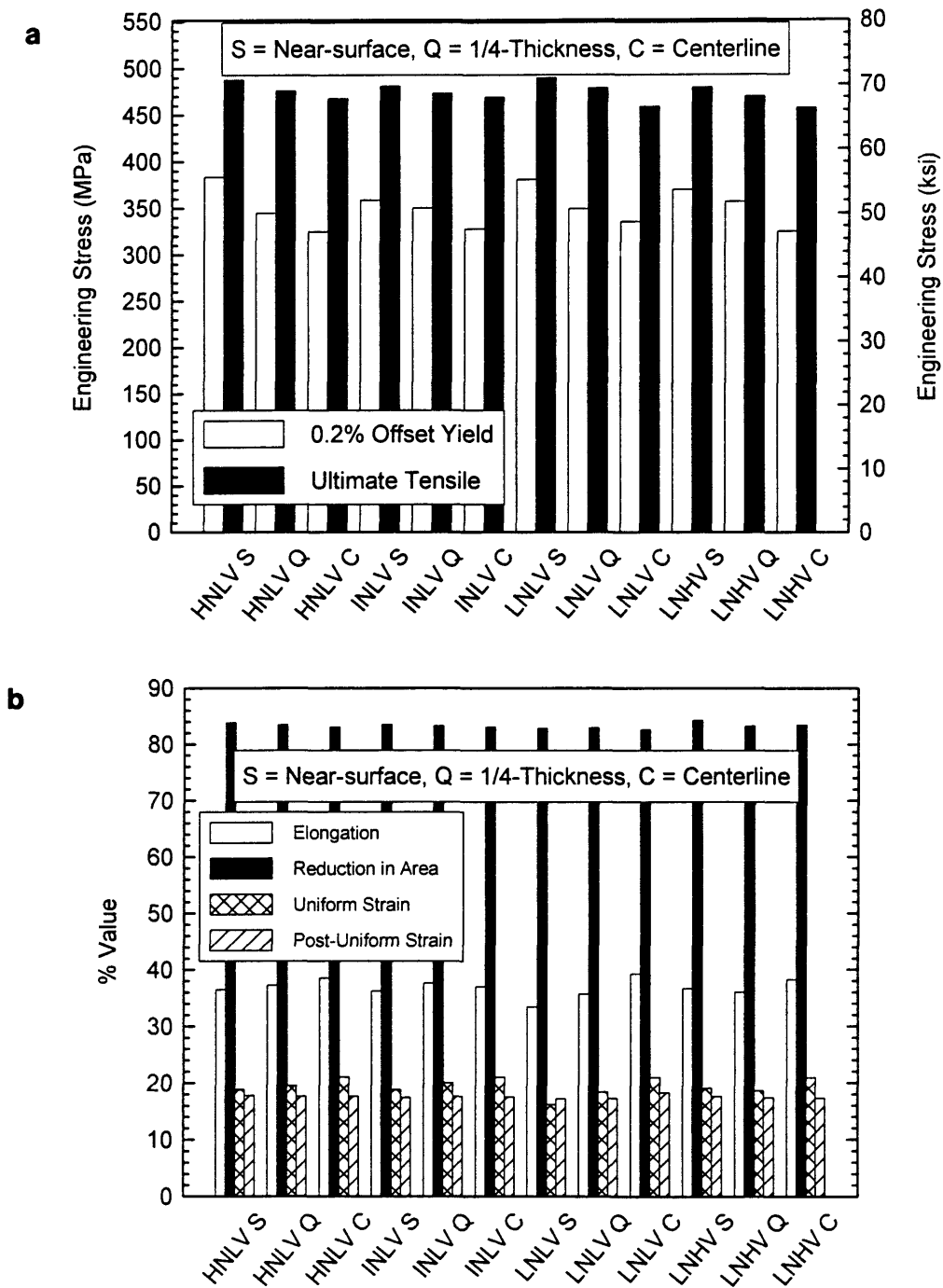
Figure 5.3.   Tensile properties from as-quenched-and-tempered materials. a) Strength values. b) Ductility values.

strengths were 350 MPa (50 ksi) and 490 MPa (70 ksi), respectively. Apparent in these two

figures is the similarity between the four alloys. Consistent with the hardness traverse, the

strength level decreases from the near-surface position to the mid-thickness position. These

materials exhibited good ductility with reductions in area of approximately 80% and

elongations of approximately 38%.

Charpy V-notch transition curves for the as-quenched-and-tempered baseplate are

shown in Figure 5.4 through Figure 5.7. Those values plotted as upper shelf, *i.e.*, energy

absorbed values of 325 J (240 ft.-lbs), correspond to specimens that did not break.

Specifically, since the maximum energy that could be measured with the Charpy machine

was 325 J, it was decided this energy value would be assigned to those specimens that

stopped the pendulum. Present on the figures are construction lines used to determine the

100 J transition temperature for each alloy. The construction lines correspond to a lower

bound, an upper bound, and a mid-point of the data. This construction was done to give

some indication of the scatter demonstrated in the Charpy testing. A summary plot of the

100 J transition temperature is shown in Figure 5.8.

As shown in Figure 5.8, alloys HNLV and INLV display similar 100 J transition

temperatures of approximately -104°C (-155°F). Alloy LNLV has a slightly higher

transition temperature of approximately -97°C (-143°F) and alloy LNHV has the highest

transition temperature of all, approximately -88°C (126°F). There is significant scatter in

the data. Alloy HNLV has the least evidence of scatter and still there is a variance of ±4°C.
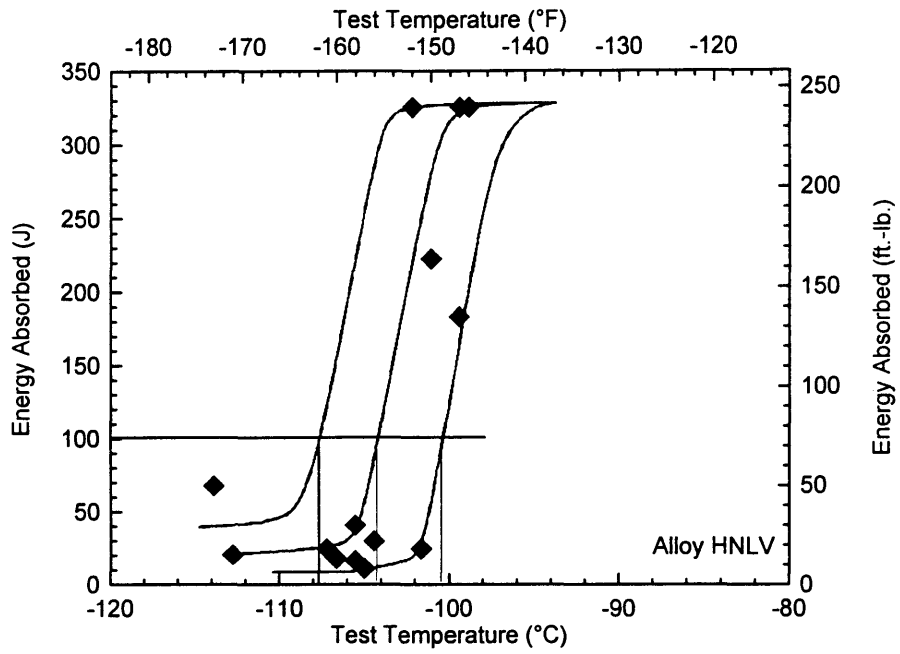
Figure 5.4.   Baseplate Charpy V-notch transition curve. Alloy HNLV.
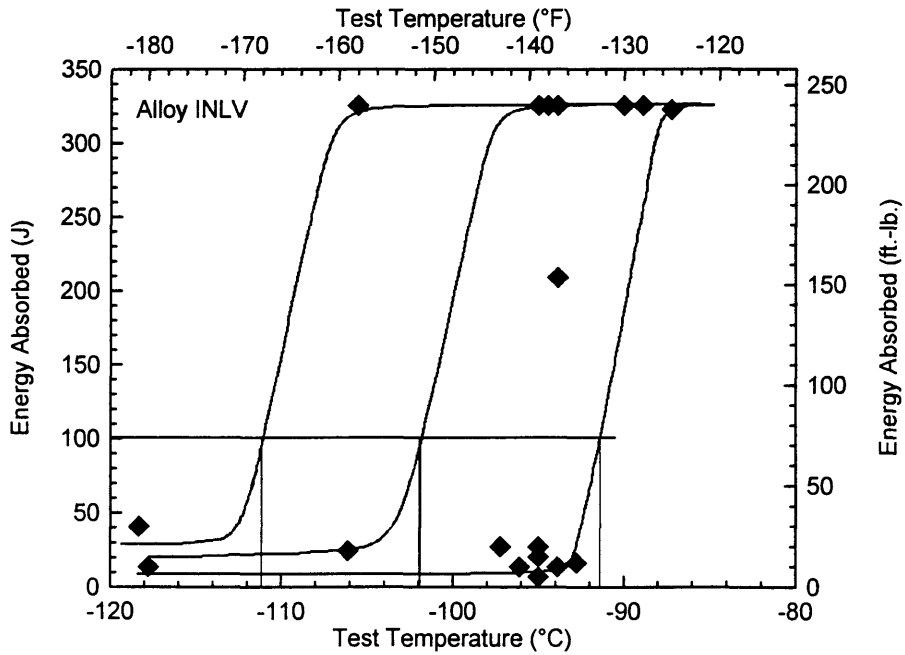
Figure 5.5.   Baseplate Charpy V-notch transition curve. Alloy INLV.
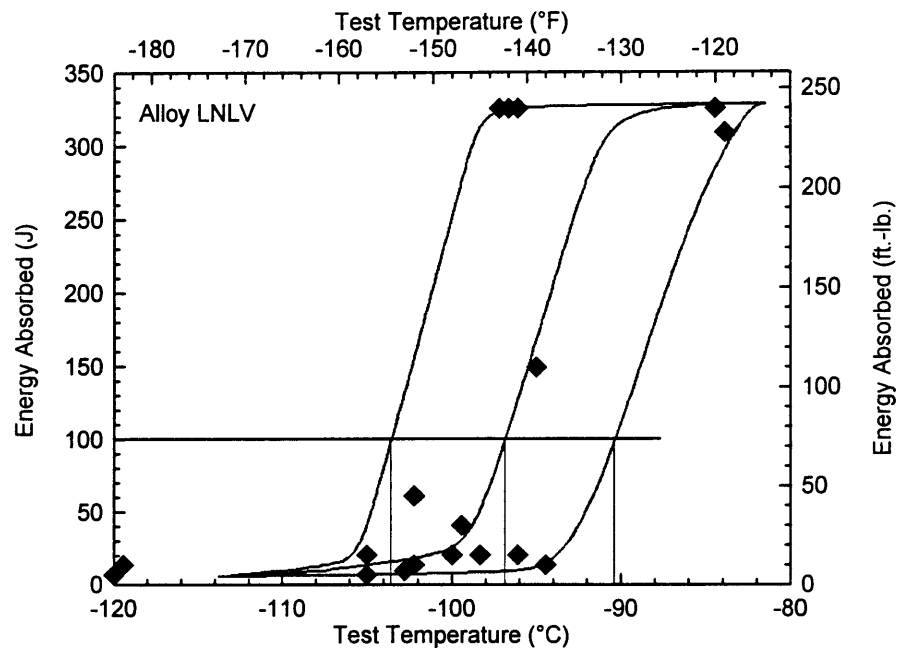
Figure 5.6.   Baseplate Charpy V-notch transition curve. Alloy LNLV.
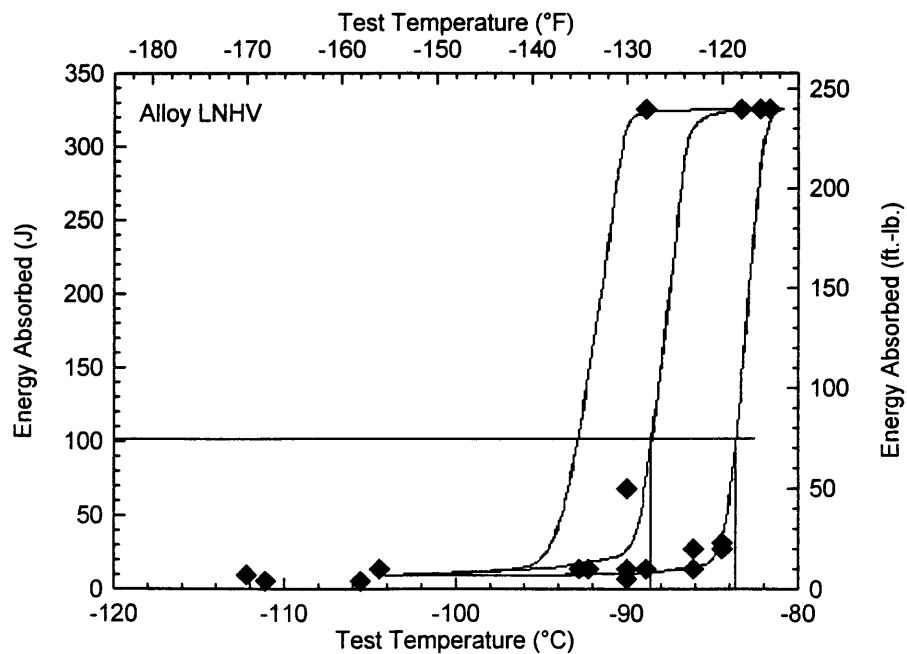
Figure 5.7.   Baseplate Charpy V-notch transition curve. Alloy LNHV.
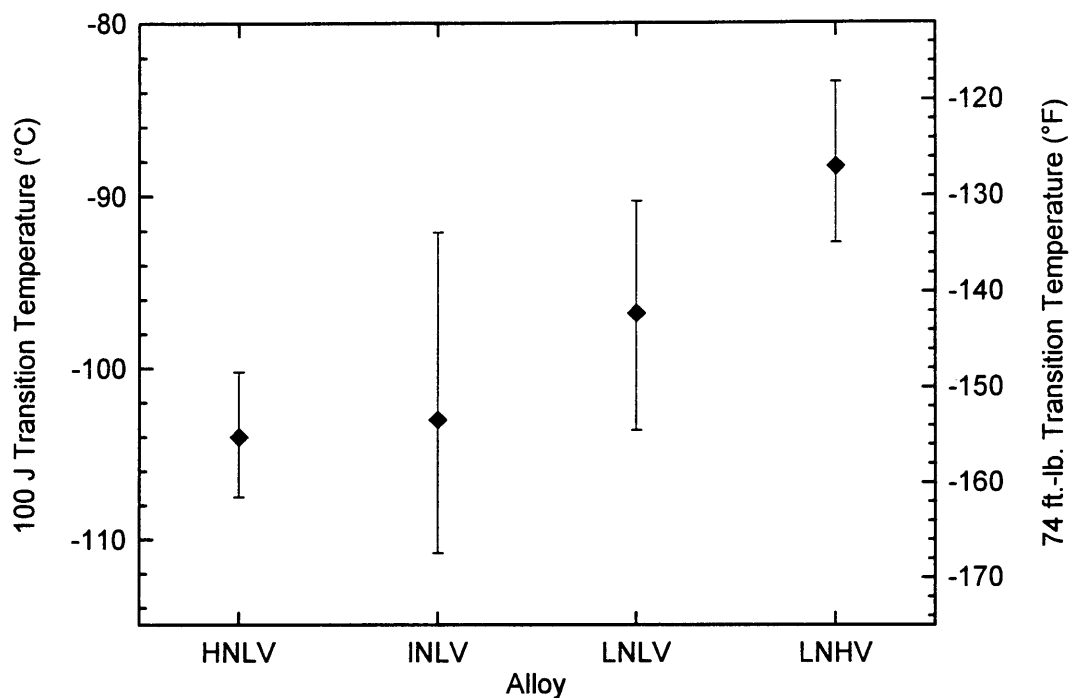
Figure 5.8.   100 joule impact transition temperature for as-quenched-and-tempered
baseplate.

Alloy INLV demonstrates the most scatter with ±10°C variation of the 100 J transition

temperature.

5.1.3 Titanium Nitride Precipitates

Typical transmission electron microscope photomicrographs of carbon extraction

replicas from the baseplate are shown in Figure 5.9. These photomicrographs were taken

with a scanning transmission electron microscope (STEM) in transmission mode.
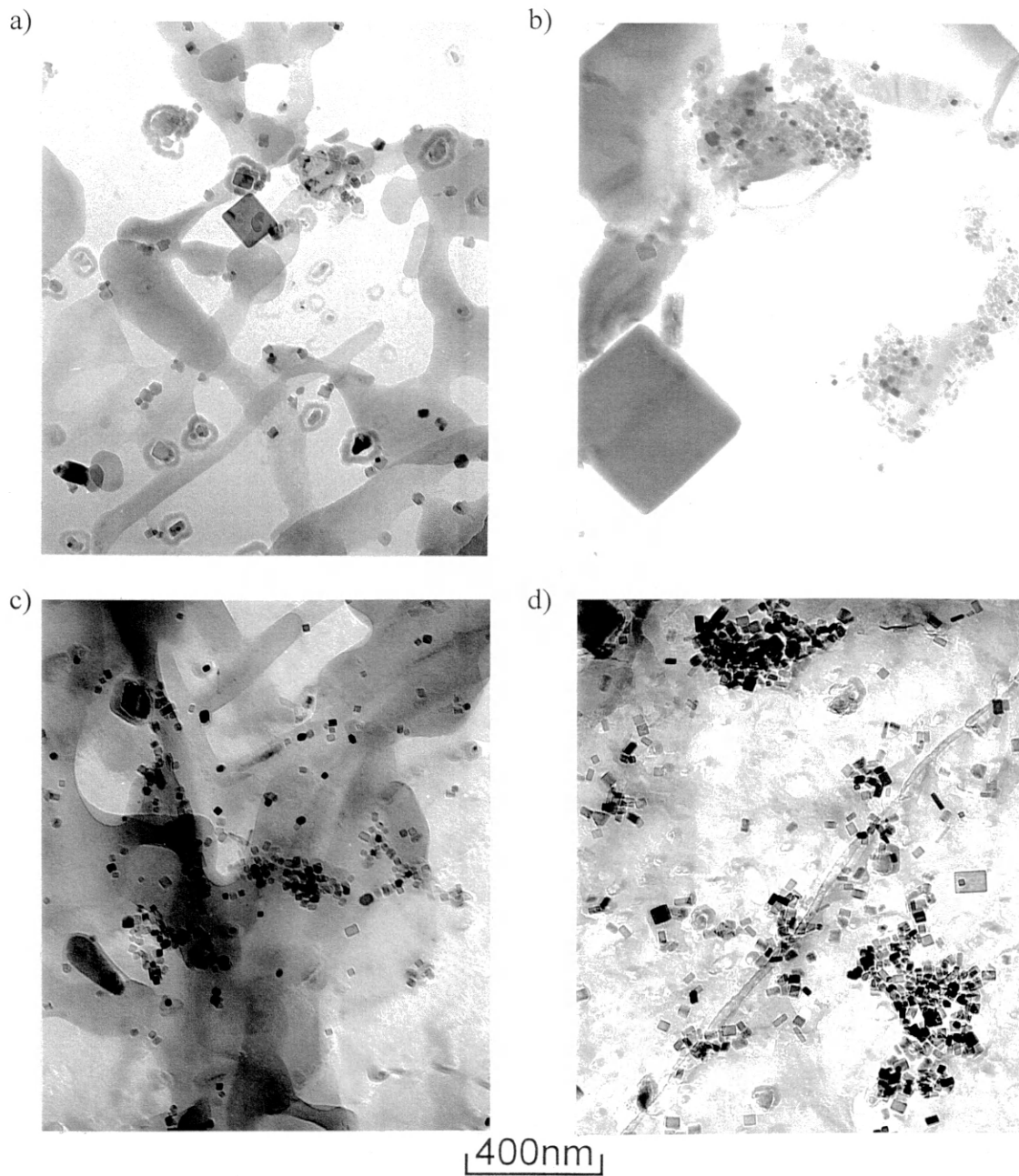
Figure 5.9.   Typical TEM photomicrographs of carbon extraction replicas taken of as-quenched-and-tempered plate. a) Alloy HNLV. b) Alloy INLV. c) Alloy LNLV. d) Alloy LNHV.

Apparent in these fields is the presence of both small (< 15 nm) and large (> 200 nm) TiN

particles. Aside from the characteristic cubic or rectangular prism morphology,

confirmation that the precipitates were titanium nitride was performed using EDS in the

STEM. Particles found during TEM analysis were measured and plotted in histograms,

which are shown in Figure 5.10. Also present in the figure are average particle size values

both including and excluding particles larger than 100 nm. These average values are

summarized in Table 5.1.

Table 5.1. Average Titanium Nitride Precipitate Edge Length for As-Quenched-and-
Tempered Baseplate. All values in nm.

Alloy	Average Size Excluding > 100 nm Particles	Average Size Including > 100 nm Particles
HNLV	18.9	29.0
INLV	20.3	38.0
LNLV	25.3	39.4
LNHV	30.4	54.6

Note that the particle size axis in Figure 5.10 is not linear. This approach was taken

to accentuate the lower end of the size scale to provide information about the small, grain-

size-controlling titanium nitride precipitates. The precipitation process should result in a

normal distribution (80), therefore, the data are not presented in a log-normal fashion.
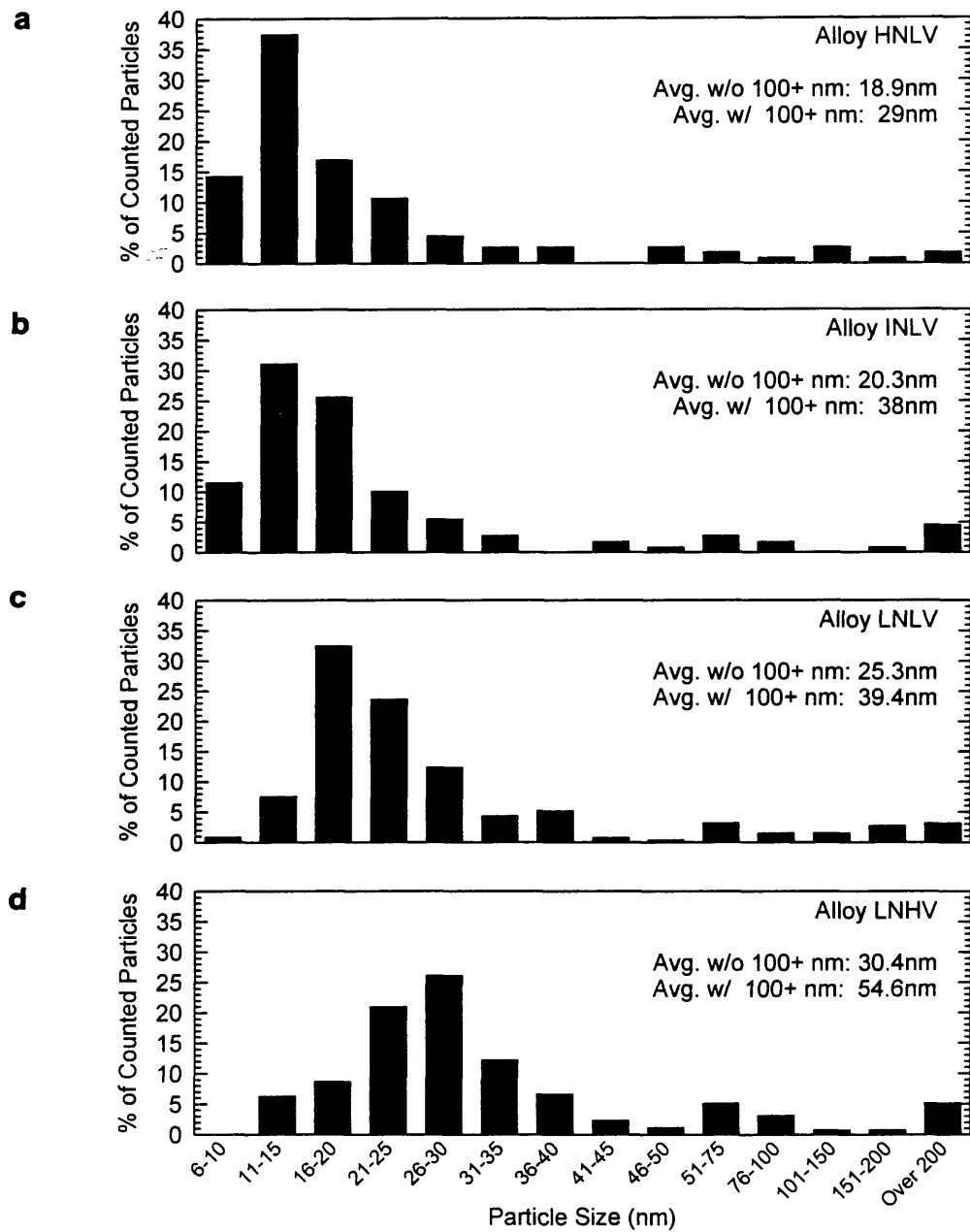
Figure 5.10. Titanium nitride precipitate histograms of as-quenched-and-tempered materials. a) Alloy HNLV. b) Alloy INLV. c) Alloy LNLV. d) Alloy LNHV.

As shown in Figure 5.10 and Table 5.1, there is a clear shift in the particle size

distribution toward larger sizes from alloy HNLV to alloy LNLV, as well as alloy LNHV.

The initial precipitation temperature for each of the four alloys was calculated to

determine if this temperature was related to the trend in titanium nitride precipitate size.

This calculation is easily performed by solving a solubility product relation, such as

equations 1.11 through 1.15, for temperature and inputting the appropriate chemical

compositions. Using equations 1.12 and 1.14 for liquid and austenite, respectively, the

resulting initial precipitation temperatures were calculated. The results of these calculations

are shown in Table 5.2.

It is interesting to note that the solubility product for liquid steel predicts

precipitation at temperatures where the steel is in a solid state, while the solubility product

for the solid (austenite) phase indicates that precipitation will occur at a temperature where

the steel would be liquid. Despite these anomalies, the same trend is shown for both sets of

Table 5.2. Calculated Initial Precipitation Temperatures for Titanium Nitride.

Alloy	Precipitation Temperature (liquid solubility product), °C (°F)	Precipitation Temperature (austenite solubility product), °C (°F)
HNLV	1357 (2474)	1612 (2935)
INLV	1344 (2451)	1576 (2869)
LNLV	1312 (2393)	1495 (2723)
LNHV	1366 (2491)	1635 (2977)

calculations: the precipitation temperature decreases from alloys HNLV through LNLV, and the highest precipitation temperature occurs for alloy LNHV (the increased volume fraction alloy). Based on these calculations alone, alloy LNHV is expected to have the largest particle size, followed by alloys HNLV through LNLV. Excluding alloy LNHV, this trend is opposite to that shown in Figure 5.10. Clearly, the initial precipitation temperature is not controlling the titanium nitride precipitate size in these alloys.

5.2 Submerged Arc Welds

Figure 5.11 shows photomicrographs of the bead-on-plate welds performed to create a baseline for further welding simulations to be performed on the baseplates described in section 5.1. Evident from the figure is that the 8 kJ/mm heat input weld deposits considerably more material than does the 4 kJ/mm heat input weld. Also shown in the figure is the extent of the heat-affected zone, which is outlined by the white lines in the micrographs. The 8 kJ/mm heat input weld clearly demonstrates a heat-affected zone that extends further into the plate than the 4 kJ/mm heat input weld.

The microstructures of the coarse-grained heat-affected zones are shown in Figure 5.12 through Figure 5.15. In the photomicrographs shown, the fusion zone is on the left-hand side and the coarse-grained heat-affected zone is immediately adjacent to the fusion line.

a)

b)
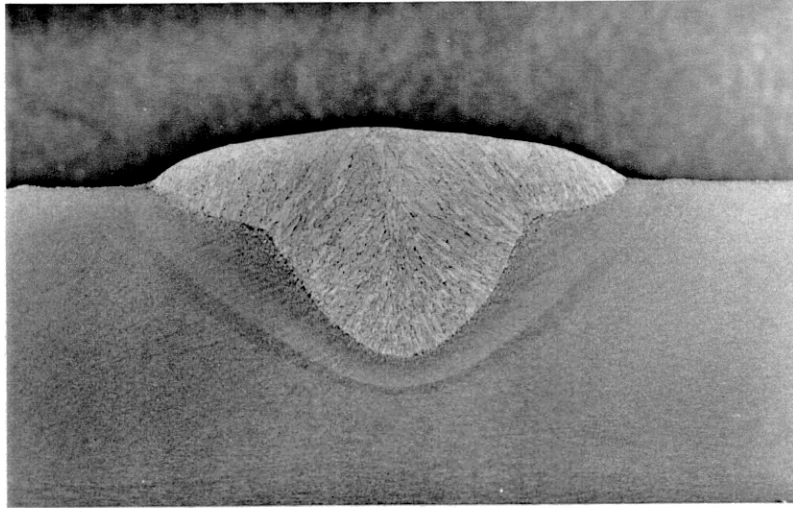
⌐0.8mm⌐
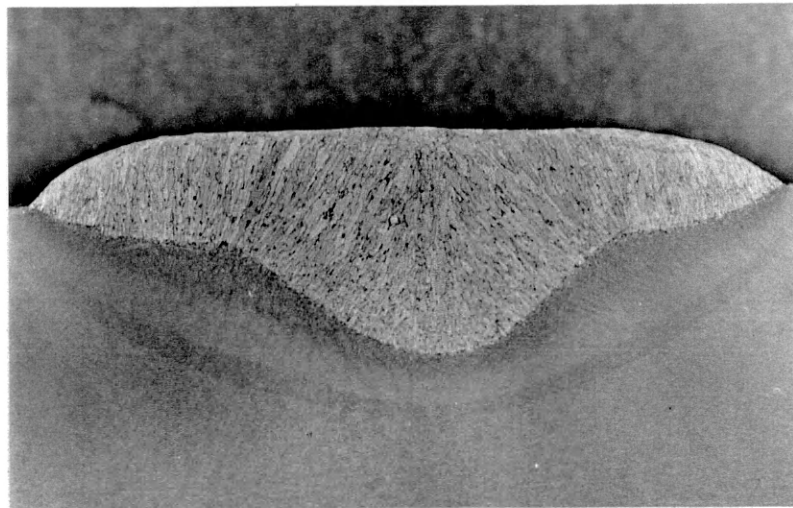
Figure 5.11. Submerged arc, bead-on-plate welds. a) 4 kJ/mm heat input. b) 8 kJ/mm heat input. Nital etch. Light micrographs.

a)

b)

75µm
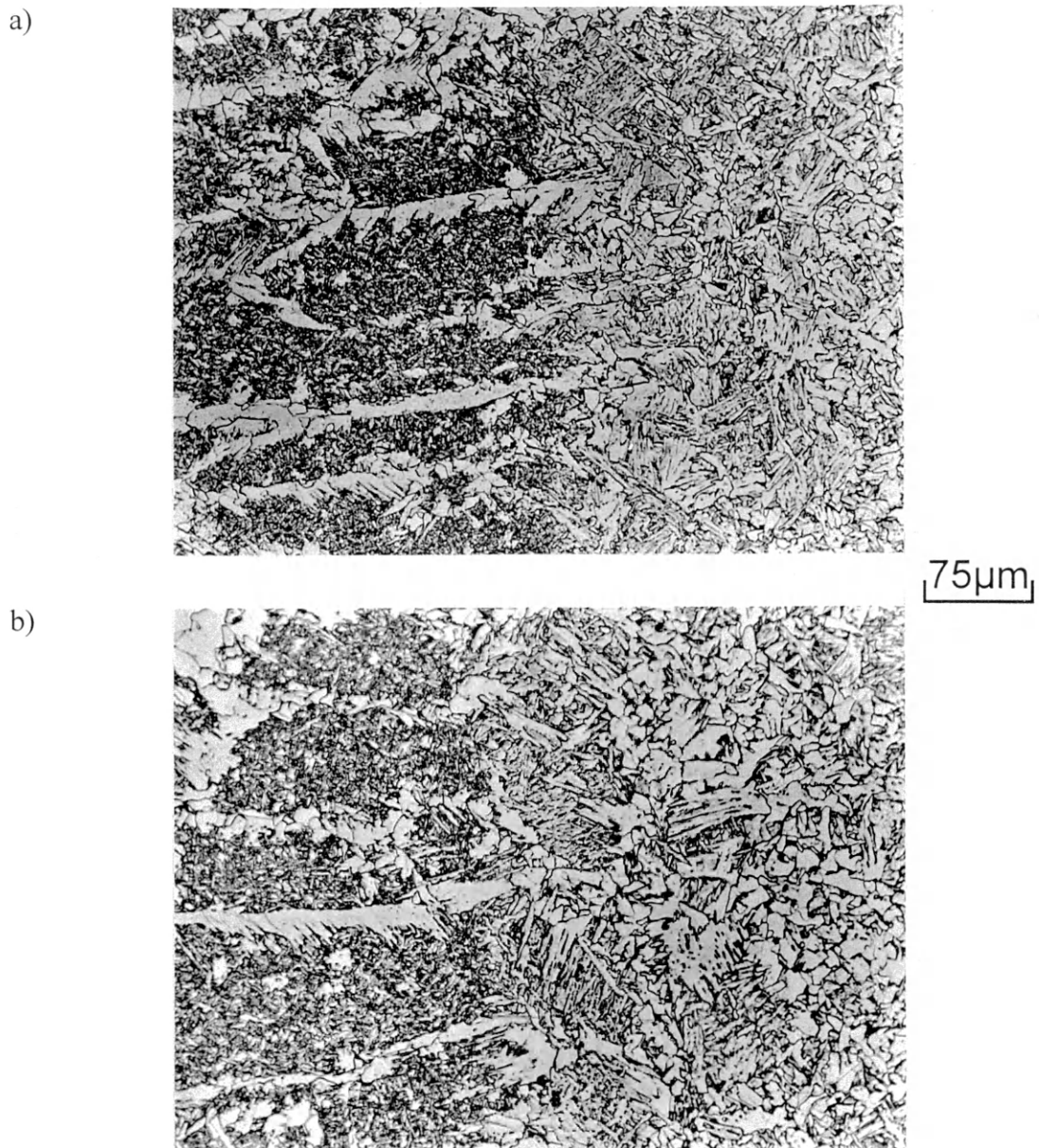
Figure 5.12. Coarse-grained heat-affected zone microstructures in submerged arc welds.
a) 4 kJ/mm heat input. b) 8 kJ/mm heat input. Alloy HNLV. Nital etch.
Light micrographs.

a)

b)

75µm
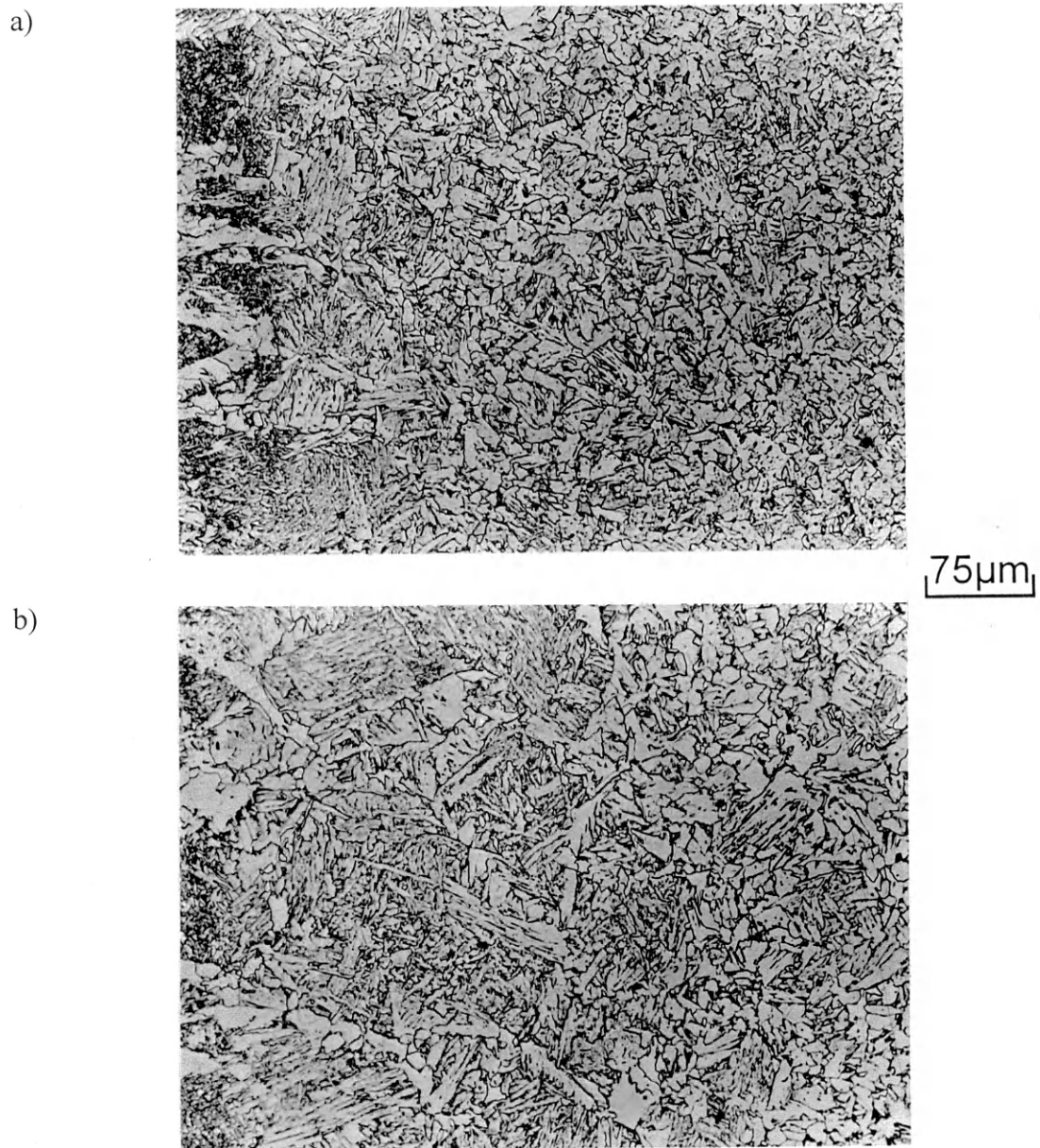
Figure 5.13. Coarse-grained heat-affected zone microstructures in submerged arc welds.
a) 4 kJ/mm heat input. b) 8 kJ/mm heat input. Alloy INLV. Nital etch.
Light micrographs.

a)

75μm

b)
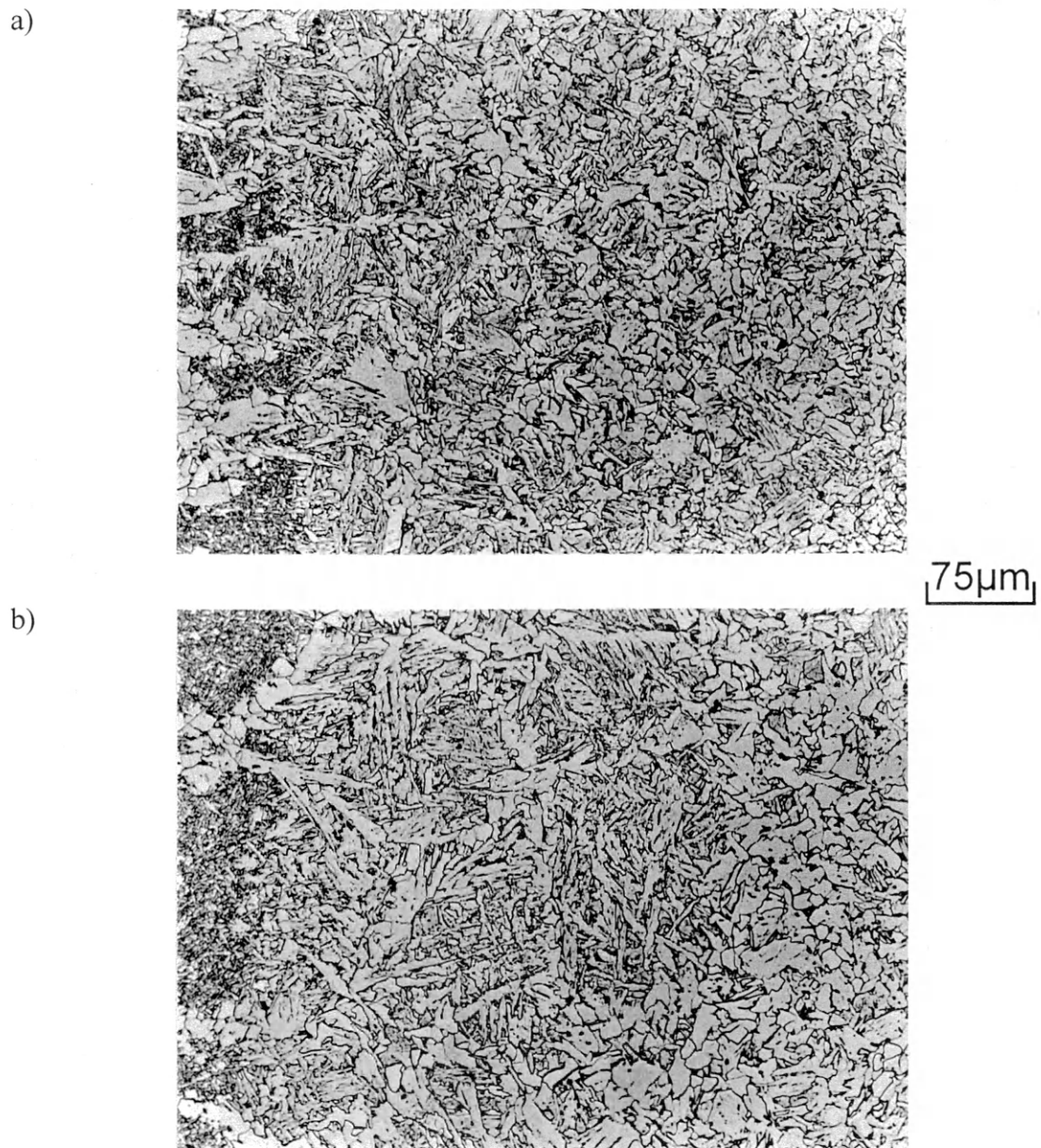
Figure 5.14. Coarse-grained heat-affected zone microstructures in submerged arc welds.
a) 4 kJ/mm heat input. b) 8 kJ/mm heat input. Alloy LNLV. Nital etch.
Light micrographs.

a)

b)

⌐75µm⌐
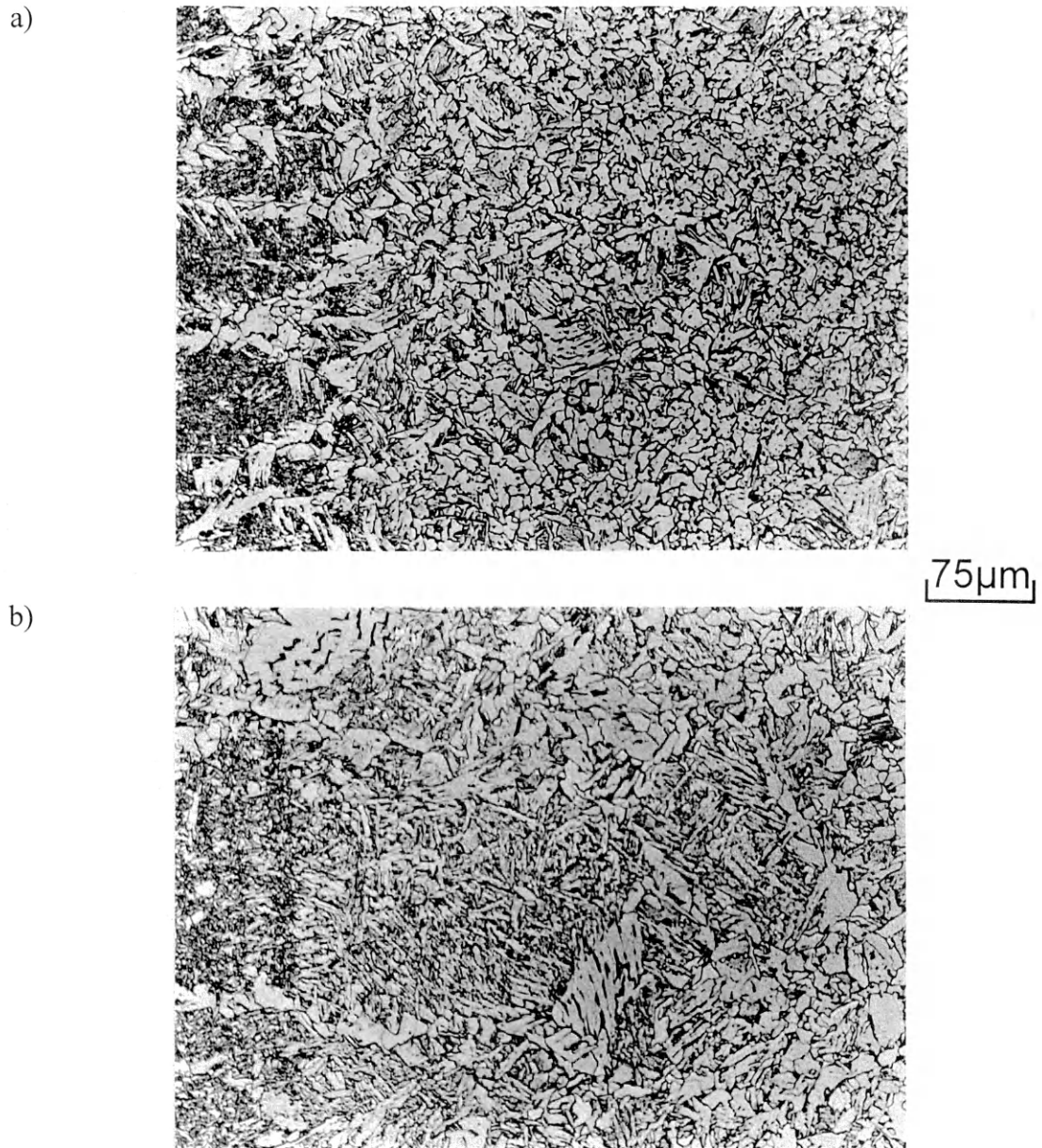
Figure 5.15. Coarse-grained heat-affected zone microstructures in submerged arc welds. a) 4 kJ/mm heat input. b) 8 kJ/mm heat input. Alloy LNHV. Nital etch. Light micrographs.

In conjunction with the microstructure of the various coarse-grained heat-affected zones, microhardness testing was performed. The results of this testing are shown in Figure 5.16. Generally, the hardness of the 4 kJ/mm heat input coarse-grained heat affected zone falls between 198 and 214 VHN. There is a trend of decreasing hardness from alloy HNLV to alloy LNHV. However, all average values fall with the 198 to 214 VHN range.

The 8 kJ/mm heat input specimens do not display as well defined a trend as is demonstrated in the 4 kJ/mm specimens. The 8 kJ/mm heat input specimens were observed to have a similar general hardness: approximately 203 ± 5 VHN. There is more scatter in the hardness for alloys HNLV and INLV in the 8 kJ/mm specimens as compared to the 4 kJ/mm specimens.

5.3 Thermal Simulation Validation

Photomicrographs showing the microstructures of the material subjected to the coarse-grained heat-affected zone simulations are shown in Figure 5.17 through Figure 5.20. The thermal cycles used for these simulations are shown in Figure 4.1. Ideally, these microstructures would perfectly match the previously shown microstructures for the coarse-grained heat-affected zone of the submerged arc welds. Apparent from comparison between the micrographs of the actual welds (Figure 5.12 through Figure 5.15) and the simulated heat-affected zones (Figure 5.17 though Figure 5.20) is that the Gleeble
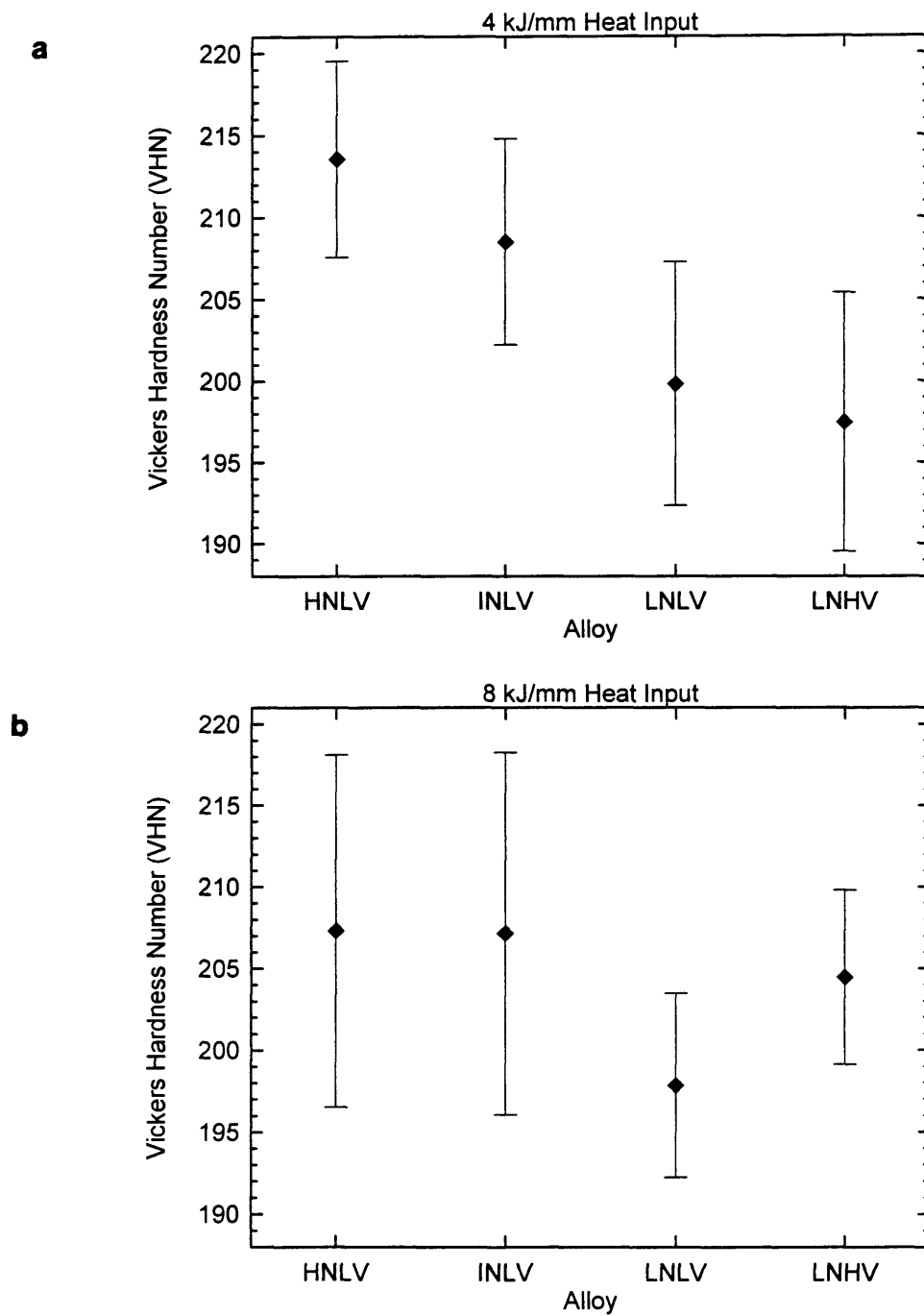
Figure 5.16. Vickers hardness number for coarse-grained heat-affected zone in a) 4 kJ/mm heat input and b) 8 kJ/mm heat input submerged-arc welds. Error bars are standard deviation.

a)

b)

75μm
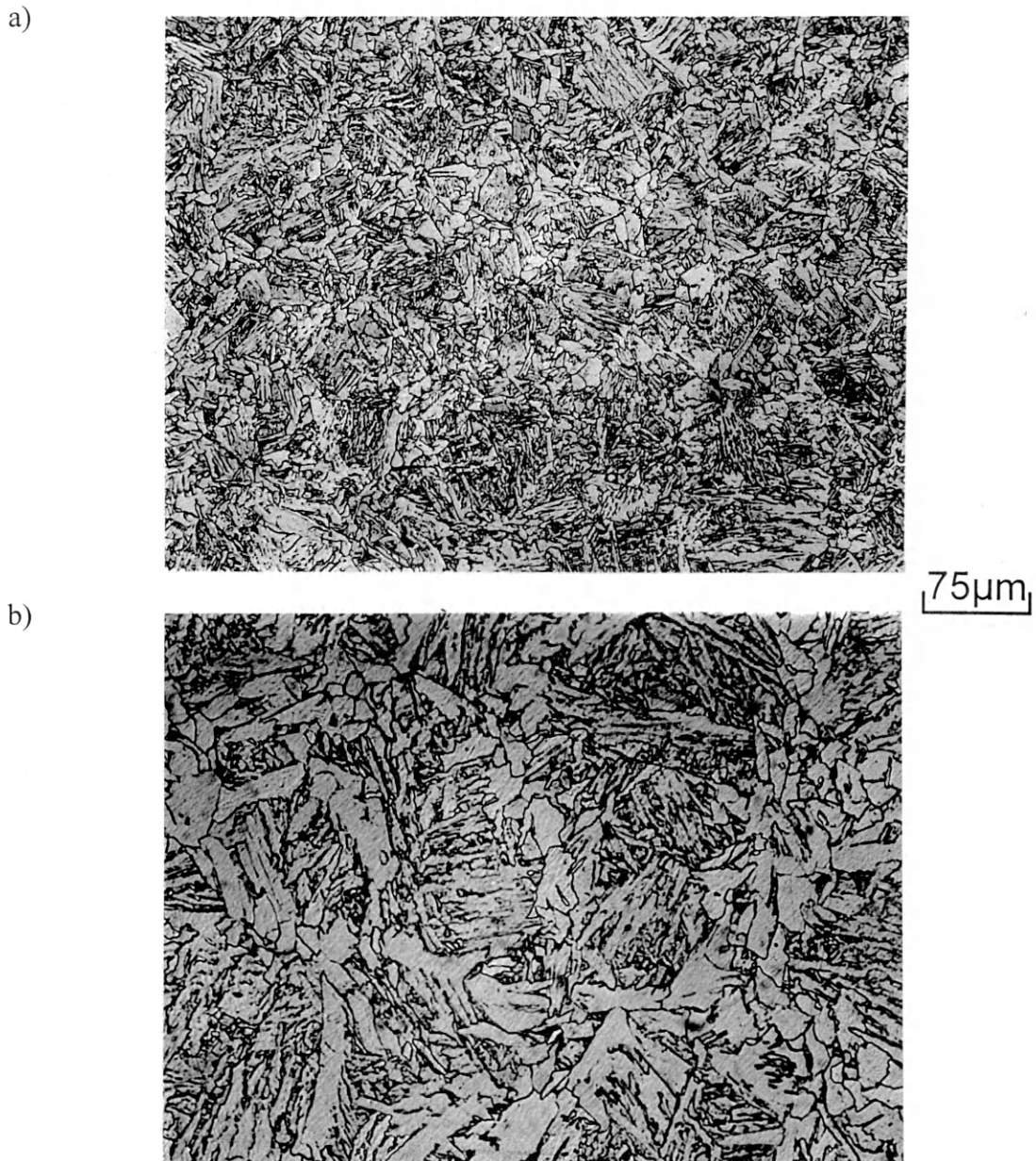
Figure 5.17. Simulated coarse-grained heat-affected zone microstructures. a) 4 kJ/mm heat input. b) 8 kJ/mm heat input. Alloy HNLV. Nital etch. Light micrographs.

a)

b)

75μm
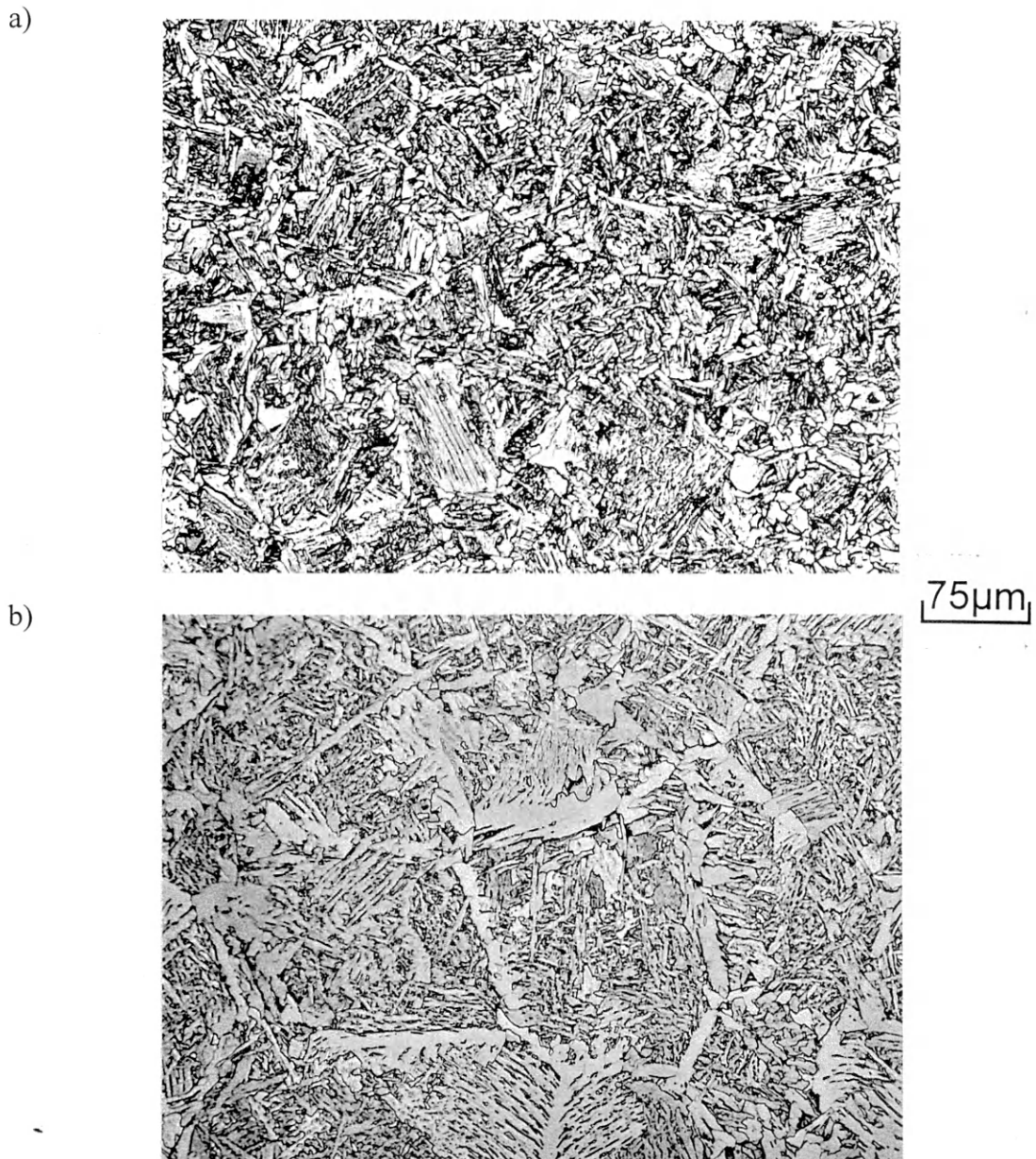
Figure 5.18. Simulated coarse-grained heat-affected zone microstructures. a) 4 kJ/mm heat input. b) 8 kJ/mm heat input. Alloy INLV. Nital etch. Light micrographs.

a)

b)

75μm
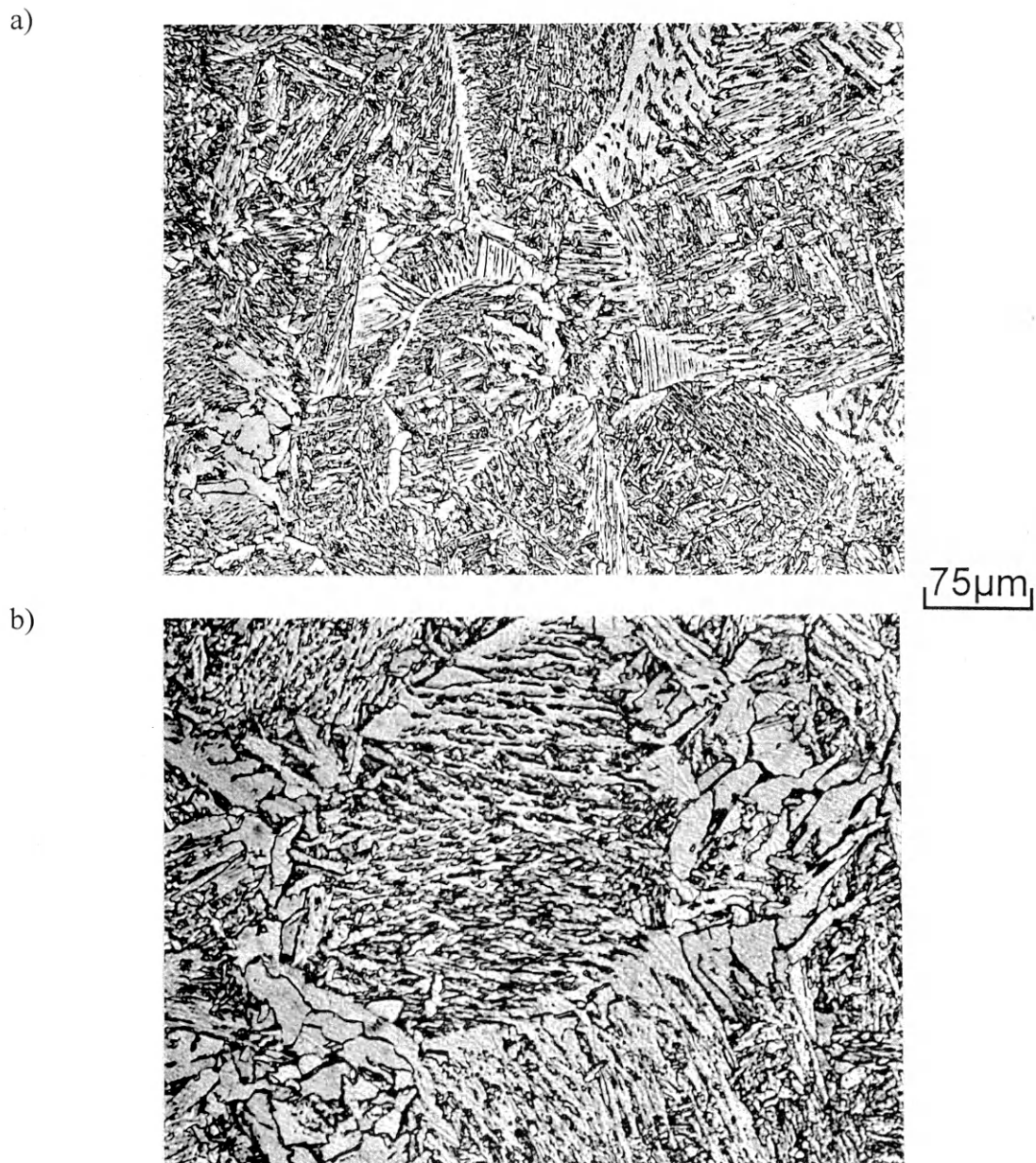
Figure 5.19. Simulated coarse-grained heat-affected zone microstructures. a) 4 kJ/mm
heat input. b) 8 kJ/mm heat input. Alloy LNLV. Nital etch. Light
micrographs.

a)

b)

75μm
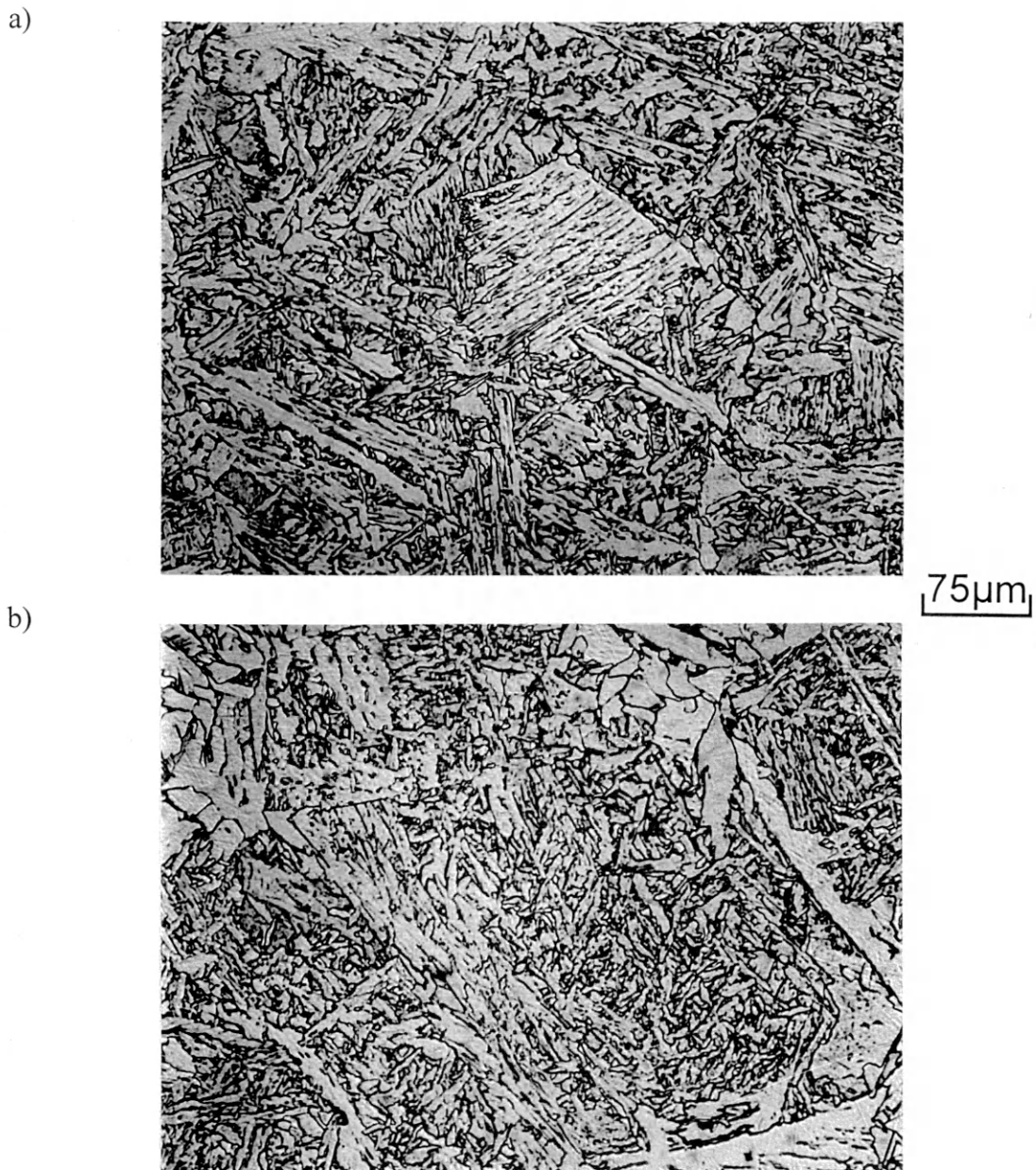
Figure 5.20. Simulated coarse-grained heat-affected zone microstructures. a) 4 kJ/mm heat input. b) 8 kJ/mm heat input. Alloy LNHV. Nital etch. Light micrographs.

simulation specimens generally have coarser microstructures than do the submerged-arc welded specimens. This is a common occurrence with Gleeble simulations as there is a larger region of material that achieves the temperatures required to coarsen the austenite grains. In an actual weld, the grain-coarsened material is bounded by relatively fine-grained material, limiting the grain-coarsened region.

As it is common to find small differences in microstructure between actual welds and simulations, microhardness testing was performed to ensure similar properties between the two conditions. The results for the submerged-arc welded specimens were previously shown (Figure 5.16). The hardness values for the simulated heat-affected zone specimens are shown in Figure 5.21.

The 4 kJ/mm heat input hardness data show a general decrease in hardness from alloys HNLV to LNLV. However, the average values for all four alloys fell with a range of 205 ± 6 VHN. The 8 kJ/mm specimens had similar hardness values with all of their average hardnesses falling within a range of ± 7 VHN centered at 202 VHN. There was not a general trend observed in the 8 kJ/mm heat input specimens as was observed in the 4 kJ/mm heat input specimens. A slight increase in hardness was observed from alloy HNLV to alloy INLV, followed by a decrease to alloy LNLV. Alloy LNHV demonstrated a higher hardness than LNLV but lower than HNLV or INLV.

At this stage of the study, the magnitude of the hardness values is secondary. What is important is that the actual submerged-arc weld coarse-grained heat-affected zones have
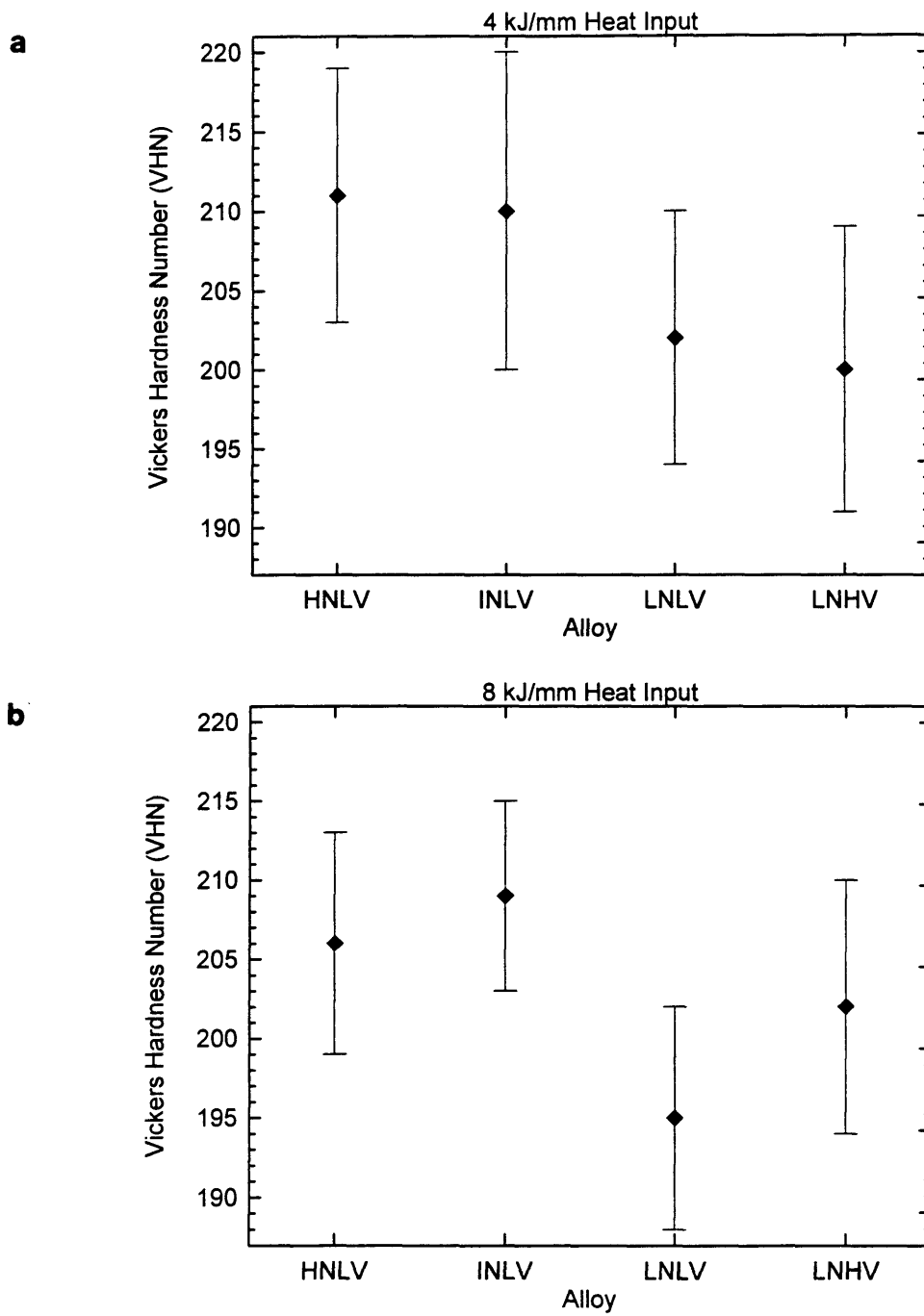
Figure 5.21. Vickers hardness number for coarse-grained heat-affected zone in a) 4 kJ/mm heat input and b) 8 kJ/mm heat input weld simulations. Error bars are standard deviation.

similar hardness values as the simulated coarse-grained heat-affected zone specimens.

properties. Figure 5.22 shows comparison plots between the hardness of the actual and

simulated weld specimens. It is clearly shown in these plots that the hardness of the

simulated heat-affected zone specimens matches the hardness of the actual submerged arc

weld heat-affected zone specimens.

5.4 Simulated Heat-Affected Zone Characterization

Based on the similarities of the microstructures and hardnesses of the simulated

heat-affected zones and the actual weld heat-affected zones, it was decided that the thermal

cycles shown in Figure 4.1 were a reasonable representation of the submerged arc weld

CGHAZ. Now that appropriate thermal cycles have been designed, analysis of thermally-

cycled materials can be undertaken. This analysis will begin with the titanium nitride

precipitates.

5.4.1 Titanium Nitride Precipitate Analysis

The titanium nitride precipitates in the simulated coarse-grained heat-affected zone

were studied in the same fashion as in the baseplate. Figure 5.23 and Figure 5.24 show

representative photomicrographs from carbon extraction replicas of the 4 kJ/mm and 8
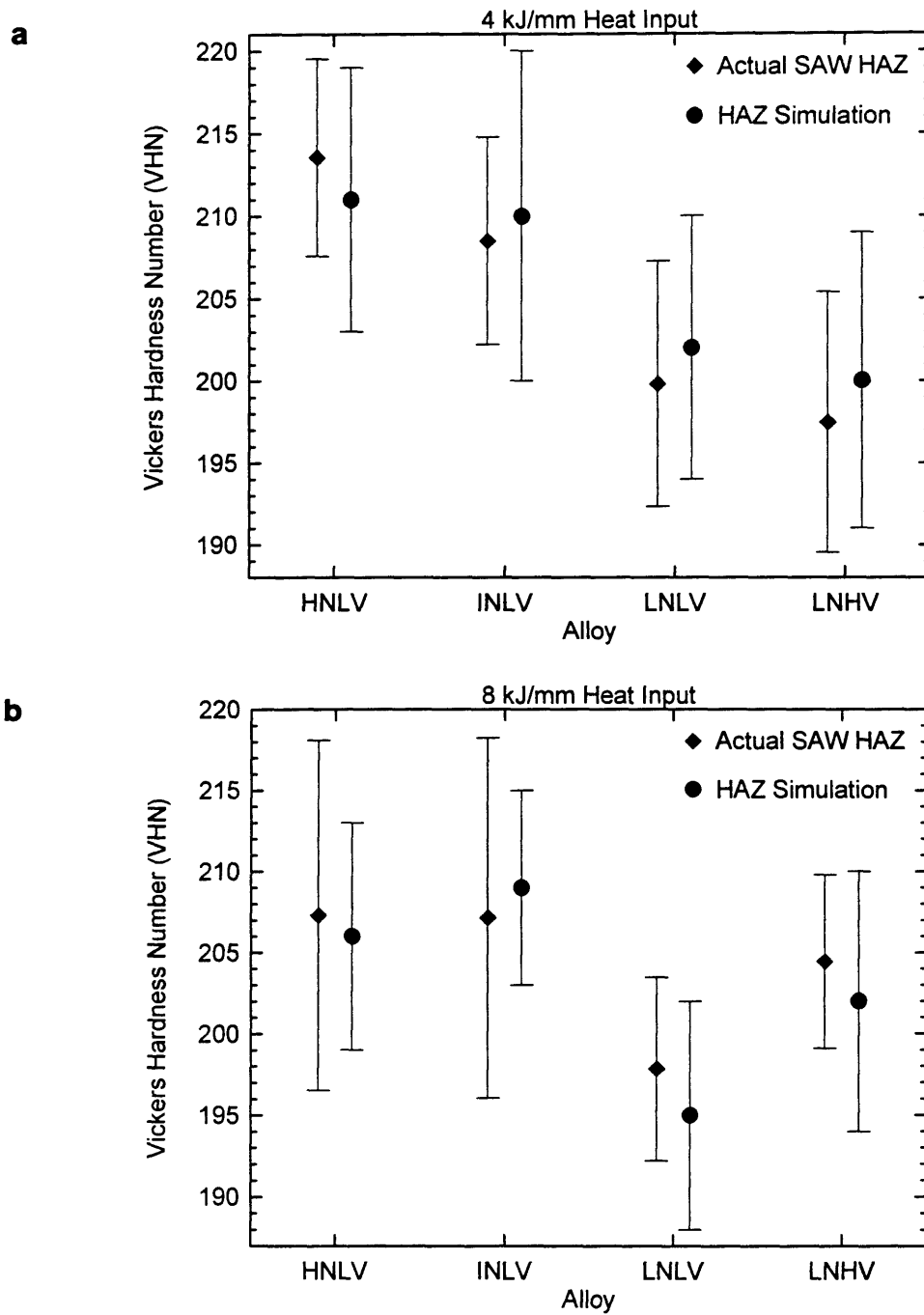
Figure 5.22. Comparison of hardness for simulated and actual coarse-grained heat-affected zones. a) 4 kJ/mm heat input. 8 kJ/mm heat input.
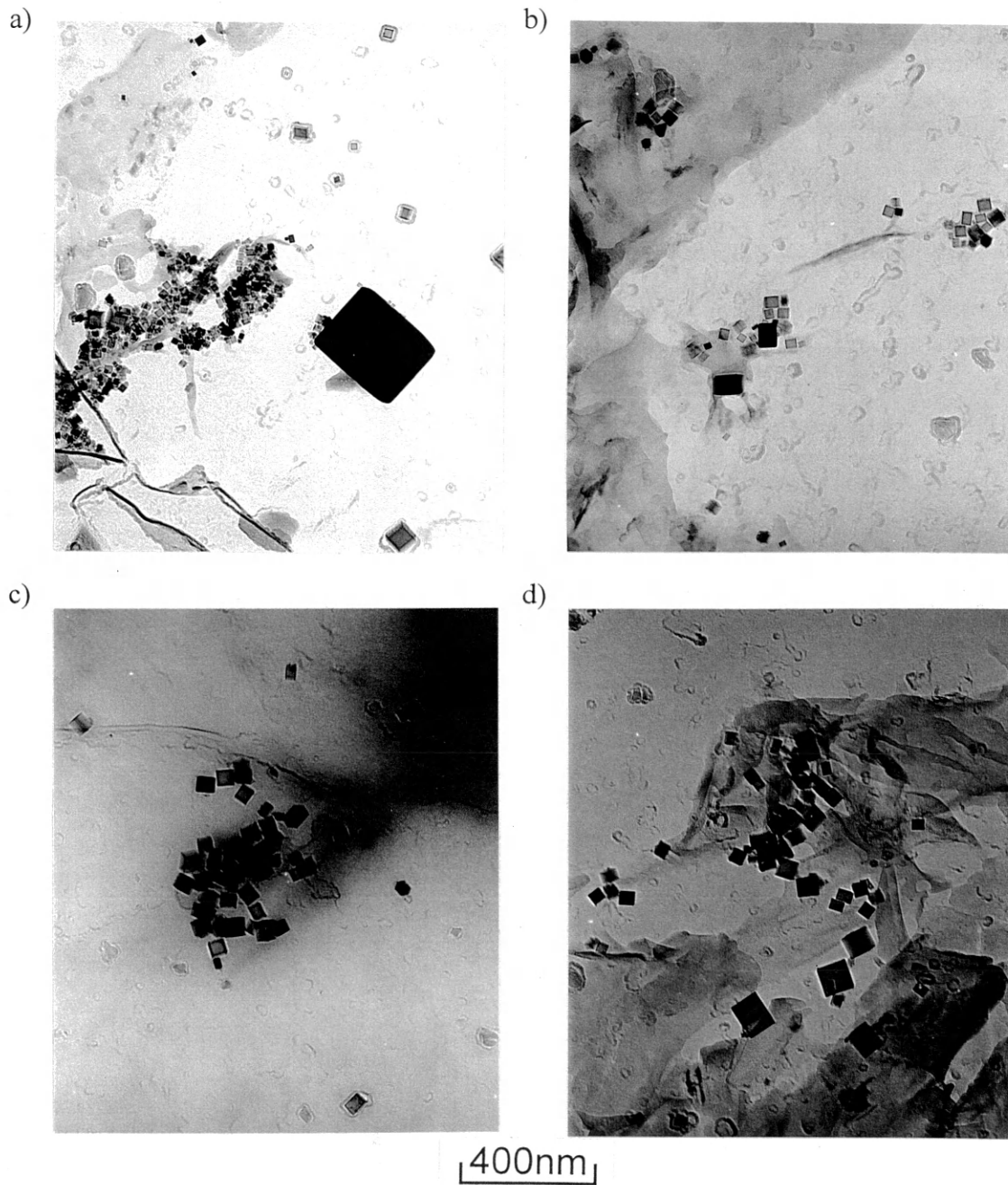
Figure 5.23. TEM photomicrographs of carbon extraction replicas taken from thermally cycled specimens. 4 kJ/mm heat input. 1350°C peak temperature. a) Alloy HNLV. b) Alloy INLV. c) Alloy LNLV. d) Alloy LNHV.
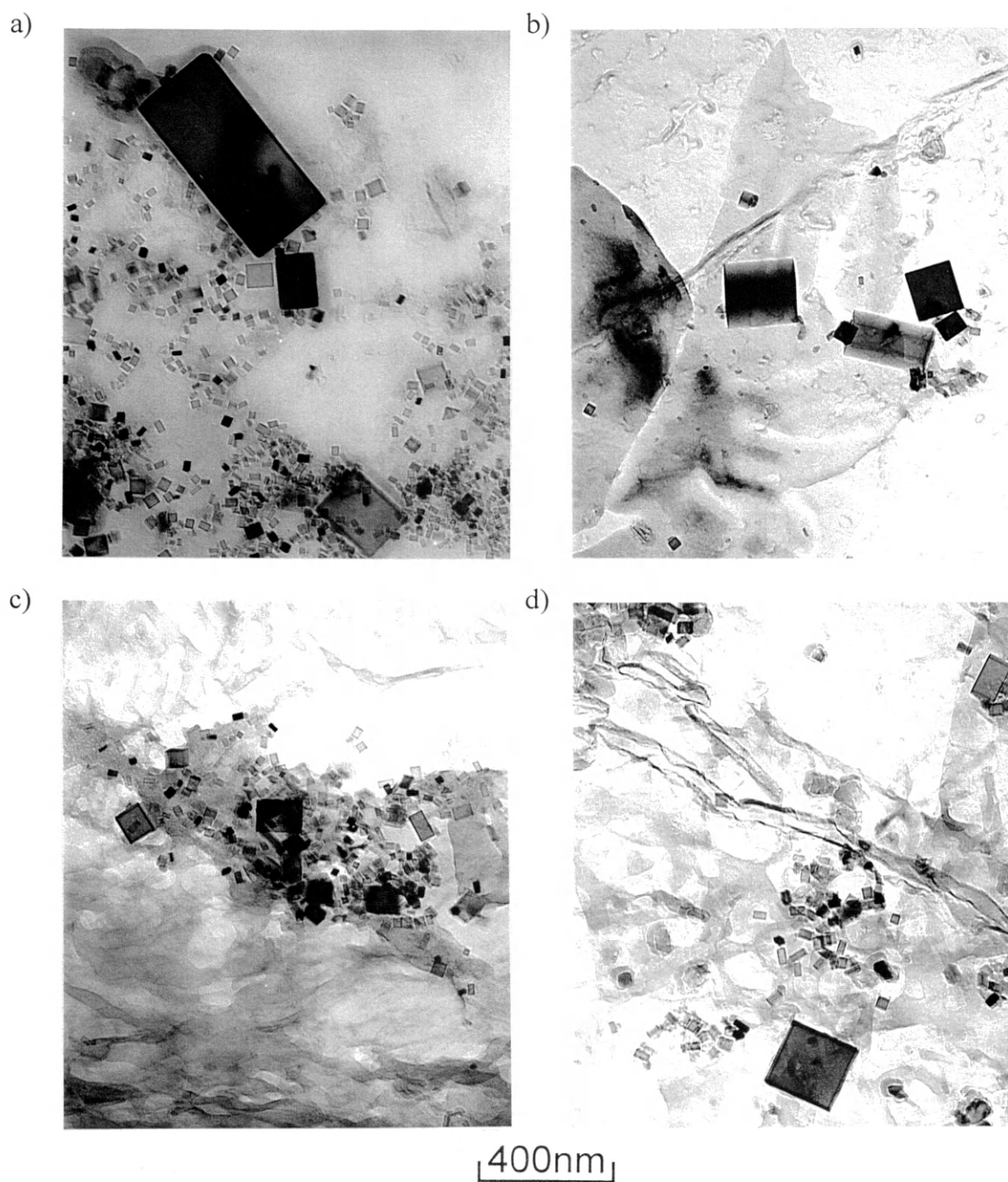
Figure 5.24. TEM photomicrographs of carbon extraction replicas taken from thermally cycled specimens. 8 kJ/mm heat input. 1350°C peak temperature. a) Alloy HNLV. b) Alloy INLV. c) Alloy LNLV. d) Alloy LNHV.

kJ/mm heat inputs, 1350°C peak temperature thermal cycles, respectively. The corresponding particle size histograms are shown in Figure 5.25 and Figure 5.26. Again, the average values for titanium nitride precipitate size are tabulated for ease of comparison (see Table 5.3).

Table 5.3. Average Titanium Nitride Precipitate Sizes for Thermally Cycled Material (Values in nm).

Alloy	4 kJ/mm Heat Input		8 kJ/mm Heat Input	
	Excluding > 100 nm	Including > 100 nm	Excluding > 100 nm	Including > 100 nm
HNLV	22.0	25.0	32.4	46.2
INLV	29.8	58.4	33.2	48.1
LNLV	38.6	57.8	36.0	64.6
LNHV	45.1	53.1	42.0	76.0

As was seen in the baseplate example (Figure 5.10), the particle size increases from alloy HNLV to alloy LNLV, and alloy LNHV contains the largest precipitates. This trend is shown quite well in the 4 kJ/mm heat input data when neglecting the large, greater-than-100-nm precipitates. Both the results from the baseplate and thermally cycled specimens support the premise that increased free nitrogen helps prevent titanium nitride precipitate growth. Also supported is the hypothesis that increased additions of alloy, to create higher
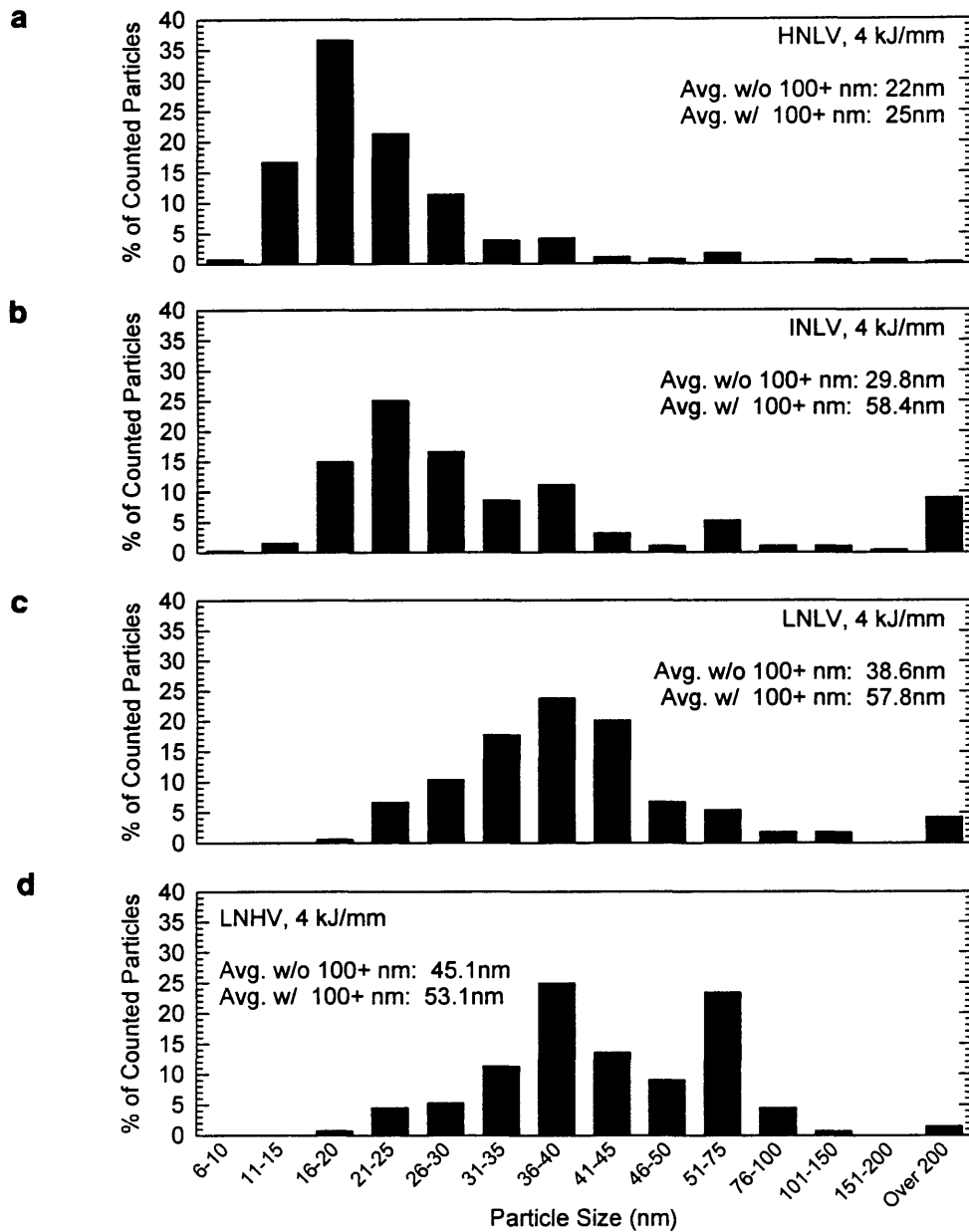
Figure 5.25. Titanium nitride precipitate size histograms of thermally cycled material. 4 kJ/mm heat input. 1350°C peak temperature. a) Alloy HNLV. b) Alloy INLV. c) Alloy LNLV. d) Alloy LNHV.
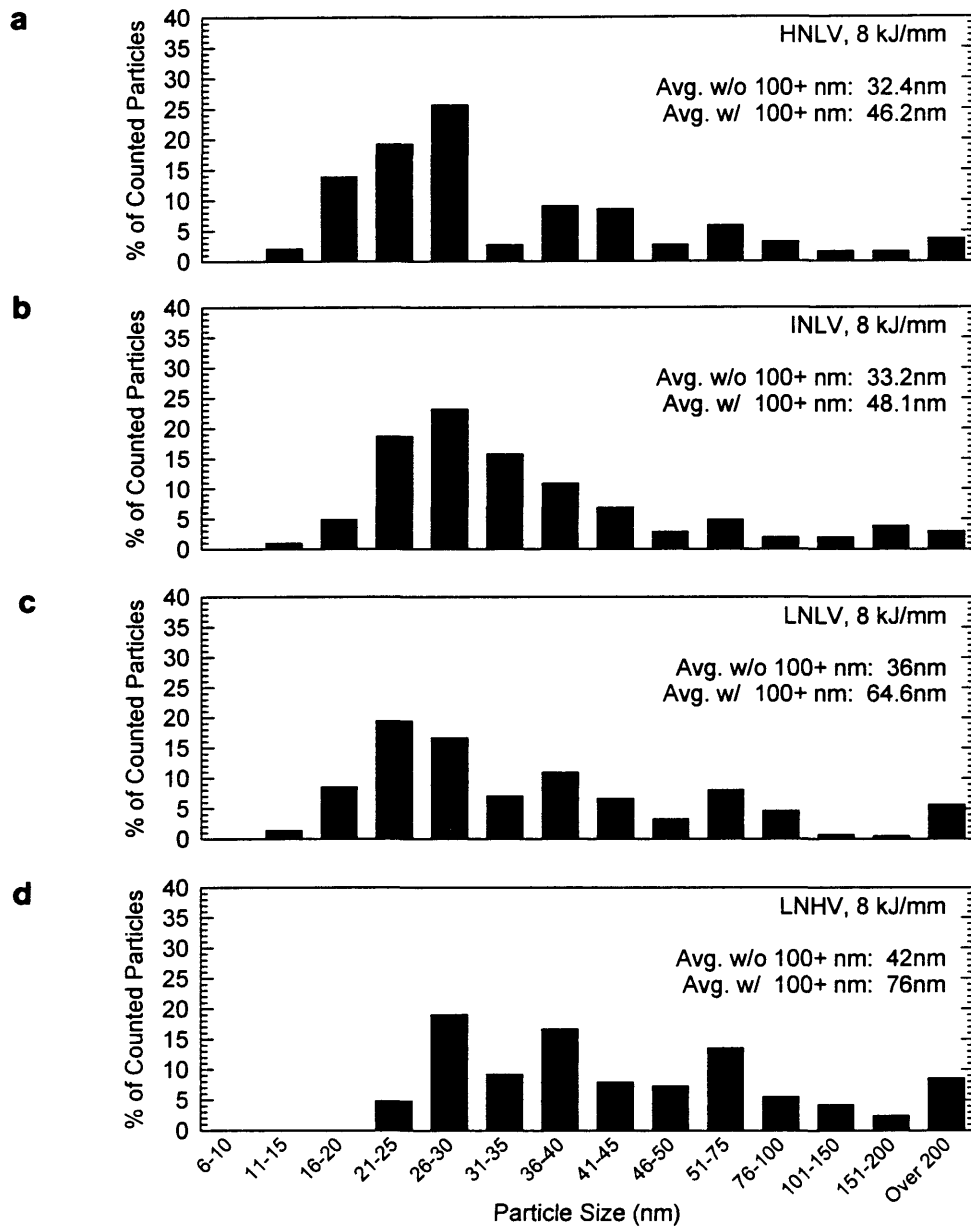
Figure 5.26. Titanium nitride precipitate size histograms of thermally cycled material. 8 kJ/mm heat input. 1350°C peak temperature. a) Alloy HNLV. b) Alloy INLV. c) Alloy LNLV. d) Alloy LNHV.

volume fractions of precipitate, results in larger precipitate size. The issues associated with precipitate coarsening will be considered at greater length in the Discussion section.

5.4.2 Prior-Austenite Grain Size

One of the critical measurements made during the course of this study was that of the prior-austenite grain size. It has already been discussed how important the austenite grain size can be to the final performance of a material. The prior-austenite grain size measurements would determine if the titanium nitride precipitates just discussed were effective in grain size control.

As outlined in the Experimental Procedure, alternate thermal cycles were required to provide microstructures suitable for revealing the prior-austenite grain size. In the Experimental Procedure section, four thermal cycles were shown associated with heat-affected zone simulations: the 4 kJ/mm heat input cycles with three peak temperatures (1250°C, 1350°C, and 1400°C) and the 8 kJ/mm heat input cycle with a 1350°C peak temperature. The 1250°C and 1400°C peak temperature cycles were implemented based on results of prior-austenite grain size of the specimens thermally cycled with peak temperatures of 1350°. Once the grain size results for the 1350°C peak temperature studies are presented, particularly for the 4 kJ/mm heat input specimens, it will become clear why the alternate peak temperatures were necessary.

Figure 5.27 provides examples of the prior-austenite grain structure in thermally cycled materials. Figure 5.28 shows the measured prior-austenite grain size for the 1350°C peak temperature, 4 kJ/mm and 8 kJ/mm heat input specimens. As shown in the figures, the 8 kJ/mm heat input specimens demonstrated a smaller prior-austenite grain size, with the exception of alloy LNLV. This result is not expected from standard metallurgical theory due to the increased time at high temperatures for high heat input specimens.

It is believed that the observed smaller grain size is a manifestation of the etching response of the specimens, where in the 8 kJ/mm heat input specimens, ferritic components of the microstructure are revealed in the etching process similar to prior-austenite grain boundaries. Consequently the number of intercepts counted is artificially increased, yielding a smaller measured austenite grain size. Perhaps the increased hardenability of alloy LNLV, due to the overly large prior-austenite grain size, precluded the formation of any ferrite, resulting in a more representative measure of the prior-austenite grain size, which is indeed larger than that observed in the corresponding 4 kJ/mm specimens.

Despite the difference in the magnitudes of the prior-austenite grain size between the 4 kJ/mm and 8 kJ/mm heat input specimens, a consistent trend is observed among the alloys. The trend clearly shows that prior-austenite grain size increases from alloys HNLV to LNLV, and decreases from LNLV to LNHV. This trend mirrors that shown by the

a)

b)

60μm
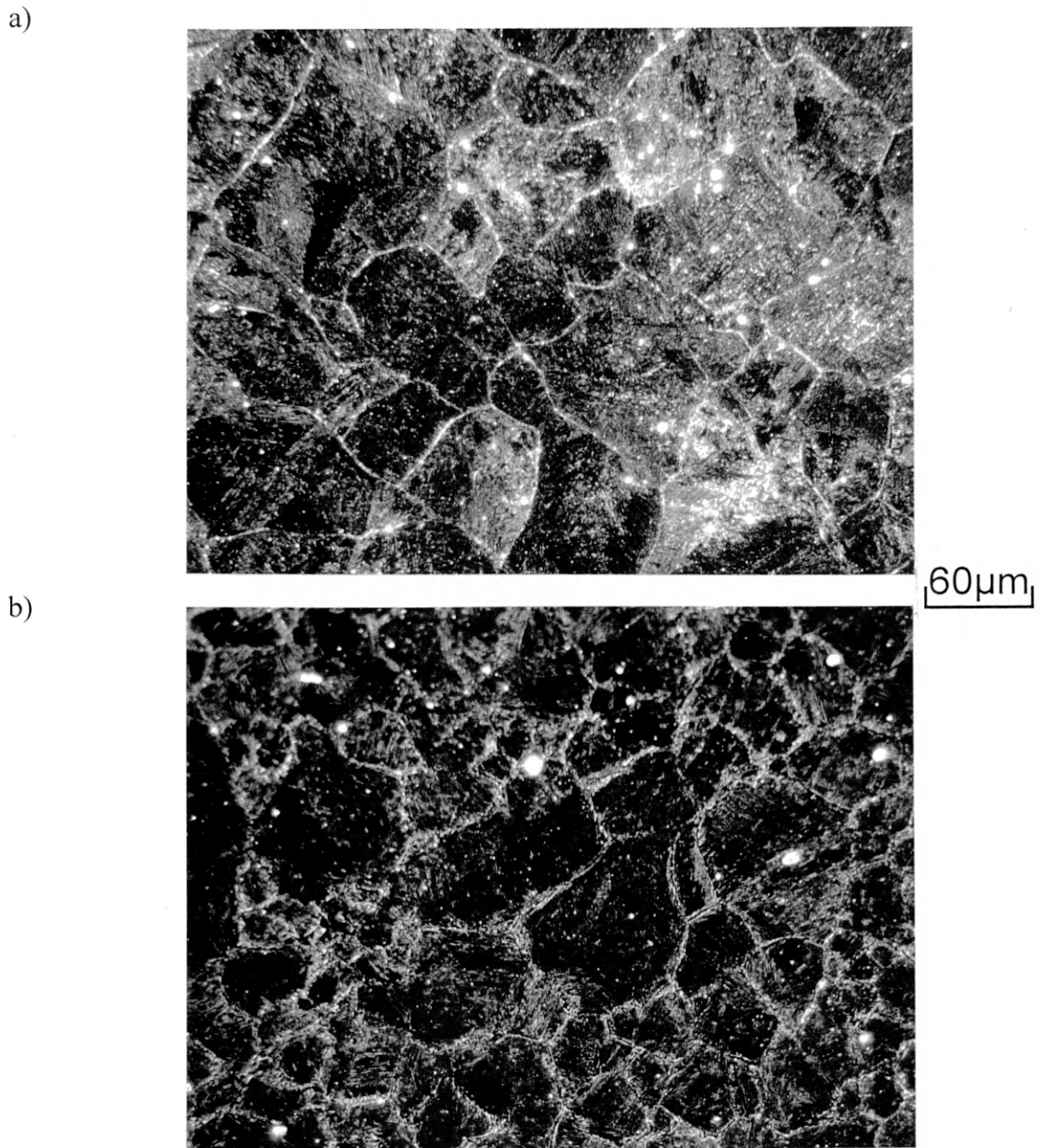
Figure 5.27. Examples of prior-austenite grain structure for thermally cycled specimens. a) 4 kJ/mm heat input, 1350°C peak temperature. b) 8 kJ/mm heat input, 1350°C peak temperature. Alloy HNLV. Dark-field light micrographs.
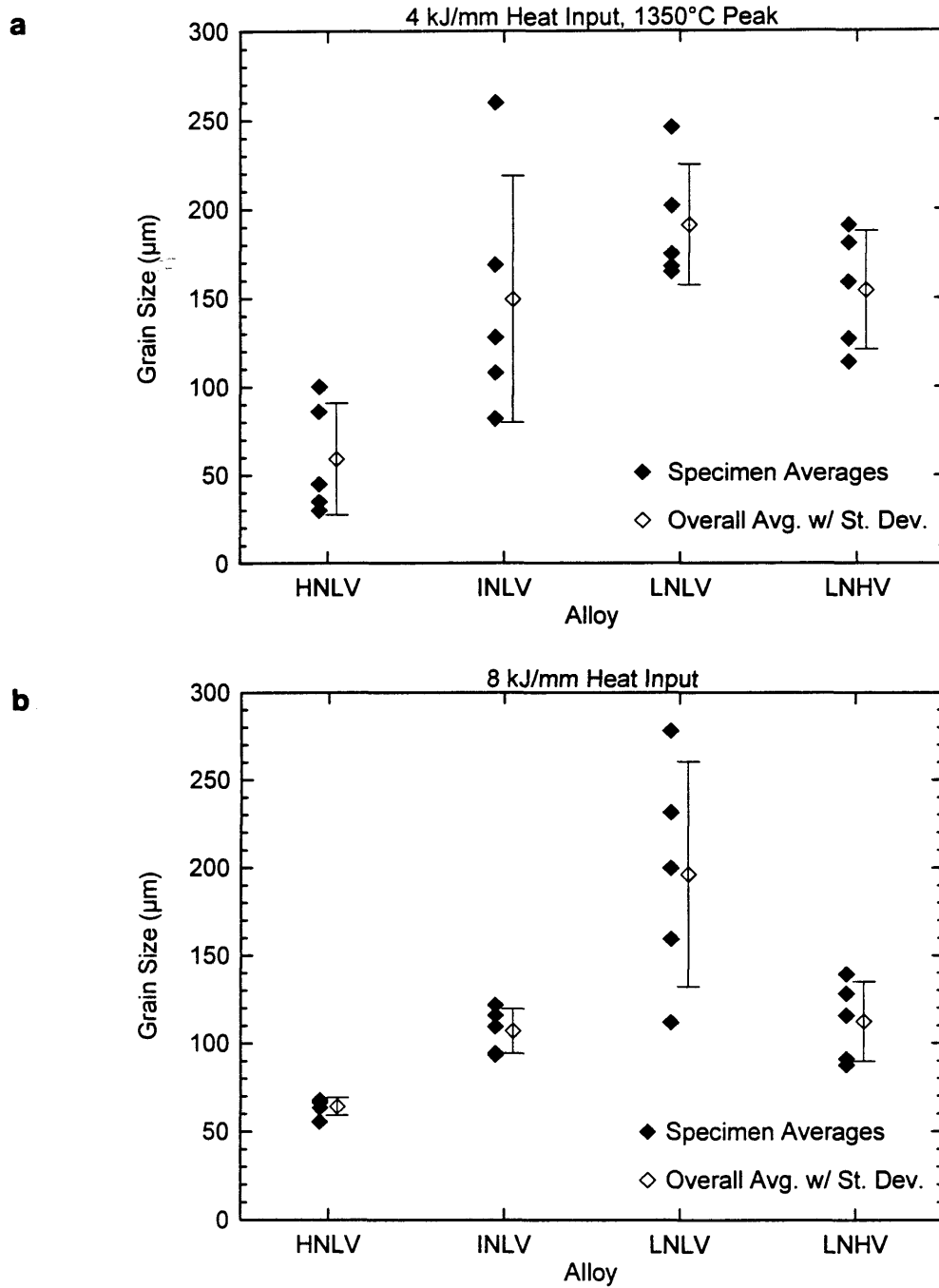
Figure 5.28. Prior-austenite grain size for 1350°C peak temperature specimens. a) 4
kJ/mm and b) 8 kJ/mm heat input. Individual averages for five test
specimens and an overall average with standard deviation are shown.

titanium nitride precipitate size for the first three alloys, with the increased volume fraction of TiN in alloy LNHV accounting for the increased grain size control despite relatively large precipitate size.

Particularly evident in Figure 5.28 is the significant variation in grain size demonstrated by each of the four alloys. In the 4 kJ/mm heat input condition, alloy INLV had the largest variation in grain size with a standard deviation of 70 μm. The other three alloys had very similar variation: 32 μm for alloy HNLV, 34 μm for alloy LNLV, and 33 μm for alloy LNHV. The effect of austenite grain size on subsequent transformation products, and therefore properties, has already been addressed. Given the large variation seen with the 1350°C peak temperature, it would be very difficult to draw conclusions about microstructures and properties based on the four alloy compositions.

In an attempt to help understand this situation, two alternate peak temperatures were investigated. The thermal cycles for these alternate peak temperatures were confined to a 4 kJ/mm heat input. The philosophy as to why the two alternate peak temperatures were chosen is as follows. With the 1350°C peak temperature cycles, the specimens experience temperatures where the critical titanium nitride dispersion for grain size control is lost, resulting in abnormal grain growth. It was hoped that with a peak temperature of 1250°C, the titanium nitride precipitates are present in sufficient quantity to effectively pin the austenite grains. Under this condition, slow, normal, grain growth occurs. In contrast, when the specimens are heated with the 1400°C peak temperature thermal cycle, the

hypothesis was that such dissolution of the titanium nitride occurs that there is effectively no grain size control, and hence, rapid, normal, grain growth will occur. The results of the grain size measurements for the 1250°C and 1400°C thermal cycles are shown in Figure 5.29.

It is clearly shown in Figure 5.29 that the 1250°C peak temperature produced specimens with consistently fine grain size. Not only was there a small variation between the samples for a given alloy, the largest standard deviation was 2.9 μm for alloy INLV, but all of the alloys had average grain sizes that fell between 32 μm and 37 μm. This result allows comparisons between the alloys based on chemistry and titanium nitride precipitate distributions. Transformation products will not vary due to grain size variation with this thermal cycle.

Figure 5.29 also shows the prior-austenite grain size for the 1400°C peak temperature specimens. In general, these data are very similar to that demonstrated by the 1350°C peak temperature, 4 kJ/mm heat input specimens (see Figure 5.28). With the exception of alloy HNLV, the overall average values for the 1400°C and 1350°C peak temperature specimens are nearly identical. With a 1350°C peak temperature, alloy HNLV has an average grain size of approximately 60 μm, while with a 1400°C peak temperature the grain size increases to approximately 108 μm. Curiously, the 1400°C peak temperature specimens for the other three alloys demonstrate prior-austenite grain sizes that are slightly smaller than the 1350°C peak temperature specimens. Also, the variation for each alloy is
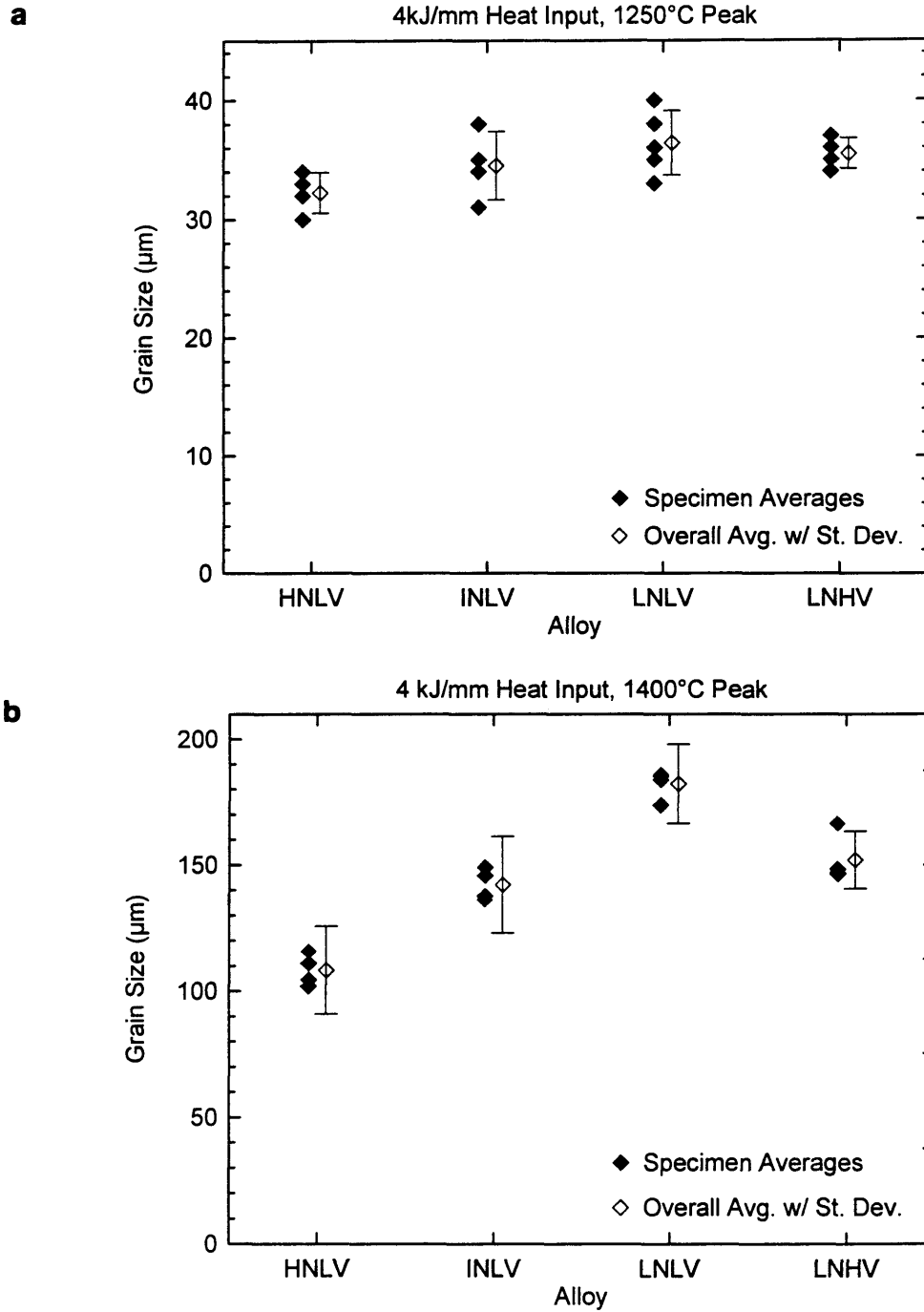
Figure 5.29. Prior-austenite grain size for 4 kJ/mm heat input specimens. a) 1250°C peak temperature. b) 1400°C peak temperature.

smaller with the 1400°C peak temperature thermal cycle than with the 1350°C peak temperature thermal cycle. Table 5.4 summarizes the overall average values and standard deviation for the 4 kJ/mm heat input thermal cycles. With the exclusion of alloy HNLV, it cannot be said that the prior-austenite grain size is different between the two higher peak temperature thermal cycles.

Table 5.4. Prior-austenite grain sizes for 4 kJ/mm heat input specimens with standard deviation. All values in μm.

Alloy	1250°C Peak Grain Size (St. Dev.)	1350°C Peak Grain Size (St. Dev.)	1400°C Peak Grain Size (St. Dev.)
HNLV	32.3 (1.7)	59.2 (31.7)	108.2 (17.5)
INLV	34.5 (2.9)	149.4 (69.5)	142.1 (19.2)
LNLV	36.4 (2.7)	191.2 (33.9)	182.2 (15.8)
LNHV	35.5 (1.3)	154.4 (33.4)	152.0 (11.4)

5.4.3 Microstructures of Alternate Peak Temperature Specimens

Representative microstructures from the 1350°C peak temperature materials have already been shown in section 5.3. It is therefore appropriate to provide representative micrographs for the 1250°C and 1400°C peak temperature conditions at this time, prior to presenting the mechanical property data. The following figures, Figure 5.30 through Figure 5.33 show these microstructures. While it may not be immediately apparent from the microstructures, the 1250°C peak temperature specimens have significantly more primary ferrite present and the size scale of the microstructure, or effective ferrite grain size, is smaller, as compared to the 1400°C peak temperature specimens. This will be supported in section 5.4.6.

5.4.4 Charpy V-Notch Testing

In a similar fashion to what was seen in the baseplate analysis, a 100 J transition temperature criterion was implemented for the thermally-cycled materials. CVN transition curves for alloy HNLV are shown in Figure 5.34 through Figure 5.37. The other transition curves are shown in Appendix B. The 100 J transition temperatures for each thermal cycle are plotted in Appendix B and compiled in Table 5.5.

a)

b)

30μm
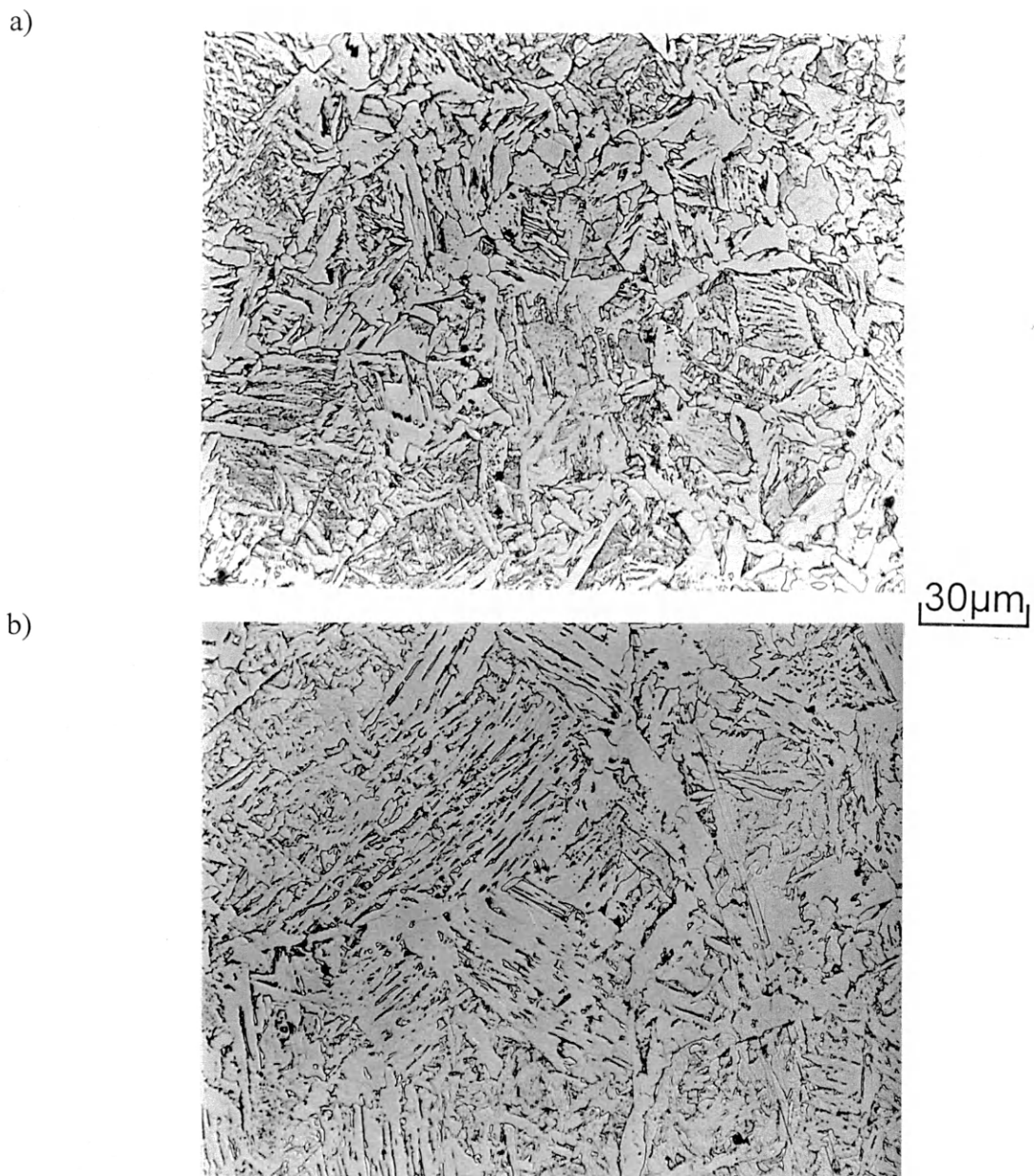
Figure 5.30. Representative light micrographs for material cycled with a 4 kJ/mm heat input. a) 1250°C and b) 1400°C peak temperature. Alloy HNLV. Nital etch.

a)

b)

30μm
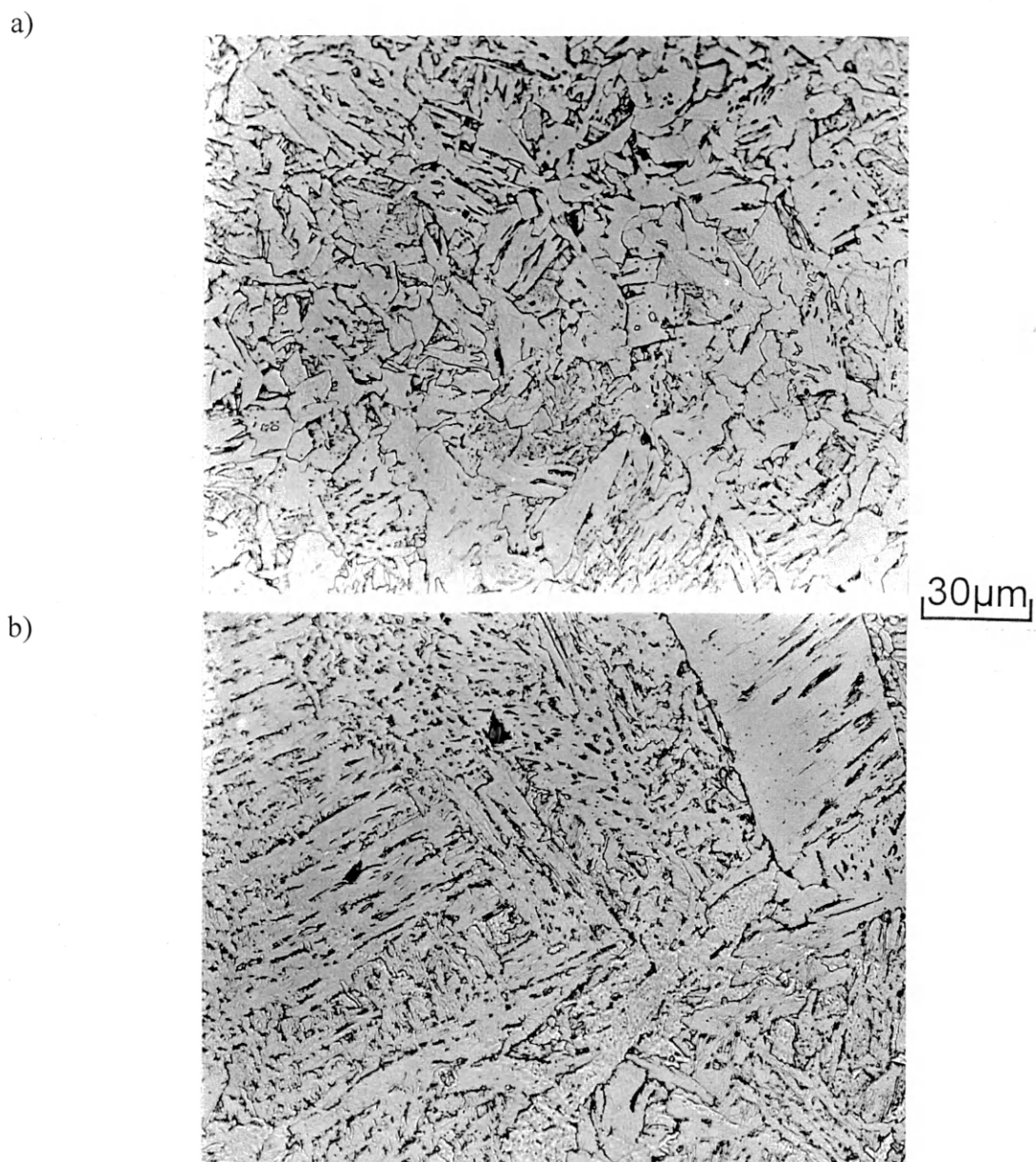
Figure 5.31. Representative light micrographs for material cycled with a 4 kJ/mm heat
input. a) 1250°C and b) 1400°C peak temperature. Alloy INLV. Nital
etch.

a)

b)

30μm
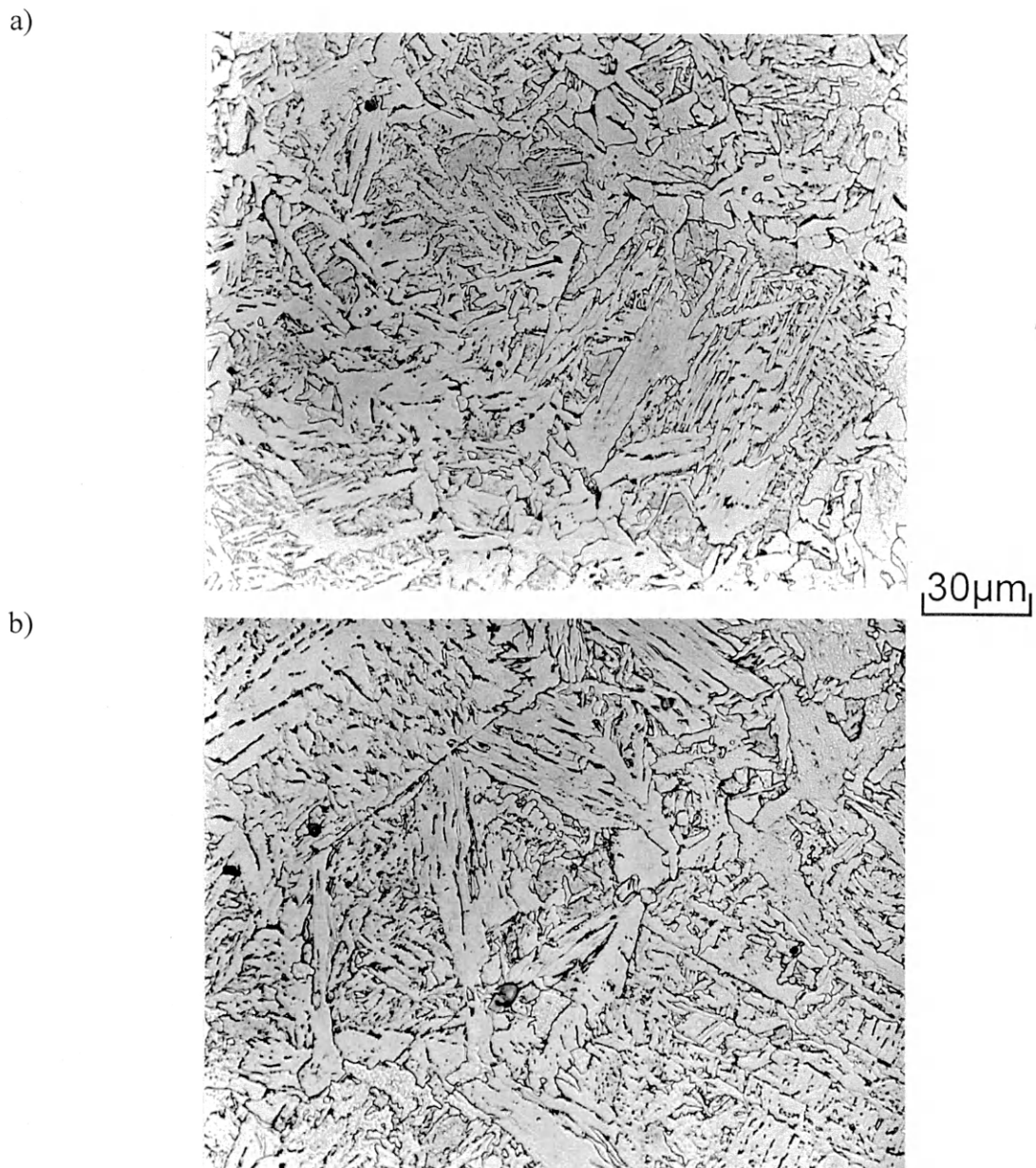
Figure 5.32. Representative light micrographs for material cycled with a 4 kJ/mm heat input. a) 1250°C and b) 1400°C peak temperature. Alloy LNLV. Nital etch.

a)

b)

30μm
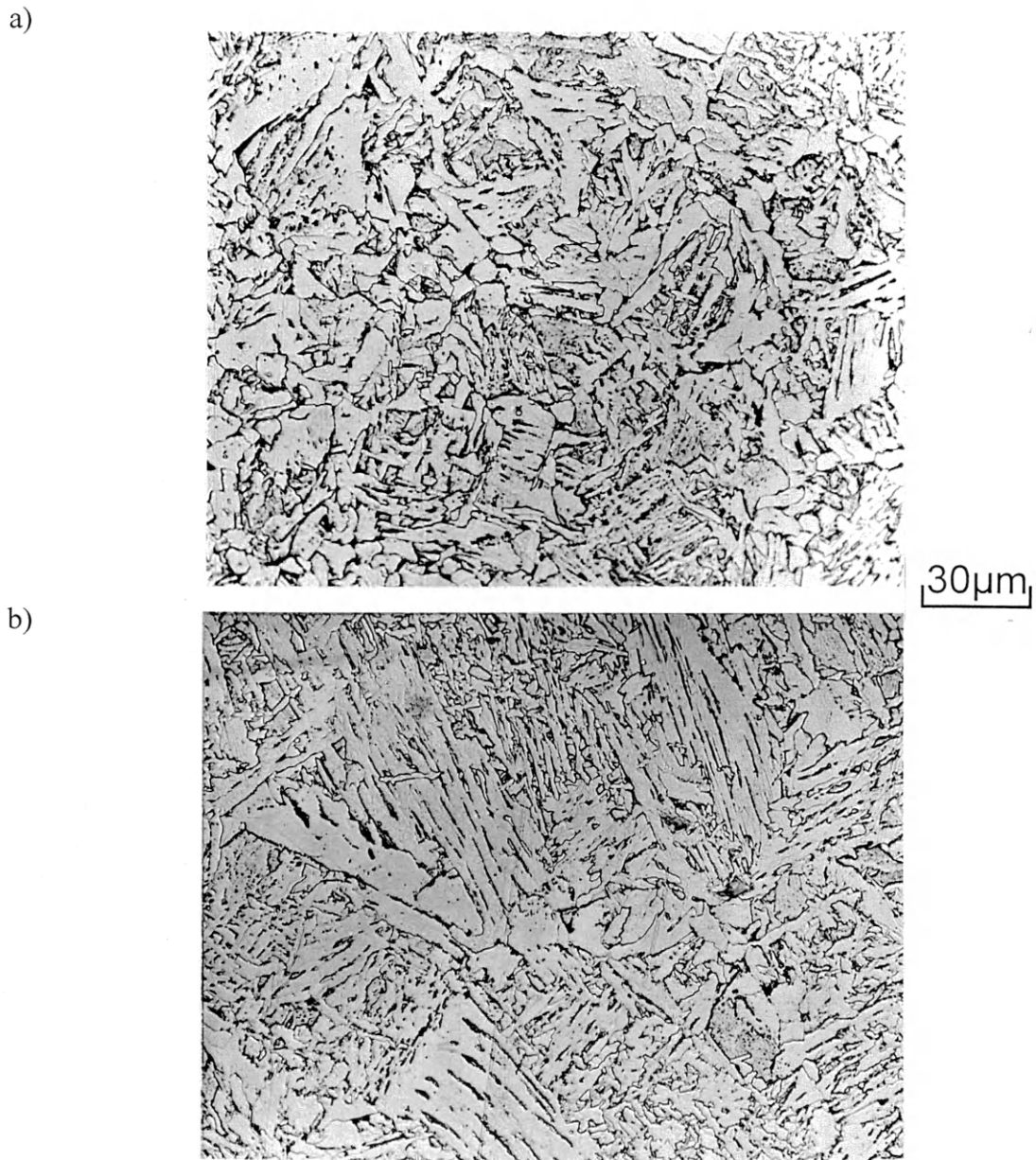
Figure 5.33. Representative light micrographs for material cycled with a 4 kJ/mm heat input. a) 1250°C and b) 1400°C peak temperature. Alloy LNHV. Nital etch.
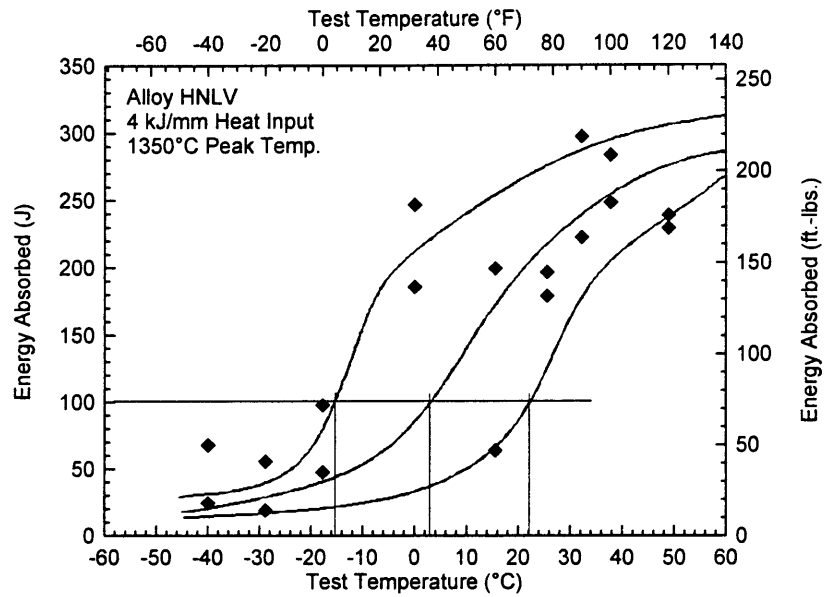
Figure 5.34. Charpy V-notch transition curve for alloy HNLV. 4 kJ/mm heat input. 1350°C peak temperature.
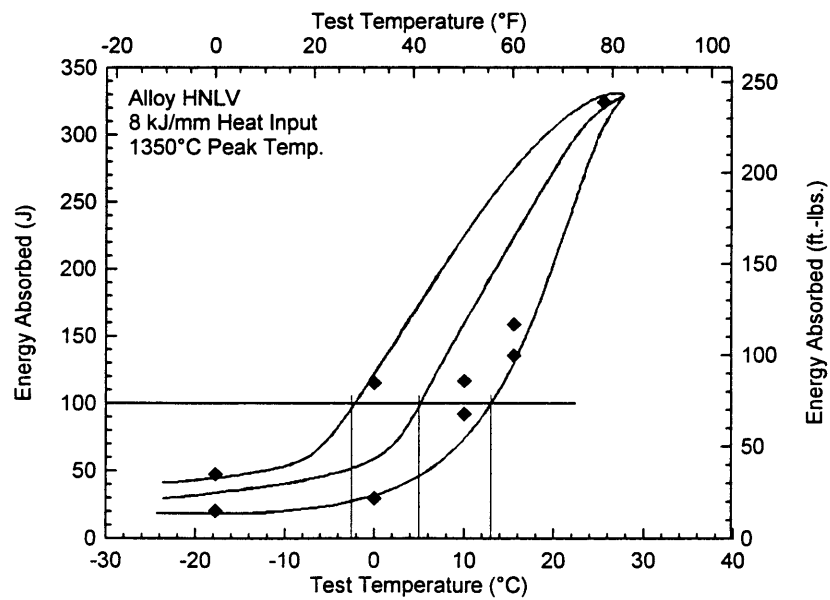
Figure 5.35. Charpy V-notch transition curve for alloy HNLV. 8 kJ/mm heat input. 1350°C peak temperature.
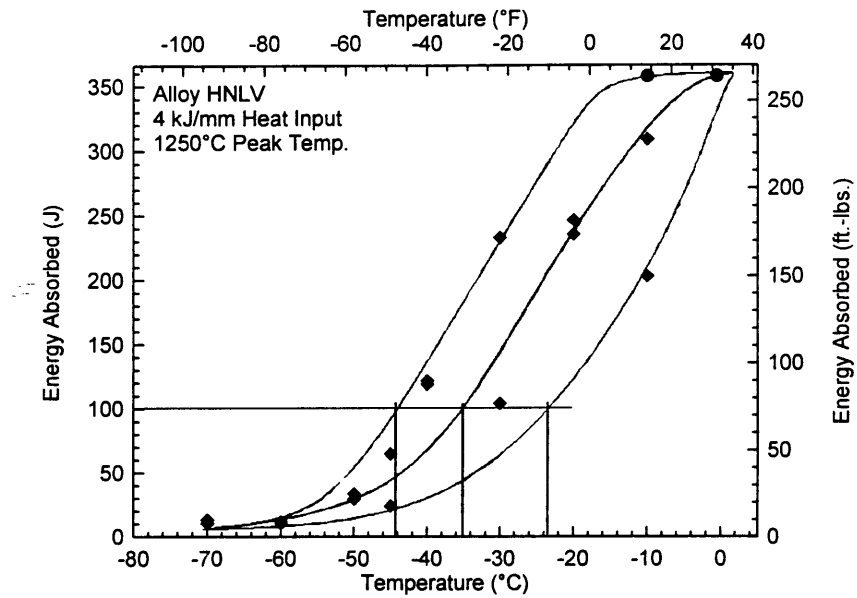
Figure 5.36. Charpy V-notch transition curve for alloy HNLV. 4 kJ/mm heat input. 1250°C peak temperature.
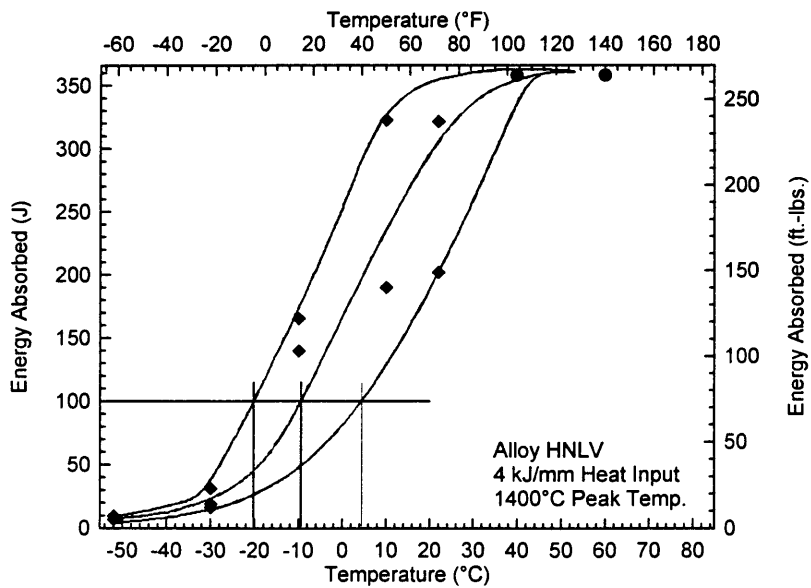
Figure 5.37. Charpy V-notch transition curve for alloy HNLV. 4 kJ/mm heat input. 1400°C peak temperature.

Table 5.5. Charpy V-notch transition temperature for thermally-cycled materials (Values in °C).

Alloy and Condition	100 J Transition Temperature	100 J TT Lower Bound	100 J TT Upper Bound
HNLV, 4 kJ/mm H.I., 1350°C Peak Temp.	3	-16	22
INLV, 4 kJ/mm H.I., 1350°C Peak Temp.	2	-10	12
LNLV, 4 kJ/mm H.I., 1350°C Peak Temp.	8.5	0	19.5
LNHV, 4 kJ/mm H.I., 1350°C Peak Temp.	-3	-14.5	10
HNLV, 8 kJ/mm H.I., 1350°C Peak Temp.	5	-2.5	13
INLV, 8 kJ/mm H.I., 1350°C Peak Temp.	4.5	-5	14
LNLV, 8 kJ/mm H.I., 1350°C Peak Temp.	1	-4	6
LNHV, 8 kJ/mm H.I., 1350°C Peak Temp.	3	-8	14.5
HNLV, 4 kJ/mm H.I., 1250°C Peak Temp.	-35	-44	-23
INLV, 4 kJ/mm H.I., 1250°C Peak Temp.	-47	-53.5	-38
LNLV, 4 kJ/mm H.I., 1250°C Peak Temp.	-56	-68	-43.5
LNHV, 4 kJ/mm H.I., 1250°C Peak Temp.	-46	-51	-41
HNLV, 4 kJ/mm H.I., 1400°C Peak Temp.	-9	-20	5
INLV, 4 kJ/mm H.I., 1400°C Peak Temp.	-4.5	-16	21
LNLV, 4 kJ/mm H.I., 1400°C Peak Temp.	-3	-12	7
LNHV, 4 kJ/mm H.I., 1400°C Peak Temp.	18.5	14	23
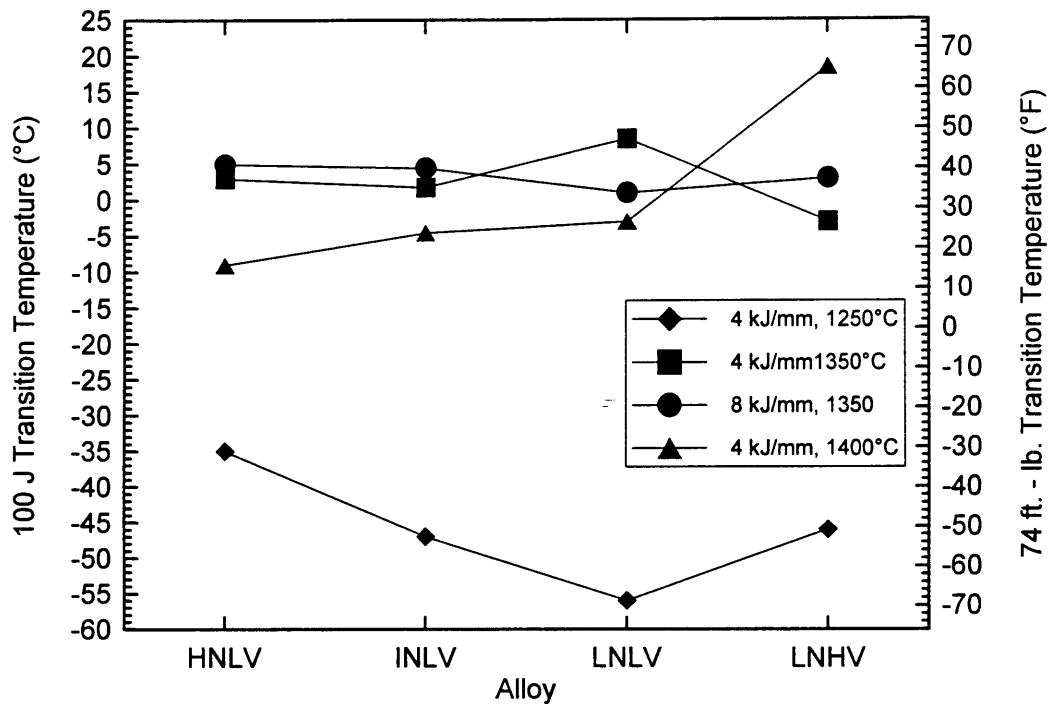
Figure 5.38. Summary plot of 100 J transition temperature for thermally-cycled material.

A summary plot of these data is shown in Figure 5.38 for ease of comparison. The

transition temperature curves show that there is significant scatter observed in the CVN

testing (error bars were not shown in Figure 5.38 to prevent confusion). Additionally,

Figure 5.38 shows that the 100 J transition temperature results group into two "bands"

according to thermal cycle. The 1250°C peak temperature cycle results in relatively good

toughness with transition temperatures of -35°C and below. With the low peak

temperature, there is a well-defined trend of decreasing transition temperature from -35°C

for alloy HNLV, through -47°C for alloy INLV, to -56°C for alloy LNLV. There is then an

increase in transition temperature from alloy LNLV to -46°C for alloy LNHV. The decrease in transition temperature for the first three alloys corresponds to a supposed decrease in free nitrogen content that was designed into the alloys. The difference between alloys LNLV and LNHV could be explained as a result of an increase in large titanium nitride precipitates in the latter alloy (designed to have high volume fraction of TiN).

The other band of data comes from the increased peak temperature thermal cycles. These thermal cycles produce 100 J transition temperatures between approximately -10°C and 19°C. The latter number is from alloy LNHV with a 1400°C peak temperature cycle. Although the error bars are not shown in Figure 5.38, this value is the only one for the higher peak temperature thermal cycles that does not have significant overlap with another condition. Given the variation in the Charpy results, it is difficult to say that there is any difference in properties between alloys HNLV through LNLV for the increased peak temperature thermal cycles.

Based on the results shown in Figure 5.38, one might expect significant microstructural differences between the alloys thermally cycled with the 1250°C peak temperature and the higher peak temperatures.

5.4.5 Hardness of Thermally-Cycled Materials

Figure 5.39 shows a summary of the average hardness for the thermally-cycled materials. Plots for the individual thermal cycles are shown in Appendix C. The error bars were omitted from each data point in Figure 5.39 to prevent cluttering the plot. However, the standard deviation values for each data point were averaged to provide an idea of the variation associated with these data. This average value of the standard deviation is shown in the figure (labeled "St. Dev.").
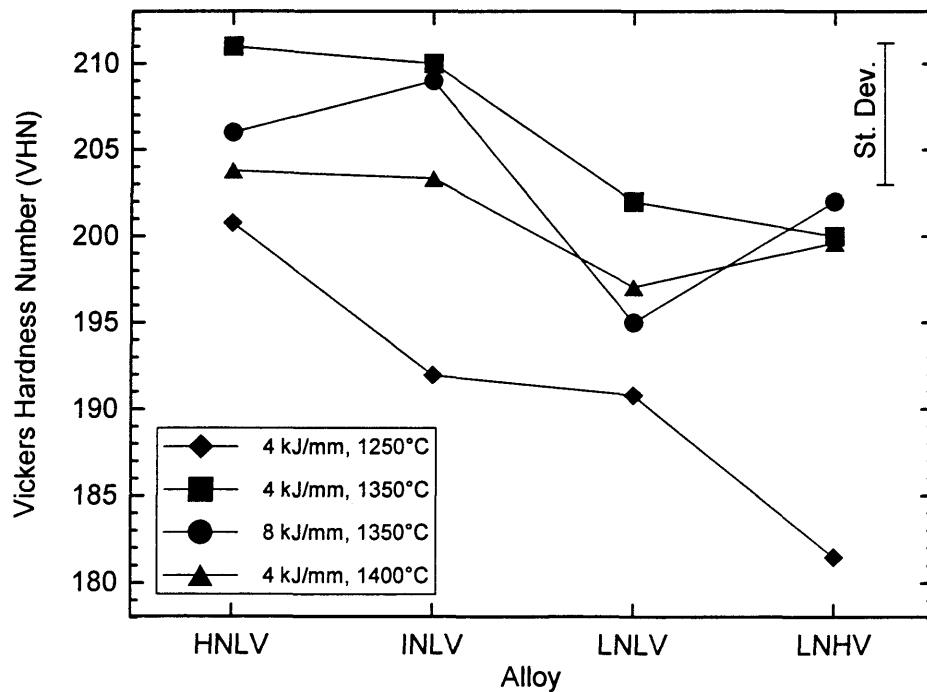
Figure 5.39. Hardness of thermally-cycled materials.

As was seen in the transition temperature data, the 1250°C peak temperature thermal cycle results in a relatively well-behaved trend. There is a consistent decrease in hardness from a high of 201 VHN for alloy HNLV through 192 VHN to 191 VHN for alloys INLV and LNLV, respectively. There is then a significant drop from alloy LNLV to LNHV, which has a hardness of 181 VHN.

When comparing the 1250°C peak temperature specimens to the specimens subjected to the 4 kJ/mm heat input, 1350°C peak temperature specimens, the trend in hardness data is similar, with a smaller range of values between the alloys. Alloys HNLV and INLV have average hardnesses that are very similar, 211 VHN and 210 VHN, respectively. There is then a drop to 202 VHN and 200 VHN for alloys LNLV and LNHV, respectively.

The 1400°C peak temperature specimens behave in a similar fashion to the 4 kJ/mm heat input, 1350°C peak temperature specimens. There is a drop in hardness from a peak of 204 for alloy HNLV to 203 for INLV and 197 for LNLV. The hardness then increases to 200 VHN for alloy LNHV. While there appears to be a trend for the first three alloys, it is difficult to be positive due to the standard deviation of the data.

The 8 kJ/mm heat input specimens have hardness values between the 4 kJ/mm heat input 1350°C and 1400°C specimens for alloys HNLV and INLV. For alloy LNLV, the 8 kJ/mm heat input specimens have hardness values lower than the other two high peak

temperature specimens. For alloy LNHV, the 8 kJ/mm heat input specimens have the highest hardness values.

The thermal cycles with peak temperatures of 1350°C and 1400°C result in very similar hardness values for alloy LNHV. Given the magnitude of the standard deviation, it is difficult to say that there is significant difference in hardness due to a thermal cycle employed with a peak temperature above 1250°C. There may be a general trend toward decreasing hardness from alloy HNLV to alloy LNLV and perhaps a slight rise from alloy LNLV to LNHV.

In order to determine the reasons for the properties shown in the CVN and VHN testing, a quantitative evaluation of the microstructure was performed. The results of these examinations are presented in the following section.

5.4.6 Quantitative Microstructural Evaluation

The microstructures of the thermally-cycled materials were evaluated to determine the volume fraction, as well as a size scale, of the components present. Given the similarity between the 8 kJ/mm heat input and 4 kJ/mm heat input specimens, the quantitative analysis was restricted to the 4 kJ/mm heat input thermal cycles. It is believed that better measures of the prior-austenite grain sizes are possessed for the 4 kJ/mm heat input specimens than the 8 kJ/mm heat input specimens.

5.4.6.1 Volume Fraction of Microstructural Components

The volume fraction of the microstructural constituents for each thermal condition

are presented in Appendix D. Summary plots for the various constituents for all of the

thermal cycles are shown in Figure 5.40 through Figure 5.45. These figures were generated

from point-counting the microstructure at 1000x. Figure 5.46 shows the volume fraction of

large titanium nitride inclusions for the thermally cycled materials. These titanium nitride

volume fraction measurements are somewhat different than the point-counted data in that

the volume fraction was calculated from the inclusion number density (note that the average

inclusion size was between 2.1 µm and 3.9 µm for all conditions). With the number density

(# of inclusions per unit area) and an average particle size, an areal fraction was computed.

This areal fraction is equivalent to the volume fraction (81). Again the error bars are not

included in the summary plots to prevent cluttering the figures. The standard deviation of

the data is shown as error bars on the plots in Appendix D.

In examining the primary ferrite content of the thermally cycled materials, it is

reassuring to observe the increased primary ferrite content of the materials thermally cycled

with the 1250°C peak temperature as compared to the higher peak temperatures. For alloys

HNLV through LNLV the primary ferrite content is approximately 35% after a 1250°C

peak temperature thermal cycle and drops off to approximately 25% after the 1350°C peak

temperature thermal cycle. The materials subjected to 1400°C peak temperature excursion
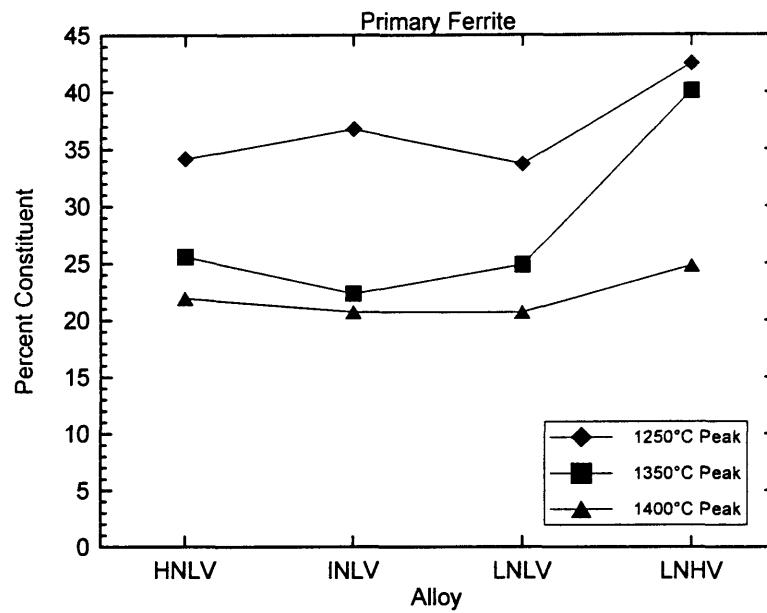
Figure 5.40. Volume fraction of primary ferrite for thermally-cycled materials.
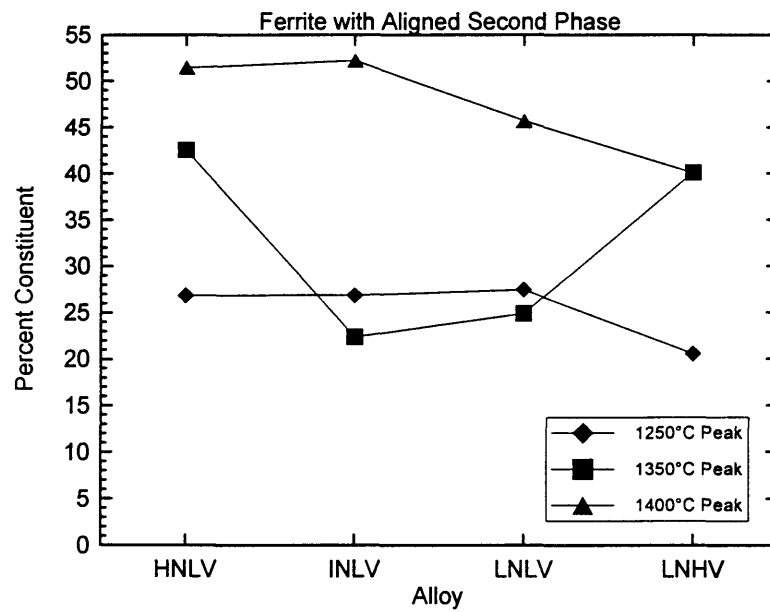
Figure 5.41. Volume fraction of ferrite with an aligned second phase for thermally-cycled materials.
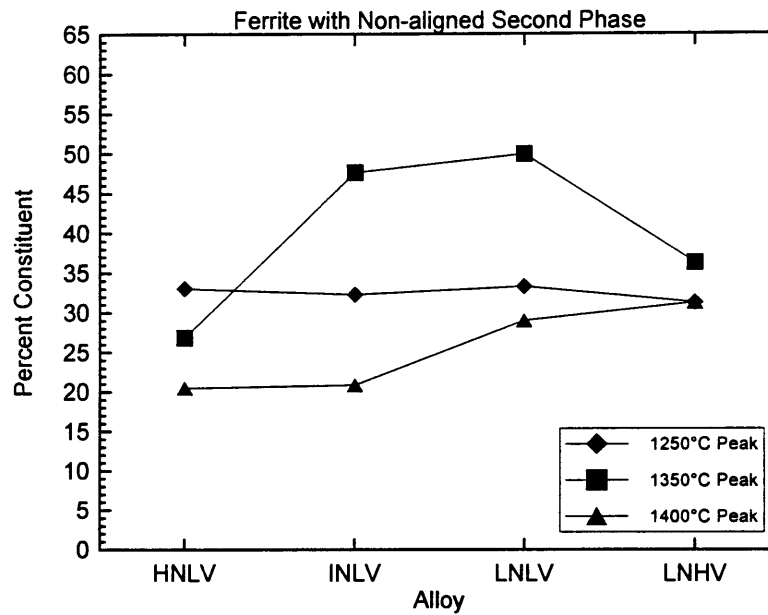
Figure 5.42. Volume fraction of ferrite with a non-aligned second phase for thermally-cycled materials.
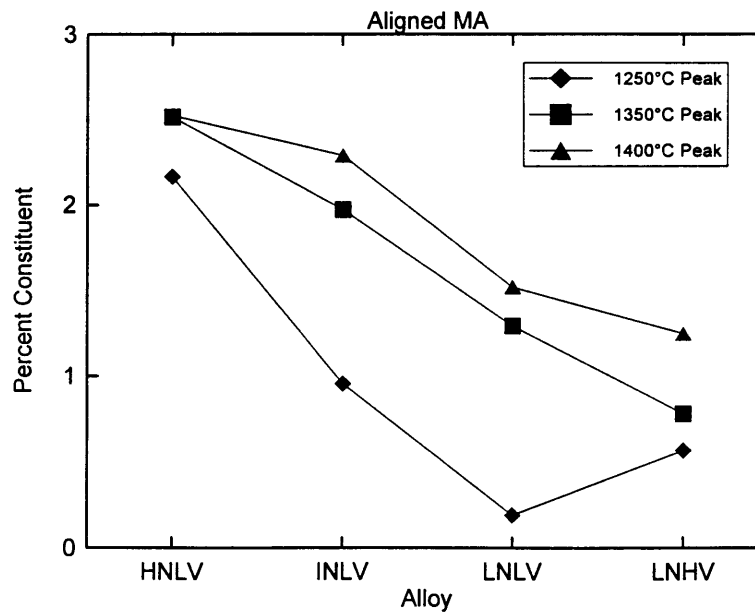
Figure 5.43. Volume fraction of aligned MA constituent for thermally-cycled materials.
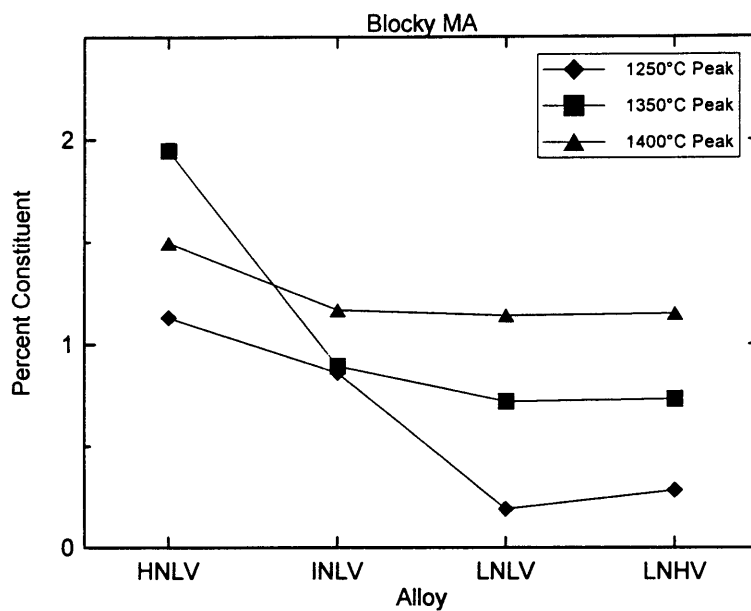
Figure 5.44. Volume fraction of blocky MA constituent for thermally-cycled materials.
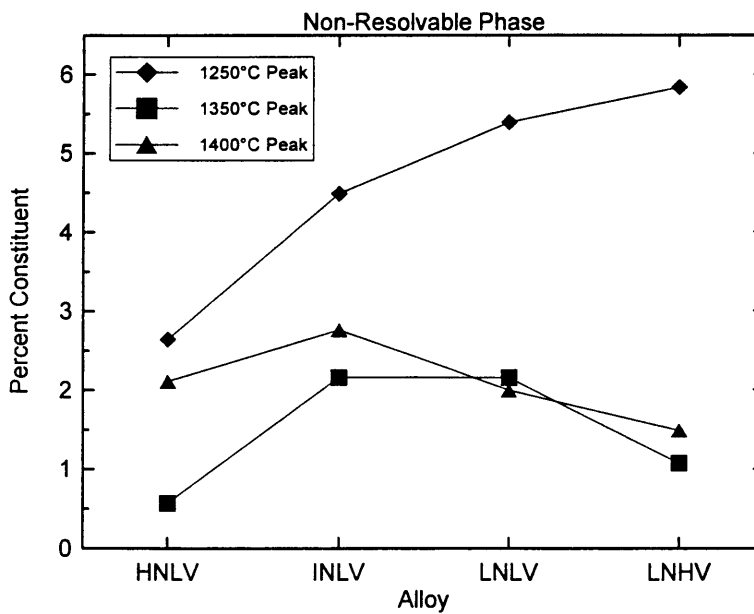
Figure 5.45. Volume fraction of non-resolvable second phase for thermally-cycled materials.
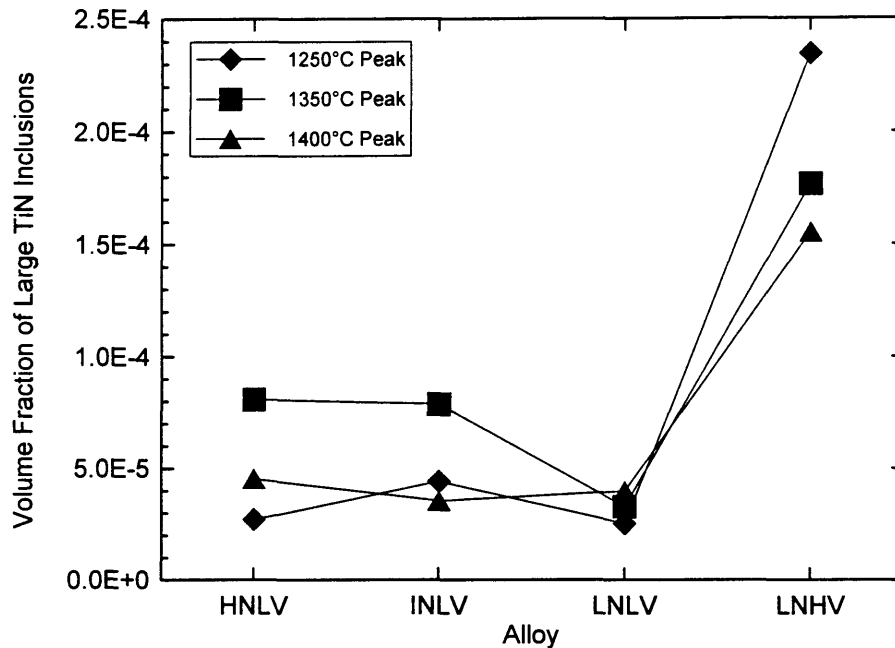
Figure 5.46. Volume fraction of large titanium nitride inclusions for thermally-cycled
materials.

demonstrate similar values as those subject to the 1350°C peak temperature, with primary

ferrite content of approximately 21%. It is difficult to say that there is a statistical

difference among these three alloys for each thermal condition.

It is encouraging that the general trend of primary ferrite content corresponds to the

prior-austenite grain size data already presented. With the fine prior-austenite grain size of

the 1250°C peak temperature specimens, there is a high density of primary ferrite

nucleation sites, and thus there should be a high primary ferrite content. With the increased

grain size observed with the higher peak temperature thermal cycles, the ferrite nucleation

sites are reduced, and consequently less primary ferrite should be present. Comparing the

data for the two highest peak temperatures, the primary ferrite content reflects what would be expected based on prior-austenite grain size data. One would expect a larger grain size with the 1400°C peak temperature thermal cycle than the 1350°C peak temperature cycle, and consequently lower primary ferrite content. The measured prior-austenite grain size for these two conditions was very similar, as is the primary ferrite content, it is difficult to say that there is a significant difference observed for either of the two measurements.

An interesting observation is that there is no appreciable difference observed in primary ferrite content between alloys HNLV through INLV for each thermal condition. This result is easily explained for the 1250°C peak temperature specimens due to the great similarity in the prior-austenite grain size observed in specimens subjected to this thermal cycle. However, for the 1350°C and 1400°C peak temperature thermal cycles, there are significant differences observed in the prior-austenite grain size. With the 1350°C peak temperature, alloy HNLV has an average prior-austenite grain size of 59 μm. Alloys INLV and LNLV have sizes of 149 μm and 191 μm, respectively, for this condition. One might expect to see large differences in the primary ferrite content corresponding to the large difference in prior-austenite grain size.

The only situation where an appreciable variation in primary ferrite content is observed is between alloys LNLV and LNHV, particularly for the specimens which experienced the 1350°C peak temperature thermal cycle, where the primary ferrite content

is greater for alloy LNHV than alloy LNLV. This variation is also observed in specimens from the other two thermal cycles, however, it is not as well defined.

Another consistent difference between alloys LNLV and LNHV is the drastic increase in titanium nitride inclusion volume fraction (Figure 5.46). It should be noted that the increase in volume fraction of the titanium nitride inclusions is more a manifestation an increase in the number density than any difference in inclusion size. The largest inclusions were not observed in specimens from alloy LNHV, but the number density was at least double for specimens from alloy LNHV as compared to the other three alloys. The observed increase in primary ferrite content for alloy LNHV suggests that the large titanium nitride inclusions are nucleating primary ferrite This hypothesis has additional evidence in the form of what appears to be primary ferrite nucleated in conjunction with titanium nitride inclusions as observed with the light microscope. A photomicrograph showing this observation is provided in Figure 5.47.

While there is a difference in the classification scheme between ferrite with aligned (FS(A)) and non-aligned (FS(NA)) second phase, and the quantitative metallography provided volume fractions for each of these components, it is difficult to isolate them in terms of the general microstructure of these materials. The difficulty arises from the fact that a microstructural constituent that is viewed from different planes of polish can be quantified differently. For example, when viewed on one plane a Widmanstätten sideplate may be observed. If the plane of polish is then rotated 90°, what appeared to be
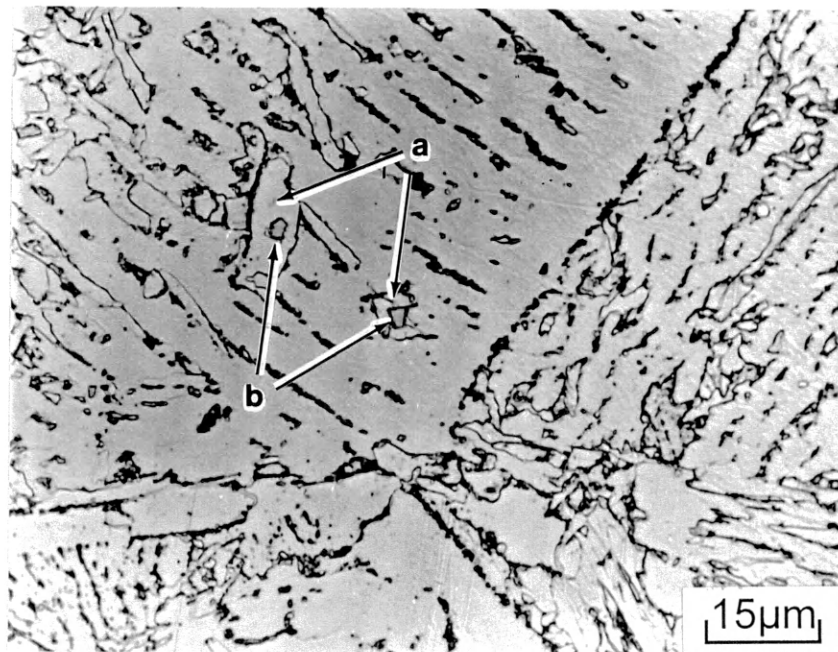
Figure 5.47. Light micrograph depicting primary ferrite (arrowed a) in conjunction with titanium nitride inclusions (arrowed b). 1000x. Nital etch.

Widmanstätten sideplate can appear to be ferrite with a non-aligned second phase. As a result, a microstructure that appears to be comprised of both FS(A) and FS(NA), may in reality be simply FS(A) with differently oriented regions which have the appearance of FS(NA).

Given this complication, perhaps it is best to consider the "bainitic" component of the microstructure, or the combination of FS(A) and FS(NA). Given the small volume fractions observed for the second phase constituents, the volume fraction of the "bainitic" component is what remains after subtracting the primary ferrite volume fraction from unity. For the materials and thermal cycles used in this study, the austenite which remains after primary ferrite formation during cooling transforms to the "bainitic" component. Consequently, the discussion presented previously on the primary ferrite content can be applied to the "bainite" content as well.

Interpretation is difficult where the second phase components of the microstructure are concerned given the small volume fractions of the constituents. Complicating the matter is the standard deviation associated with volume fraction measurements of the constituents. In most cases the standard deviation is well over half the average measured values, and in many cases exceeds the average. With this qualification, there are some trends observed among the second phase constituents. The volume fraction of the aligned MA islands decreases from alloy HNLV to LNLV, for all three thermal cycles. This trend of decreasing volume fraction continues to alloy LNHV for the two higher peak temperature

thermal cycles and is reversed at the lower peak temperature. There is a similar pattern for the lower peak temperature specimens in reference to the blocky MA as well. However, there is very little difference in blocky MA content between the alloys when thermally cycled to the two higher peak temperatures.

When considering the non-resolvable second phase, the specimens that experienced the 1250°C peak temperature had consistently higher volume fractions than the higher peak temperature specimens, which were very similar. It is believed that the non-resolvable phase is carbide or small MA islands. The 1250°C peak temperature specimens have a significantly higher primary ferrite content than the specimens subjected to the higher peak temperatures. As the primary ferrite has extremely low carbon solubility, the carbon is rejected in the remaining austenite. The highly enriched austenite regions can then readily transform to martensite or carbide rich structures as well as remain untransformed.

5.4.6.2 Mean Free Path

A lineal intercept method was used to determine the distance between various microstructural features. It was hoped that this analysis would provide a mean free path between constituents which may prove instructive regarding the Charpy V-notch transition temperature of the alloys subjected to the different thermal conditions. The features included in this analysis were: ferrite high-angle boundaries, ferrite / aligned MA

constituent boundaries, ferrite / blocky MA constituent boundaries, and boundaries between ferrite and the unresolvable second phase. The distance between these features, or the feature's mean free path, are shown for each thermal condition in Appendix D. Summary plots for each constituent are provided in Figure 5.48 through Figure 5.51.

The ferrite high-angle boundary mean free path can be considered an "effective" ferrite grain size. Generally these data sort according to peak temperature, as would be expected from the prior-austenite grain size results. For the 1250°C peak temperature specimens, the effective ferrite grain size is approximately 10 μm. All four alloys have very similar values. Increasing the peak temperature to 1350°C results in an increase in effective ferrite grain size to approximately 13 μm, with the exclusion of alloy LNLV which has a value of approximately 23 μm. For this thermal condition, alloy LNLV has a large significant variation in measured mean free path with a standard deviation of 10 μm, as compared with standard deviations of less than 5 μm for the other three alloys (see Figure 12.23). The specimens cycled with the 1400°C peak temperature resulted in values for effective ferrite grain size between 21 μm and 25 μm. This range of values falls well within the standard deviation demonstrated by the four alloys (see Figure 12.24), and as a result, one cannot say that there is a difference demonstrated among four alloys when subjected to 1400°C peak temperature thermal cycle.
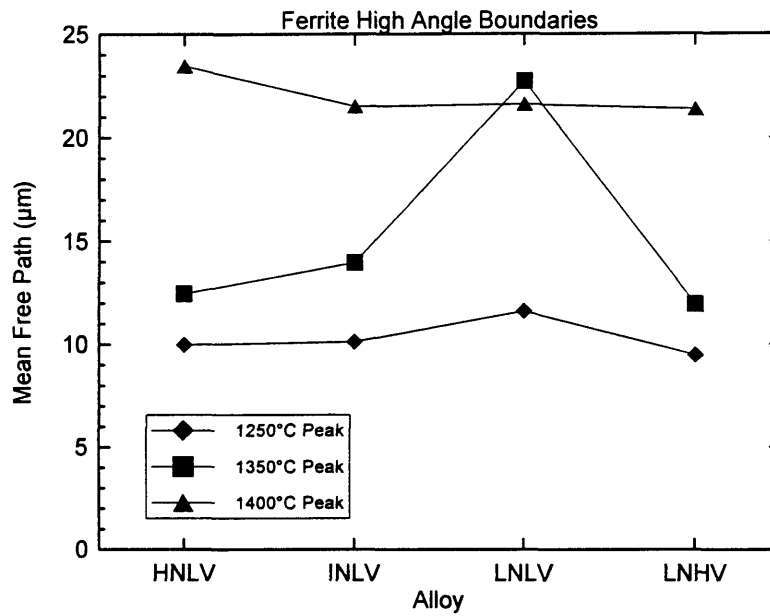
Figure 5.48. Mean free path between ferrite high angle boundaries in thermally cycled materials.
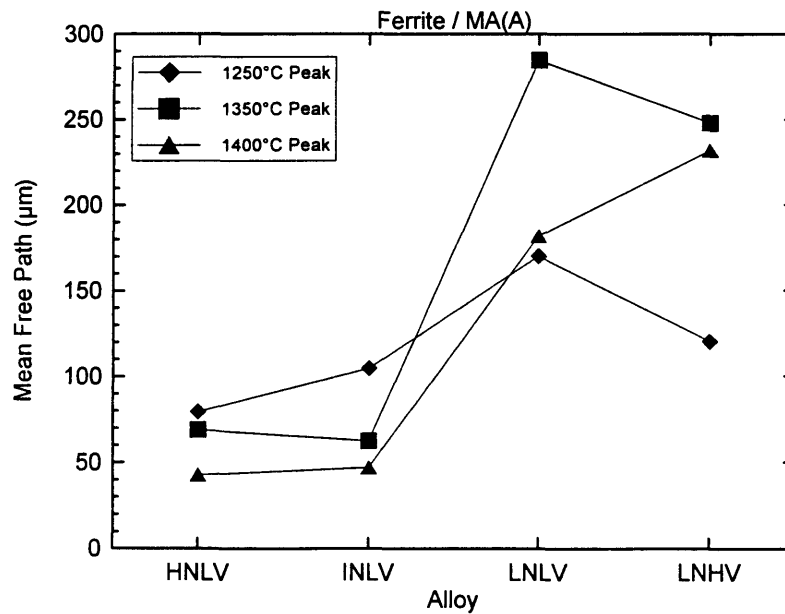
Figure 5.49. Mean free path between ferrite - aligned MA island constituent in thermally cycled materials.
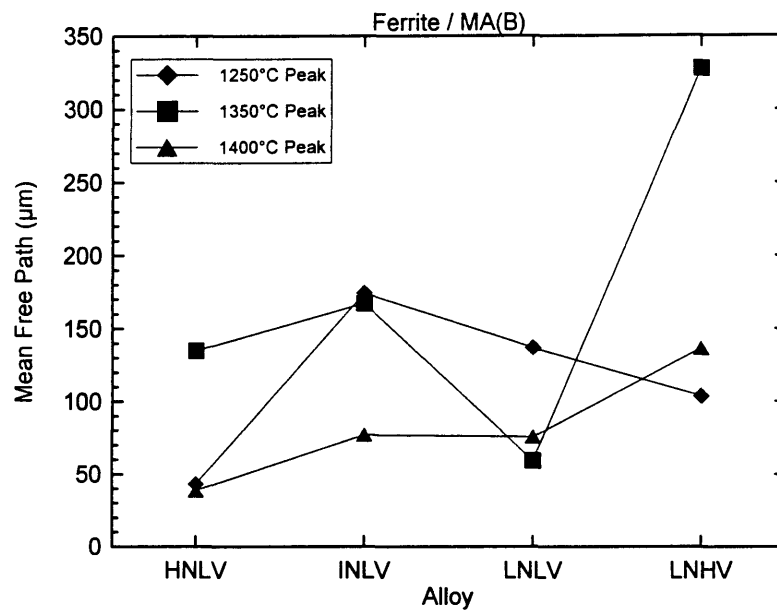
Figure 5.50. Mean free path between ferrite - blocky MA constituent boundaries in thermally cycled materials.
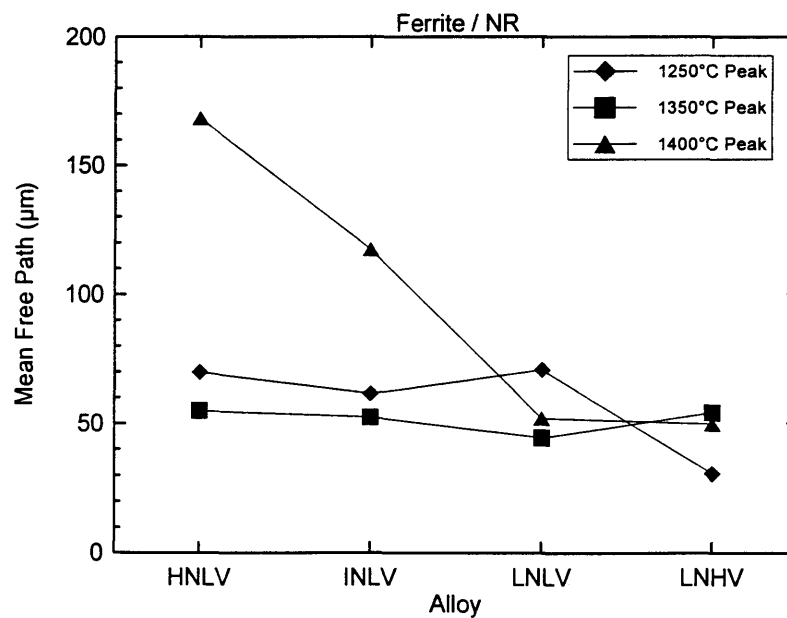
Figure 5.51. Mean free path between ferrite - non-resolvable second phase boundaries in thermally cycled materials.

The mean free path measurements between the ferrite and aligned MA constituent are marked by significant scatter, as shown in the graphs in Appendix D. The large standard deviation may result from examined fields of view not containing aligned MA constituent, or, the horizontal lines used to determine the mean free path not intersecting an aligned MA island. When intersections were absent, the entire length of the horizontal lines (500 µm) was chosen as the value of the mean free path. On the other hand, when the line grid intersects a packet of ferrite with an aligned second phase of MA constituent, the mean distance between MA islands is then the ferrite lath width, which is considerably smaller than 500 µm, perhaps 5 µm. This large span of possible measurements contributes greatly to the scatter observed in the data. With that introduction, there appears to be a general trend of increasing mean free path of the ferrite and aligned MA constituent boundaries from alloys HNLV to LNLV for all three peak temperatures, as shown in Figure 5.49. There is then a decrease in the mean free path from alloy LNLV to LNHV in both the 1250°C and 1350°C peak temperature conditions. With the 1400°C peak temperature thermal cycle, the mean free path increases from alloy LNLV to LNHV.

In considering the boundaries between ferrite and blocky MA islands, as shown in Figure 5.50, it is difficult to discern any trends between either the alloys or the peak temperatures. These data are also marked by significant standard deviations, as shown in Figure 12.28 through Figure 12.30.

The last category measured in the mean free path analysis was the boundaries

between ferrite and the unresolvable second phase, the results of which are provided in

Figure 5.51. Again there is appreciable scatter in these data (see Figure 12.31 through

Figure 12.33). For the 1250°C and 1350°C peak temperature thermal cycles, the mean free

path of the ferrite - unresolvable phase boundaries is very similar for all alloys and both

thermal cycles, with values between 30 μm and 70 μm. The 1400°C peak temperature

thermal cycle does not fit well with the other two peak temperatures for the alloys HNLV

and LNLV, with considerably larger mean free path values. However, these two values also

demonstrated the largest standard deviation of any of the alloys or conditions.

5.4.7 Continuous Cooling Transformation Testing

In an attempt to determine if there were significant differences in transformation

behavior for the four alloys, a continuous-cooling-transformation study was done. This

study was constrained to the extremes of the peak temperature range, 1250°C and 1400°C.

The thermal cycles used for the CCT work are shown in Figure 4.4.

The CCT testing was done in the Gleeble and the sensitivity of the dilatometry data

is such that it is difficult to interpret intermediate transformations. As a result, it was

decided to determine the initial transformation start temperature and the final transformation

finish temperature. For reference, martensite start temperatures, as well as bainite start, Ac_1,

and Ac_3 temperatures, were calculated.

The martensite start temperature was calculated with the Andrews product equation

(82) shown below:

$$M_s \ (^\circ C) = 512 - 453C - 16.9Ni + 15Cr - 9.5Mo + 217(C)^2 \\ - 71.5(C)(Mn) - 67.6(C)(Cr)$$

Eqn. 5.1

The bainite start temperature was determined from the following relation (83):

$$B_s \ (^\circ C) = 830 - 270C - 90Mn - 37Ni - 70Cr - 83Mo$$

Eqn. 5.2

In his paper Andrews (82) also provides values for the Ac_3 and Ac_1 temperatures:

$$Ac_3 \ (^\circ C) = 910 - 203\sqrt{C} - 15.2Ni + 44.7Si + 104V \\ + 31.5Mo + 13.1W$$

Eqn. 5.3

$$Ac_1 \ (^\circ C) = 723 - 10.7Mn - 16.7Ni + 29.1Si + 16.9Cr \\ + 290As + 6.38W$$

Eqn. 5.4

Using equations 5.1 through 5.4, temperatures for the respective transformations

were calculated, and are shown in Table 5.6.

Clearly from the calculated transformation values presented in Table 5.6, the four

alloys should have similar observed transformation based on chemistry. However,

variations in prior-austenite grain size could result in different transformation phenomena.

Table 5.6. Calculated transformation temperatures of alloys. All temperatures in °C.

Alloy	Martensite Start	Bainite Start	Ac_3	Ac_1
HNLV	463	667	814	710
INLV	465	668	814	710
LNLV	463	664	813	710
LNHV	466	673	816	710

Also, the possible nucleation of primary ferrite at titanium nitride inclusions that has

previously been presented could be important when considering alloy LNHV.

Table 5.7 and Table 5.8 show the observed transformation start and finish

temperatures for the materials thermally cycled to peak temperatures of 1250°C and

1400°C, respectively. Examples of the corresponding microstructures for alloy HNLV are

shown in Figure 5.52 and Figure 5.53 (see Appendix E for microstructures of the other three

alloys).

The effect of cooling rate on these transformation temperatures is clearly seen in the

tables. As the cooling rate decreases, or Δt_{8-5} increases, the transformation temperatures

increase. This is in agreement with standard metallurgical tenets.

Table 5.7. Transformation temperatures for specimens thermally cycled to a peak temperature of 1250°C. All values in °C.

Alloy	Δt_{8-5} = 3 seconds		Δt_{8-5} = 30 seconds		Δt_{8-5} = 300 seconds	
	Trans. Start	Trans. Finish	Trans. Start	Trans. Finish	Trans. Start	Trans. Finish.
HNLV	695	355	750	540	800	601
INLV	695	363	740	545	798	580
LNLV	695	370	745	548	800	595
LNHV	695	390	770	550	800	595

Table 5.8. Transformation temperatures for specimens thermally cycled to a peak temperature of 1400°C. All values in °C.

Alloy	Δt_{8-5} = 3 seconds		Δt_{8-5} = 30 seconds		Δt_{8-5} = 300 seconds	
	Trans. Start	Trans. Finish	Trans. Start	Trans. Finish	Trans. Start	Trans. Finish.
HNLV	641	325	682	488	757	578
INLV	649	335	703	507	763	576
LNLV	655	335	674	480	737	564
LNHV	640	327	675	517	746	555

a)

b)

c)
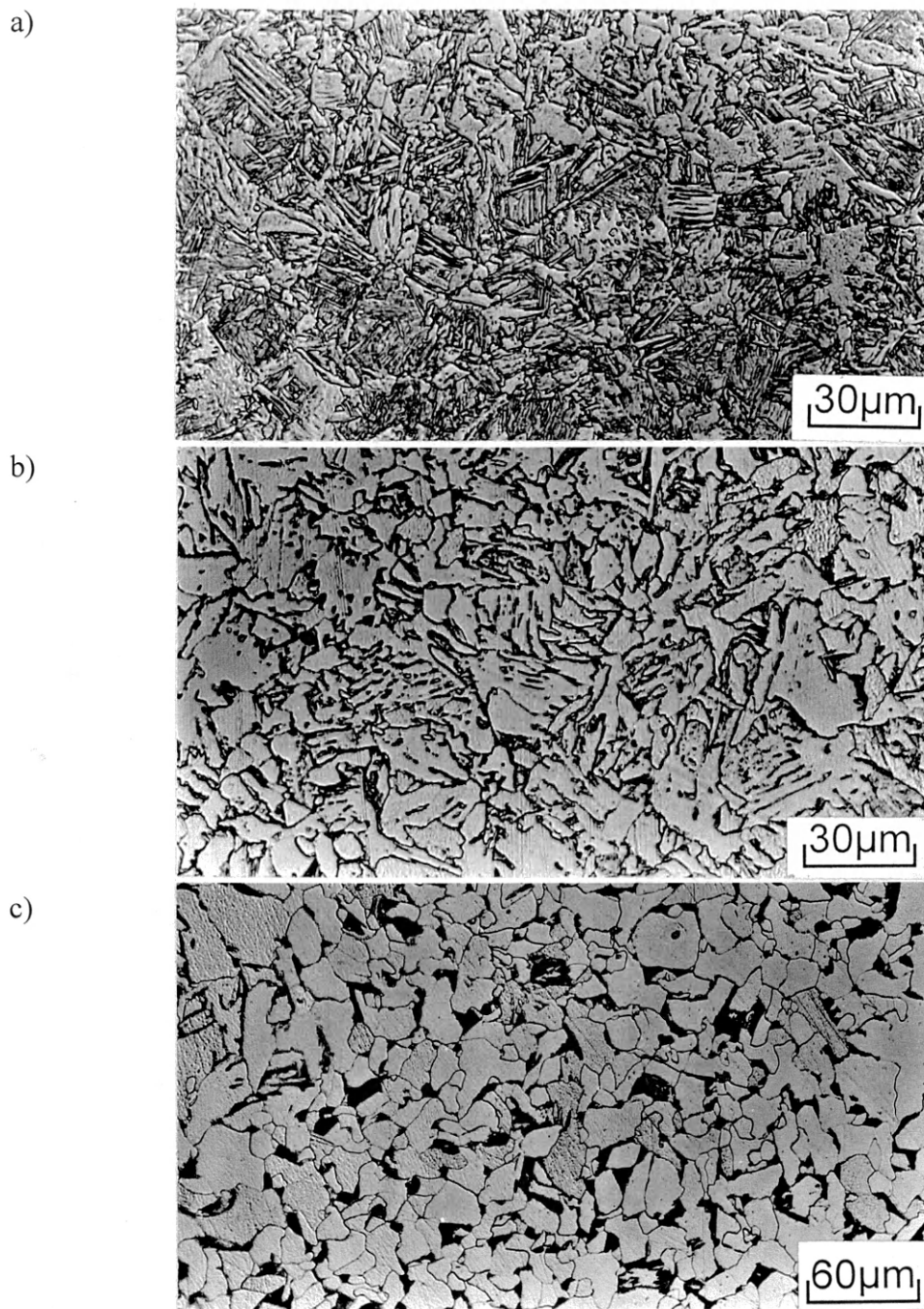
Figure 5.52. Typical microstructures of CCT specimens for alloy HNLV. 1250°C peak temperature. Δt_{8-5} times of: a) 3 seconds, b) 30 seconds, c) 300 seconds.
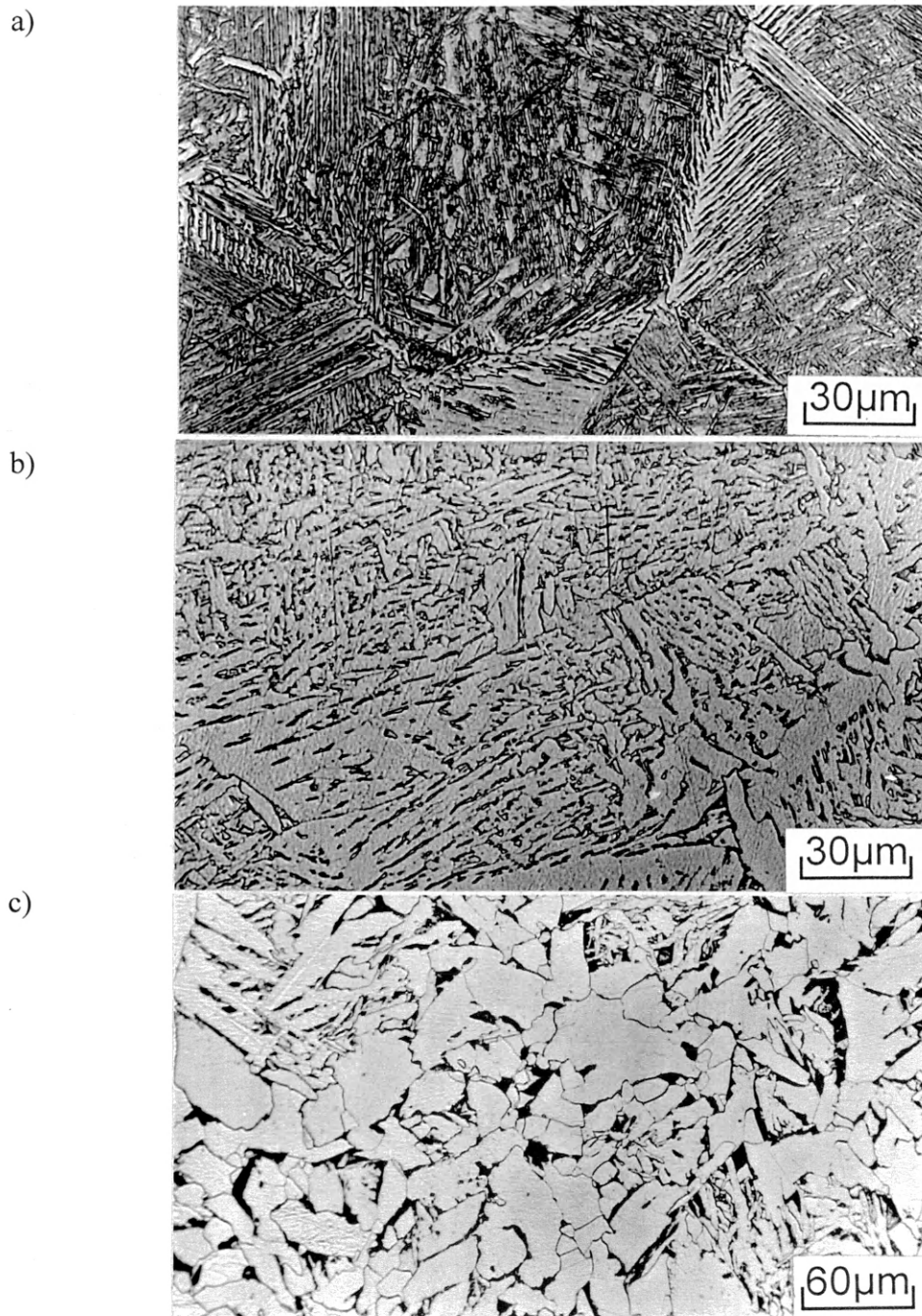
Figure 5.53. Typical microstructures of CCT specimens for alloy HNLV. 1400°C peak temperature. Δt_{8-5} times of: a) 3 seconds, b) 30 seconds, c) 300 seconds.

Whether there is a difference in transformation characteristics between the alloys for each thermal cycle is more uncertain. As a result of the method of testing, there could easily be a 20°C range to any measured transformation temperature. Figure 5.54 graphically compares the transformation temperatures for the 1250°C and 1400°C peak temperature thermal cycle specimens. While there does appear to be transformation temperature differences observed with the intermediate cooling rate thermal cycles, unfortunately the differences are within experimental error and are not explainable from standard metallurgical theory.

In all cases the increased peak temperature had the effect of depressing the transformation temperatures, as expected. With the increased peak temperature the austenite grain size increases. There is also a possible increase in the dissolution of second phase particles increases. These two phenomena will cause an increase in hardenability.

The hardnesses of the CCT specimens were also measured, the results of which are shown in Figure 5.55. The hardness of the 1400°C peak temperature specimens is greater than the 1250°C peak temperature specimens. This is consistent with the transformation temperature data in that lower transformation temperatures should lead to increased hardness. The hardness increase can result from finer microstructures (ferrite grain size for example) or entirely different transformation products such as martensite. Interestingly, the hardness of alloy LNHV is consistently lower for all conditions excluding the slow cooling rate and high peak temperature. While the difference is not great, it could be consistent data
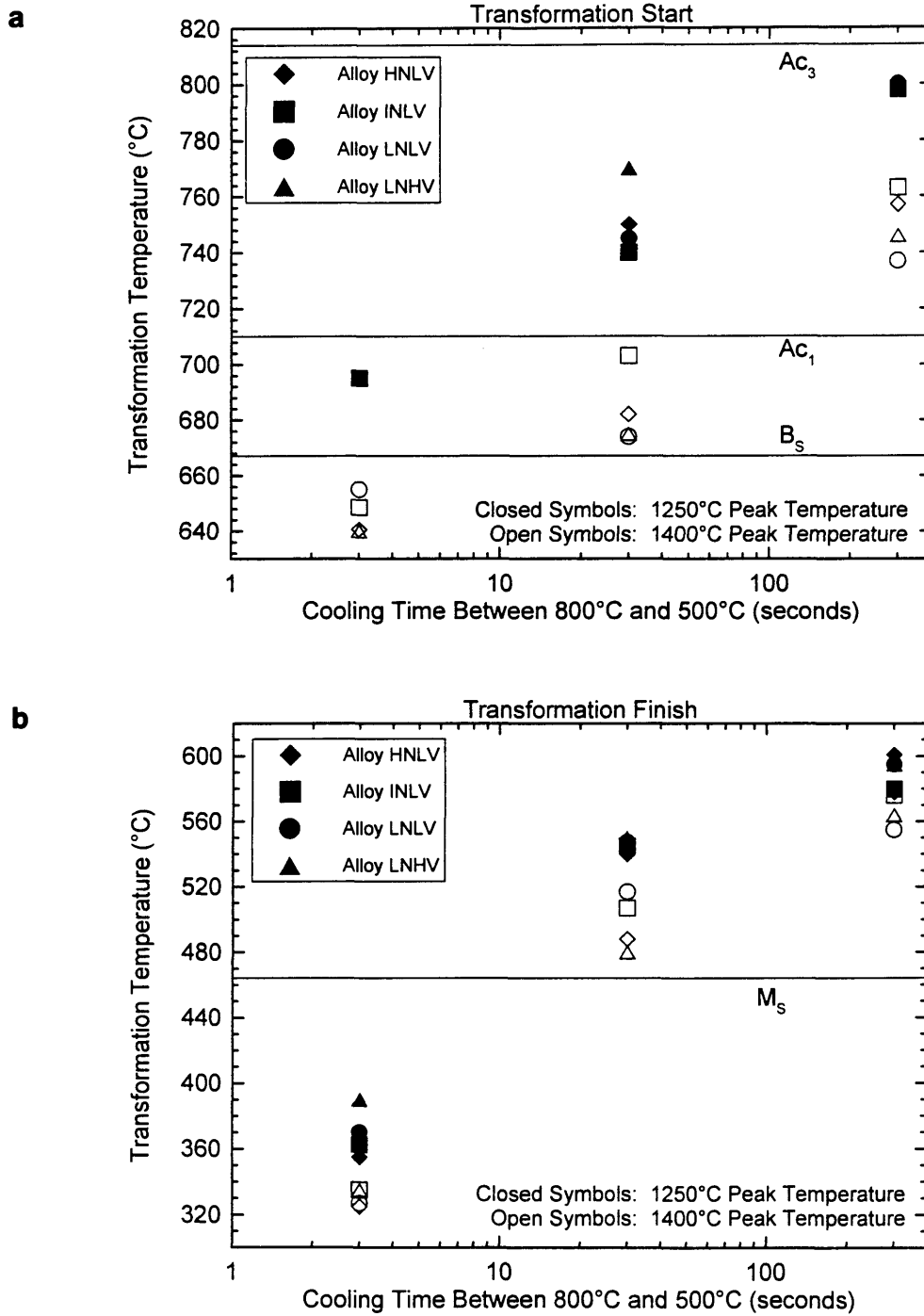
Figure 5.54. Transformation temperatures for thermally cycled materials. a) Transformation start temperatures. b) Transformation finish temperatures.
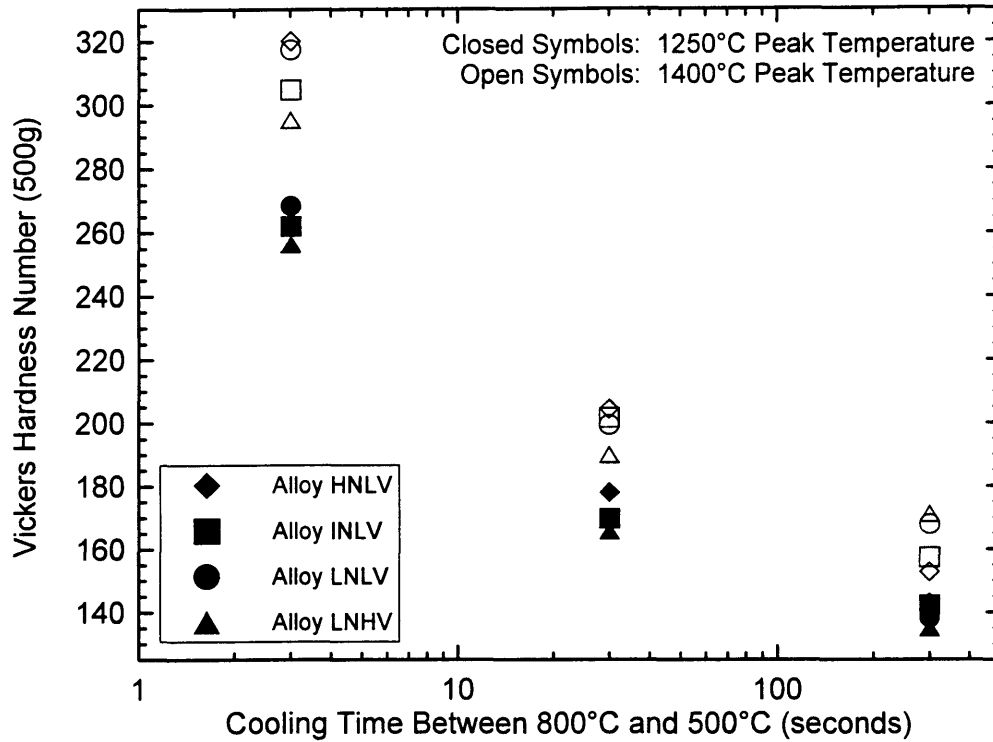
Figure 5.55. Hardness of continuous cooling transformation test specimens.

varied with cooling rate, with values of approximately 21 VHN for the fastest cooling rate

(highest hardness), and between with an increase in primary ferrite volume fraction. The

standard deviation of the hardness 4 and 8 VHN for the two slower cooling rates. Given the

standard deviation of the data for hardness, it is again very difficult to say that there is a

difference between the four alloys.

6.0 DISCUSSION

The measured quantities for many tests were presented in the Results section. In this section discussion will focus on the interpretation of the some of the more important results previously shown. This discussion will begin with the titanium nitride precipiates.

The Wagner equation was determined based on Ostwald ripening. However, there is another possible mechanism whereby the titanium nitride precipitates can coarsening as a result of thermal cycling (84). During the heating portion of the thermal experience, the titanium nitride precipitates dissolve with the smaller precipitates completely disappearing and the larger precipitates decreasing in size. During the cooling portion of the cycle, due to the decreasing solubility of titanium nitride, titanium and nitrogen can diffuse to the still-existing titanium nitride precipitates, causing growth. The shape of the precipitate is irrelevant in this model, accounting for a shortcoming in the Ostwald ripening approach. With Ostwald ripening the particles must be curved, and the cubic nature of titanium nitride particles clearly do not have significantly curved surfaces.

6.1 Titanium Nitride Precipitates

Two classes of titanium nitride precipitates were examined in this study: large titanium nitride "inclusions" that are larger than 1 μm in size, and smaller titanium nitride "precipitates" that were visible in the TEM. One would expect the smaller precipitates to be affected during the thermal simulations implemented in this study. Therefore, the discussion will begin with those precipitates and their coarsening during the welding simulations.

6.1.1 Titanium Nitride Precipitate Coarsening

Precipitate coarsening has been already addressed to some extent in the Introduction, in the form of the Wagner equation (Eqn. 1.9), reproduced below:

$$r_t^3 - r_0^3 = \frac{8\sigma\, D[M]V}{9RT} \cdot t \qquad \text{Eqn. 1.9}$$

Based on the above equation the difference in the cube of the particle sizes should be directly proportional to the product of diffusivity of the relevant atomic species (D) and the concentration of that species in the matrix ([M]).

It is generally accepted that the microalloying element in the system, *i.e.* aluminum, niobium, vanadium, or titanium, should be "relevant atomic species". When this is true, the diffusivity - concentration product should be significantly less for the metallic element (Al,

Nb, V, Ti) than for the interstitial element which is present in the precipitate (C or N). To

ensure that this was the case in the present study, the diffusivity - concentration product

needed to be calculated. The concentration can be calculated based on the solubility

relations already presented. The diffusivity values needed to be determined. These values

can be determined with the following relations (54):

$$D_{Ti} = 15\exp\left(\frac{-250kJ}{RT}\right), \quad \left[\frac{mm^2}{sec}\right] \qquad \text{Eqn. 6.1}$$

$$D_N = 91\exp\left(\frac{-169kJ}{RT}\right), \quad \left[\frac{mm^2}{sec}\right] \qquad \text{Eqn. 6.2}$$

Using a temperature of 1350°C, the diffusivity and species in solution at

temperature was calculated, then combined to determine the diffusivity-concentration

product desired. The results of these calculations are shown in Figure 6.1. Clearly shown

in the figure is that the diffusivity-concentration product for titanium is much less than for

nitrogen, by approximately four orders of magnitude. Based on these values, titanium

should indeed be the relevant atomic species regarding coarsening of titanium nitride

precipitates.

Given that titanium is the relevant atomic species, then the difference between final

precipitate volume and initial precipitate volume should scale linearly with titanium's

diffusivity-concentration product. Plots were created to determine if this was the case, and

are shown in Figure 6.2. The plots shown in the figure are for the 4 kJ/mm heat input and 8 kJ/mm heat input thermal cycles each with a 1350°C peak temperature. Included in the plots are data corresponding to average titanium nitride precipitate size including and excluding the precipitates larger than 100 nm in size.

Obvious from the plot in Figure 6.2 is that there is indeed a trend toward increasing precipitate size with increasing titanium diffusivity-concentration product. However, the correlation coefficient (R^2) is not as high as one would hope, and depends upon which average values are chosen, either including or excluding the precipitates larger than 100 nm. With the 4 kJ/mm heat input, best results are obtained when neglecting the precipitates that are larger than 100 nm. While with the 8 kJ/mm heat input the converse is true, it is better to include the large precipitates.

The relatively low correlation coefficients were disconcerting and an attempt to improve upon them was undertaken. The Wagner equation is for an isothermal system. Clearly the welding simulations performed in this study are not isothermal. Based on this information, an attempt was made to account for the non-isothermal nature of the thermal cycles applied in this work.
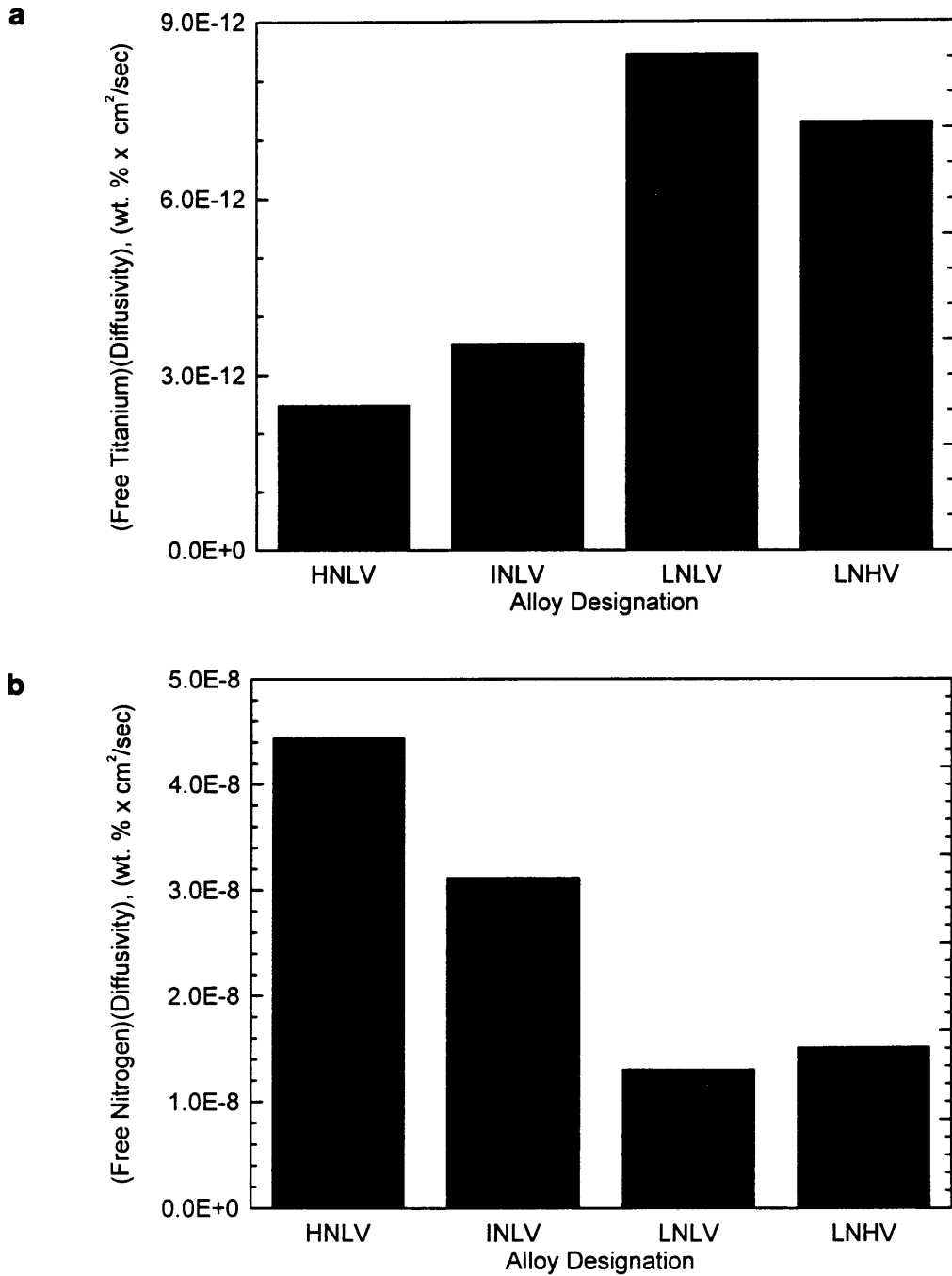
Figure 6.1. Diffusivity-concentration product for a) titanium and b) nitrogen. Calculated for a temperature of 1350°C.
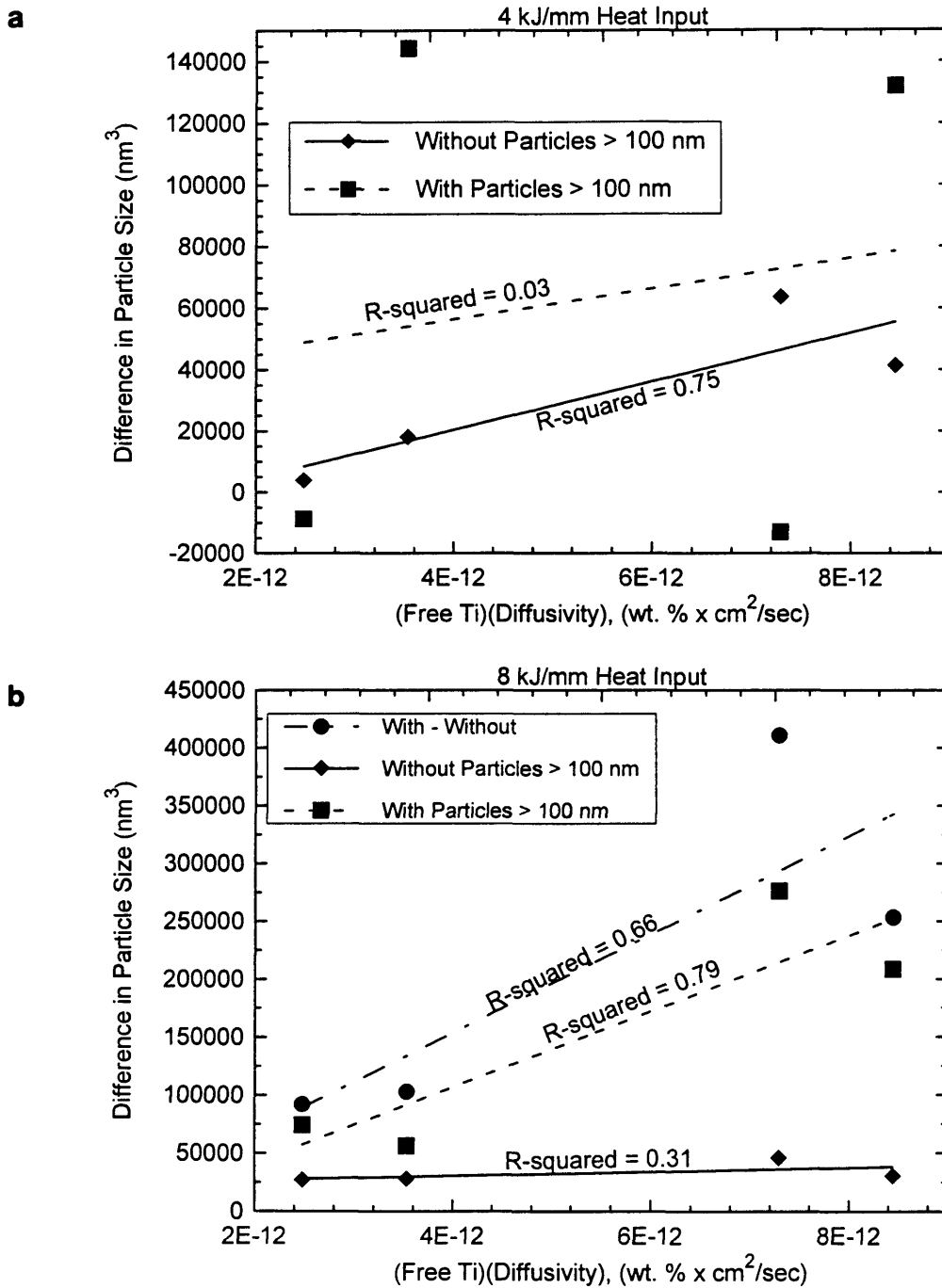
Figure 6.2.   Plot depicting relationship between the diffusivity-concentration product
and the difference in the cube of the particle size. a) 4 kJ/mm heat input. b)
8 kJ/mm heat input.

Ion, *et al.*, have presented a modification of the standard Wagner equation to accommodate non-isothermal conditions (85). The reported equation is shown below:

$$r_t^3 - r_0^3 = \frac{kt}{T} \exp\left(\frac{-Q}{RT}\right)$$

Eqn. 6.3

where k "contains constants which depend on matrix composition and Q is the activation energy for diffusion between the precipitates". This modified equation is not useful in that the question "what is k?" still must be answered. However, the situation can be improved by using what is known about diffusion coefficients and by comparing Eqn. 6.3 to Eqn. 1.9. It is known that (86):

$$D = D_0 \exp\frac{-Q}{RT}$$

Eqn. 6.4

This allows the determination of k:

$$k = \frac{8\sigma D_0 [M] V}{9R}$$

Eqn. 6.5

To arrive at a particle size after thermal cycling, one can integrate over the time-temperature cycle using an equation of the form (87):

$$r_t^3 - r_0^3 = k \int_{t_1}^{t_2} \frac{1}{T} \exp\left(\frac{-Q}{RT}\right) dt$$

Eqn. 6.6

Now there is a way to account for the non-isothermal nature of the weld simulation.

However, the composition of the matrix is not constant over the thermal cycle, as it is

assumed to be in Eqn. 6.5. Rather, the composition varies according to the solubility

product. With this in mind, a new modification to the above model is made.

Knowing the time-temperature cycle and the solubility product for titanium nitride,

it is possible to derive an expression for titanium concentration as a function of time, then

the titanium concentration remains inside the integral of Eqn. 6.6. This leaves the final

expression to determine the particle size of titanium nitride after a thermal cycle:

$$r_t^3 - r_0^3 = \frac{8D_0\sigma V}{9R} \int_{t_1}^{t_2} \frac{[Ti]\exp\frac{-Q}{RT}}{T} dt \qquad \text{Eqn. 6.7}$$

General constants, those that are independent of specific alloy, are available in the

literature with the exception of a specific value for the interfacial energy of titanium nitride

precipitates in an austenite matrix, σ. These constants are shown in Table 6.1. Since two

Table 6.1. Alloy Independent Constants Used in Prepitate Growth Model.

Constant	Value	Reference
D_0	15 mm^2/sec	54
Q	240 kJ, 250 kJ	54, 87
V	11.85 cm^3/mole	88
σ	0.5 - 1.0 J/m^2	89
R	8.314 J/(mole·K)	88

values for the activation energy for titanium diffusion were found, the average of these

values (Q = 245 kJ) was used in the calculations. Similarly, the midpoint of the range of

values for interfacial energy was chosen for use in the calculations, $\sigma = 0.75$ J/m^2.

To calculate the titanium content as a function of temperature, and therefore time,

the total titanium and nitrogen additions must be known. Also the initial precipitate size

must be known. This model is based on spherical precipitates and uses the initial radius as

the beginning precipitate size. For the purposes of this study, the initial precipitate size will

be defined as one-half the average edge length of the titanium nitride precipitates measured

in the as-quenched-and-tempered condition. The average used neglects the precipitates

larger than 100 nm in size. The total titanium and nitrogen additions, as well as the initial

precipitate size are provided in Table 6.2.

Table 6.2. Pertinent Values for Each Alloy Used in the Precipitate Growth Model.

Alloy	$[N]_{total}$, (wt. %)	$[Ti]_{total}$, (wt. %)	r_0, (nm)
HNLV	0.015	0.008	9.47
INLV	0.011	0.009	10.16
LNLV	0.005	0.012	12.63
LNHV	0.007	0.019	15.19

The remaining factor to be determined is the function of temperature with respect to time for the thermal cycles used in the study. These were determined from the actual thermal histories experience by the specimens. Polynomial curve fits were used to create the time-temperature functions required for the model. The thermal cycles had to be curve fit in two pieces, one for the heating portion and one for the cooling portion of the curves, to achieve a function that closely reproduced the experimental data. Figure 6.3 shows the curve fits and corresponding polynomial coefficients for the 1350°C peak temperature thermal cycles. These thermal cycles are addressed first since experimental measurements of precipitate size from these cycles have been made and can be used to compare to the values from the model. The other two thermal cycles (with 1250°C and 1400°C peak temperatures) will be presented later.

Figure 6.4 shows the comparison between the predicted titanium nitride precipitate size based on the model and the experimentally determined values. As shown in the figure, there is good agreement between the actual and predicted precipitate sizes. This agreement allows for confidence in extending the model to the other thermal cycles for comparison.

Figure 6.5 shows the thermal cycles used for the 4 kJ/mm heat input, with 1250°C and 1400°C peak temperatures. These thermal cycles result in predicted precipitate sizes as shown in Figure 6.6. The predicted average precipitate size sorts as one would expect, with a large separation between the 1250°C and 1350°C peak temperature thermal cycles and a

a

4 kJ/mm Heat Input, 1350°C Peak Temperature

Temperature (°C) vs Time (seconds)

0 - 9.0 seconds
Polynomial Coefficients

Degree	Value
Degree 0:	34.6724
Degree 1:	-54.4732
Degree 2:	-52.4878
Degree 3:	171.411
Degree 4:	-73.0238
Degree 5:	14.2469
Degree 6:	-1.48168
Degree 7:	0.0799074
Degree 8:	-0.00176155

9 - 80 seconds
Polynomial Coefficients

Degree	Value
Degree 0:	-1103.14
Degree 1:	920.232
Degree 2:	-137.286
Degree 3:	10.8629
Degree 4:	-0.524123
Degree 5:	0.0162178
Degree 6:	-0.000328093
Degree 7:	4.3172E-006
Degree 8:	-3.56164E-008
Degree 9:	1.67405E-010
Degree 10:	-3.4225E-013

b

8 kJ/mm Heat Input, 1350°C Peak Temperature

Temperature (°C) vs Time (seconds)

1 - 15 seconds
Polynomial Coefficients

Degree	Value
Degree 0:	930.443
Degree 1:	-2381.05
Degree 2:	2361.85
Degree 3:	-1175.83
Degree 4:	354.094
Degree 5:	-67.5936
Degree 6:	8.32656
Degree 7:	-0.658796
Degree 8:	0.0323021
Degree 9:	-0.00089291
Degree 10:	1.06345E-005

15 - 150 seconds
Polynomial Coefficients

Degree	Value
Degree 0:	2469.89
Degree 1:	-191.585
Degree 2:	13.7648
Degree 3:	-0.576926
Degree 4:	0.0141762
Degree 5:	-0.000212494
Degree 6:	1.96982E-006
Degree 7:	-1.10274E-008
Degree 8:	3.41735E-011
Degree 9:	-4.50233E-014

Figure 6.3.   Time-temperature functions used in the precipitate growth model. a) 4 kJ/mm heat input, 1350°C peak temperature. b) 8 kJ/mm heat input, 1350°C peak temperature.
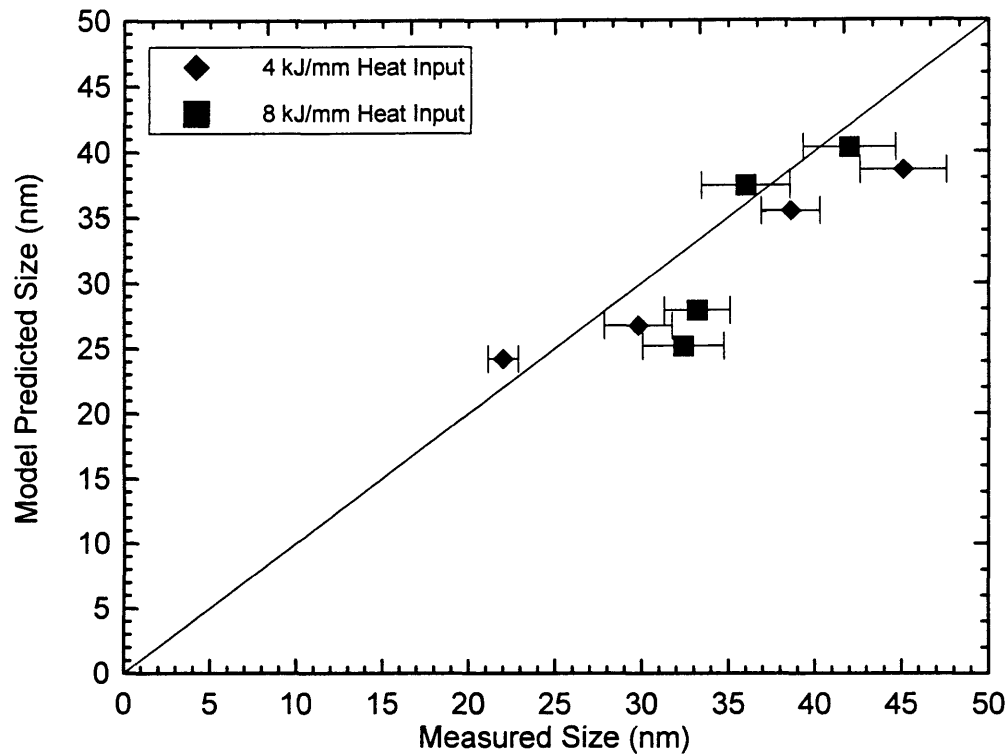
Figure 6.4. Comparison between measured titanium nitride precipitate size and the size predicted by the coarsening model. Data for all four alloys is shown. Error bars are 95% confidence limits.

HNLV and INLV. The opposite trend is observed for alloys LNLV and LNHV.

The data shown in Figure 6.6 are the predicted final size of the titanium nitride precipitates after thermal cycling. These data not only is a function of coarsening rate but also reflect the difference in initial precipitate size that was observed in the as-quenched-and-tempered baseplate. While this is interesting from the standpoint of resultant properties, it may also be instructive to concentrate simply on the amount of coarsening observed due to the thermal cycle for each of the alloys.
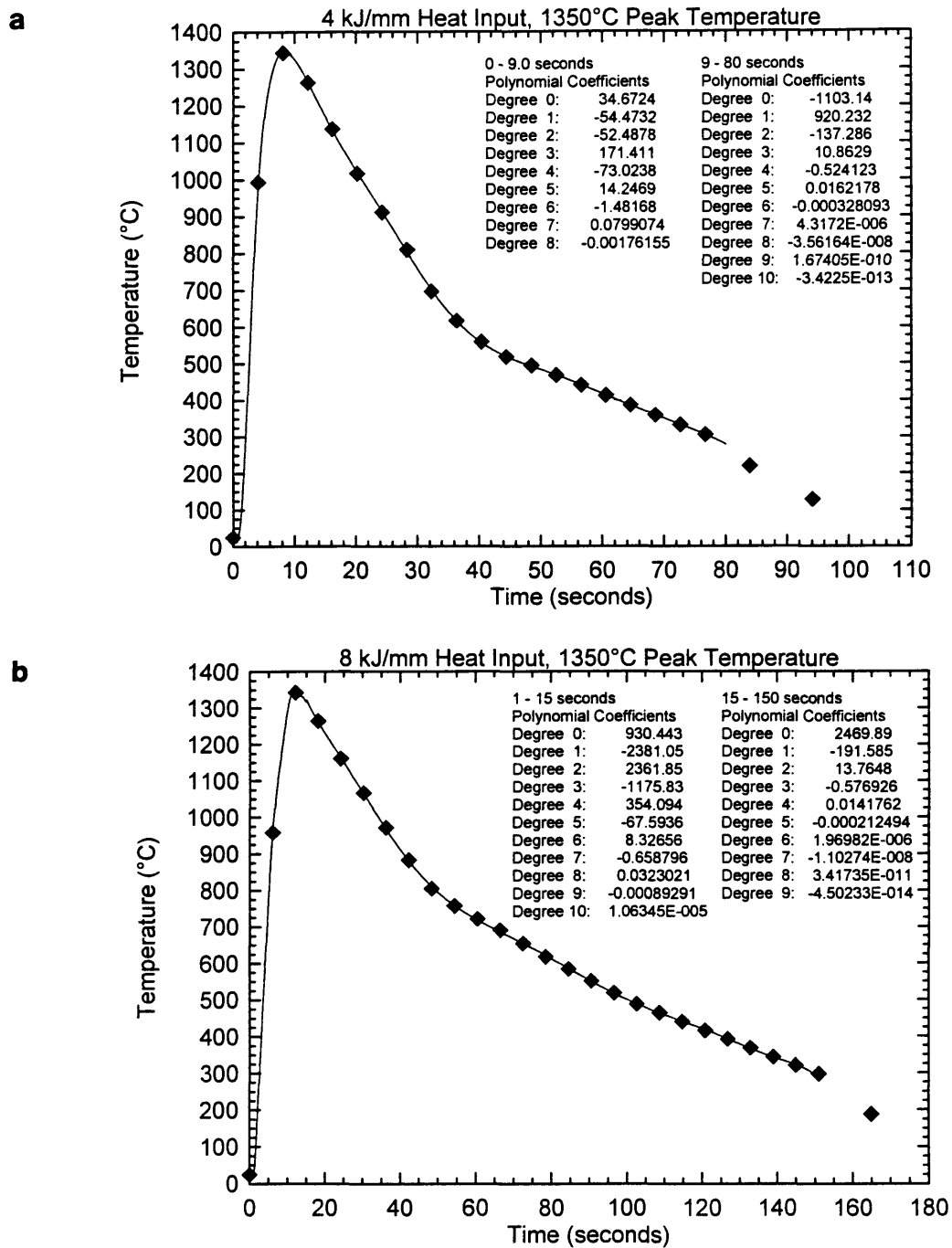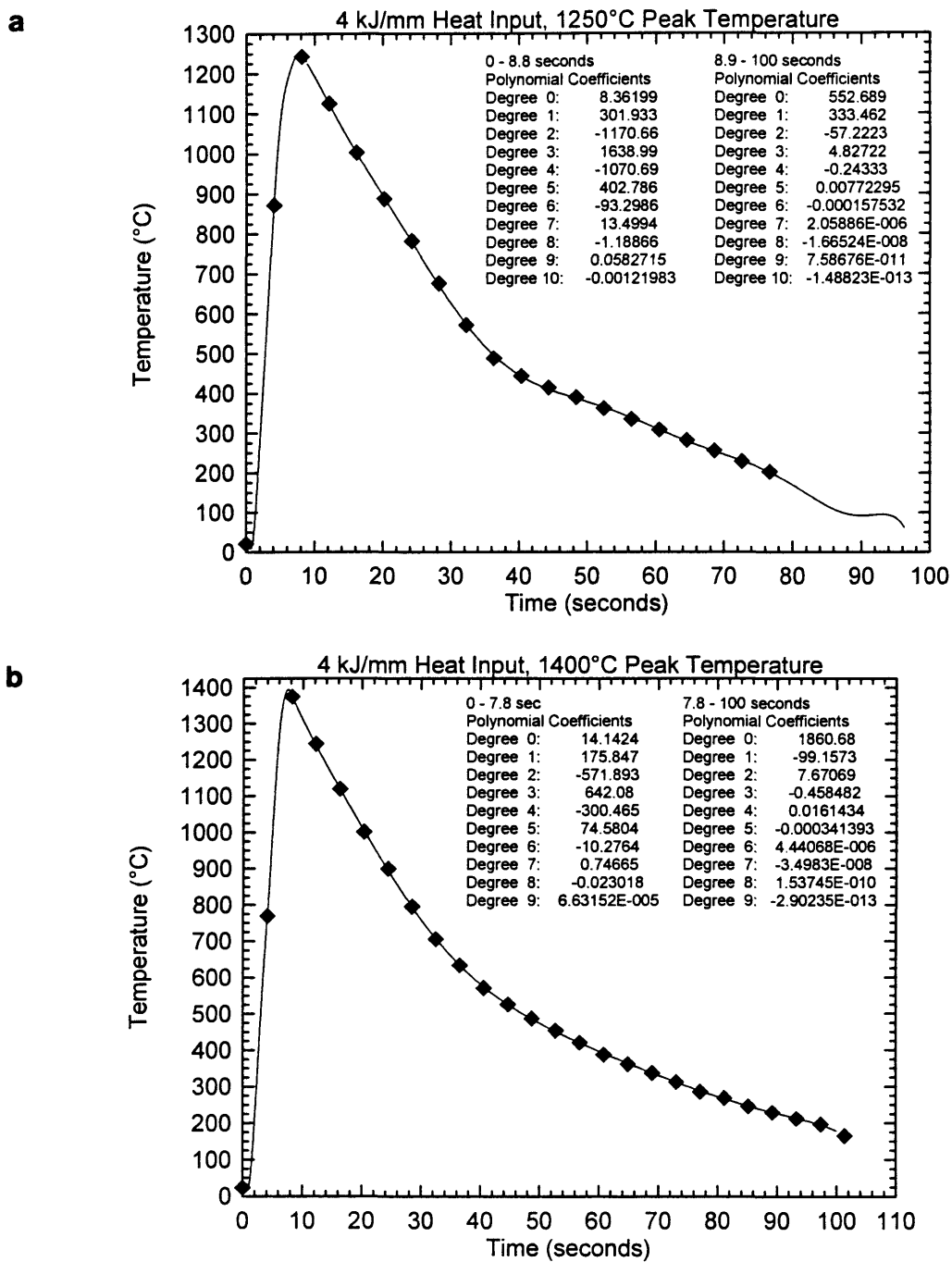
Figure 6.5. Time-temperature functions used in the precipitate growth model. a) 4 kJ/mm heat input, 1250°C peak temperature. b) 4 kJ/mm heat input, 1400°C peak temperature.
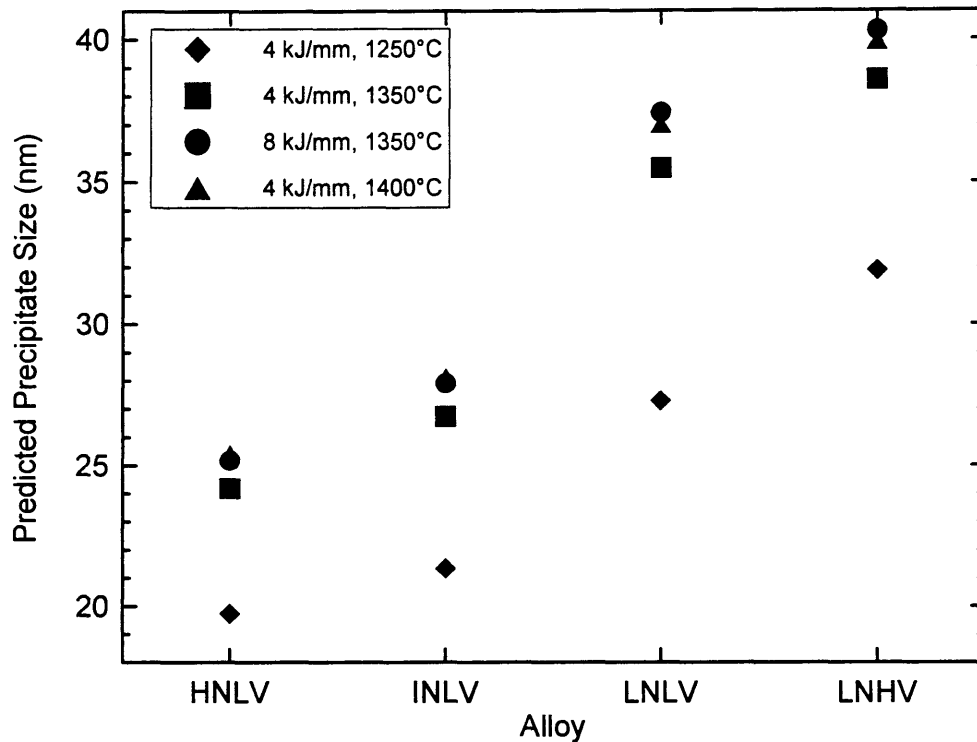
Figure 6.6.   Effect of peak temperature on predicted titanium nitride precipitate size.

Figure 6.7 shows the predicted increase in precipitate size after thermal cycling of

the four alloys. Clearly shown in the figure is that with a peak temperature of 1250°C, very

little coarsening is predicted. As the peak temperature increases to 1350°C and 1400°C,

interesting phenomena are observed. The form of the curve is the same as with the 1250°C

peak temperature, with increasing coarsening from alloys HNLV through LNLV, and a

decrease from alloy LNLV to LNHV. An interesting aspect is that there is reversal of the

highest predicted coarsening between the first two alloys and the last two alloys.
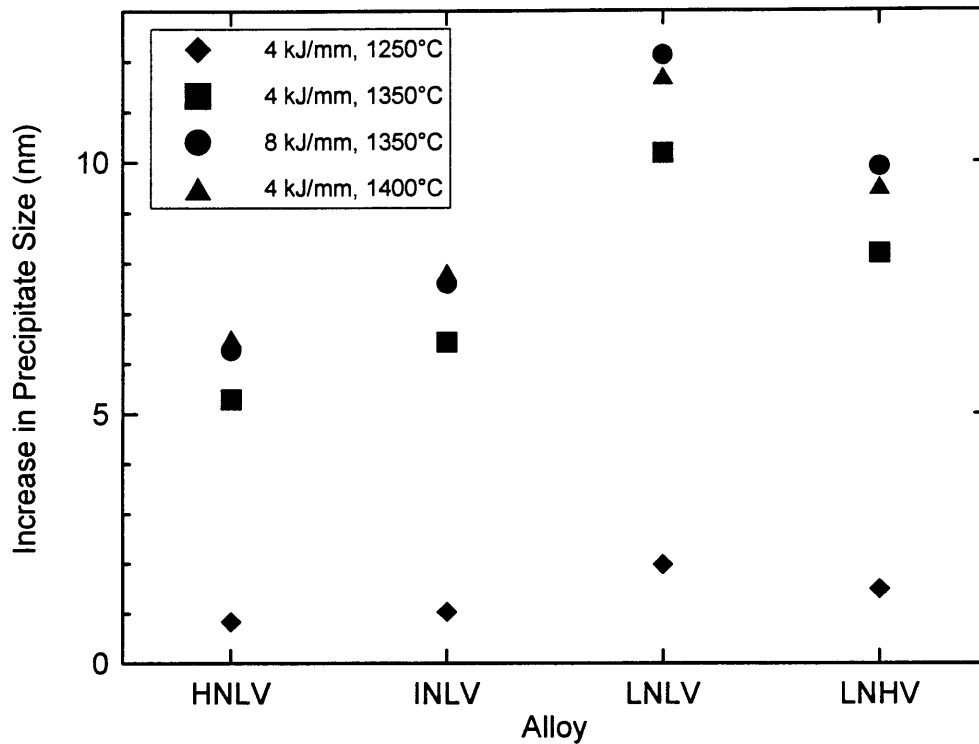
Figure 6.7. Predicted coarsening of titanium nitride precipitates after thermal cycling.

Specifically, for alloys HNLV and INLV the greatest coarsening is predicted when the peak

temperature is 1400°C. This is not unexpected, as the increased peak temperature results in

an increase in the free titanium, causing increased coarsening. However, for alloys LNLV

and LNHV, the highest coarsening is predicted when the 8 kJ/mm heat input and 1350°C

peak temperature thermal cycle is implemented. Apparently for these two alloys, there is

already enough free titanium present to result in significant coarsening at 1350°C. Under

these conditions it is the increased time at temperature that has the greatest effect on coarsening phenomena.

The study of the titanium nitride precipitate coarsening sheds light on the observed precipitate sizes for first three alloys, HNLV through LNLV. The free titanium content increases from alloy HNLV to alloy LNLV, and there is a corresponding increase in precipitate size observed for these three alloys for all thermal processing conditions, including the as-quenched-and-tempered baseplate. However, alloy LNHV is predicted to have less free titanium than alloy LNLV, and should therefore coarsen less. From a coarsening standpoint, alloy LNHV should have smaller titanium nitride precipitates than alloy LNLV. However, for all conditions alloy LNHV was observed to have the largest precipitates. It is believed that the large observed sizes for alloy LNHV are a result of high initial precipitation temperature, and the overall large sizes are extended through the thermal history of the material. The next section will address issues associated with initial precipitation temperature.

6.1.2 Initial Precipitation Temperature

The initial precipitation temperature was calculated for each of the four alloys and has already been shown in Table 5.2. These data are shown graphically in Figure 6.8, where the temperature which is plotted was determined from the austenite solubility
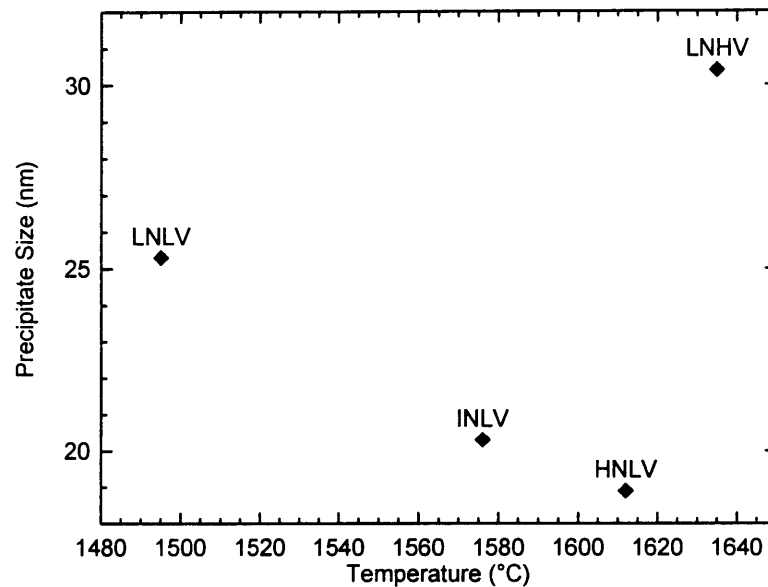
Figure 6.8. Precipitate size in as-quenched-and-tempered condition versus calculated initial precipitation temperature.

product. Shown in the figure is that precipitate size does not increase as the initial

precipitation temperature increases for the first three alloys. In fact, the reverse trend is

observed. However, alloy LNHV demonstrates the highest initial precipitation temperature

and the largest precipitates.

While the overall average titanium nitride size does not increase with initial

precipitate temperature, consideration of only the largest precipitates shows a somewhat

different behavior. Specifically, Figure 6.9 shows the relationship between the size of the

titanium nitride inclusions (> 1 μm) measured in the light microscope to the calculated

initial precipitation temperature. It is clear from the figure that there is not a well-defined
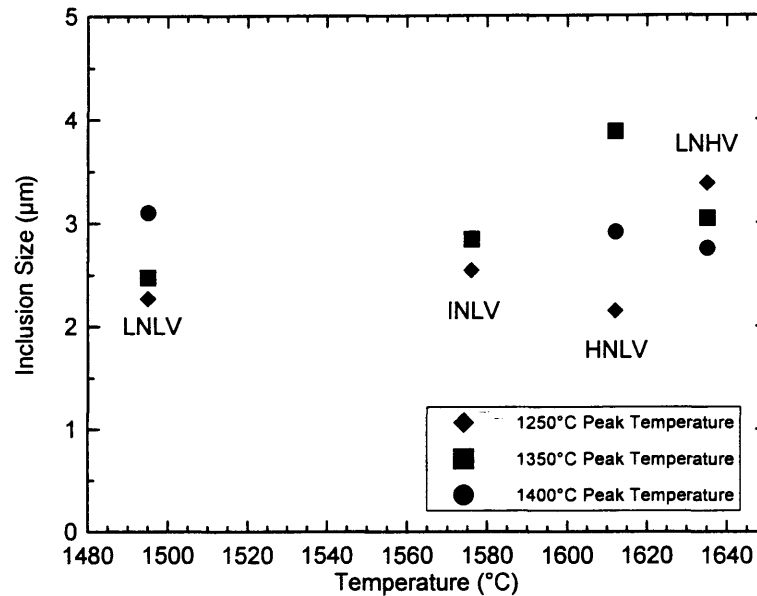
Figure 6.9. Titanium nitride inclusion size versus calculated initial precipitation
temperature.

relationship between the initial precipitation temperature and inclusion size. The average

inclusion size varies between 2 µm and 4 µm for all alloys and conditions.

The number density of titanium nitride inclusions begins to show a relationship with

initial precipitation temperature (Figure 6.10). Again, the first three alloys have very

similar values, between five and ten inclusions per square millimeter. However, there is a

marked increase in the number of inclusions for alloy LNHV. This increase in the number

density is extended to the volume fraction of large titanium nitride inclusions, shown in

Figure 6.11.

It is also believed that this increased precipitation temperature is significant

regarding the smaller titanium nitride precipitates in alloy LNHV, resulting in larger

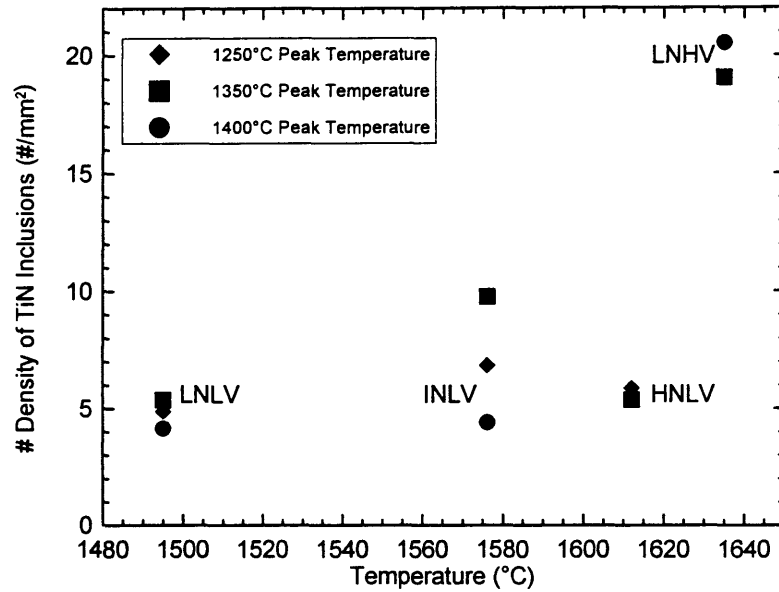Figure 6.10. Titanium nitride inclusion number density as a function of initial precipitation temperature.
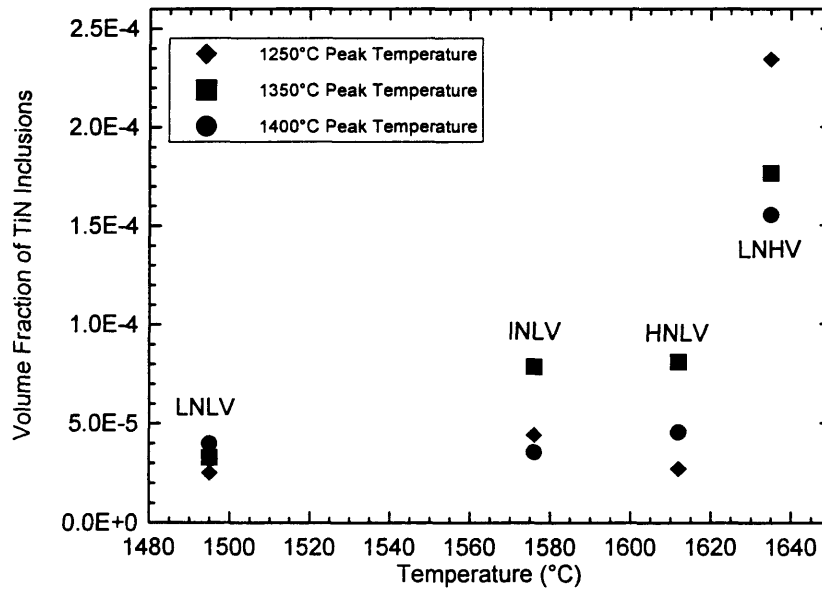
Figure 6.11. Volume fraction of titanium nitride inclusions as a function of initial precipitation temperature.

titanium nitride precipitate sizes in the small range (< 100 nm) upon cooling from ingot casting. Although alloy LNLV coarsens at a greater rate, not enough time is spent at temperature during subsequent processing to overcome the initial precipitate size differences. As a result, alloy LNHV has the largest precipitate size throughout the thermal history of the specimens.

6.2 Prior-Austenite Grain Size

Now that there are values for the titanium nitride size and volume fraction for all of the 4 kJ/mm heat input thermal cycles studied in this work, a comparison between the measured and predicted prior-austenite grain size can be made. Predicted grain size was obtained from Zener and Gladman models. For these comparisons to be valid, the volume fraction of the small, less than 100 nm precipitates must be determined. This value can be determined by using the overall volume fraction that was calculated in the design of the alloys and subtracting the measured volume fraction of the large titanium nitride inclusions. Table 6.3 shows the results of these calculations. Using the volume fraction remaining for grain size control and the precipitate size calculated from the precipitate coarsening model, the Zener and Gladman equations can then be used to calculate a predicted prior-austenite grain size. The prediction based on the Zener relation will be examined first.

Table 6.3. Volume Fraction Values Used in Grain Size Comparison.

Alloy and Condition	Total Calculated Volume Fraction	Measured Volume Fraction of TiN Inclusions	Predicted Volume Fraction of "Fine" Precipitates
HNLV, 1250°C	1.36E-04	2.71E-05	1.09E-04
INLV, 1250°C	1.47E-04	4.42E-05	1.02E-04
LNLV, 1250°C	1.52E-04	2.52E-05	1.27E-04
LNHV, 1250°C	2.83E-04	2.34E-04	4.83E-05
HNLV, 1350°C	1.17E-04	8.09E-05	3.64E-05
INLV, 1350°C	1.21E-04	7.88E-05	4.19E-05
LNLV, 1350°C	1.01E-04	3.28E-05	6.80E-05
LNHV, 1350°C	2.31E-04	1.77E-04	5.45E-05
HNLV, 1400°C	1.04E-04	4.55E-05	5.82E-05
INLV, 1400°C	1.02E-04	3.56E-05	6.65E-05
LNLV, 1400°C	6.97E-05	3.98E-05	2.99E-05
LNHV, 1400°C	2.00E-04	1.55E-04	4.45E-05

Figure 6.12 shows a comparison between the measured prior-austenite grain size and the predicted grain size based on the Zener equation. Clear from the figure is that the Zener approach predicts grain sizes that are significantly larger than what was measured.
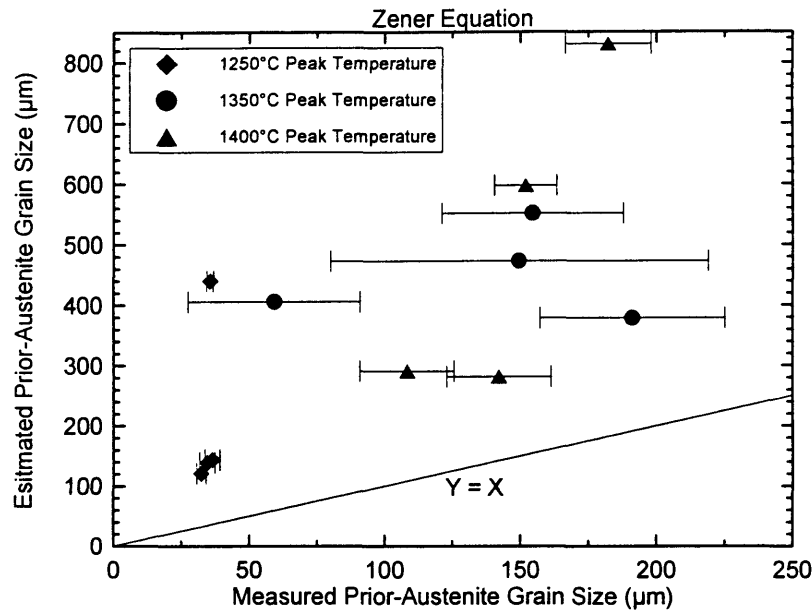
Figure 6.12. Comparison between measured prior-austenite grain size and the grain size predicted using the Zener equation. Error bars are standard deviation.

Since the Zener model does not predict the grain size very well, the Gladman approach was also examined.

In the Introduction it was stated the grain size heterogeneity factor, z, in the Gladman equation varied between 1.5 and 2. The comparison between measured values and predicted values for prior-austenite grain size will begin where z=1.5. This condition is depicted in Figure 6.13. Apparent from this figure is that the Gladman relation predicts prior-austenite grain sizes that are significantly smaller than what has been measured. However, there is an effect observed when the grain size heterogeneity factor is increased. Figure 6.14 shows the comparison between the measured and predicted values of the prior-
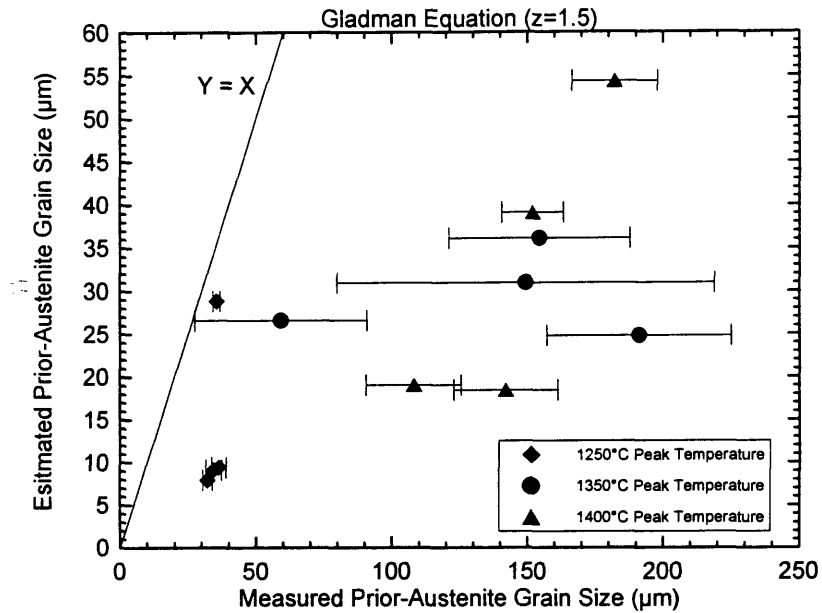
Figure 6.13. Comparison of measured and predicted prior-austenite grain size based on the Gladman equation with z = 1.5. Error bars are standard deviation.

austenite grain size when the grain size heterogeneity factor is increased to z = 1.75 and z = 2.0. Significant improvement is made in the approximation when z = 2.0; however, the predicted values are still generally lower than the measured grain size.

The converse calculation can also be made, where the critical particle size that results in the measured grain size can be determined. This has been done with the z factor being defined as 2.0, since this value resulted in the best agreement in the grain size comparison. Figure 6.15 shows a plot comparing the predicted precipitate size from the particle coarsening model versus the critical precipitate size predicted by Gladman's model based on the measured prior-austenite grain size. The calculated critical size is generally
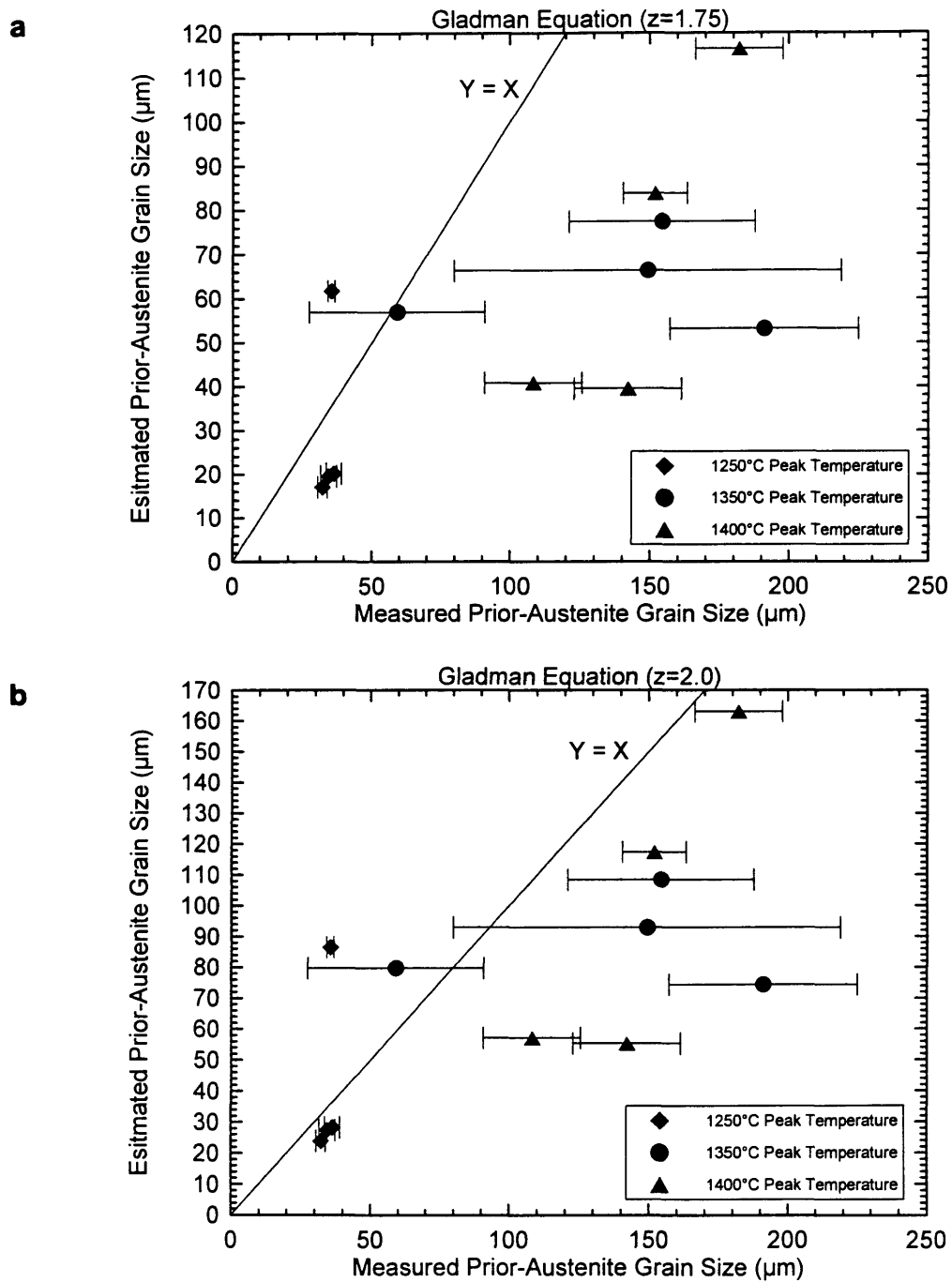
Figure 6.14. Comparison between measured and predicted prior-austenite grain size using the Gladman equation. a) z = 1.75. b) z = 2.0.
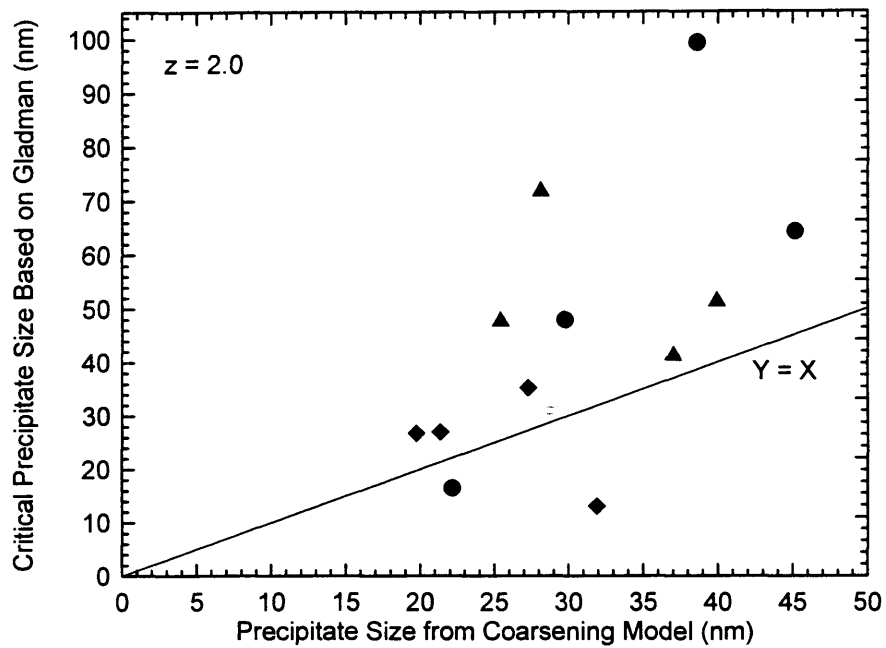
Figure 6.15. Comparison between precipitate size predicted from the precipitate coarsening model and the critcal precipitate size from the Gladman equation based on measured prior-austenite grain size.

larger than the model predicts for the thermal cycles used in this study. This is in agreement with the grain size comparison since larger precipitates would result in larger grain size and a larger grain size was observed than would have been predicted using the Gladman equation.

6.3 Ferrite Nucleation at Titanium Nitride Inclusions

The intragranular nucleation of ferrite at nonmetallic inclusions is a well accepted phenomenon. Much of the work in this area has been associated with intragranular acicular

ferrite (as defined in the IIW classification system, see section 1.4.6 and Figure 1.10) in weld metals (90,91). Titanium nitride inclusions have been shown to promote acicular ferrite formation in steels (92); however, most of the analyses have focused on oxide inclusions. It has been reported that the minimum size for inclusions to be effective at nucleating acicular ferrite is approximately 0.5 µm (90,93). This size is slightly smaller than the smallest titanium nitride inclusions observed in the light microscope (~1 µm). It is almost certainly the case that the observed increase of primary ferrite volume fraction reported in the present work for alloy LNHV (Figure 5.40) is the result of acicular ferrite nucleation at the large titanium nitride inclusions present in higher quantities for alloy LNHV (see Figure 5.46).

In the IIW classification there is a distinction between primary ferrite and acicular ferrite. However, in the classification system used in the present study, there is no such distinction made. Simply put, under the classification system implemented in this work, if there was no indication of second phase precipitates, or MA islands, present in the area under examination, it was quantified as primary ferrite. Therefore, it is probable that the titanium nitride inclusions are nucleating what the IIW would define as acicular ferrite intragranularly, and it is being classified as primary ferrite, resulting in increased measured primary ferrite volume fraction.

Acicular ferrite is a fine structure and as such will reduce the effective ferrite grain size (92,94). Therefore, if acicular ferrite is nucleated at the titanium nitride inclusions, it

will be revealed in the present study as an increase in the measured primary ferrite volume

fraction and a decrease in the mean free path between ferrite high angle boundaries. To

reinforce the idea that titanium nitride inclusions are nucleating acicular ferrite in the case of

alloy LNHV, Figure 6.16 shows the measured primary ferrite volume fraction and mean

free path between ferrite high angle boundaries as a function of titanium nitride inclusion

volume fraction. Since alloys HNLV, INLV, and LNLV have similar values for the

measured quantities of interest in Figure 6.16 (with the exception of effective ferrite grain

size for alloy LNLV with a 1350°C peak temperature), those values have been averaged to

show the effect of the significant increase in the inclusion volume fraction demonstrated by

alloy LNHV.

For the 1250°C peak temperature specimens, a significant increase in primary ferrite

content is apparent in Figure 6.16(a); however, only a slight decrease in effective ferrite

grain size is observed. The grain size effect may be limited because the specimens cycled

with the 1250°C peak temperature had an overall small grain size at the outset. Therefore

any acicular ferrite present does not significantly change the size of the microstructure. The

is very strong evidence for acicular ferrite nucleation in the specimens cycled with the

1350°C peak temperature. Both a significant increase in primary ferrite content and a

significant decrease in the mean free path between ferrite high angle boundaries are
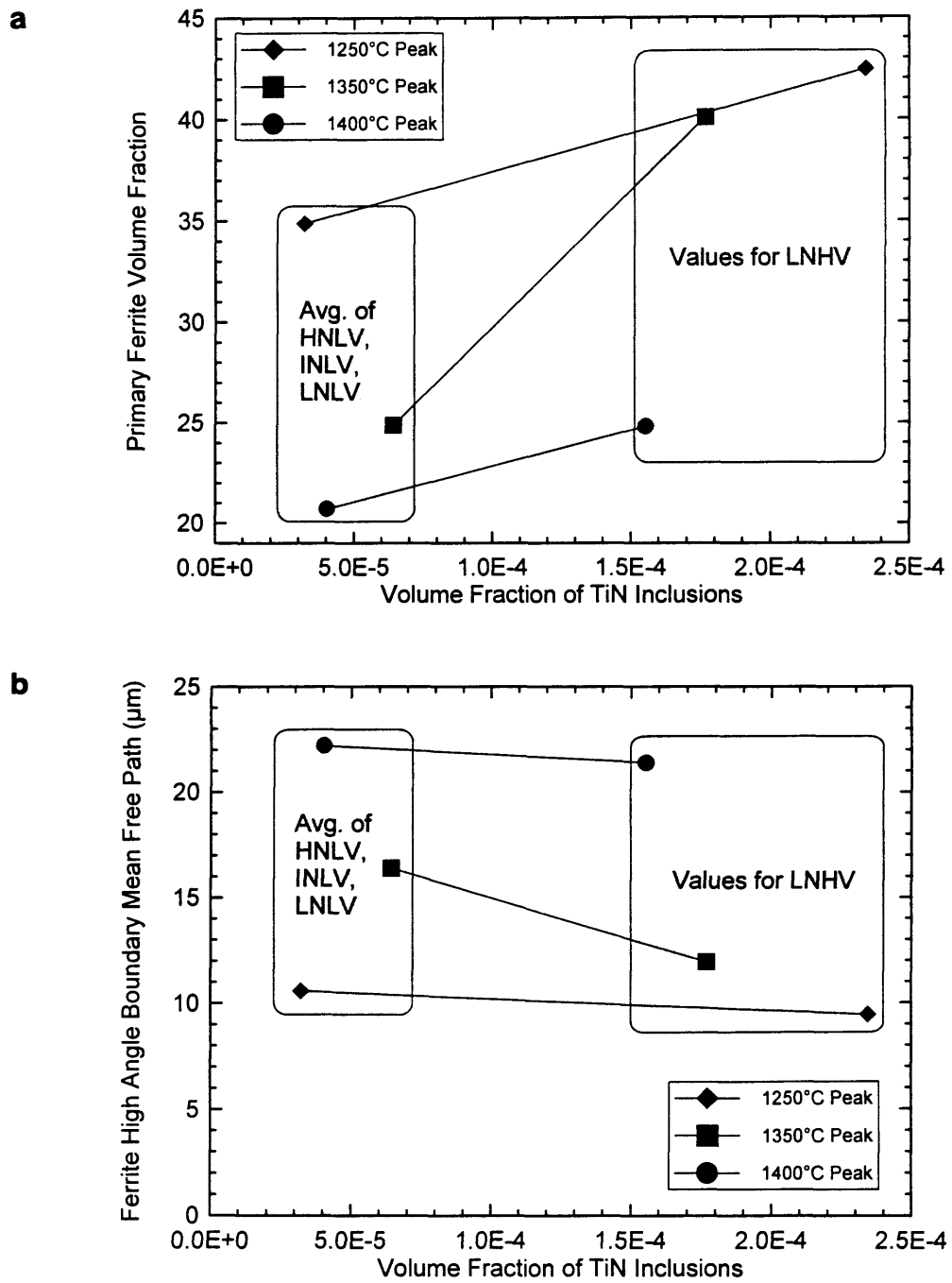
demonstrated in Figure 6.16.

Figure 6.16. Effect of titanium nitride inclusion volume fraction on the (a) primary ferrite volume fraction and (b) mean free path between ferrite high angle boundaries.

Since there was not a significant increase in the measured primary ferrite content for the 1400°C peak temperature thermal cycles, it is unlikely that much acicular ferrite was nucleated. This is further supported by the consistent mean free path between the ferrite high angle boundaries. However, these specimens also have the lowest titanium nitride inclusion volume fraction.

That non-aligned acicular ferrite improves the toughness of weld metals is well established (90,95,96). This is chiefly attributed to the relatively small effective grain size (92,94). In the next section the implication of the acicular ferrite content on the impact transition temperature data will be discussed.

6.4 Effect of Microstructural Constituents on CVN Transition Temperature

Throughout the course of this study many microstructural parameters have been measured. It was hoped that a significant difference in microstructure would be found that could then be correlated to Charpy V-notch test performance. A regression analysis was performed between the measured, or calculated, microstructural features and the 100 J transition temperature. The regression analysis was confined to the 4 kJ/mm heat input specimens because these were the specimens that had quantified microstructure.

With these constraints, twelve values of the Charpy V-notch transition temperature were the dependent variables. This allows ten independent variables to be examined at a

given time. Since several of the measured microstructural features shown in the Results sections are interrelated, and there are a limited number of independent variables that can be included in the regresion analysis, some of the variables that were used in the regression are not simply the quantities measured and reported in the Results section. For example, the bainitic component of the microstructure, ferrite with aligned and non-aligned second phases, are clearly related to the primary ferrite content. As the primary ferrite increases, the bainitic component decreases.

After some thought, six categories were used in the regression analysis. The categories were: calculated free nitrogen, volume fraction of large titanium nitride inclusions, primary ferrite volume fraction, the mean free path between ferrite high-angle boundaries, the combined volume fraction of MA constituent and the unresolvable second phase, and lastly the mean free path between second-phase constituents. A modification was made for two of the values, free nitrogen content and ferrite high angle boundary mean free path, to accommodate reported correlations. Pickering reported a square root dependence for free nitrogen content on impact transition temperature, as shown in equation 1.6. Also reported in that equation is a Hall-Petch type dependence for the ferrite grain size. The mean free path between ferrite high angle boundaries can be considered an "effective" ferrite grain size, thus this value was raised to the -½ power in the regression analysis.

Prior to conducting the regression analysis, the measured or calculated values of interest were normalized to a scale between 0 and 1. This approach also resulted in non-

dimensional parameters. The normalizing was performed according to the following

relation:

$$X_{norm} = \frac{X_i - X_{min}}{X_{max} - X_{min}}$$ Eqn. 6.8

where X_{norm} is the normalized value of the variable, X_i is the value being normalized, X_{min} is

the minimum in the range of variables being normalized, and X_{max} is the maximum of the

range being normalized. By using these normalized variables, the relative effect of each

microstructural component can be quantified without concern for units or the range that the

variable initially possessed. However, it should be noted that this approach is not effective

in predicting the properties of other materials based on the present analysis. Rather, it is

intended to simply determine the magnitude of the effect certain microstructural

components have on the 100-J transition temperature. This magnitude is given as the

coefficient of the variable, with higher absolute values of the coefficients indicating more

significant effects. It should be noted that the dependent variable, in this case Charpy V-

100-J notch transition temperature, was not normalized.

With the previous discussion of the approach for the regression analysis provided,

the focus can now be turned to the results. The results shown in Table 6.4 are from the

multivariable regression analysis done with Microsoft Excel™. What is of particular

interest is that coefficients with corresponding t-statistic values lower in magnitude than 2.0,

Table 6.4. Results of Regression Analysis for Microstructure Effect on Transition Temperature.

Category	Coefficient	Standard Error	t-Statistic
Intercept	24.3	9.1	2.7
Volume Fraction of Large Titanium Nitride Inclusions	33.6	11.1	3.0
Primary Ferrite Volume Fraction	-52.8	20.8	-2.5
("Effective Ferrite Grain Size)$^{-\frac{1}{2}}$	-14.6	17.4	-0.8
Combined Second Phase Volume Fraction	-42.7	11.6	-3.7
Free Nitrogen	16.5	9.8	1.7

are not statistically significant at a 95% confidence level (97). That is, one cannot say with certainty that there is a correlation between the measured variable (with a t-statistic value of less than 2.0) and the dependent variable. With this qualification being noted, the statistically significant variables for the above regression analysis are: the volume fraction of the second phase components, volume fraction of titanium nitride inclusions, the and the primary ferrite volume fraction.

Clearly, the other microstructural components play a role in impact transition temperature; however, the issue here is that the alloy system investigated either inherently

has a large variation in the measured quantities, or there is not enough difference in the quantities for the given thermal history experienced, or possibly both. Another possibility is that for the regression analysis that was conducted, the most important combination of variables, or their current forms (e.g. $d^{-\frac{1}{2}}$), may not have been chosen. Regardless of the reason, the regression analysis did not prove as beneficial in determining the relative effect of microstructural features on the impact transition temperature as was hoped. Additionally, the regression analysis shows that as the volume fraction of the second phase increases, the impact transition temperature should decrease, or the material should have better toughness. This result is in contrast to what would be expected as shown in the equation from Pickering (equation 1.6). In that equation, as the pearlite content increases (analogous to an increase in second phase components), the impact transition temperature increases, or toughness decreases.

Unfortunately, this alloy system is not well suited to the quantitative regression analysis attempted for the microstructures produced in specimens from the three peak temperatures and four alloys. What is left is a more qualitative examination of the properties and how the microstructural features can influence them. Perhaps the best place to start is with the materials thermally cycled to a peak temperature of 1250°C.

6.4.1 1250°C Peak Temperature Thermal Cycles

For the specimens cycled with a peak temperature of 1250°C, it is thought that the influence of acicular ferrite content is insignificant, probably due to the overall softness of the microstructure associated with the high initial primary ferrite content. Hence, another explanation for the observed transition temperature data is required.

When the alloys examined in this study are thermally cycled with a peak temperature of 1250°C, a strong trend is observed, as shown in Figure 5.38 and Figure 10.14. The 100-J transition temperature clearly decreases from alloy HNLV to alloy LNLV. First, it should be noted that there is not a significant difference in the effective ferrite grain size for all four of the alloys (see Figure 5.48 and Figure 12.22) However, these alloys were designed to have different free nitrogen contents at the outset of the study, providing an obvious comparison. With this in mind, the impact transition temperature was compared to the expected free nitrogen content for the alloys at 1250°C. The results of this comparison are shown in Figure 6.17. This figure shows a strong, apparently linear, relationship between free nitrogen content and 100-J transition temperature. Also shown in the figure is a plot corresponding to the Pickering equation where the impact transition temperature has a square-root dependence with free nitrogen content (*i.e.*, he showed ITT = ...+ 700N$^{1/2}$+ ...). The constant from Pickering's equation was modified so that the curve would fit within the axes of the plot.
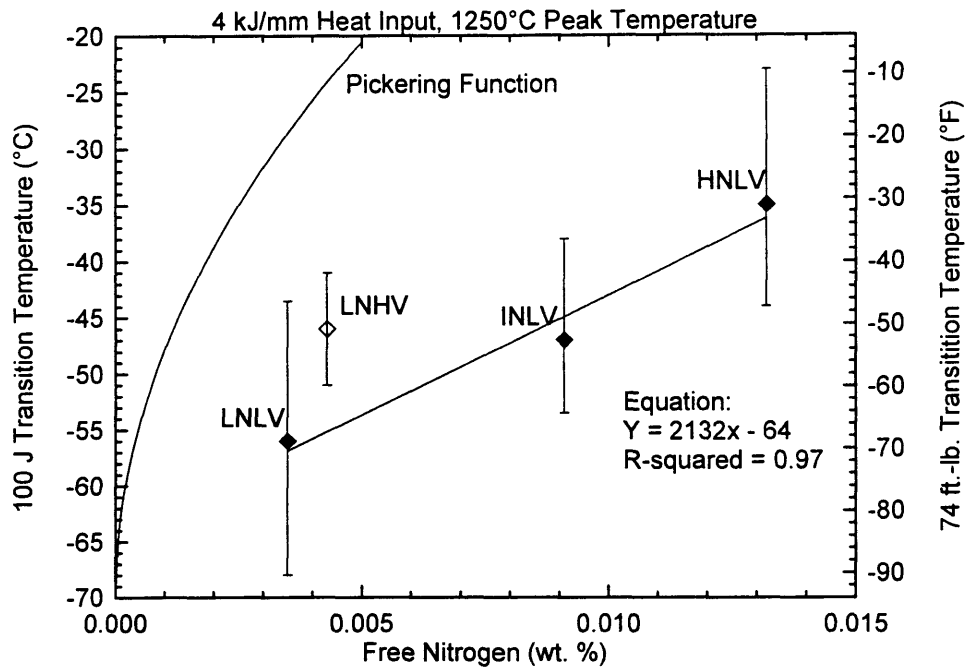
Figure 6.17. Impact transition temperature as a function of calculated free nitrogen at 1250°C.

The square-root dependence predicted by Pickering does not correlate well with observations. It is possible that this discrepancy is associated with the different microstructures found in the current study as compared to the Pickering work. The Pickering study was done with ferrite-pearlite steels, whereas the current work is associated with microstructures that have a large fraction of bainitic component in the microstructure (FS(A) and FS(NA)). Bainitic microstructures have considerably greater dislocation densities than primary ferrite or ferrite-pearlite microstructures (98). Presumably the increased dislocation density of the bainitic microstructures will provide sinks for free nitrogen, and consequently, more free nitrogen will be necessary to effectively pin all of the

dislocations. This statement is reflected by the fact that the Pickering relation predicts a greater influence of nitrogen than has been seen in the present work. Additionally, the data in Figure 6.17 is consistent with previous work (99) which showed a 2-4°C increase in transition temperature per 0.001% nitrogen in HAZ's of C-Mn steels.

Alloy LNHV does not fit directly with the other three alloys when considering the free nitrogen content due to its increased volume fraction of titanium nitride. However, one can hypothesize that the increased titanium nitride volume fraction has the effect of scaling the data to increased transition temperatures. Based on the theories presented in the Introduction, the increased volume fraction of large titanium nitride inclusions that has been observed in alloy LNHV is likely playing the dominant role in decreased toughness as opposed to the smaller titanium nitride precipitates that were observed in the TEM.

While the effect due to increased titanium nitride inclusions may appear obvious, there is another microstructural difference observed between alloy LNLV and alloy LNHV (note that one should compare alloy LNHV to alloy LNLV due to the similar free nitrogen content). This difference is the primary ferrite content, with primary ferrite volume fraction being greater for alloy LNHV. It is unlikely that the increased primary ferrite content is causing the increase in transition temperature. Primary ferrite is generally softer, and unless the ferrite grain size is quite large, has better transition temperatures than the lower-temperature transformation products. Remember that the as-quenched-and-tempered material was predominantly primary ferrite and had significantly lower transition

temperatures than any of the simulated heat-affected zone materials. Perhaps the primary

ferrite content in the materials thermally cycled with the 1250°C peak temperature is

already high enough that increasing it by less than 10% makes little difference.

6.4.2 1350°C Peak Temperature Thermal Cycles

The materials subjected to the higher peak temperature thermal cycles are more

difficult to interpret due to the large scatter in the data and the similarity in transition

temperatures, particularly for alloys HNLV, INLV, and LNLV. This being said, there are

some interesting aspects of the observed microstructures and transition temperatures that

can be correlated.

The 1350°C peak temperature materials were the only ones that exhibited a decrease

in transition temperature from alloys LNLV to LNHV (Figure 5.38). Also observed was a

marked increase in primary ferrite content, approximately 15% (see Figure 5.40 and Figure

12.1). The volume fraction of large titanium nitride inclusions also increases from alloy

LNLV to LNHV; however, it is not as large an increase as was demonstrated with the

1250°C peak temperatures, see Figure 5.46. The specimens cycled with the 1350°C peak

temperature were also the only ones to demonstrate a significant difference in effective

ferrite grain size, as shown in Figure 5.48 and Figure 12.23.

The differences in the magnitude of the transition temperature observed between the 1250°C and 1350°C peak temperature thermal cycle materials can be explained by the overall microstructure. With the 1250°C peak temperature specimens, the primary ferrite content is much higher and the effective ferrite grain size is much lower than for the 1350°C and 1400°C peak temperature specimens, and thus the transition temperature of the 1250°C specimens is significantly lower than for either of these higher-temperature conditions.

While there are only subtle differences in the impact transition temperatures exhibited by the alloys after the 1350°C thermal treatment, what differences are observed can be attributed to the competing effects between ferrite grain size and free nitrogen content.

The hypothesis of competing mechanisms can be applied to the observation that there are only subtle differences in transition temperature for the alloys subjected to the 1350°C peak temperature thermal cycle. The increase in prior-austenite grain size from alloy HNLV to LNLV results in an increase in effective ferrite grain size (Figure 5.48 and Figure 12.23). This increase in ferrite grain size has the effect of increasing the transition temperature. However, there is also a decrease in free nitrogen content from alloy HNLV to alloy LNLV, that produces a decrease in transition temperature, as was shown in the 1250°C peak temperature specimens. These two mechanisms are counteracting one another, resulting in essentially the same transition temperature for these three alloys.

The subtle differences in transition temperature for the 1350°C peak temperature specimens further support the dual mechanism hypothesis. Let's begin by comparing the mean free path data of the ferrite high angle boundaries and the 100-J transition temperature (Figure 5.48 and Figure 5.38). There is a slight increase in the mean free path from alloy HNLV to INLV. This increase in grain size is accompanied with a slight decrease in transition temperature. The effect of decreasing free nitrogen from alloy HNLV to alloy INLV is overriding the slight change in ferrite grain size. Extending this hypothesis, there is a large increase in ferrite grain size between alloys INLV and LNLV. This increase corresponds to a increase in transition temperature. Apparently the grain size difference overcomes any benefit from decreased free nitrogen from alloy INLV to alloy LNLV. The next comparison, between alloys LNLV and LNHV is particularly compelling. Alloy LNHV has a significantly smaller effective ferrite grain size than LNLV (as a result of ferrite nucleation at titanium nitride inclusions), approximately equal to the grain size observed for alloys HNLV and INLV. What is interesting is that alloy LNHV has the lowest transition temperature of the four alloys cycled with the 1350°C peak temperature. The combination of small effective ferrite grain size and low free nitrogen results in the best toughness characteristics.

When the specimens are thermally cycled with a peak temperature of 1350°C, alloys HNLV, INLV, and LNHV have essentially the same ferrite grain size. This allows a comparison with free nitrogen content and transition temperature, as shown in Figure 6.18.
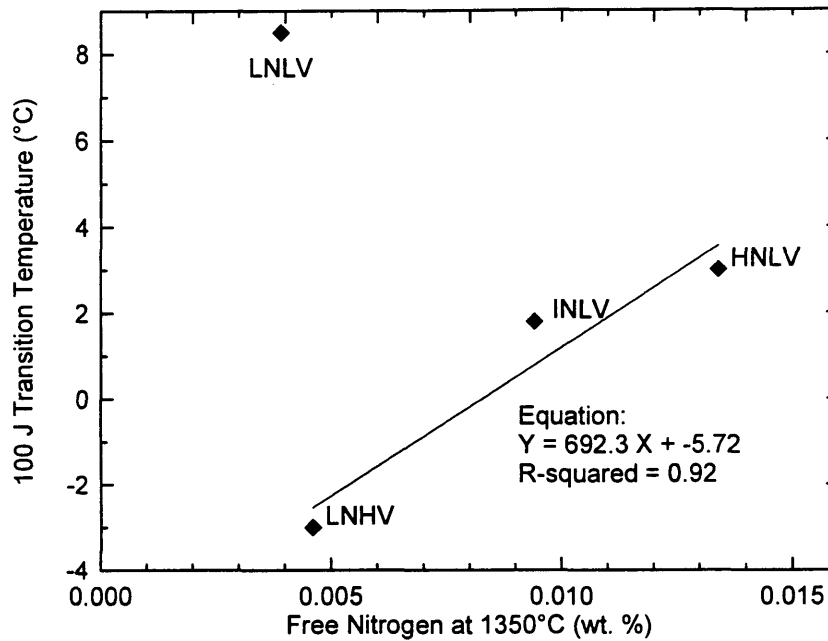
Figure 6.18. Impact transition temperature as a function of calculated free nitrogen at 1350°C.

The correlation between free nitrogen and transition temperature is not quite as strong as was shown for the 1250°C peak temperature specimens, see Figure 6.17, and the slope of the fitted line is lower as well. This decreased correlation coefficient could be a manifestation of the significant scatter observed in the Charpy V-notch testing of the 1350°C peak temperature specimens. The decreased slope of the curve is consistent with the previous discussion of the dislocation density differences between primary ferrite and bainitic microstructures. The materials cycled with a 1350°C peak temperature have higher bainitic microstructure volume fraction, and consequently higher dislocation densities.

Again, more nitrogen is required to saturate the dislocations, decreasing the slope of the

100-J impact transition temperature-free nitrogen curve.

6.4.3 1400°C Peak Temperature Thermal Cycles

Now considering the 1400°C peak temperature thermal cycles, again the transition

temperature for alloys HNLV, INLV, and LNLV are very similar, as well as the effective

ferrite grain size. Not only is ferrite grain size consistent between the alloys, it is

significantly larger than was observed for the two other peak temperatures, excluding alloy

LNLV with the 1350°C peak temperature cycle.

The 1400°C peak temperature specimens are the only ones that exhibit an increase

in transition temperature from alloy HNLV through LNLV. The cause of this increase is

unknown, as none of the measured microstructural parameters follow this trend. However,

the difference between alloy HNLV and LNLV is only approximately 5°C, and is well

within the scatter of the CVN data. Possibly there is no real difference at all.

Another significant difference between the 1400°C peak temperature and the

1350°C peak temperature materials is in the behavior of alloy LNHV. In the 1400°C peak

temperature materials, there is a marked increase in transition temperature between alloy

LNLV and LNHV, contrasting the decrease in transition temperature between these two

alloys in the 1350°C peak temperature condition. This increase can most easily be

explained by the relatively small increase in primary ferrite content, the smallest increase of all the peak temperature conditions, of approximately 4%. As was mentioned previously, it is unlikely that much primary ferrite was nucleated at titanium nitride inclusions when the material was subjected to the 1400°C peak temperature thermal cycle, and therefore cannot counteract the detrimental effect of the large titanium nitride inclusions.

6.4.4 Regression Analysis Revisited

Based on the preceding, more traditional, attempts to reveal the microstructural effects on impact toughness, another regression analysis was performed. This analysis focused on those components shown to significantly affect the toughness for the 1250°C and 1350°C peak temperature thermal cycles. The data from the materials subjected to the 1400°C peak temperature thermal cycles were omitted due to the inability to explain the observed transition temperatures for alloys HNLV through LNLV after that thermal cycle. The results of this modified regression analysis are shown in Table 6.5.

As shown in Table 6.5, the confidence level of the coefficients is greatly increased by the modifications to the regression analysis. It is clear that variables which play significant roles in the impact properties have been chosen. This confidence allows statements to be made regarding the relative effect of the microstructural components on the impact transition temperature.

Table 6.5. Results of modified regression analysis.

Category	Coefficient	Standard Error	t-Statistic
Intercept	13.3	8.7	1.5
Free Nitrogen	41.4	9.9	4.2
Volume Fraction of Large Titanium Nitride Inclusions	43.8	11.5	3.8
("Effective Ferrite Grain Size)$^{-1/2}$	-96.0	13.5	-7.1

As shown in Table 6.5, free nitrogen and titanium nitrides have a similar detrimental role on the transition temperature. However, it must be remembered that it is likely that the magnitude of free nitrogen effect is different for the 1250°C and 1350°C peak temperature thermal cycles due to the microstructural differences and corresponding bainitic content. The effective ferrite grain size was found to have a very significant effect on the transition temperature, with a coefficient greater than twice that observed for the free nitrogen content and titanium nitride inclusion volume fraction.

6.4.5 Summary of Microstructural Effects

Figure 6.19 depicts the effect of titanium nitride inclusion content on the 100-J transition temperature. Shown on the figure is the comparison between alloy LNLV and

LNHV (connected by the lines). Since these two materials have essentially the same free

nitrogen content, differences in transition temperature should result from differences in

ferrite grain size, primary ferrite content, or titanium nitride inclusion content. There are no

appreciable differences in ferrite content or grain size between alloys LNLV and LNHV

when the materials are subjected to 1250°C or 1400°C peak temperature thermal cycles, and

consequently, the increase in titanium nitride inclusion content decreases the toughness.

When the materials are thermally cycled with a peak temperature of 1350°C, primary ferrite

in nucleated intragranularly. This intragranular nucleation increases the primary ferrite

content and reduces the effective ferrite grain size. These two beneficial microstructural

changes override the detrimental effect of more titanium nitride inclusions, and thus, the

transition temperature decreases.
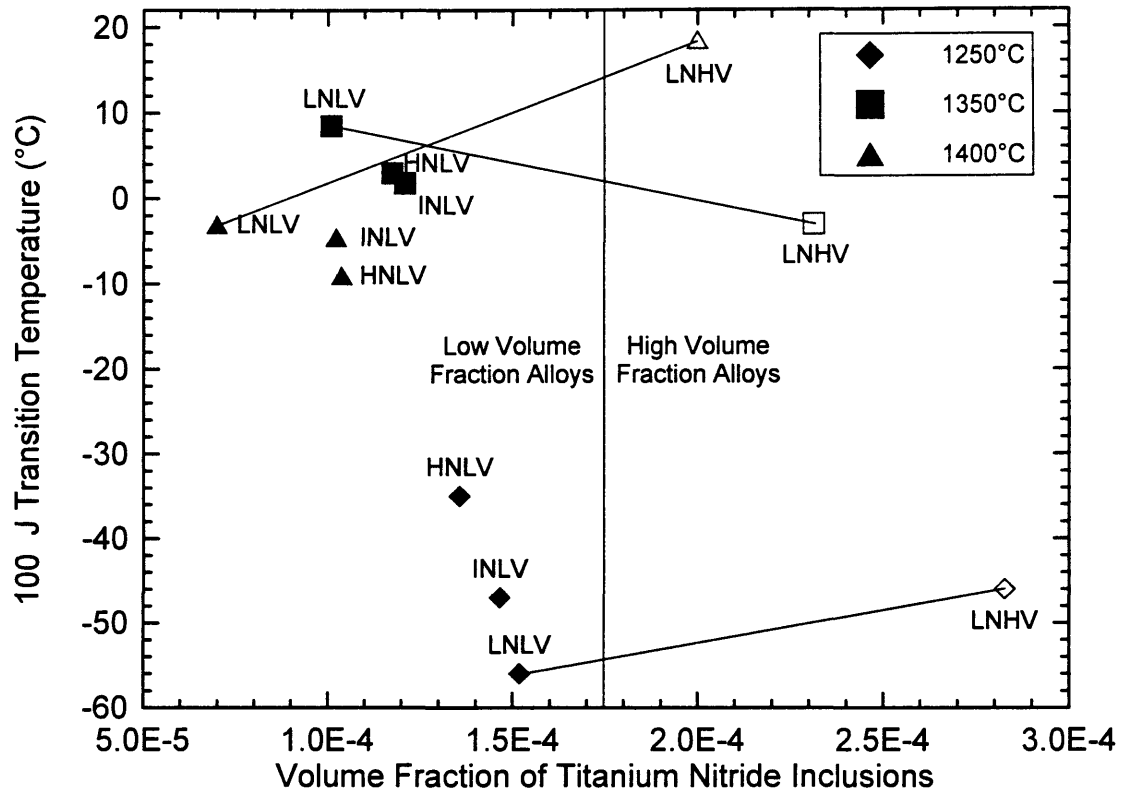
Figure 6.19 Effect of titanium nitride inclusion volume fraction on 100 J transition temperature.

7.0 CONCLUSIONS AND SUMMARY

Four alloys containing (in wt. %) 0.08C, 1.5Mn, 0.2Si, 0.2Ni, 0.025Al and various

levels of titanium and nitrogen were produced as laboratory heats. A Gleeble 1500

thermomechanical test system was used to simulate heat-affected zones of welds, and

different heat inputs and peak temperatures were examined. The main points of this study

are reported below.

1. Impact toughness was measured based on 100-J transition temperatures from Charpy V-

   notch testing, and measured values ranged from approximately 20°C to -55°C.

   However, for a specific thermal cycle (defined by peak temperature and heat input), the

   difference in 100-J transition temperature for the alloys studied was small, typically less

   than about 10°C. Only two cases exceeded this narrow range in transition temperature:

   (a) alloys HNLV through LNLV with a 4-kJ/mm heat input and peak temperature of

   1250°C and (b) alloy LNLV vs. LNHV with a 4-kJ/mm heat input and peak

   temperature of 1400°C.

2. For titanium nitride precipitates smaller than 1 μm, the average size is influenced

   significantly by coarsening during cooling of the original ingot. This statement is

   strongly supported by data collected from the low-volume-fraction alloys, *i.e.*, alloys

   HNLV, INLV, and LNLV. Consistent with this conclusion, the temperature at which

titanium nitride initially forms does not play the key role in determining the relative sizes of precipitates in these alloys. For the high-volume-fraction alloy (LNHV), the average size of the titanium nitride precipitates results from both a high initial precipitation temperature and moderately high coarsening rate.

3. For certain alloy/thermal-cycle conditions, large titanium nitride precipitates provide nucleation sites for primary ferrite. As a result, primary ferrite volume fraction increases, and effective ferrite grain size decreases.

4. The presence of titanium nitride inclusions (*i.e.*, those larger than 1 μm in size) has a direct negative effect on the Charpy V-notch 100-J transition temperature of these alloys; however, these particles have an indirect positive effect via the nucleation of primary ferrite. Specifically, alloys HNLV, INLV, and LNLV have essentially the same volume fraction of titanium nitride inclusions (approximately 5×10^{-5}), resulting in very similar 100-J transition temperatures (approximately 0°C) for the two higher-peak-temperature thermal cycles (*i.e.*, 1350°C and 1400°C). Alloy LNHV has a significantly higher volume fraction of inclusions, at about 2×10^{-4}. Upon comparing alloys with the same free nitrogen content (LNLV vs. LNHV), for a 1250°C peak temperature, the 100-J transition temperature increases only slightly. For a 1400°C peak temperature, this volume fraction difference is associated with an increase in the 100-J transition temperature of about 25°C. For a 1350°C peak temperature, the high volume fraction of titanium nitride inclusions in alloy LNHV is associated with a decrease in the 100-J transition temperature compared with alloy LNLV because of a

notable increase in the primary ferrite volume fraction. The reasons why the titanium

nitride particles are significant in nucleating primary ferrite only for the 1350°C peak

temperature are uncertain.

5. The presence of free nitrogen has a direct negative effect on the Charpy V-notch 100-J

    transition temperature of these alloys. This effect is most evident in comparatively fine

    microstructures, *i.e.*, those generated from thermal simulations with a 1250°C peak

    temperature. Specifically, as the free nitrogen content increases from 0.004% to

    0.012%, the 100-J transition temperature increases by about 20°C. At higher peak

    temperatures, differences in other microstructural features are hypothesized to play

    important roles which tend to mask the free nitrogen contribution.

6. The increased dislocation density associated with a bainitic microstructure (compared to

    primary or polygonal ferrite) appears to decrease the negative effect of free nitrogen

    since the dislocations are too numerous to pin with a limited supply of nitrogen atoms.

    This statement is supported by the classic work of Pickering on ferrite/pearlite steels

    which predicts a larger effect from free nitrogen than has been observed in the present

    study.

7. For the limited range of primary ferrite contents encountered in the current study, the

    presence of this microconstituent has a beneficial effect on the 100-J transition

    temperature.

8. In general, refinement of microstructure provided a beneficial effect on the 100-J

    transition temperature, although the grain-size effect is masked by other contributions

and, therefore, is not as dominant as expected. Specifically, fine austenite grain size is associated with fine ferrite grain size and comparatively small mean-free paths between other microconstituents.

9. For the low-volume-fraction alloys, as free nitrogen level increased, the free titanium level decreased, and, consequently, the coarsening rate of titanium nitride precipitates decreased. The average size of the titanium nitride precipitates (for sizes below 100 nm) correlated directly with the average size of austenite grains produced during simulated welding cycles. Measured austenite grain sizes agreed best with grain sizes predicted from the model by Gladman when a heterogeneity factor of two was assumed.

10. Because of the presence of several competing factors which influence the 100-J transition temperature, there is no one alloy which out-performs the other alloys at all peak temperatures with a heat input of 4 kJ/mm. At a peak temperature of 1250°C, alloy LNLV provides the best performance because of the comparatively low free nitrogen level and low volume fraction of coarse titanium nitride particles. At 1350°C, alloy LNHV benefits significantly from primary ferrite which is nucleated at large titanium nitride particles, while alloy LNLV suffers because of coarse grain size resulting from a comparatively low stability of fine titanium nitride precipitates. The 1400°C peak temperature produces similar performance for all of the low-volume-fraction alloys (HNLV, INLV, and LNLV), whereas the high-volume-fraction alloy (LNHV) is associated with the worst impact properties.

8.0 REFERENCES CITED

1. R. Varughese, A.W. Pense, "Microstructural Development in the Coarse-Grained, Heat-Affected Zone in Titanium-Vanadium Microalloyed HSLA Steels", Materials Characterization, vol. 30, no. 1, pp. 35-43.

2. H. Görrs, H. Krebs, W. Dahl, "Investigations of the Influence of Titanium Addition to the Base Material on Toughness Properties of the HAZ", Steel Research, vol. 63, no. 12, pp. 554-557

3. J.-L. Lee, Y.-T. Pan, "Effect of Killing Time on the Microstructure and Toughness of the Heat-Affected Zone in Ti-Killed Steels", Metallurgical Transactions, vol. 22A, no. 11, 1991, pp. 2818-2822.

4. A.M. Sage, R.C. Cochrane, D. Howse, "The Development of a Normalized Ti Treated Vanadium Steel with Improved HAZ Toughness", *Proceedings of the International Conference on Processing, Microstructure and Properties of Microalloyed and Other Modern High Strength Low Alloy Steels*, ed. by A.J. DeArdo, ISS, Warrendale, PA, pp. 443-460.

5. L.J. Cuddy, J.S. Lally, L.F. Porter, "Improvement of Toughness in the HAZ of High-Heat-Input Welds in Ship Steels", *HSLA Steels: Technology & Applications*, ed. By M. Korchynsky, ASM, Metals Park, OH, 1983, pp. 697-703.

6. K. Easterling, *Introduction to the Physical Metallurgy of Welding*, Second Edition, Butterworth-Heinemann, Oxford, Great Britain, 1992, pp. 130-132.

7. A.J. DeArdo, "An Overview of Microalloyed Steels", *Proceedings of the 8th Process Technology Conference - The Effect of Microalloys on the Hot Working of Ferrous Alloys*, ed. By J.E. Hartman, M. Korchynsky, A.J. DeArdo, ISS, Warrendale, PA, 1988, pp. 67-75.

8.   Y. Tomita, R. Yamaba, K. Okamoto, S Aihara, T. Haze, K. Ito, "Recent Developments in Heavy Section Steel Plates for Offshore Structures", *HSLA Steels: Metallurgy and Applications*, ed. By J.M. Gray, T. Ko, Z. Shouhua, W. Baorong, X. Xishan, ASM, Metals Park, OH, 1985, pp. 641-650.

9.   F.B. Pickering, "Titanium Nitride Technology", *35th MWSP Conference Proceedings*, ISS, Warrendale, PA, 1994, pp. 447-491.

10. C. Zener, Referred to by C.S. Smith, "Grains, Phases, Interfaces: An Interpretation of Microstructure", Transactions AIME, vol. 175, 1948, pg. 15-51.

11. T. Gladman, "On the Theory of the Effect of Precipitate Particles on Grain Growth in Metals", Proceedings of the Royal Society of London - Series A, vol. 294, Oct. 18, 1966, pp. 298-309.

12. T. Gladman, "Grain Refinement in Multiple Microalloyed Steels", *HSLA Steels: Processing, Properties, and Applications*, ed. By G. Tither, S. Zhang, TMS, Warrendale, PA, 1990, pp. 3-14.

13. F.B. Pickering, "The Effect of Composition and Microstructure on Ductility and Toughness", *Toward Improved Ductility and Toughness*, Climax Molybdenum Development Company (Japan) LTD., 1971, pp. 9-31.

14. K. Easterling, "The Heat Affected Zone", Chapter 3, *Introduction to the Physical Metallurgy of Welding*, Second Edition, Butterworth-Heinemann, Oxford, Great Britain, 1992, pp. 126-190.

15. J.M.B. Losz, K.D. Challenger, "HAZ Microstructures in HSLA Steel Weldments", unknown location, pp. 207-223.

16. E. Räsänen, J. Tenkula, "Phase Changes in the Welded Joints of Constructional Steels", Scandinavian Journal of Metallurgy, vol. 1, 1972, pp. 75-80.

17. Ø. Grong, *Metallurgical Modelling of Welding*, The Institute of Metals, London, England, 1994, pg. 406.

18. G. Krauss, S.W. Thompson, "Ferritic Microstructures in Continuously Cooled Low- and Ultralow Carbon Steels", ISIJ International, vol. 35, no. 8, pp. 937-945.

19. "Guide to the Light Microscope Examination of Ferritic Steel Weld Metals", IIW Doc. No. IX-1533-88, IXJ-123-87, Revision 2, 1988, IIW.

20. H.I. Aaronson, W.T. Reynolds, Jr., G.J. Shiflet, G. Spanos, "Bainite Viewed Three Different Ways", Metallurgical Transactions, vol. 21A, no. 6, 1990, pp. 1343-1380.

21. Y. Ohmori, H. Ohtani, T. Kunitake, "The Bainite in Low Carbon Low Alloy High Strength Steels", Transactions ISIJ, vol. 11, 1971, pp. 250-259.

22. B.L. Bramfitt, J.G. Speer, "A Perspective on the Morphology of Bainite", Metallurgical Transactions, vol. 21A, no. 4, 1990, pp. 817-829.

23. H.K.D.H. Bhadesia, J.W. Christian, "Bainite in Steels", Metallurgical Transactions, vol. 21A, no. 4, 1990, pp. 767-797.

24. H. Ohtani, S. Okaguchi, F. Fujishiro, Y. Ohmori, "Morphology and Properties of Low-Carbon Bainites", Metallurgical Transactions, vol. 21A, no. 4, 1990, pp. 887-888.

25. W.T. Reynolds, Jr., H.I. Aaronson, G. Spanos, Mater. Trans. JIM, vol. 32, no. 8, 1991, pg. 737.

26. L.J. Habraken, M. Economopoulos, "Bainitic Microstructures in Low-Carbon Alloy Steels and Their Mechanical Properties", *Transformation and Hardenability in Steels,* Climax Molybdenum Company of Michigan, 1977, pp. 69-106.

27. G.E. Dieter, *Mechanical Metallurgy,* 3rd Edition, McGraw-Hill, New York, NY, 1986, pp. 282-283.

28. G. Krauss, *Steels: Heat Treatment and Processing Principles,* ASM, Metals Park, OH, 1990, pg. 134.

29. A.A. Griffith, "The Phenomena of Rupture and Flow in Solids", Phil. Trans. Roy. Soc. A, vol. 221, 1920, pp. 163-198.

30. G.E. Dieter, *Mechanical Metallurgy,* 3rd Edition, McGraw-Hill, New York, NY, 1986, pp. 243-249.

31. E. Orowan, "Fracture and Strength of Solids", Reports on Progress in Physics, vol. 12, 1948, pp. 185-233.

32. G.E. Dieter, *Mechanical Metallurgy,* 3rd Edition, McGraw-Hill, New York, NY, 1986, pp. 256-259.

33. A.H. Cottrell, "Theory of Brittle Fracture in Steel and Similar Metals", Transactions of the Metallurgical Society of AIME, vol. 212, 1958, pp. 192-203.

34. G.E. Dieter, *Mechanical Metallurgy,* 3rd Edition, McGraw-Hill, New York, NY, 1986, pp. 260-261.

35. W.S. Owen, D.H. Whitmore, M. Cohen, B.L. Averbach, "Relation of Charpy Impact Properties to Microstructure of Three Ship Steels", Welding Research Supplement, vol. 36, no. 11, 1957, pp. 503s-511s.

36. D. Tian, L.P. Karjalainen, B. Qian, X. Chen, "Correlation Between Microstructural Features of Granular Bainite, Roughness of Fracture Surface and Toughness of Simulated CGHAZ in QT Type HSLA Steels", Scandinavian Journal of Metallurgy, vol. 25, no. 2, 1996, pp. 87-94.

37. D.P. Fairchild, D.G. Howden, W.A.T. Clark, "Cleavage Initiation in Ti Microalloyed Steels", *High Performance Steels for Structural Applications,* ed. by. R. Asfahani ASM, Metals Park, OH, 1995, pp. 235-246.

38. M.A. Linaza, J.L. Romero, I. San Martin, J.M. Rodriguez-Ibabe, J.J. Urcola, "Improvement of Toughness by Stopping Brittle Processes Nucleated in Ceramic Particles Through Thermomechanically Optimised Microstructures in Engineering Steels", *Fundamentals and Applications of Microalloying Forging Steels,* TMS, Warrendale, PA, 1996, pp. 311-325.

39. D.P. Fairchild, "A Study Concerning the Heat Affected Zone Toughness of Microalloyed Steels", Ph.D. Dissertation, The Ohio State University, 1995, pp. 205-207.

40. P. Bernasovsky, F. Matsuda, Z. Li, K. Ishihara, "The Effect of M-A Structural Constituent on Notch Toughness of the Heat-Affected Zone", Welding Research Abroad, vol. XXXIX, no 1, 1993, pp. 24-30.

41. C.L. Davis, J.E. King, "Cleavage Initiation in the Intercritically Reheated Coarse-Grained Heat-Affected Zone: Part I. Fractographic Evidence", Metallurgical Transactions vol. 25A, no. 3, 1994, pp. 563-573.

42 G. Krauss, "Heat Treated Martensitic Steels: Microstructural Systems for Advanced Manufacture", ISIJ International, vol. 35, no. 4, 1995, pp. 349-359.

43. C.L. Davis and J.E. King, "Effect of Cooling Rate on Intercritically Reheated Microstructure and Toughness in High Strength Low Alloy Steel", Materials Science and Technology, vol. 9, no. 1, 1993, pp. 8-15.

44. O.M. Akselsen, Ø. Grong, J.K. Solberg, "Structure-property relationships in intercritical heat affected zone of low-carbon microalloyed steels", Materials Science and Technology, vol. 3, no. 8, 1987, pp. 649-655.

45. T.J. George, J.J. Irani, "Control of Austenite Grain Size by Additions of Titanium", Journal of the Australian Institute of Metals, vol. 13, 1968, pp. 94-106.;

46. S. Matsuda, N. Okumura, "Effect of Distribution of TiN Precipitate Particles on the Austenite Grain Size of Low Carbon Alloy Steels, Transactions ISIJ, vol. 18, 1978, pp. 198-205.

47. M. Hillert, "On the Theory of Normal and Abnormal Grain Growth", Acta Materialia, vol. 13, no. 3, 1965, pp. 227-238.

48. L.A. Leduc, C.M. Sellars, "Hot Rolling of C-Mn-Ti Steel", Thermomechanical Processing of Microalloyed Austenite, ed. by A.J. DeArdo, G.A. Ratz, P.J. Wray, AIME, Warrendale, PA, 1981, pp. 641-654.

49. D.B. McCutcheon, J.T. McGrath, M.J. Godden, G.E. Ruddle, J.D. Embury, "The Effect of Microalloy Additions on the Heat Affected Zone Notch Toughness of C-Mn-Mo Line Pipe Steels", HSLA Steels Technology & Applications, ed. by M. Korchynsky, ASM, Metals Park, OH, 1983, pp. 881-896.

50. J.M. Sawhill, P. Boussel, J.W. Morrow, "Heat-Affected-Zone Toughness of High-Heat-Input HSLA Welds", Welding of HSLA (Microalloyed) Structural Steels, ed. by A.B. Rothwell, J.M. Gray, ASM, Metals Park, OH, 1976, pp. 235-256.

51. R.E. Dolby, "Advances in the Welding Metallurgy of Steel", *Advances in the Physical Metallurgy and Applications of Steels,* The Metals Society, London, England, 1981, pp. 111-125.

52. D.A. Porter, K.E. Easterling, *Phase Transformations in Metals and Alloys,* Second Edition, Chapman and Hall, London, England, 1992, pp. 314-316.

53. C.Z. Wagner, "Theorie der Alterung von Niedershlägen durch Umlösen (Ostwald-Reifung)", Z. Elektrochem., vol. 65, 1961, pg. 581.

54. H. Zou, J.S. Kirkaldy, "Carbonitride Precipitate Growth in Titanium/Niobium Microalloyed Steels", Metallurgical Transactions, vol. 22a, 1991, pp. 1511-1524.

55. E. Turkdogan, "Causes and Effects of Nitride and Carbonitride Precipitation During Continuous Casting", Iron and Steelmaker, vol. 16, no. 5, 1989, pp. 61-75.

56. K. Narita, "Physical Chemistry of the Groups Iva (Ti,Zr), Va (V, Nb, Ta) and the Rare Earth Elements", Transactions ISIJ, vol. 15, 1975, pp. 145-152.

57. C.M. Sellars, J.H. Benyon, "Microstructural Development During Hot Rolling of Titanium Microalloyed Steels", *High Strength Low Alloy Steels,* ed. by D.P. Dunne, T. Chandra, AIME and Australasian Institute of Metals, August 1984, pp. 142-150.

58. M. Korchynsky, "Microalloying and Thermomechanical Treatment", *Processing Microstructure and Properties of HSLA Steels,* ed. by A.J. DeArdo, TMS, Warrendale, PA, 1988, pp. 169-201.

59. W. Roberts, "Recent Innovations in Alloy Design and Processing of Microalloyed Steels", *HSLA Steels - Technology & Applications,* ASM, Metals Park, OH, 1983, pp. 33-65.

60. Houghton, G.C. Weatherly, J.D. Embury, "Characterization of Carbonitrides in Ti Bearing HSLA Steel", *Thermomechanical Processing of Microalloyed Austenite,* ed. A.J. DeArdo, G.A. Ratz, P.J. Wray, AIME, Warrendale, PA, August 1981, pp. 267-292.

61. S. Zajac, T. Siwecki, B. Hutchinson, M. Attlegard, "Recrystallization Controlled Rolling and Accelerated Cooling for High Strength and Toughness in V-Ti-N Steels", Metallurgical Transactions, vol. 22a, 1991, pp. 2681-2694.

62. H. Adrian, F.B. Pickering, "Effect of Titanium Additions on Austenite Grain Growth Kinetics of Medium Carbon V-Nb Steels Containing 0.008-0.018% N", Material Science and Technology, vol. 7, no. 2, 1991, pp. 176-182.

63. S. Zajac, T. Siwecki, L.-E. Svensson, "The Influence of Plate Production Processing Route, Heat Input and Nitrogen on the HAZ Toughness in Ti-V Microalloyed Steel", *Proceedings of the International Conference on Processing, Microstructure and Properties of Microalloyed and Other Modern High Strength Low Alloy Steels*, ed. by A.J. DeArdo, ISS, Warrendale, PA, pp. 511-523.

64. S.R. Chen, S.-C. Wang, R.-I. Hsieh, "The Development of High Strength Low Alloy Steel Plates Suitable for High Heat Input Welding", *Proceedings of the International Conference on Processing, Microstructure and Properties of Microalloyed and Other Modern High Strength Low Alloy Steels*, ed. by A.J. DeArdo, ISS, Warrendale, PA, 1992, pp. 435-441.

65. P.E. Reynolds, "Effect of Titanium Treatment on Grain Size Control in Low Alloy Steels", Ironmaking and Steelmaking, vol. 18, no. 1, 1991, pp. 52-58.

66. L. Meyer, F. Heisterkamp, W. Mueschenborn, A. Thyssen-Huette, "Columbium, Titanium, and Vanadium in Normalized, Thermomechanically Treated and Cold-Rolled Steels", *Microalloying '75*, Union Carbide, New York, NY, 1977, pp. 153-167.

67. Loberg, A. Nordgren, J. Strid, K.E. Easterling, "The Role of Alloy Composition on the Stability of Nitrides in Ti-Microalloyed Steels During Weld Thermal Cycles", Metallurgical Transactions, vol. 15A, 1984, pp. 33-41.

68. Okaguchi, T. Hashimoto, "Characterization of Precipitation and Mechanical Properties in Ti Bearing HSLA Steels", Transactions ISIJ, vol. 27, 1987, pp. 467-473.

69. Suzuki, G.C. Weatherly, D.C. Houghton, "The Response of Carbo-Nitride Particles in HSLA Steels to Weld Thermal Cycles", Acta Materialia, vol. 35, no. 2, 1987, pp. 341-352.

70. Weixun, X.Diepei, A. Liege, F. Zemin, Z. Xiaogang, "The Effect of Combined Addition of Niobium and Titanium on Low Carbon-Manganese Steel (First Report)", *Microalloyed HSLA Steels, Proceedings of Microalloying '88*, ASM, Metals Park, OH, pp. 521-531.

71. D.A. Porter, K.E. Easterling, *Phase Transformations in Metals and Alloys,* Second Edition, Chapman and Hall, London, England, 1992, pp. 338-344.

72. G. Krauss, *Steels: Heat Treatment and Processing Principles,* ASM, Metals Park, OH, 1990, pp. 10-15.

73. N. Shams, "Effect of Nitrogen on Transformation Kinetics and Microstructure in Low Carbon Niobium Containing Steels", ISS Transactions, vol. 14, 1993, pp. 51-57.

74. G. Krauss, *Steels: Heat Treatment and Processing Principles,* ASM, Metals Park, OH, 1990, pg. 179.

75. *Handbook of Chemistry and Physics,* 65th Edition, CRC Press, 1984.

76. "Specifications for Steel Plates, Quenched-and-Tempered, for Offshore Structures", API Specification 2Y, Second Edition, July 1, 1990, American Petroleum Institute, Washington, DC.

77. M. Kumar, private communication, 1993.

78   T. Davis, "Austenite Grain-Coarsening Behavior and Precipitate Dispersions in Ti-Nb-Containing Modified-HSLA-80 Steels Produced by Ingot-Casting and Continuous-Casting", M.S. Thesis, Colorado School of Mines, 1995, pg. 49.

79. B. Kloberdanz, "Austenite Transformation Behavior and Structure/Property Relationships in Low-Carbon Copper-Containing Forging Steels", M.S. Thesis, Colorado School of Mines, 1992, pg. 43.

80. G. Herdan, *Small Particle Statistics,* Elsevier, Amsterdam, Netherlands, 1953, pg. 111.

81. G.F. Vander Voort, *Metallography Principles and Practice,* McGraw-Hill, New York, NY, New York, NY, 1984, pg. 426.

82. K.W. Andrews, "Empirical Formulae for the Calculation of Some Transformation Temperatures", JISI, vol. 203, 1965, pp. 721-727.

83. W.C. Leslie, *The Physical Metallurgy of Steels,* Hemisphere Publishing Corporation, 1981, pg. 202.

84. G. Krauss, private communication, Colorado School of Mines, January 13, 1997.

85. J.C. Ion, K.E. Easterling, M.F. Ashby, "A Second Report on Diagrams of Microstructure and Hardness for Heat-Affected Zones in Welds", Acta Materialia, vol. 32, no. 11, 1984, pp. 1949-1962.

86. P. Shewmon, *Diffusion in Solids*, Second Edition, TMS, Warrendale, PA, 1989, pg. 74.

87. Ø. Grong, *Metallurgical Modelling of Welding*, The Institute of Materials, London, England, 1994, pp. 314-316.

88. *Handbook of Chemistry and Physics*, 65th Edition, CRC Press, 1984.

89. D.A. Porter, K.E. Easterling, *Phase Transformations in Metals and Alloys*, Second Edition, Chapman & Hall, London, England, 1992, pg. 147.

90. J.L. Lee, "Evaluation of the Nucleation Potential of Intragranular Acicular Ferrite in Steel Weldments", Acta Materialia, vol. 42, no. 10, 1994, pp. 3291-3298.

91. Ø. Grong, A.O. Kluken, H.K. Nylund, A.L. Dons, J. Hjelen, "Catalyst Effects in Heterogeneous Nucleation of Acicular Ferrite", Metallurgical Transactions A, vol. 26A, no. 3, 1995, pp. 525-534.

92. S.St.-Laurent, G. L'Espérance, "Effects of Chemistry, Density and Size Distribution of Inclusions on the Nucleation of Acicular Ferrite of C-Mn Steel Shielded-Metal-Arc-Welding Weldments", Materials Science and Engineering, vol. 149A, no. 2, 1992, pp. 203-216.

93. F.J. Barbaro, P. Krauklis, K.E. Easterling, "Formation of Acicular Ferrite at Oxide Particles in Steels", Materials Science and Technology, vol. 5, no. 11, 1989, pp. 1057-1068.

94. Ø. Grong, *Metallurgical Modelling of Welding*, The Institute of Materials, London, England, 1994, pg. 428.

95. Ø. Grong, D.K. Matlock, "Microstructural Development in Mild and Low-Alloy Steel Weld Metals", International Metals Reviews, vol. 31, no. 1, 1986, pp. 27-48.

96. S. Liu, D.L. Olson, "The Role of Inclusions in Controlling HSLA Steel Weld Microstructures", Welding Journal, vol. 65, no.6, 1986, pp. 139s-149s.

97. C.J. Van Tyne, private communication, December, 1996.

98. S.W. Thompson, D.J. Colvin, G. Krauss, "Continuous Cooling Transformations and Microstructures in a Low-Carbon, High-Strength Low-Alloy Plate Steel", Metallurgical Transactions, vol. 21A, no. 6, 1990, pp. 1493-1507.

99. N.E. Hannerz, "Weld Metal and HAZ Toughness and Hydrogen Cracking Susceptibility of HSLA steels Influenced by Nb, Al, V, Ti, and N", *Proceedings from Rome Conference on Welding of HSLA (Microalloyed) Structural Steels*, 1976, pp. 365-385.

9.0 APPENDIX A

As-Quenched-and-Tempered Microstructures

a)

b)

c)

30μm
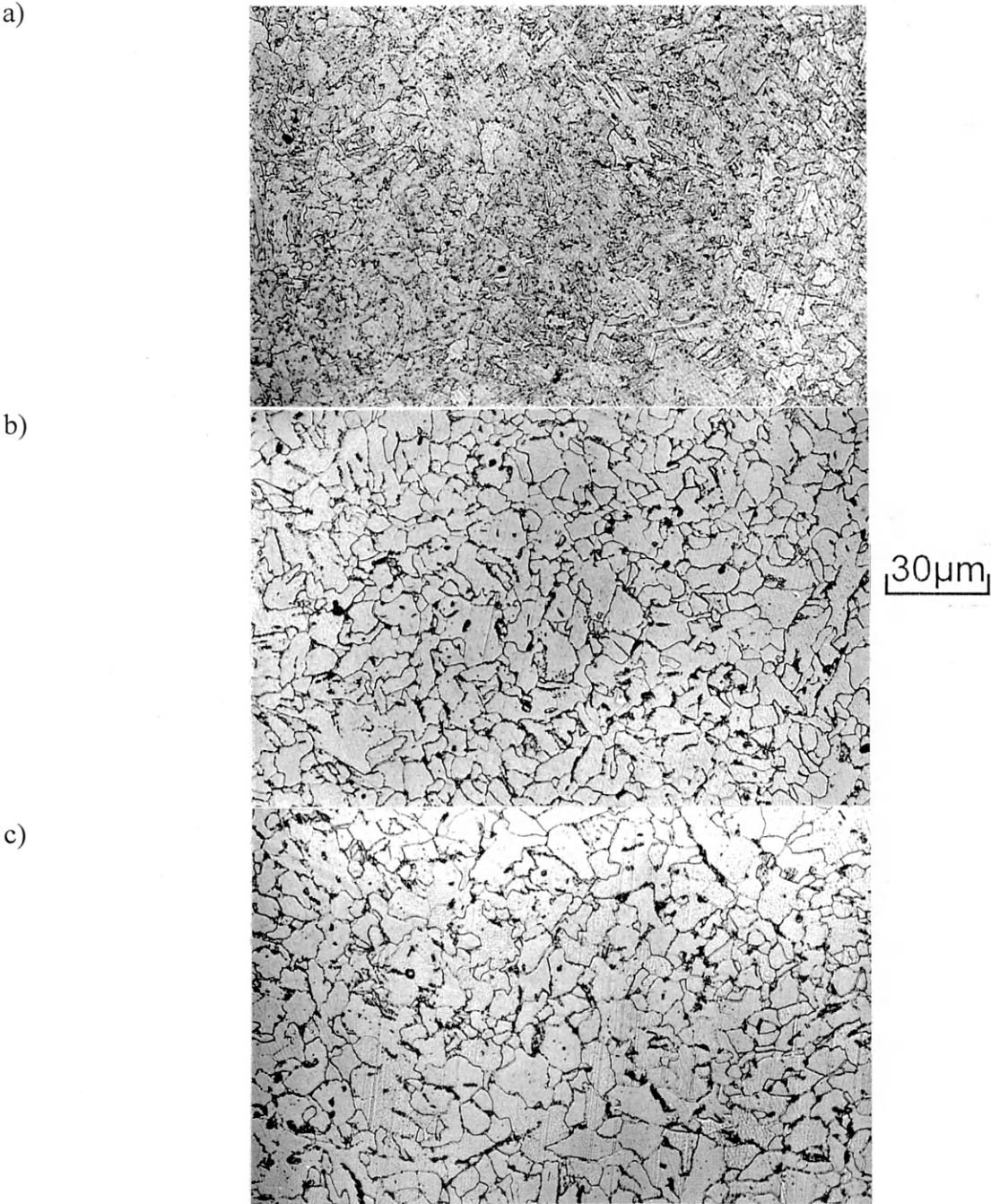
Figure 9.1.   Photomicrographs of as-quenched-and-tempered material. Alloy INLV a)
Near surface. b) 1/4-thickness. c) Mid-thickness. 500x. Nital etch.
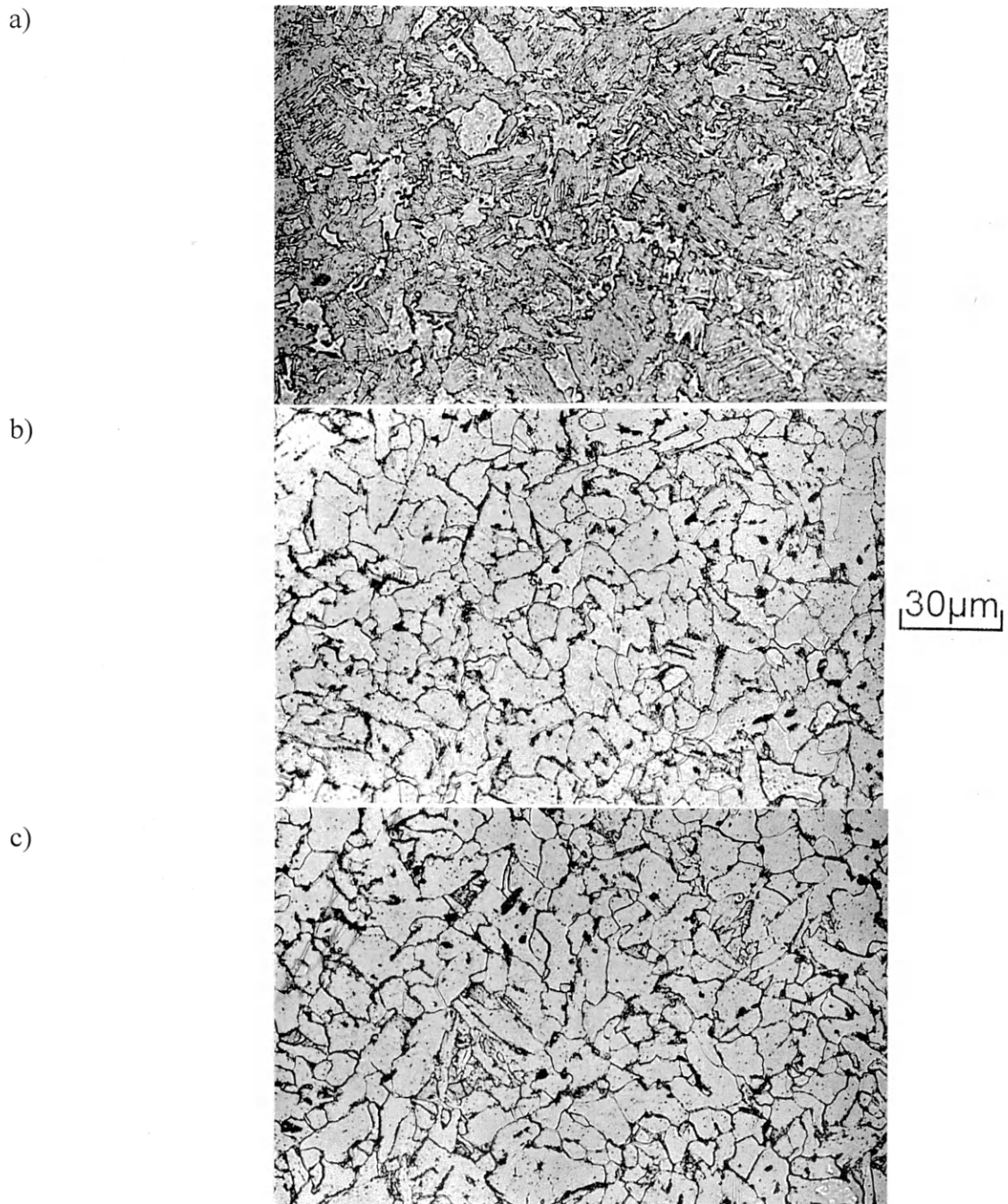
Figure 9.2. Photomicrographs of as-quenched-and-tempered material. Alloy LNLV a) Near surface. b) 1/4-thickness. c) Mid-thickness. 500x. Nital etch.

a)

b)

c)
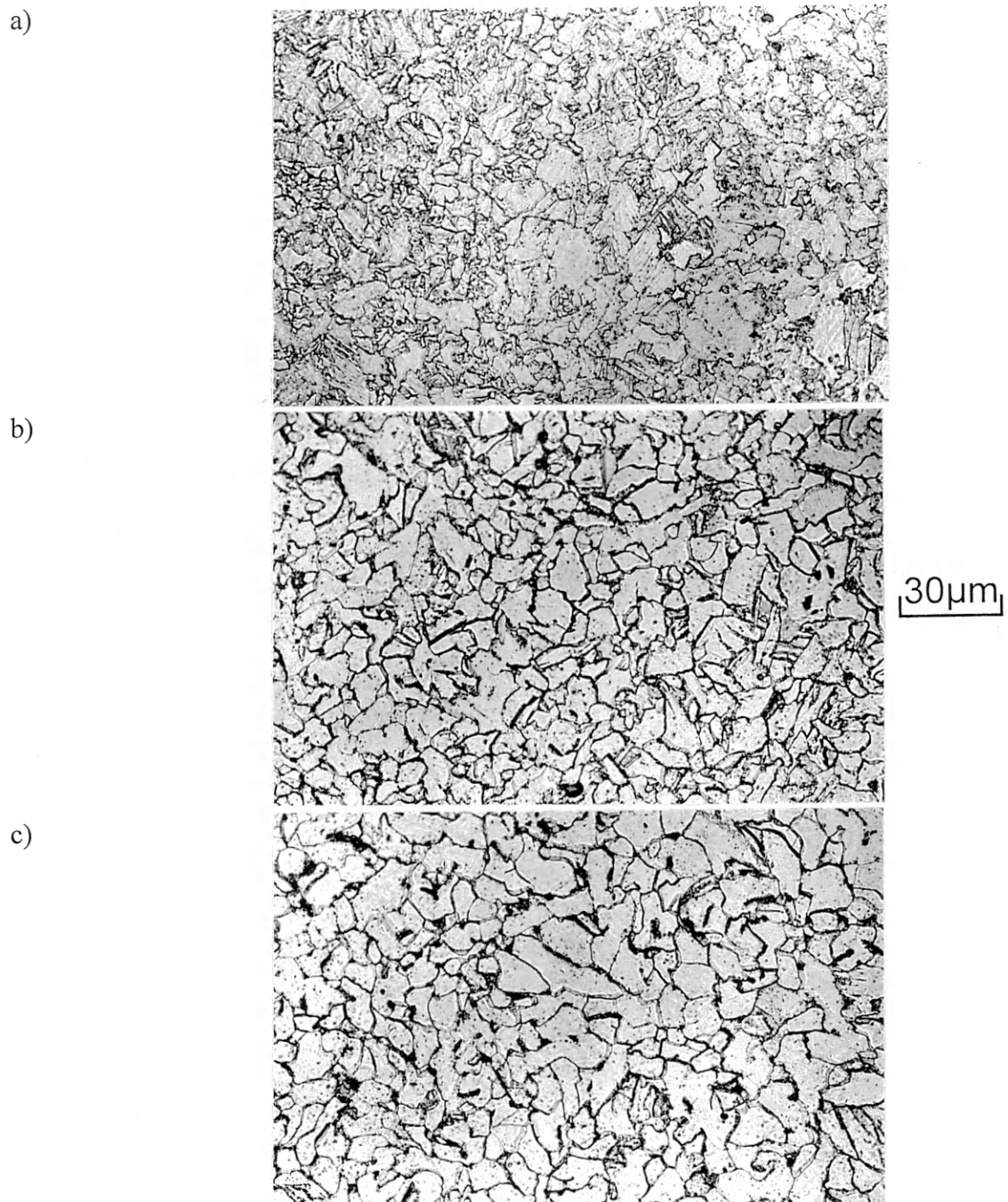
Figure 9.3. Photomicrographs of as-quenched-and-tempered material. Alloy LNHV a) Near surface. b) 1/4-thickness. c) Mid-thickness. 500x. Nital etch.

10.0 APPENDIX B

Charpy V-Notch Transition Temperature Curves for Thermally-Cycled Materials
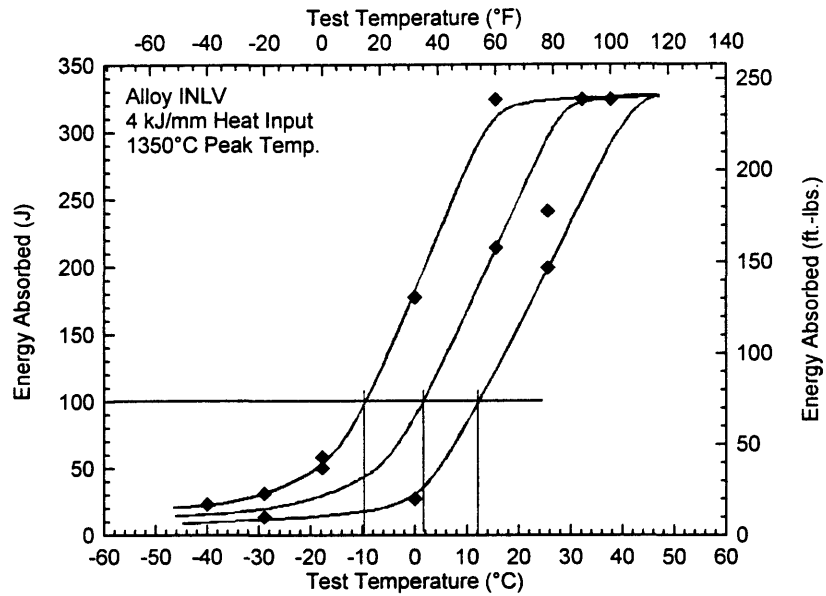
Figure 10.1. Charpy V-notch transition curve for alloy INLV. 4 kJ/mm heat input. 1350°C peak temperature.
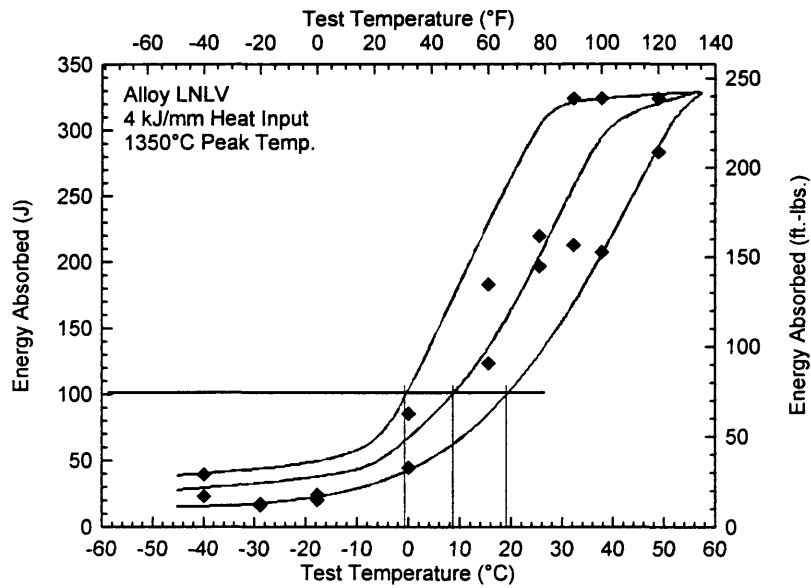
Figure 10.2. Charpy V-notch transition curve for alloy LNLV. 4 kJ/mm heat input. 1350°C peak temperature.
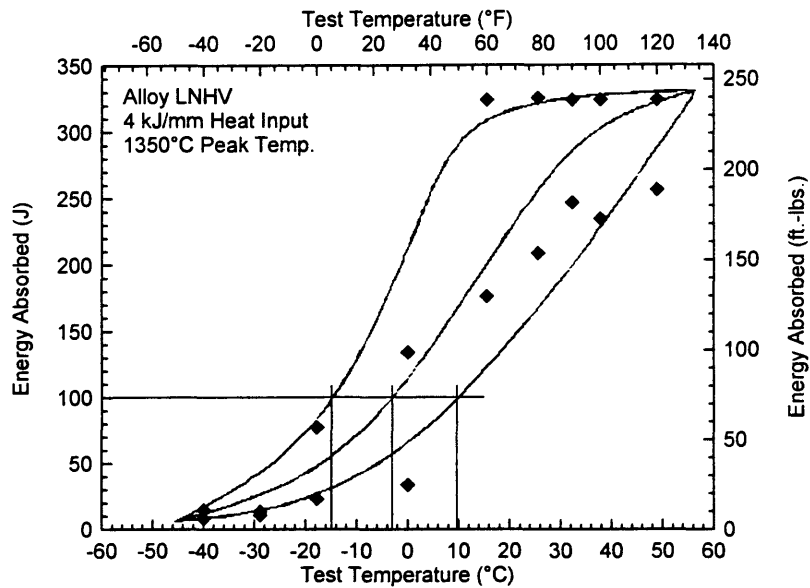
Figure 10.3. Charpy V-notch transition curve for alloy LNHV. 4 kJ/mm heat input. 1350°C peak temperature.
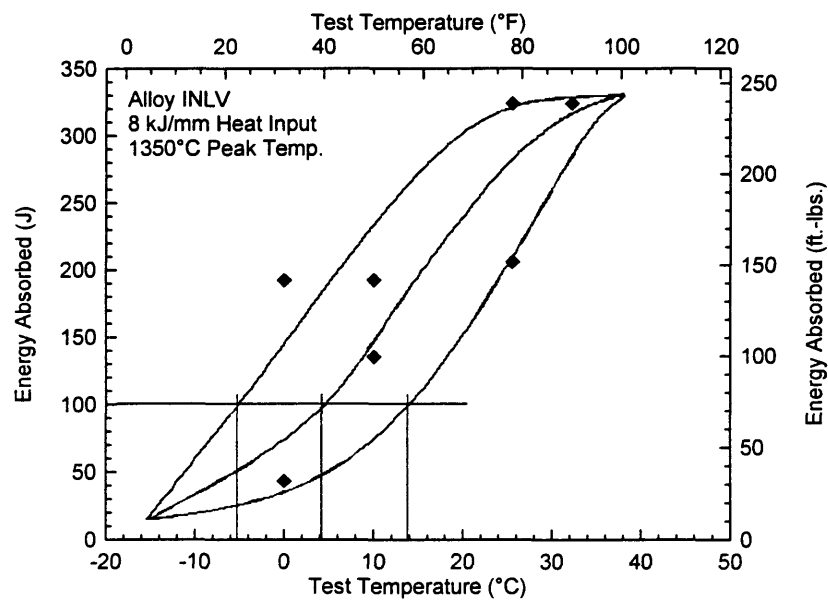
Figure 10.4. Charpy V-notch transition curve for alloy INLV. 8 kJ/mm heat input. 1350°C peak temperature.
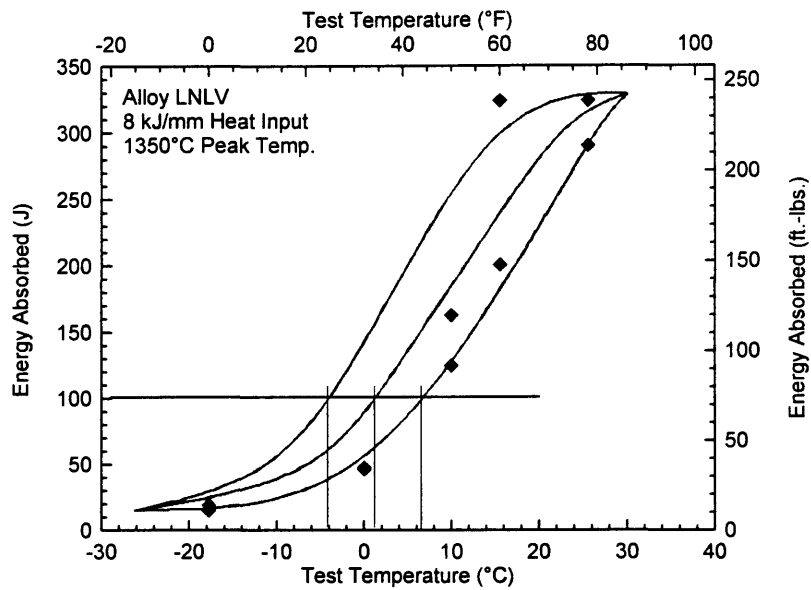
Figure 10.5. Charpy V-notch transition curve for alloy LNLV. 8 kJ/mm heat input. 1350°C peak temperature.
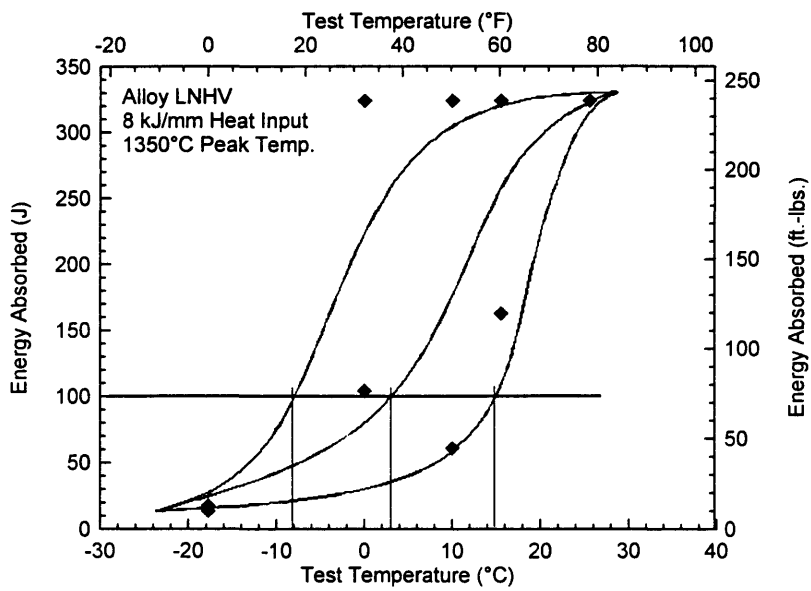
Figure 10.6. Charpy V-notch transition curve for alloy LNHV. 8 kJ/mm heat input. 1350°C peak temperature.
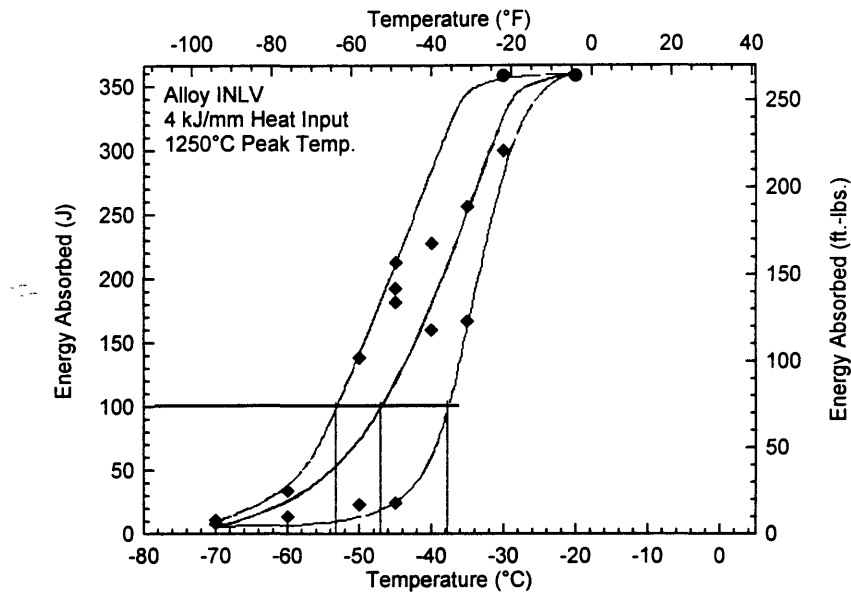
Figure 10.7. Charpy V-notch transition curve for alloy INLV. 4 kJ/mm heat input. 1250°C peak temperature.
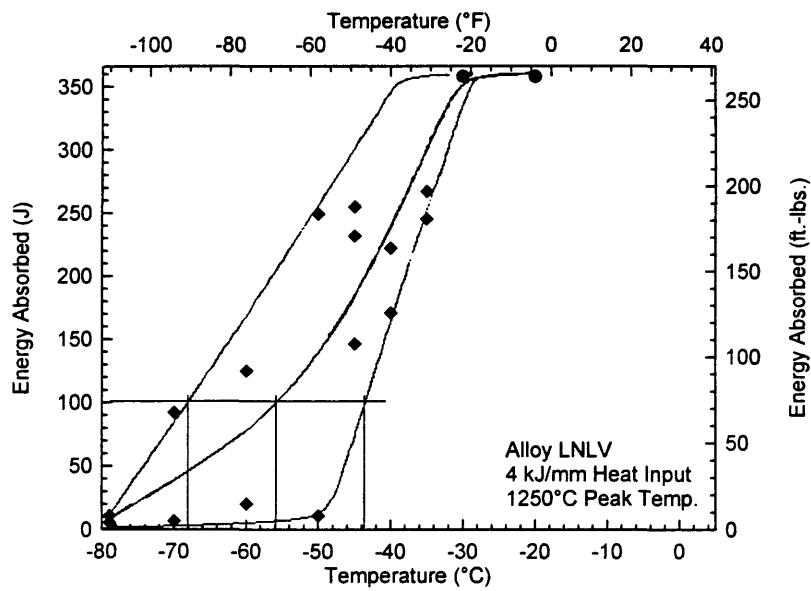
Figure 10.8. Charpy V-notch transition curve for alloy LNLV. 4 kJ/mm heat input. 1250°C peak temperature.
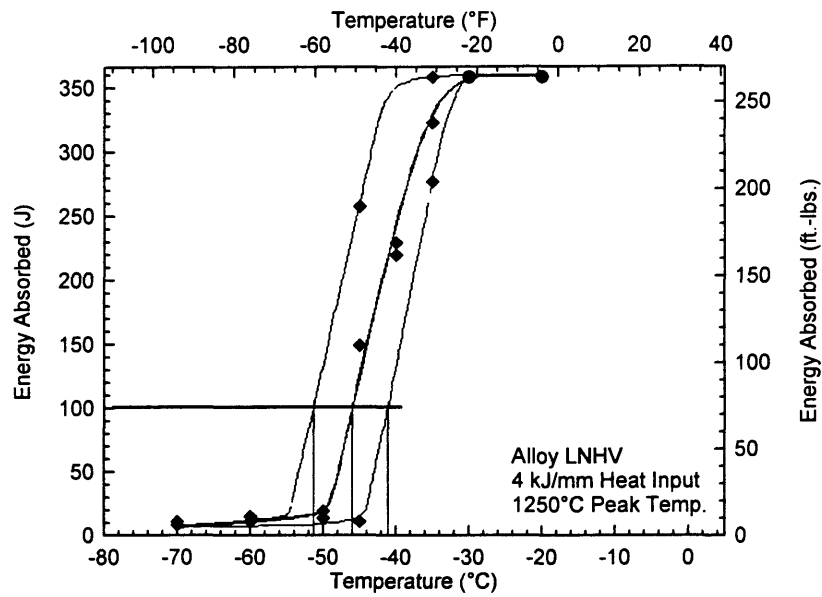
Figure 10.9. Charpy V-notch transition curve for alloy LNHV. 4 kJ/mm heat input. 1250°C peak temperature.
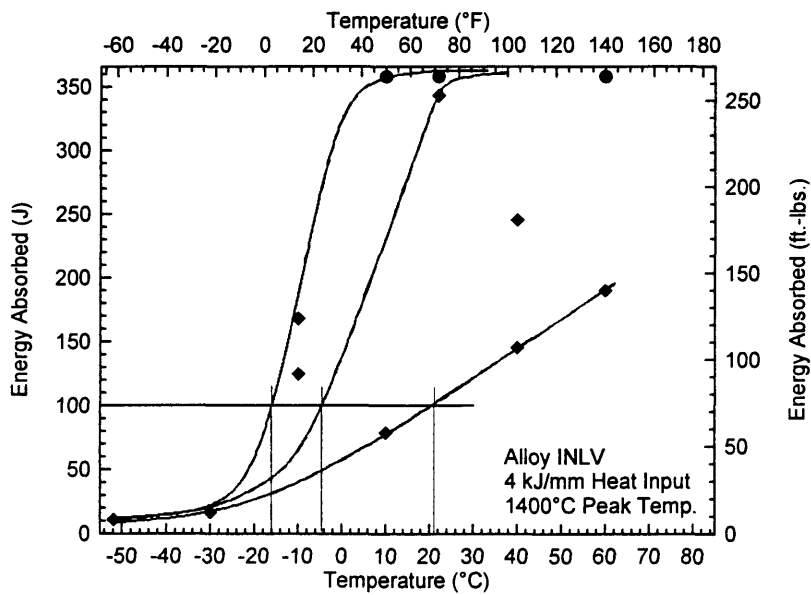
Figure 10.10.Charpy V-notch transition curve for alloy INLV. 4 kJ/mm heat input. 1400°C peak temperature.
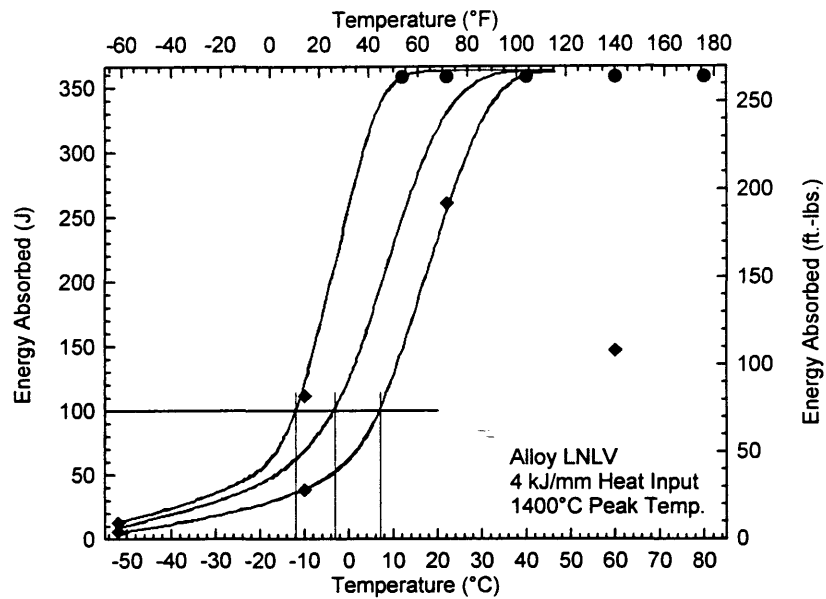
Figure 10.11. Charpy V-notch transition curve for alloy LNLV. 4 kJ/mm heat input. 1400°C peak temperature.
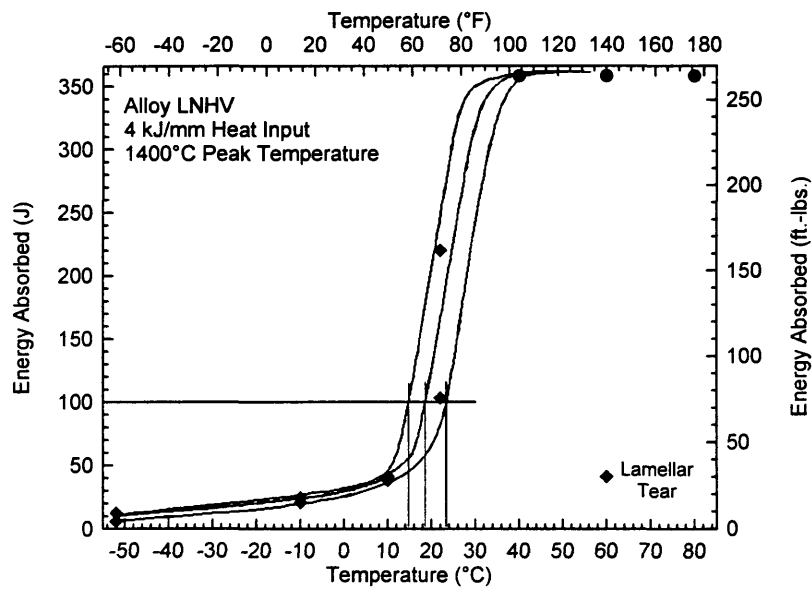
Figure 10.12. Charpy V-notch transition curve for alloy LNHV. 4 kJ/mm heat input. 1400°C peak temperature.
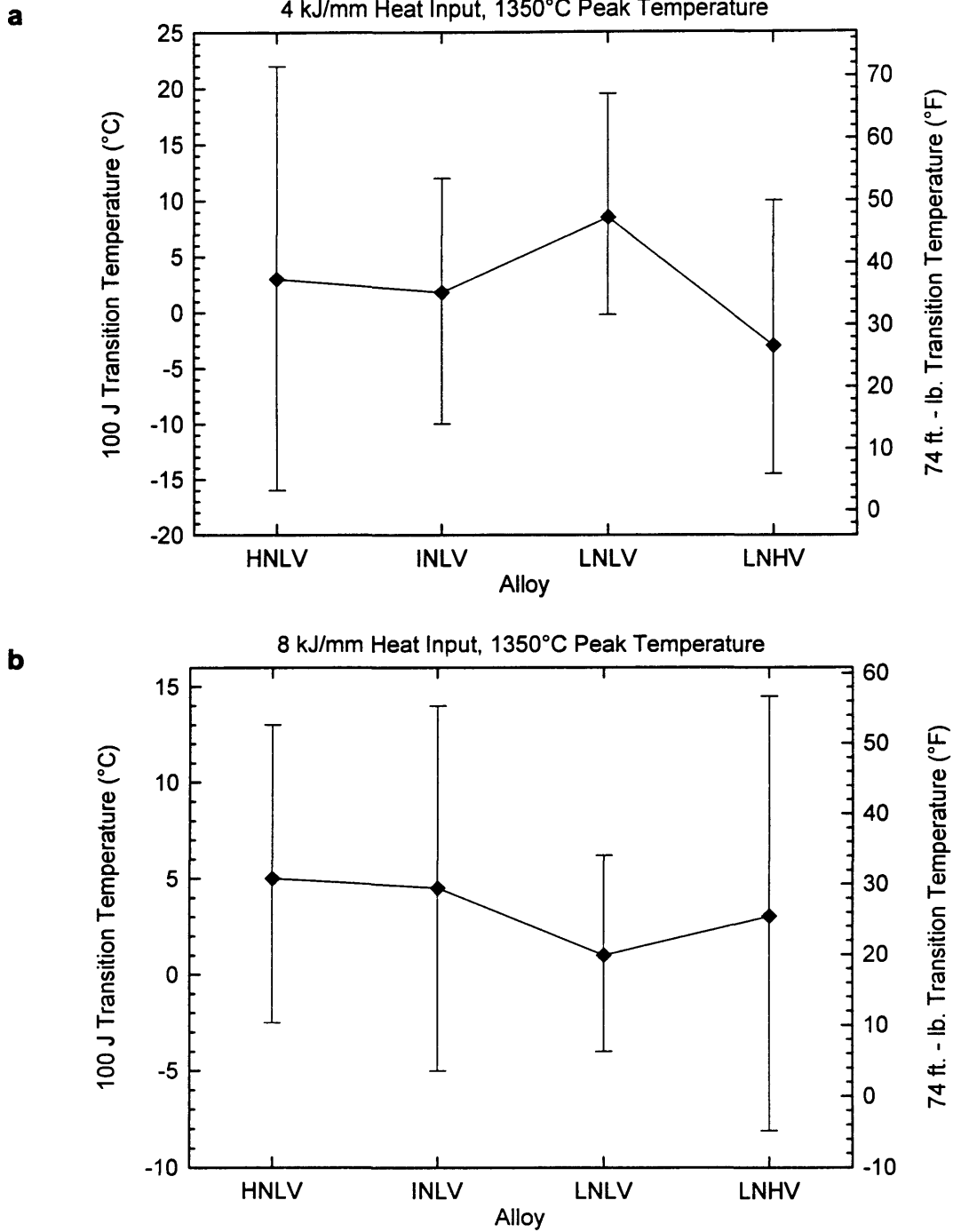
Figure 10.13.100 J transition temperature for material subjected to a) 4 kJ/mm heat input and b) 8 kJ/mm heat input, 1350°C peak temperature thermal cycle.
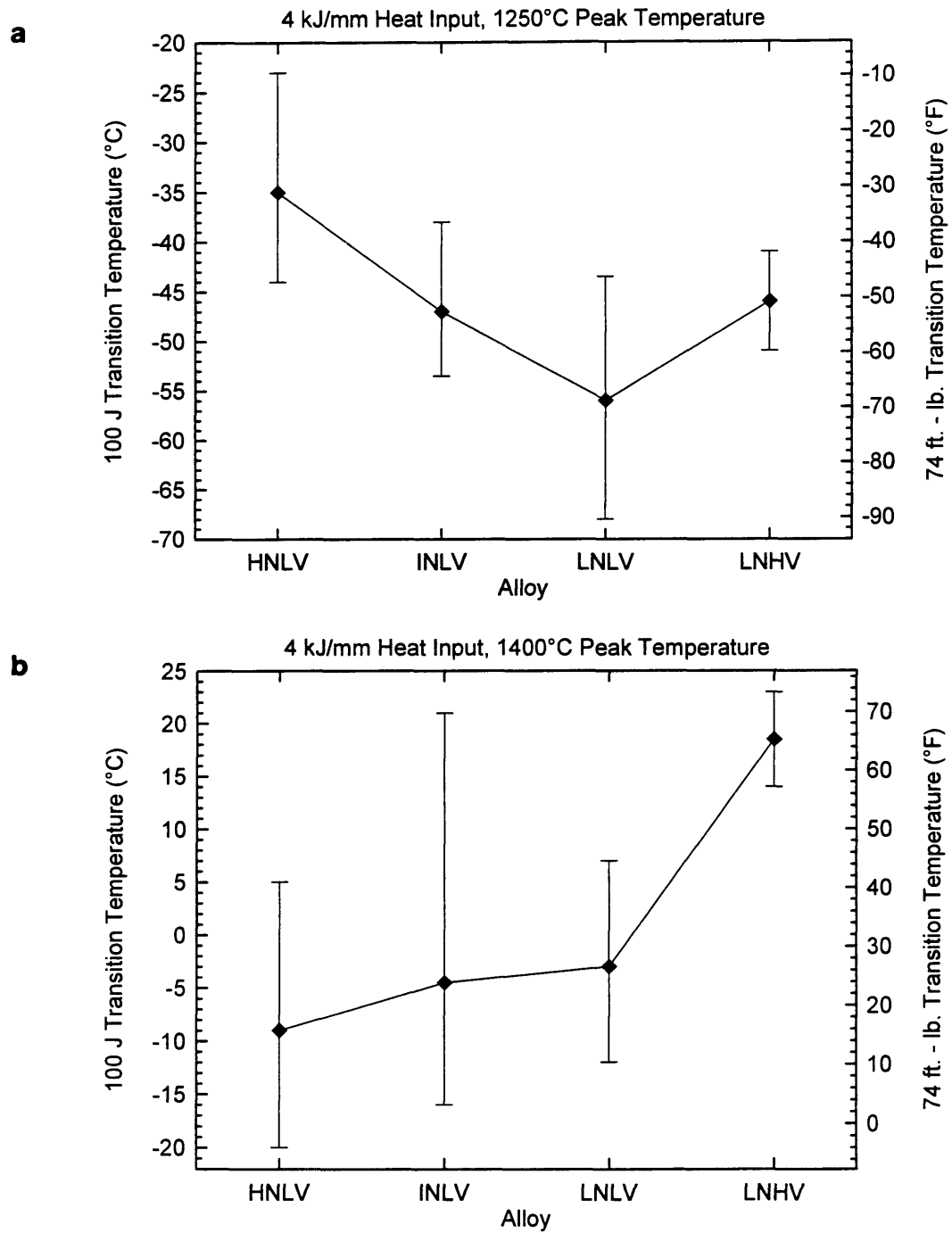
Figure 10.14. 100 J transition temperature for material subjected to 4 kJ/mm heat input thermal cycles. a) 1250°C peak temperature. b) 1400°C peak temperature.

11.0 APPENDIX C

Hardness of Thermally-Cycled Materials
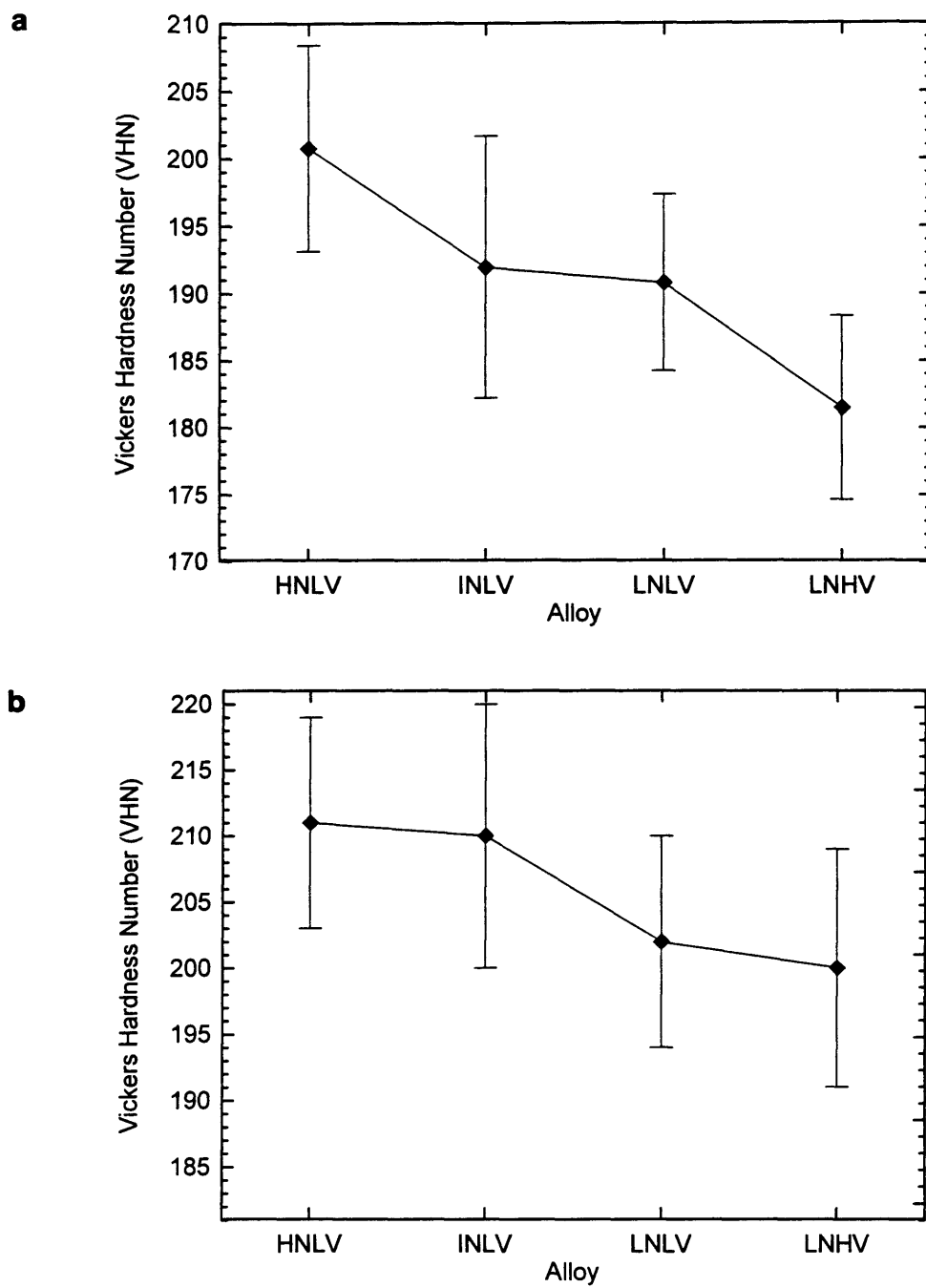
Figure 11.1. Hardness of material cycled with 4 kJ/mm heat input. a) 1250 peak
temperature. b) 1350°C peak temperature. Error bars are standard
deviation.
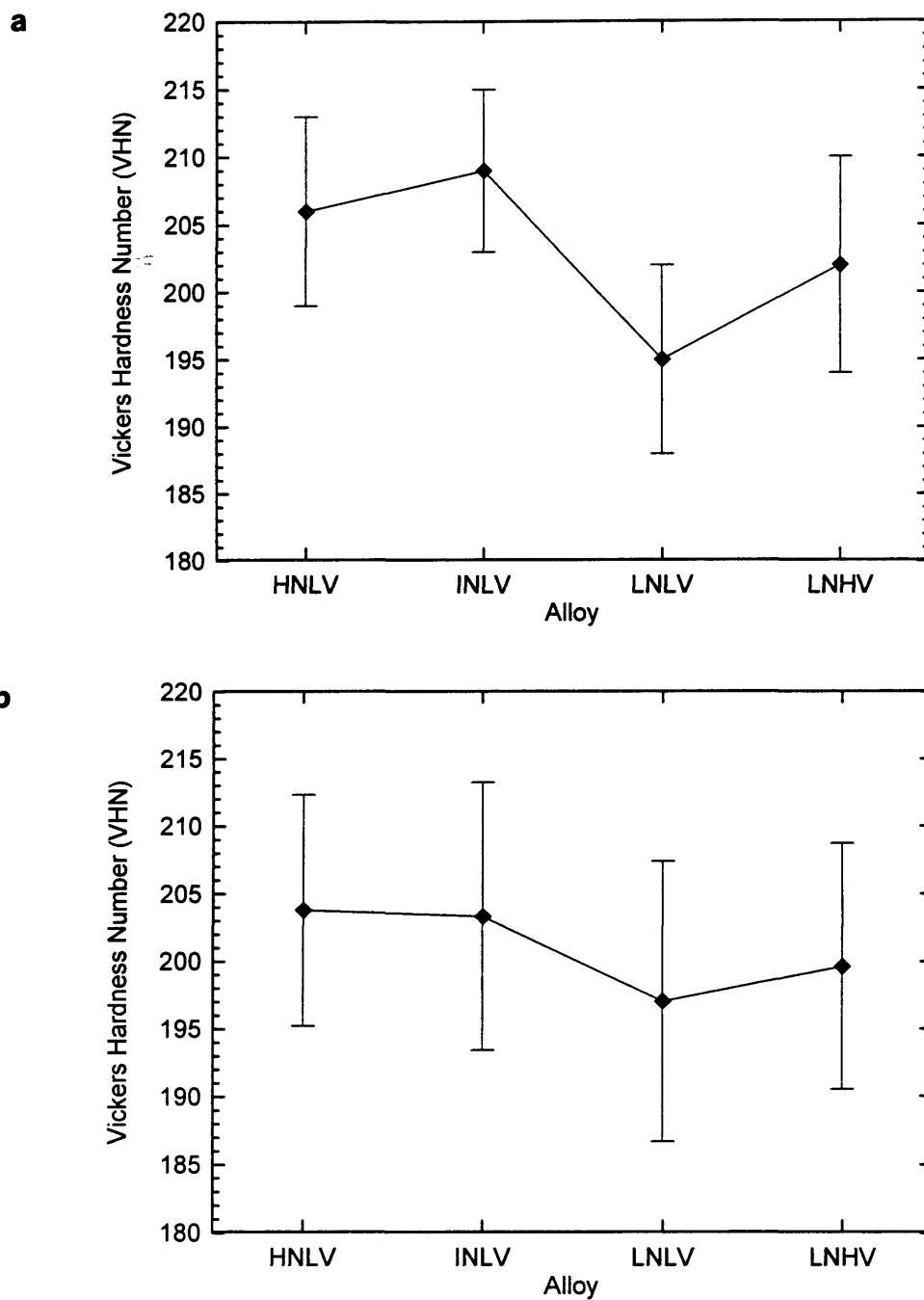
Figure 11.2. Hardness of material cycled with a) 8 kJ/mm heat input - 1350°C peak
temperature and b)4 kJ/mm heat input - 1400°C peak temperature. Error
bars are standard deviation.

12.0 APPENDIX D

Quantitative Analysis of Microstructure for Thermally-Cycled Materials
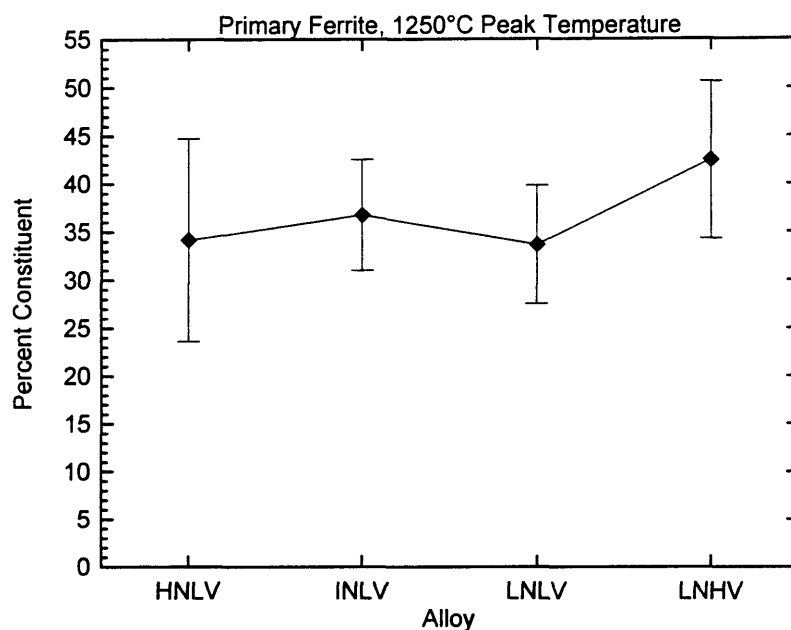
Figure 12.1. Volume fraction of primary ferrite for material thermally-cycled with a 1250°C peak temperature. Error bars are standard deviation.
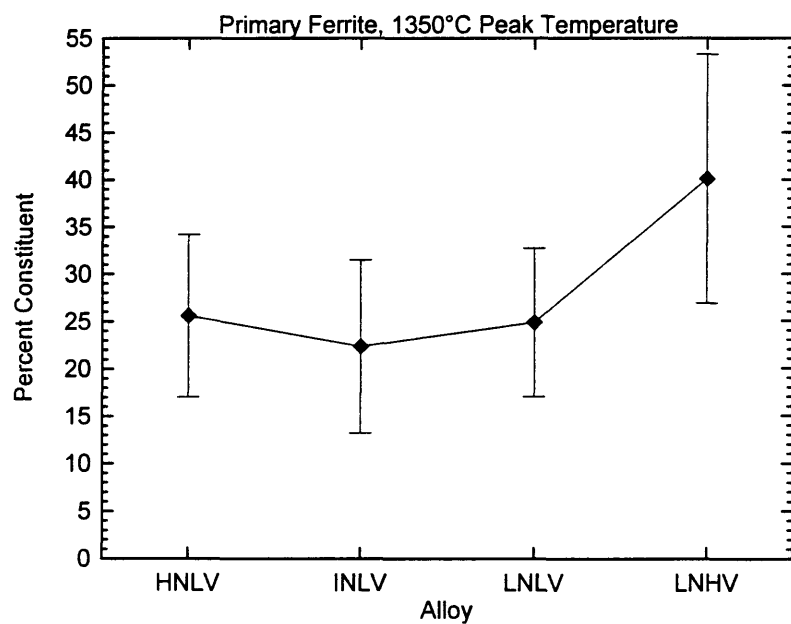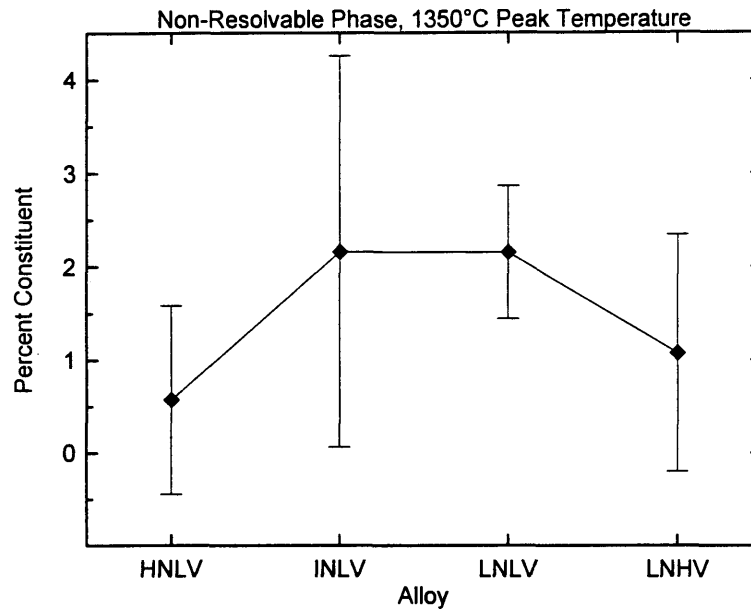

Figure 12.2. Volume fraction of primary ferrite for material thermally-cycled with a 1350°C peak temperature. Error bars are standard deviation.
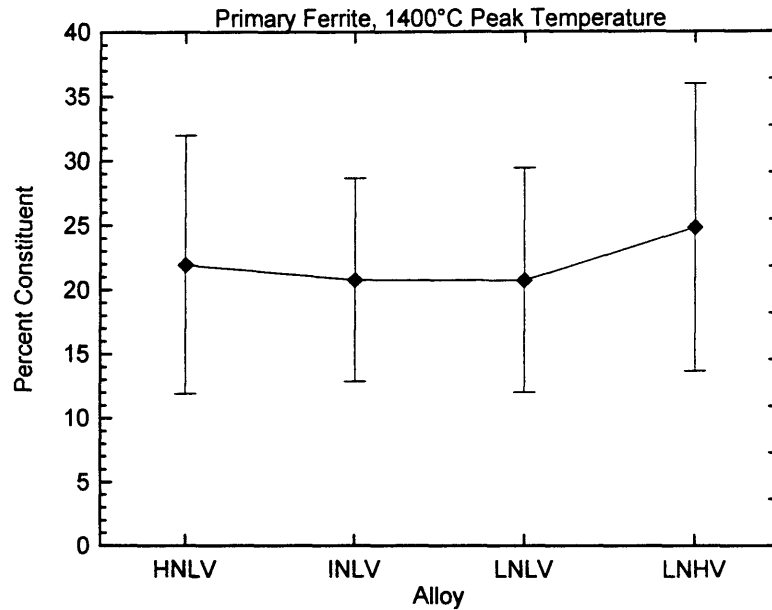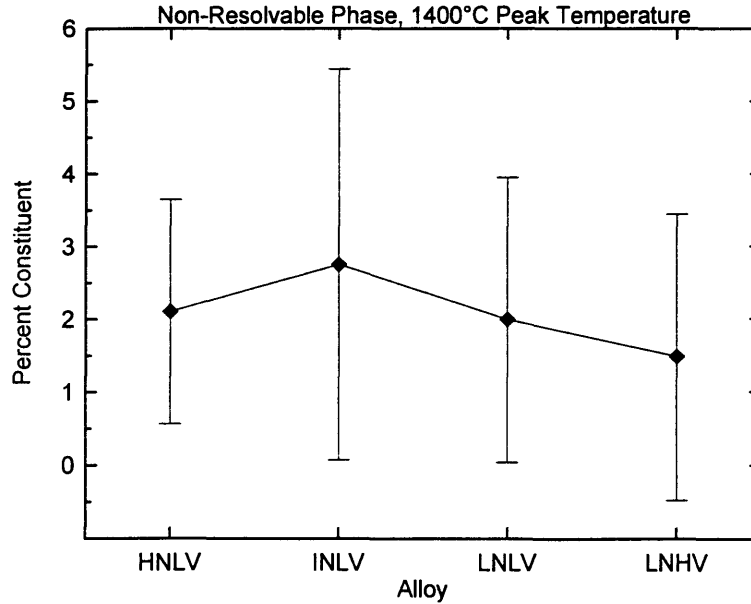
Figure 12.3. Volume fraction of primary ferrite for material thermally-cycled with a 1400°C peak temperature. Error bars are standard deviation.
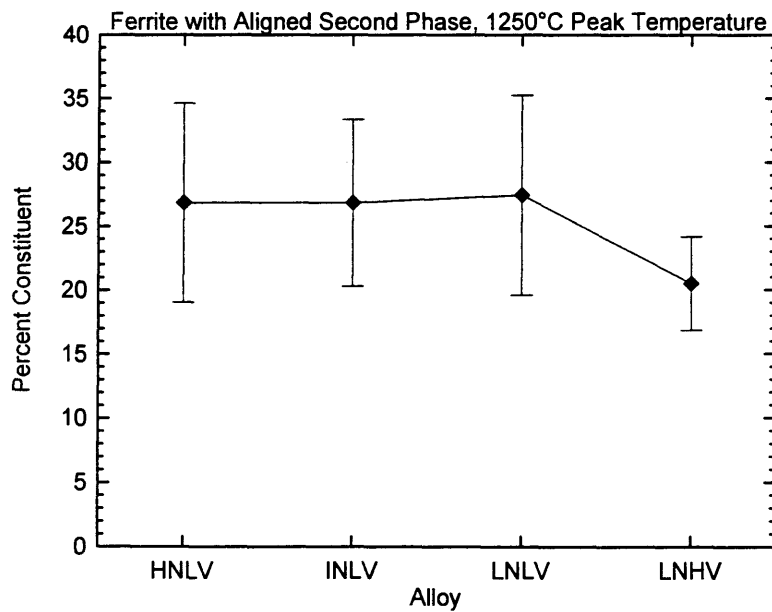
Figure 12.4. Volume fraction of ferrite with an aligned second phase for material thermally-cycled with a 1250°C peak temperature. Error bars are standard deviation.
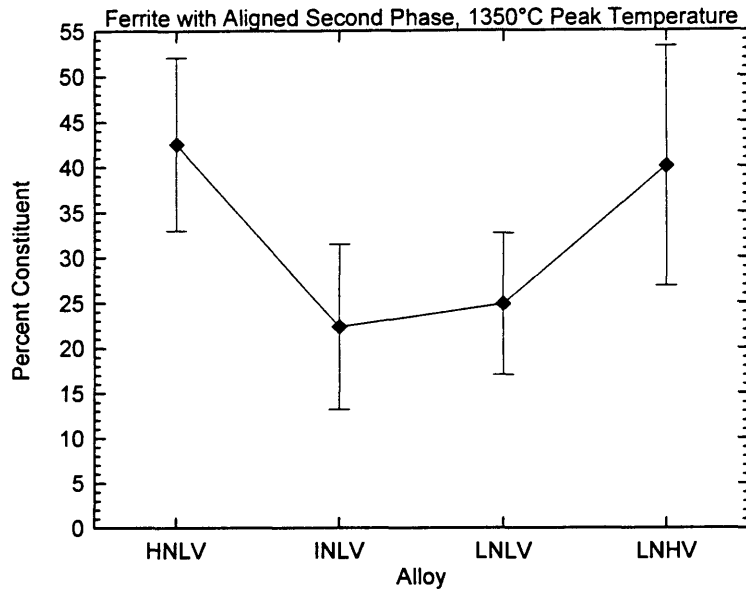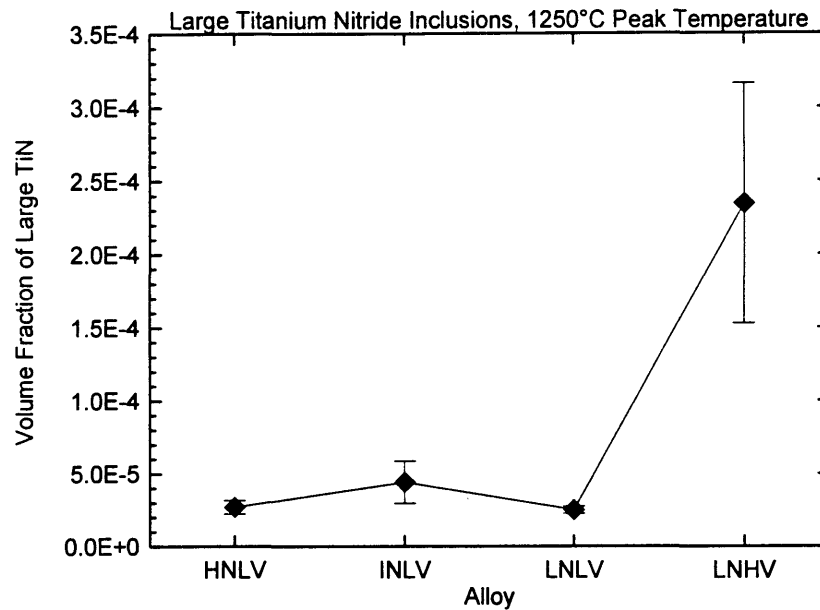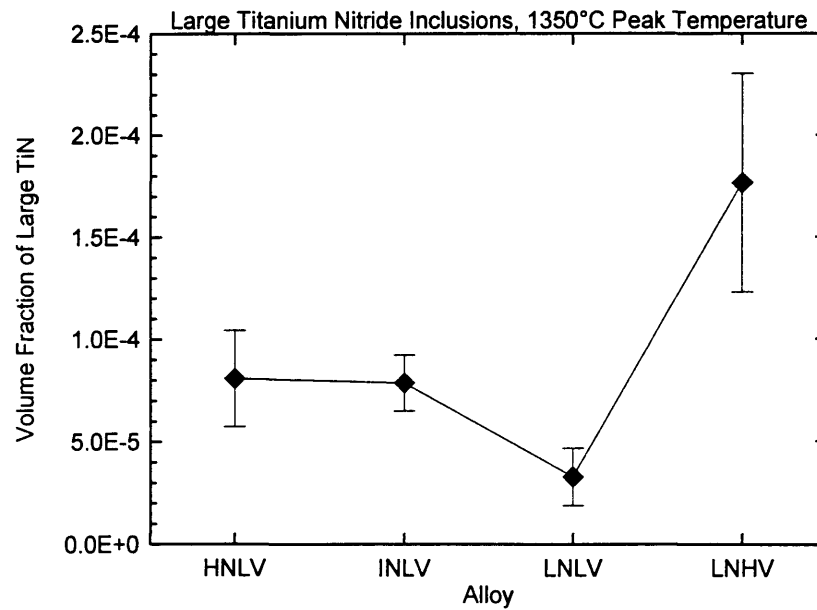
Figure 12.5. Volume fraction of ferrite with an aligned second phase for material thermally-cycled with a 1350°C peak temperature. Error bars are standard deviation.
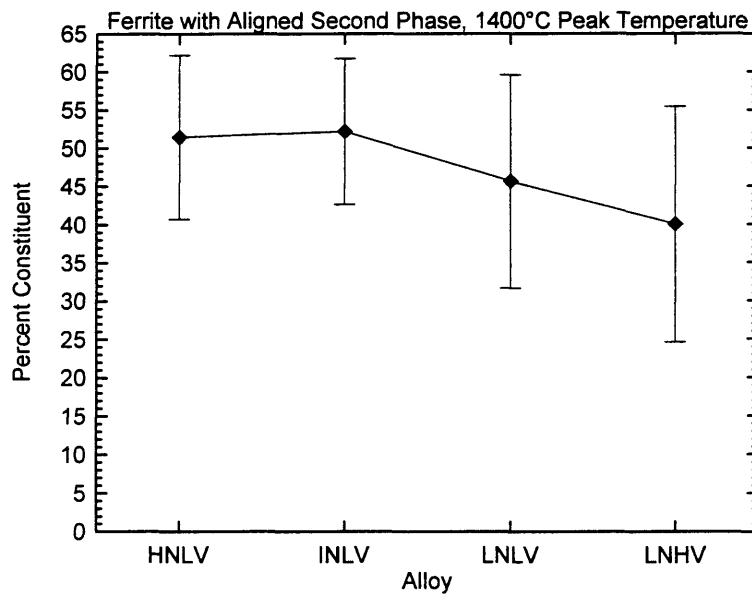
Figure 12.6. Volume fraction of ferrite with an aligned second phase for material thermally-cycled with a 1400°C peak temperature. Error bars are standard deviation.
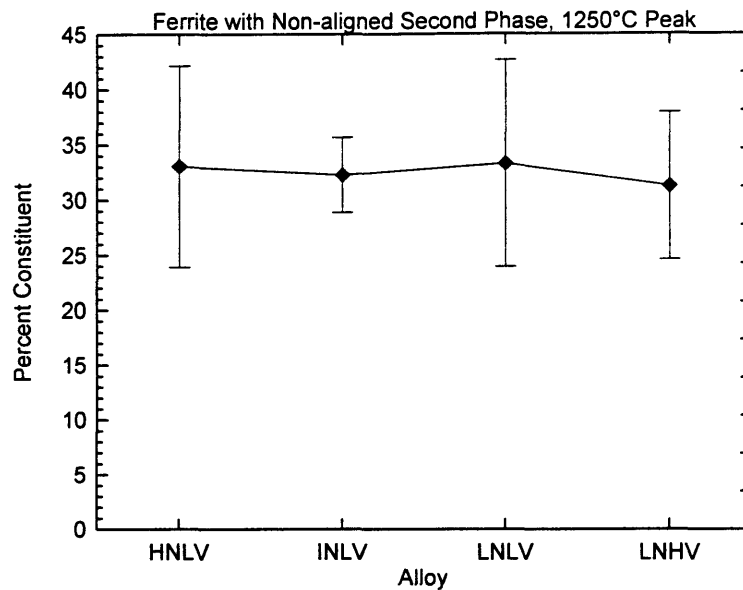
Figure 12.7. Volume fraction of ferrite with a non-aligned second phase for material thermally-cycled with a 1250°C peak temperature. Error bars are standard deviation.
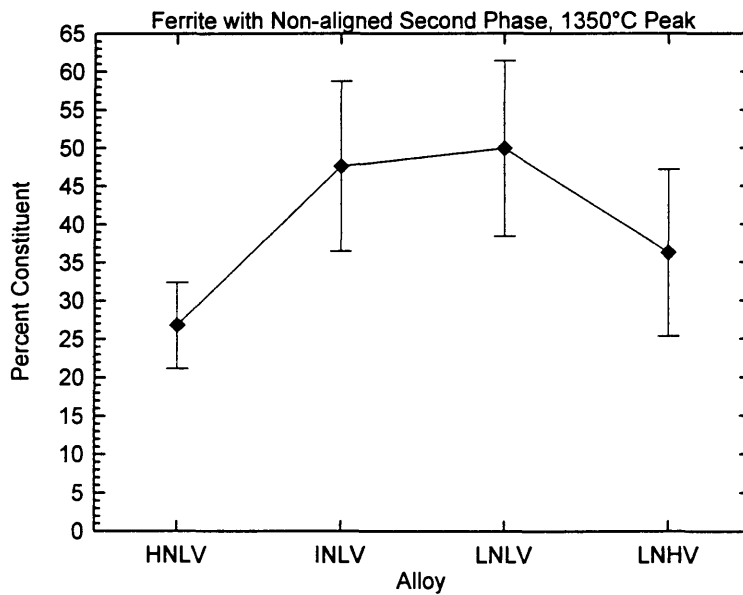
Figure 12.8. Volume fraction of ferrite with a non-aligned second phase for material thermally-cycled with a 1350°C peak temperature. Error bars are standard deviation.
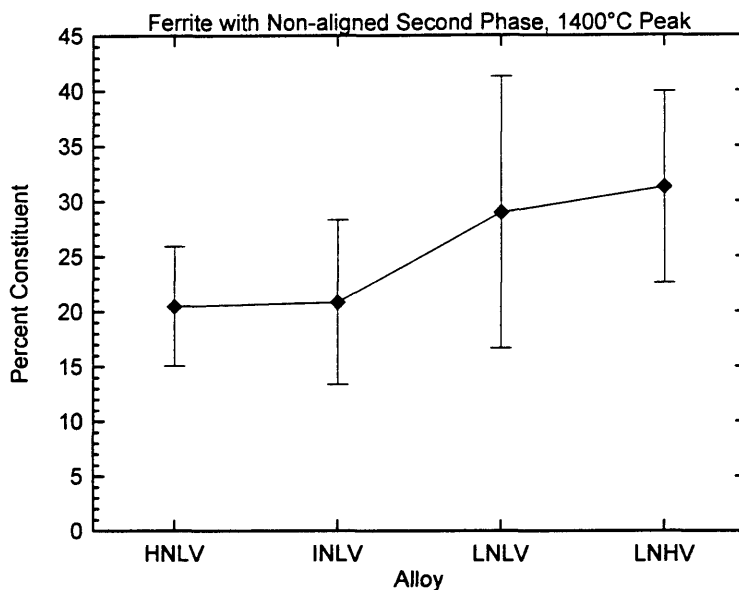
Figure 12.9. Volume fraction of ferrite with a non-aligned second phase for material thermally-cycled with a 1400°C peak temperature. Error bars are standard deviation.
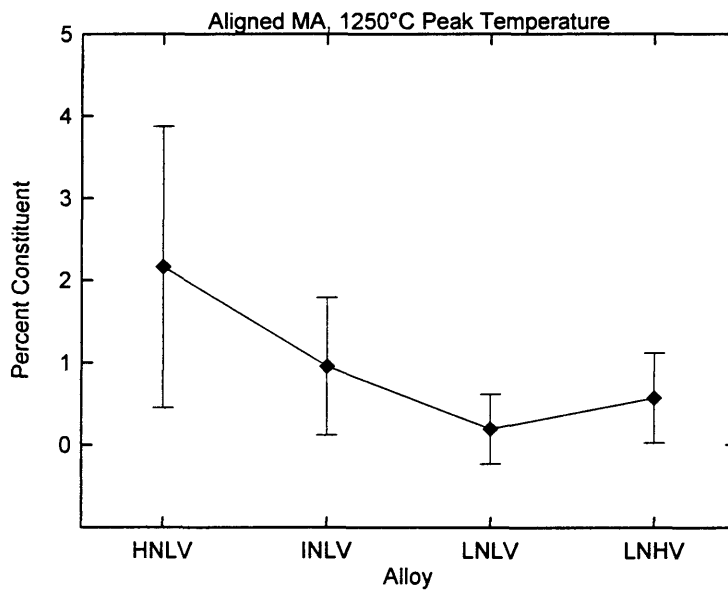
Figure 12.10. Volume fraction of aligned MA constituent for material thermally-cycled with a 1250°C peak temperature. Error bars are standard deviation.
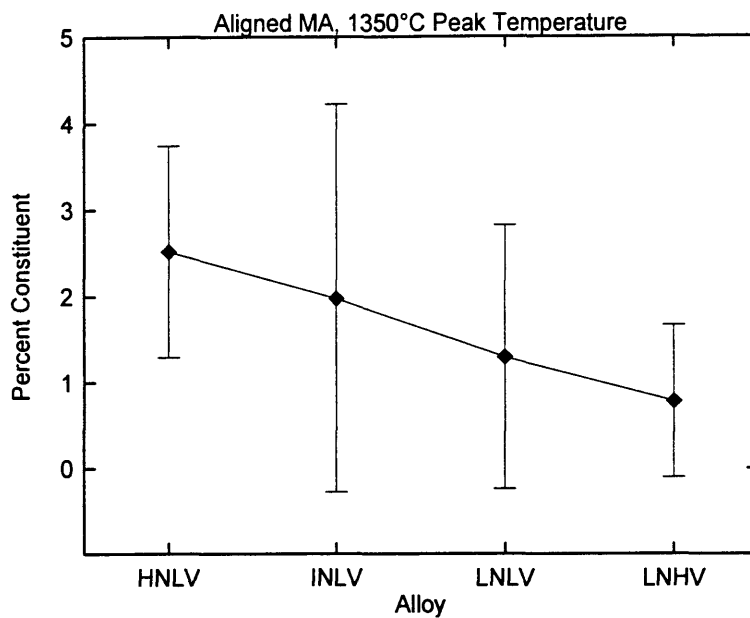
Figure 12.11. Volume fraction of aligned MA constituent for material thermally-cycled with a 1350°C peak temperature. Error bars are standard deviation.
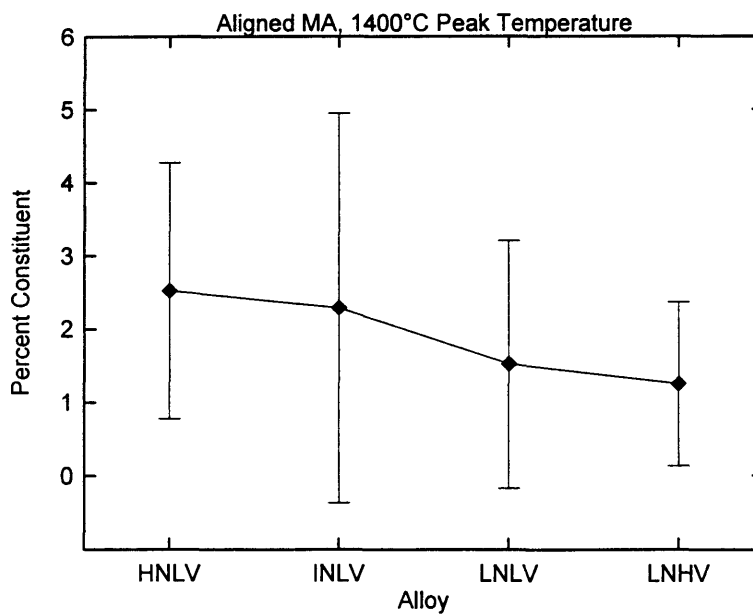
Figure 12.12. Volume fraction of aligned MA constituent for material thermally-cycled with a 1400°C peak temperature. Error bars are standard deviation.
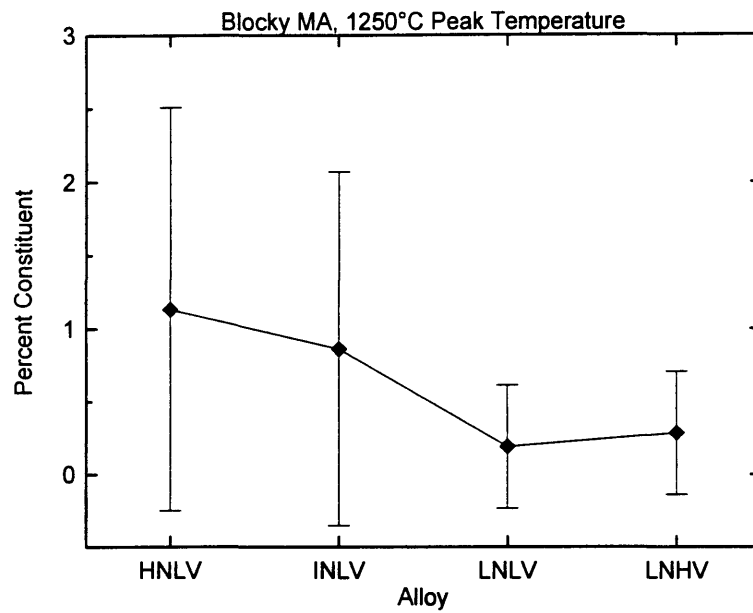
Figure 12.13.Volume fraction of blocky MA constituent for material thermally-cycled with a 1250°C peak temperature. Error bars are standard deviation.
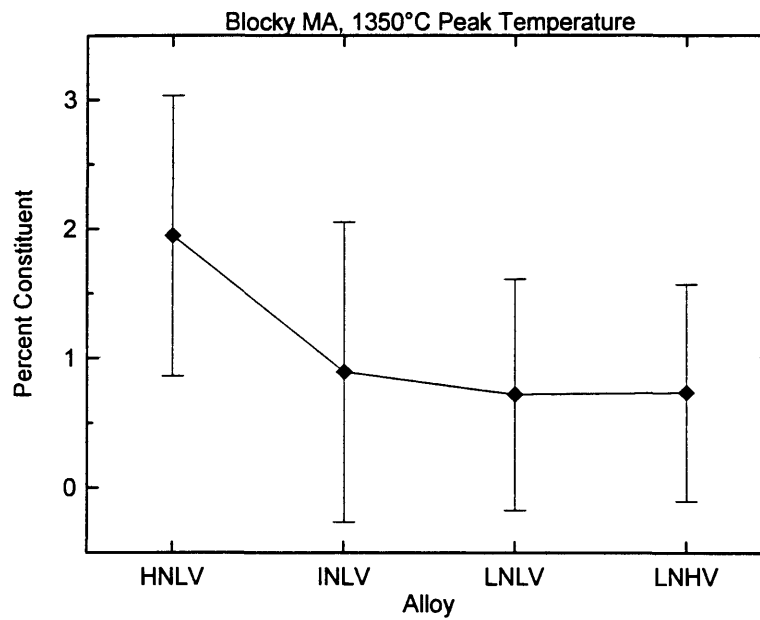
Figure 12.14.Volume fraction of blocky MA constituent for material thermally-cycled with a 1350°C peak temperature. Error bars are standard deviation.
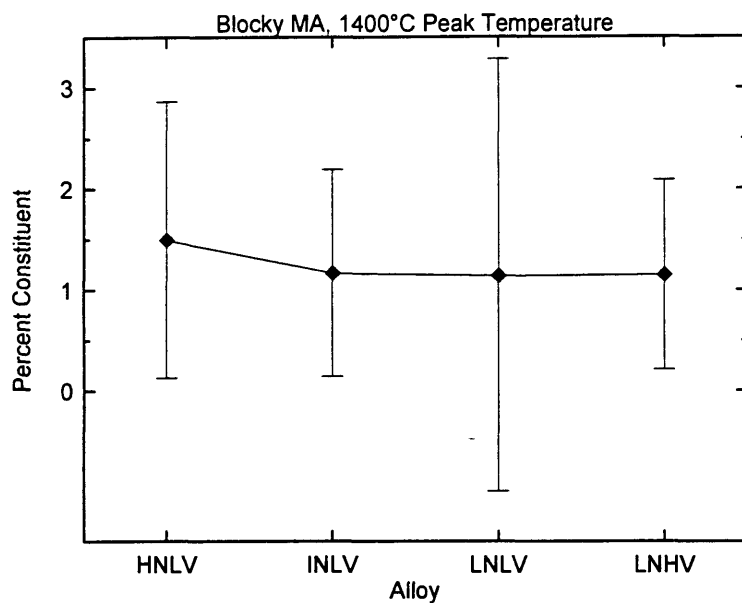
Figure 12.15.Volume fraction of blocky MA constituent for material thermally-cycled with a 1400°C peak temperature. Error bars are standard deviation.
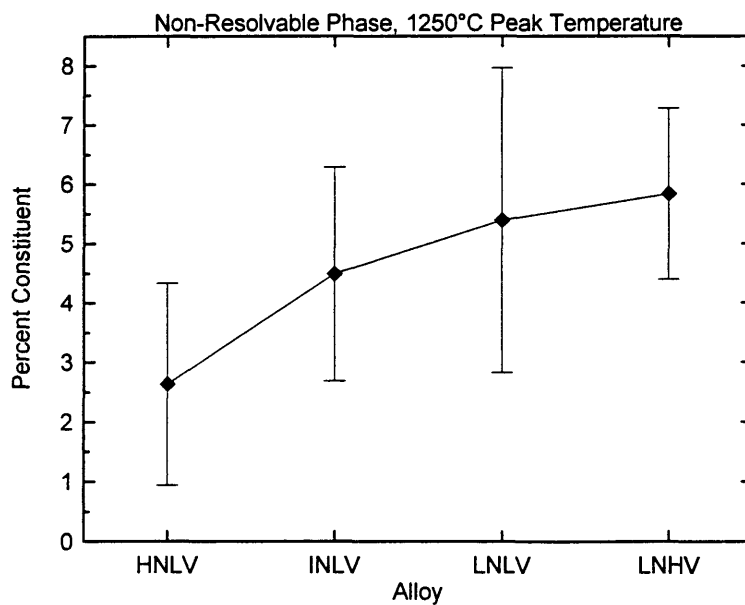
Figure 12.16.Volume fraction of non-resolvable second phase for material thermally-cycled with a 1250°C peak temperature. Error bars are standard deviation.

Figure 12.17. Volume fraction of non-resolvable second phase for material thermally-cycled with a 1350°C peak temperature. Error bars are standard deviation.

Figure 12.18. Volume fraction of non-resolvable second phase for material thermally-cycled with a 1400°C peak temperature. Error bars are standard deviation.

Figure 12.19.Volume fraction of large titanium nitride inclusions for material thermally-cycled with a 1250°C peak temperature. Error bars are standard deviation.

Figure 12.20.Volume fraction of large titanium nitride inclusions for material thermally-cycled with a 1350°C peak temperature. Error bars are standard deviation.
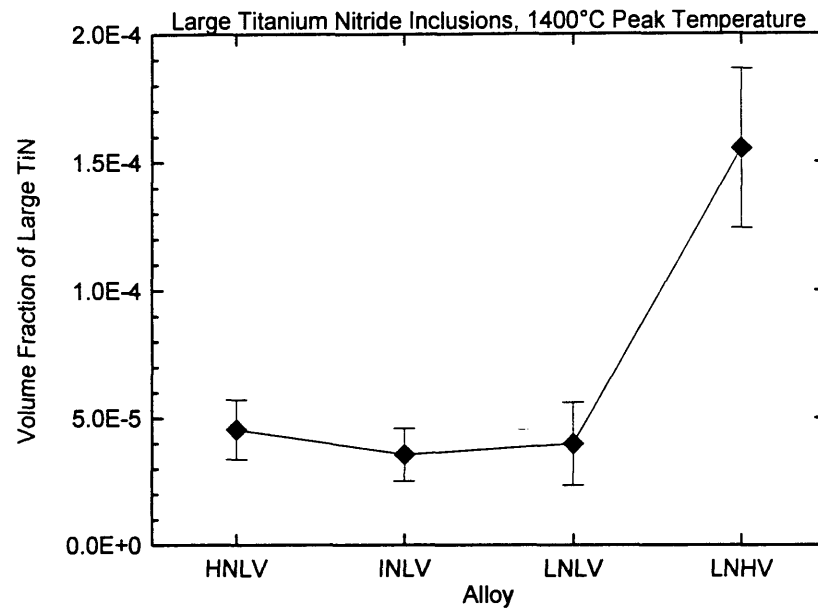
Figure 12.21.Volume fraction of large titanium nitride inclusions for material thermally-cycled with a 1400°C peak temperature. Error bars are standard deviation.
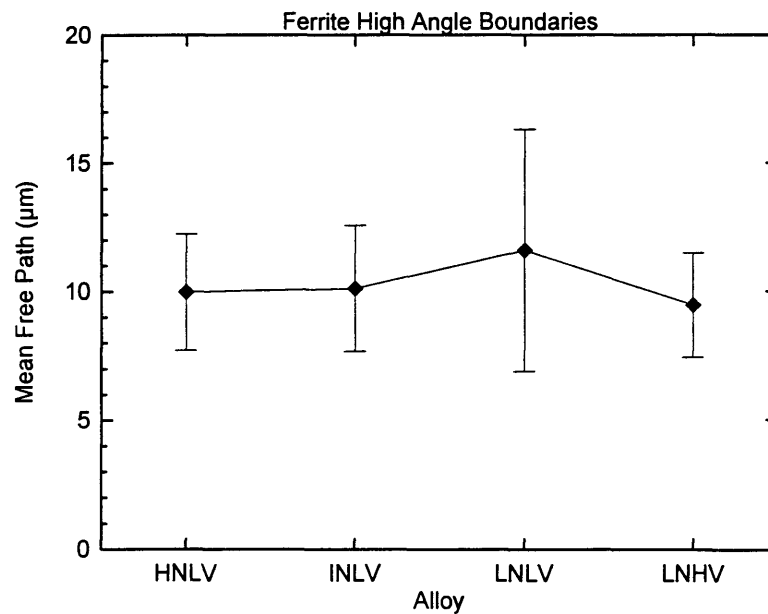
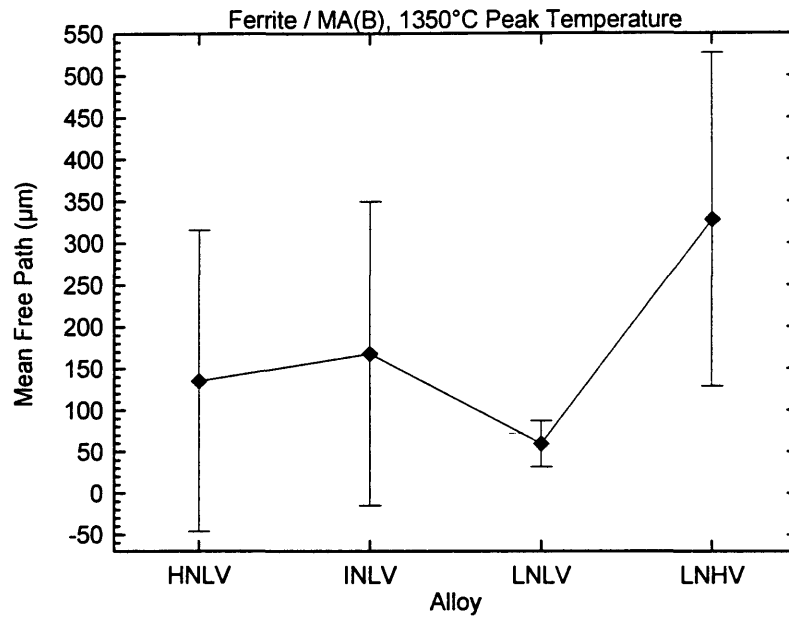Figure 12.22.Mean free path between ferrite high angle boundaries in specimens thermally cycled with a 1250°C peak temperature.
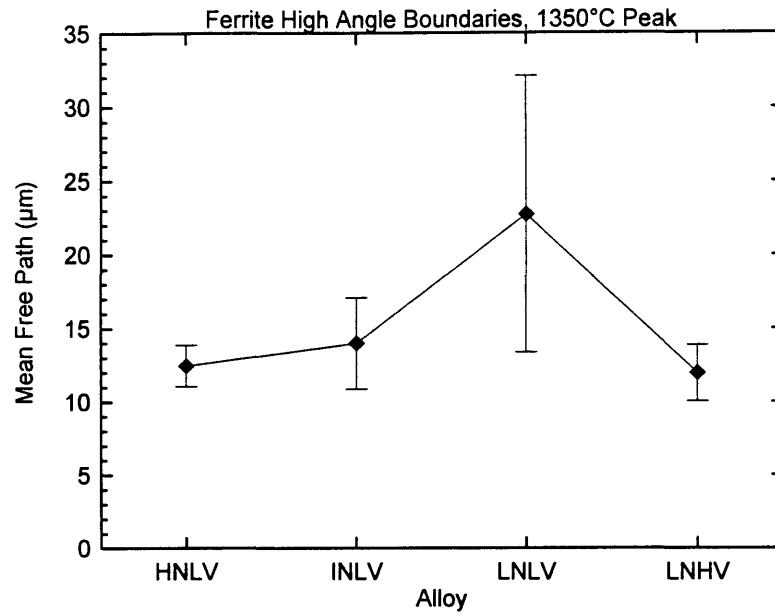
Figure 12.23.Mean free path between ferrite high angle boundaries in specimens thermally cycled with a 1350°C peak temperature.
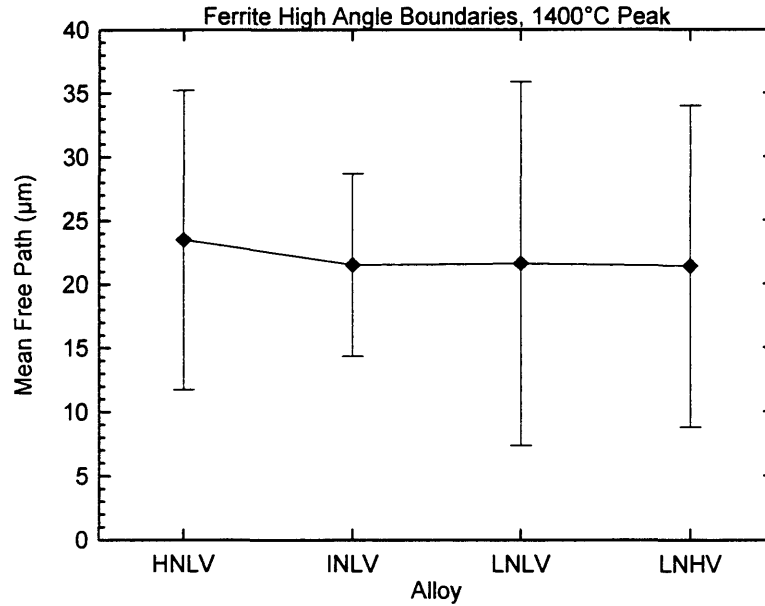
Figure 12.24.Mean free path between ferrite high angle boundaries in specimens thermally cycled with a 1400°C peak temperature.
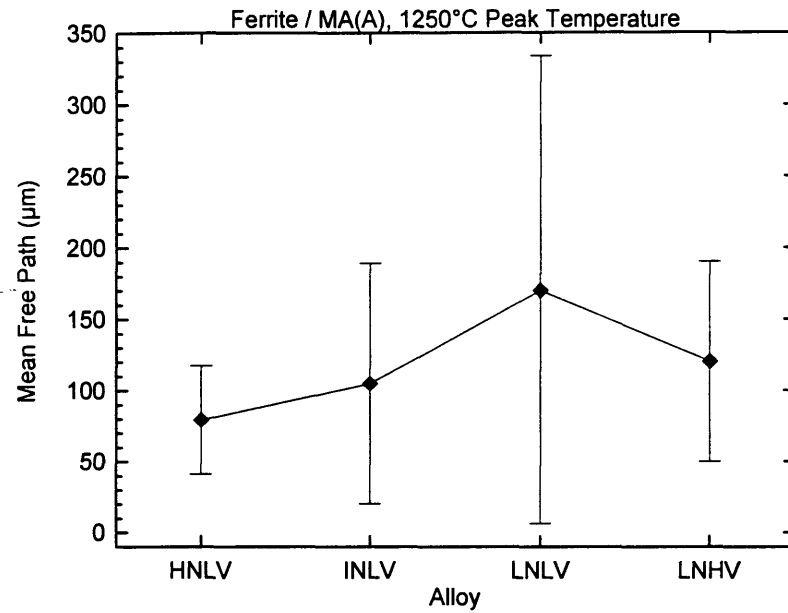
Figure 12.25.Mean free path between ferrite - aligned MA constituent boundaries in specimens thermally cycled with a 1250°C peak temperature.
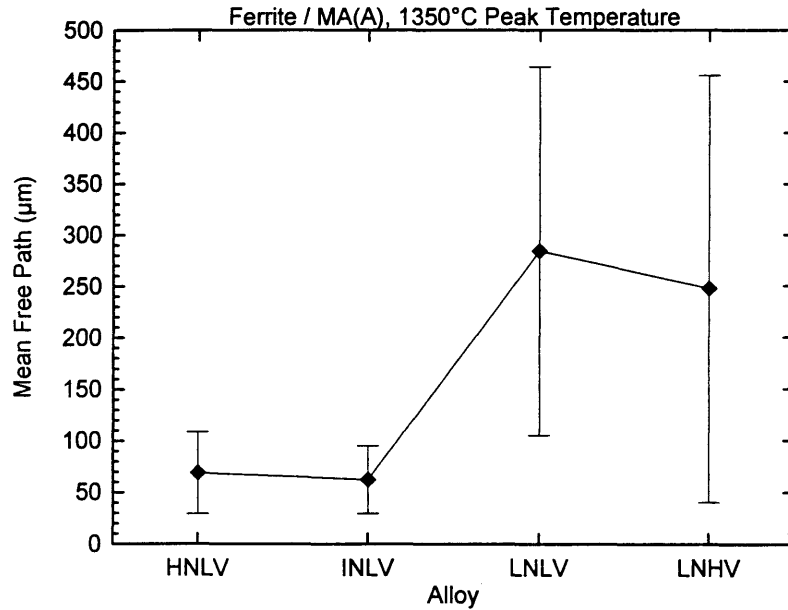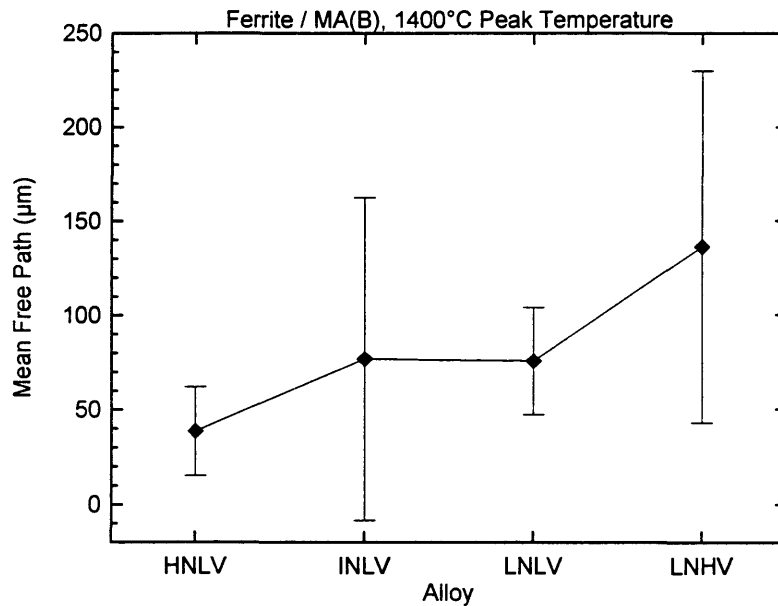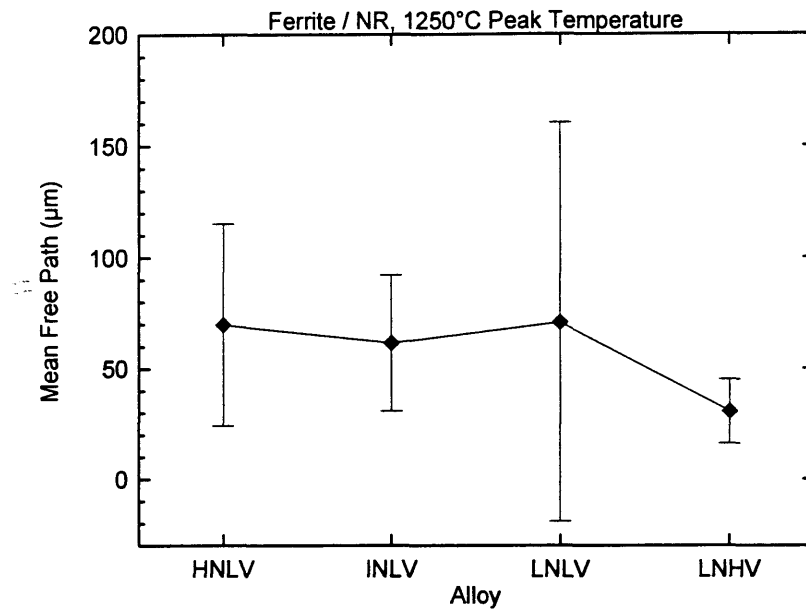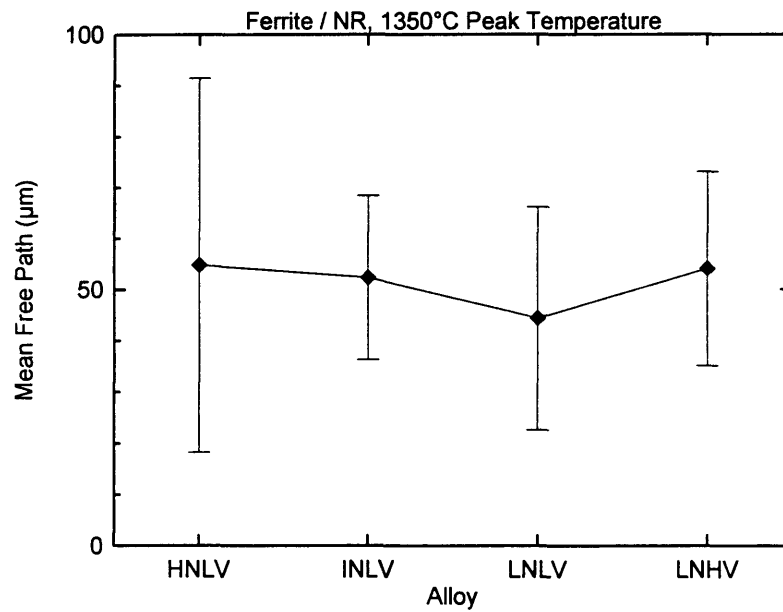

Figure 12.26.Mean free path between ferrite - aligned MA constituent boundaries in specimens thermally cycled with a 1350°C peak temperature.
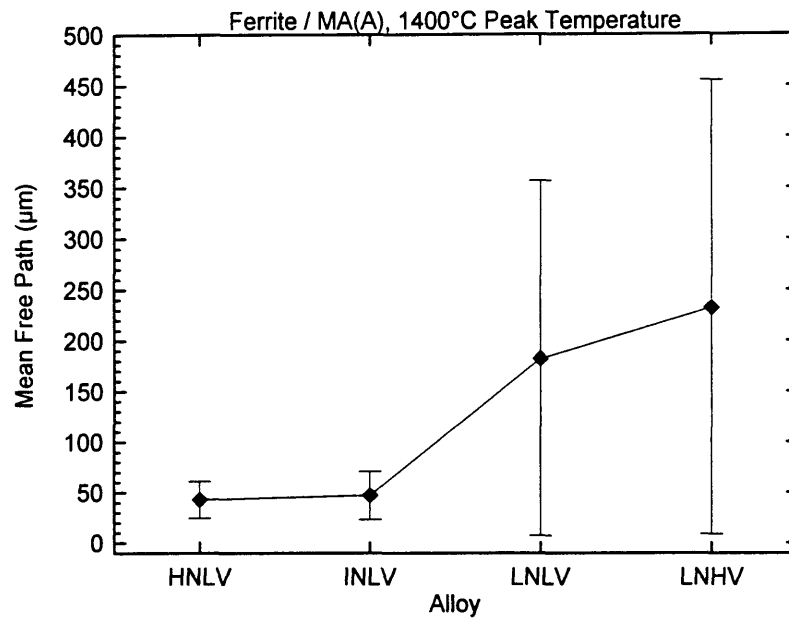
Figure 12.27.Mean free path between ferrite - aligned MA constituent boundaries in specimens thermally cycled with a 1400°C peak temperature.
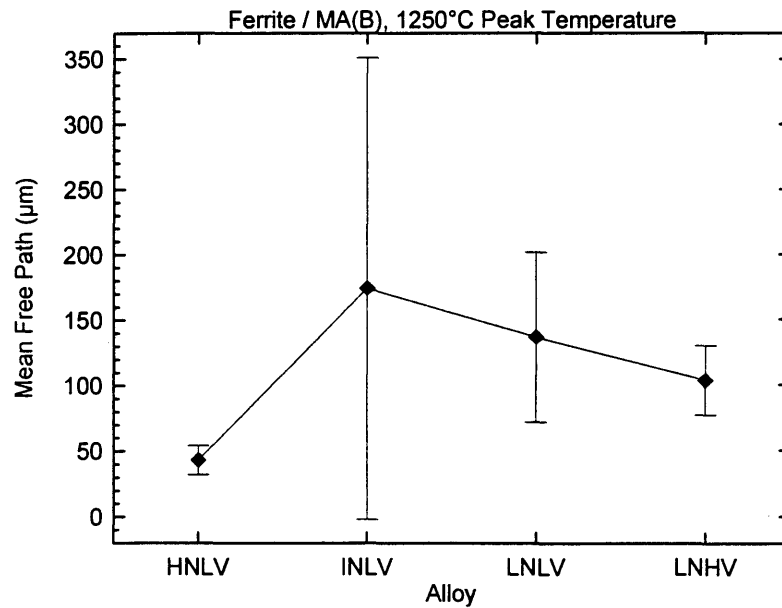
Figure 12.28.Mean free path between ferrite - blocky MA constituent boundaries in specimens thermally cycled with a 1250°C peak temperature.

Figure 12.29. Mean free path between ferrite - blocky MA constituent boundaries in specimens thermally cycled with a 1350°C peak temperature.

Figure 12.30. Mean free path between ferrite - blocky MA constituent boundaries in specimens thermally cycled with a 1400°C peak temperature.

Figure 12.31.Mean free path between ferrite - non-resolvable second phase boundaries in specimens thermally cycled with a 1250°C peak temperature.
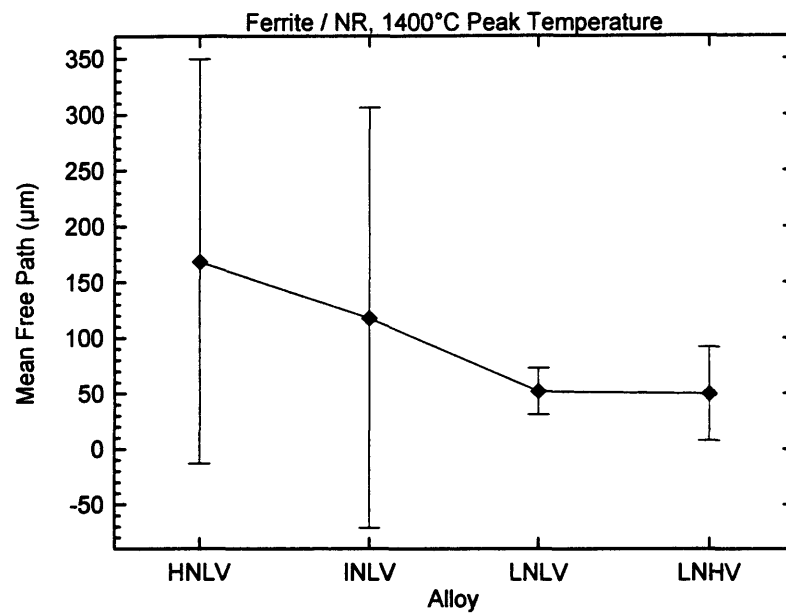

Figure 12.32.Mean free path between ferrite - non-resolvable second phase boundaries in specimens thermally cycled with a 1350°C peak temperature.

Figure 12.33.Mean free path between ferrite - non-resolvable second phase boundaries in specimens thermally cycled with a 1400°C peak temperature.

13.0 APPENDIX E

Continuous Cooling Transformation Microstructures

a)

b)

c)
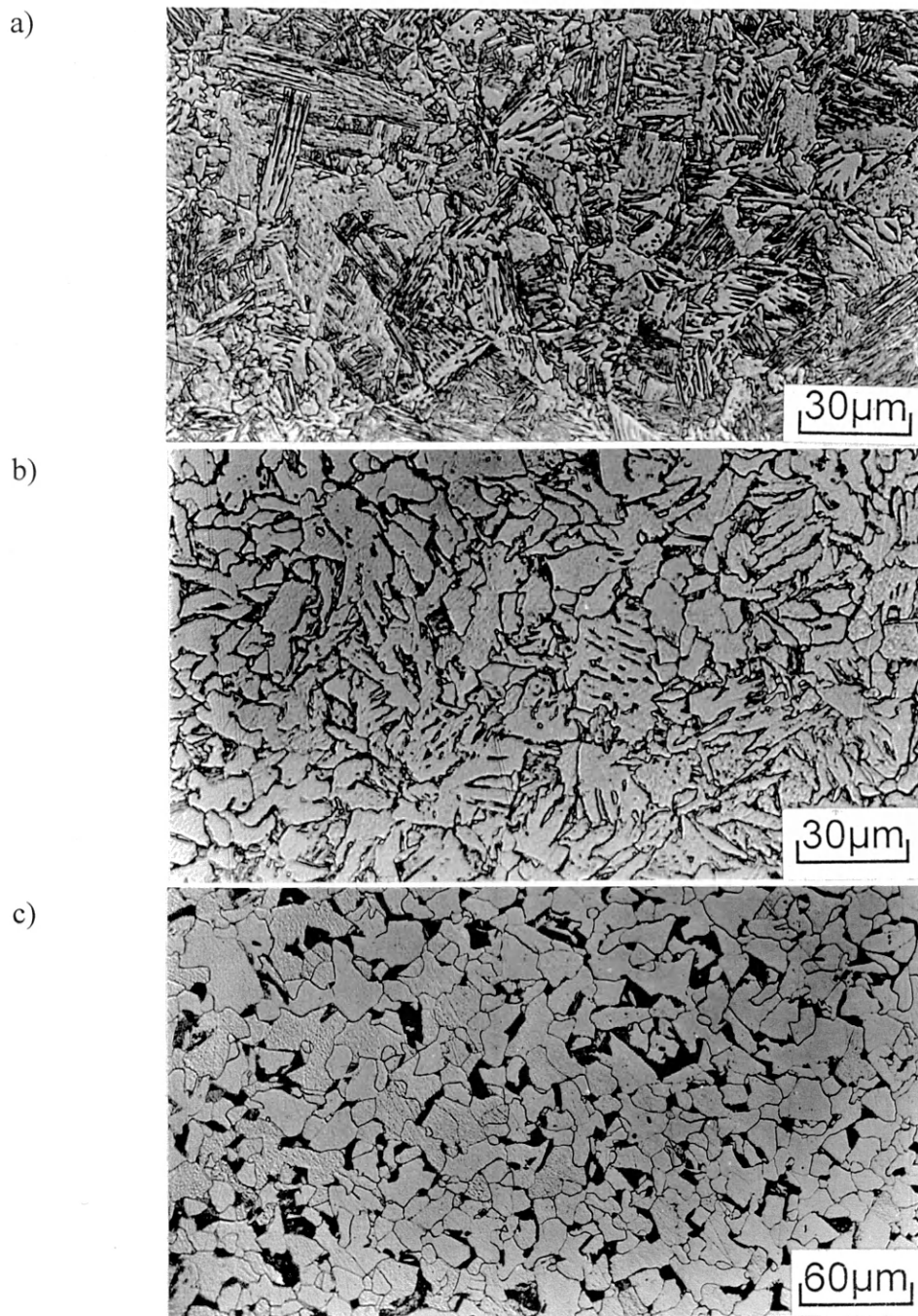
Figure 13.1. Typical microstructures of CCT specimens for alloy INLV. 1250°C peak temperature. Δt_{8-5} times of: a) 3 seconds, b) 30 seconds, c) 300 seconds.
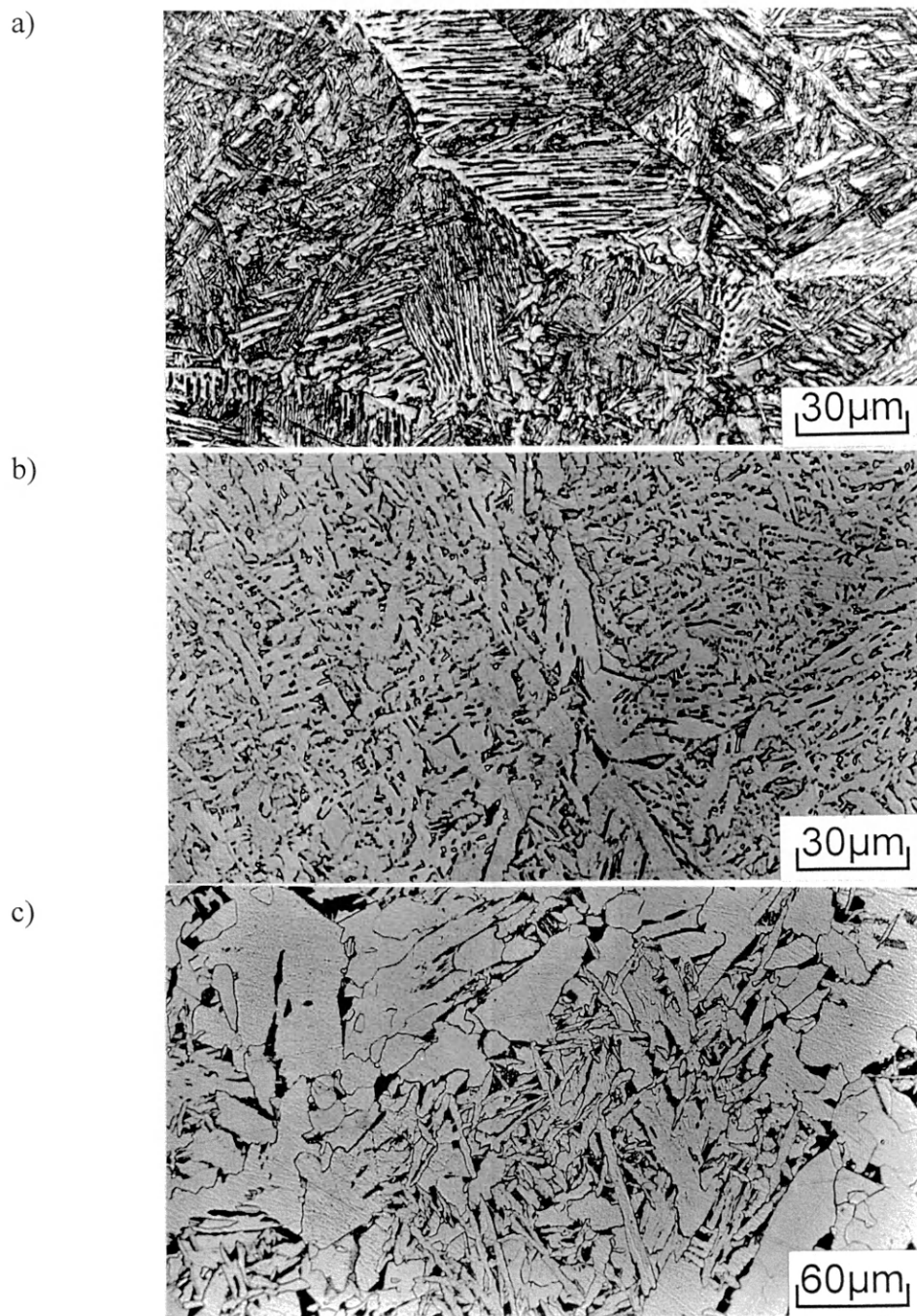
a)

b)

c)

Figure 13.2. Typical microstructures of CCT specimens for alloy INLV. 1400°C peak temperature. Δt_{8-5} times of: a) 3 seconds, b) 30 seconds, c) 300 seconds.
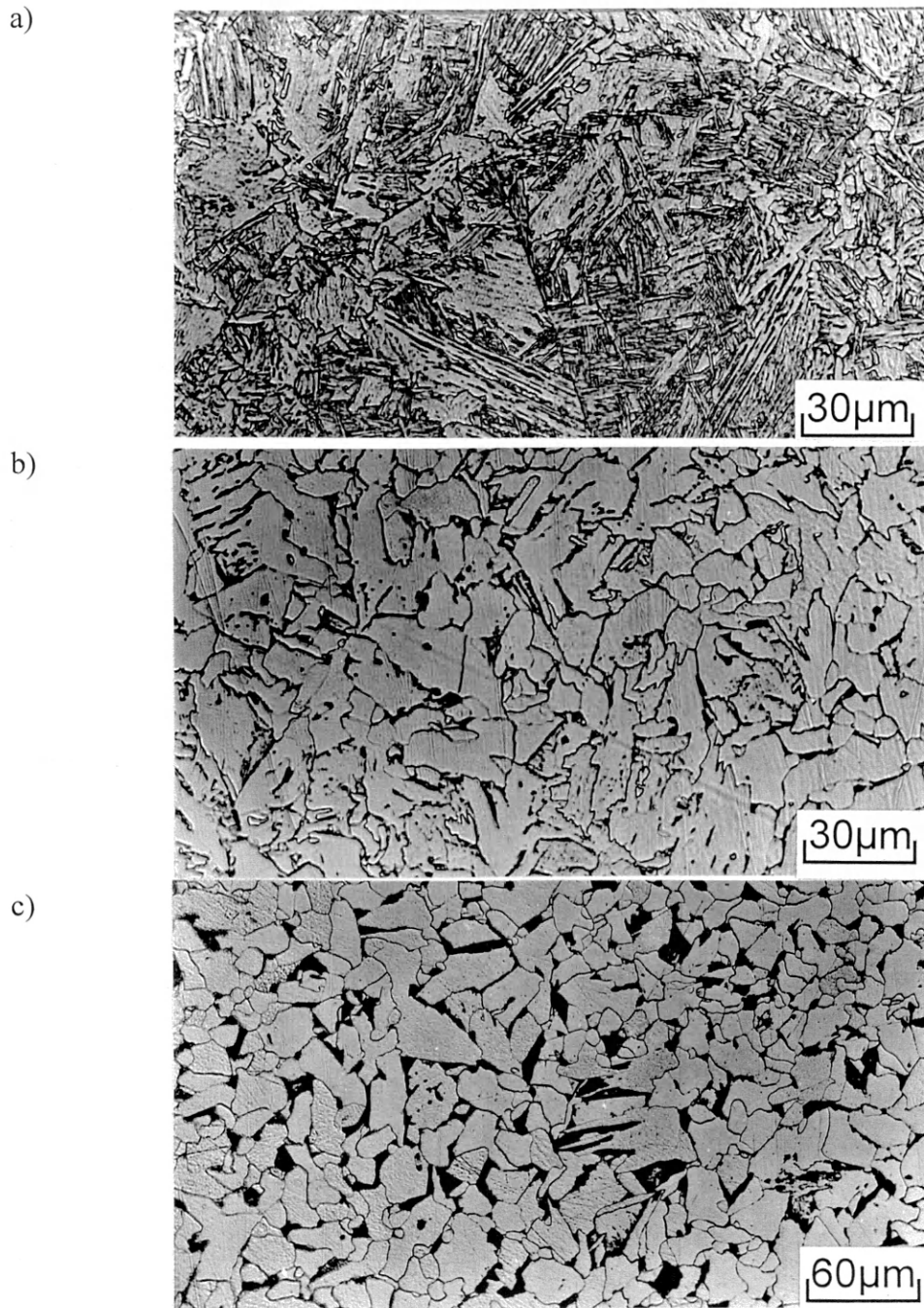
a)

b)

c)

Figure 13.3. Typical microstructures of CCT specimens for alloy LNLV. 1250°C peak temperature. Δt_{8-5} times of: a) 3 seconds, b) 30 seconds, c) 300 seconds.
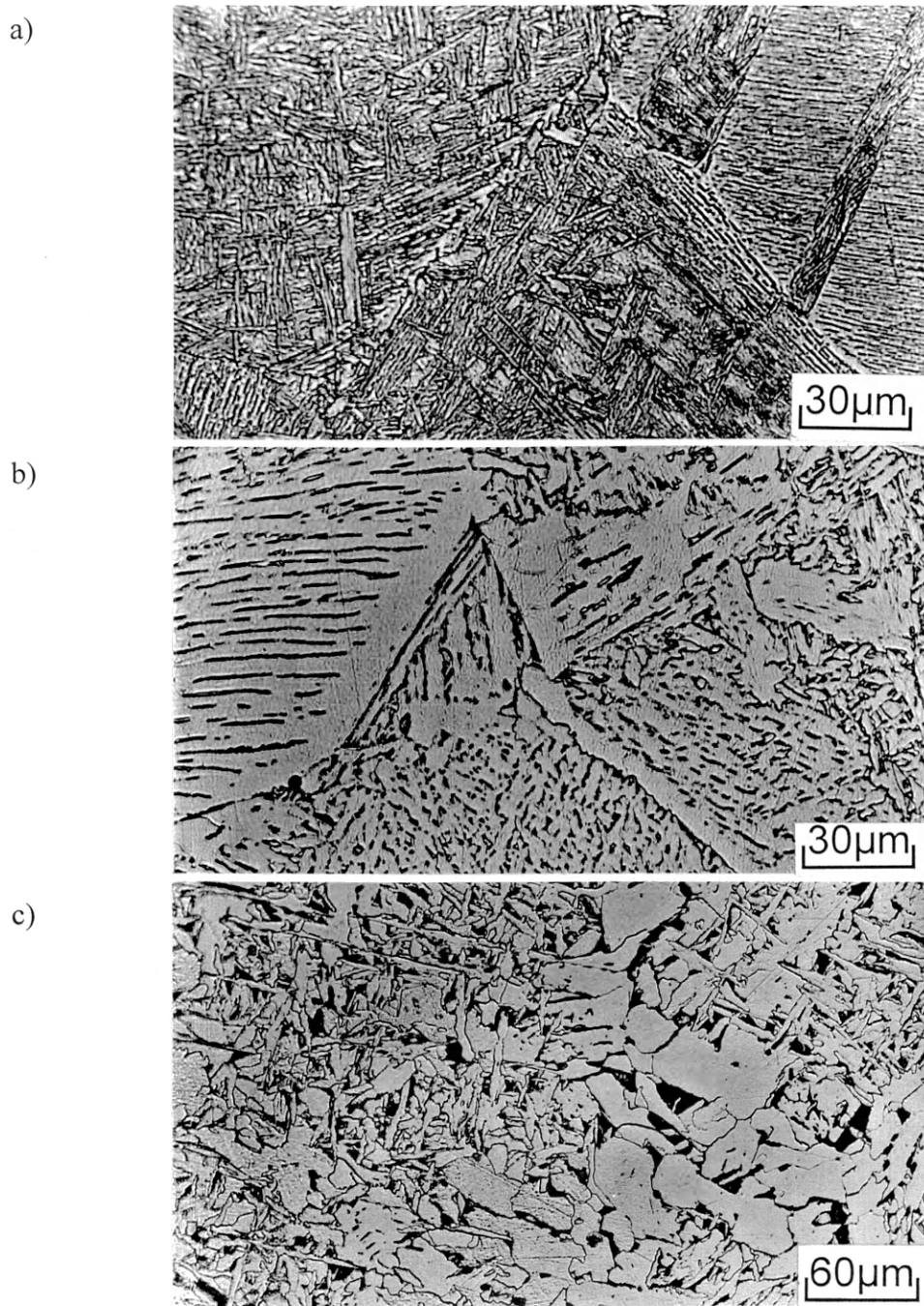
Figure 13.4. Typical microstructures of CCT specimens for alloy LNLV. 1400°C peak temperature. Δt_{8-5} times of: a) 3 seconds, b) 30 seconds, c) 300 seconds.
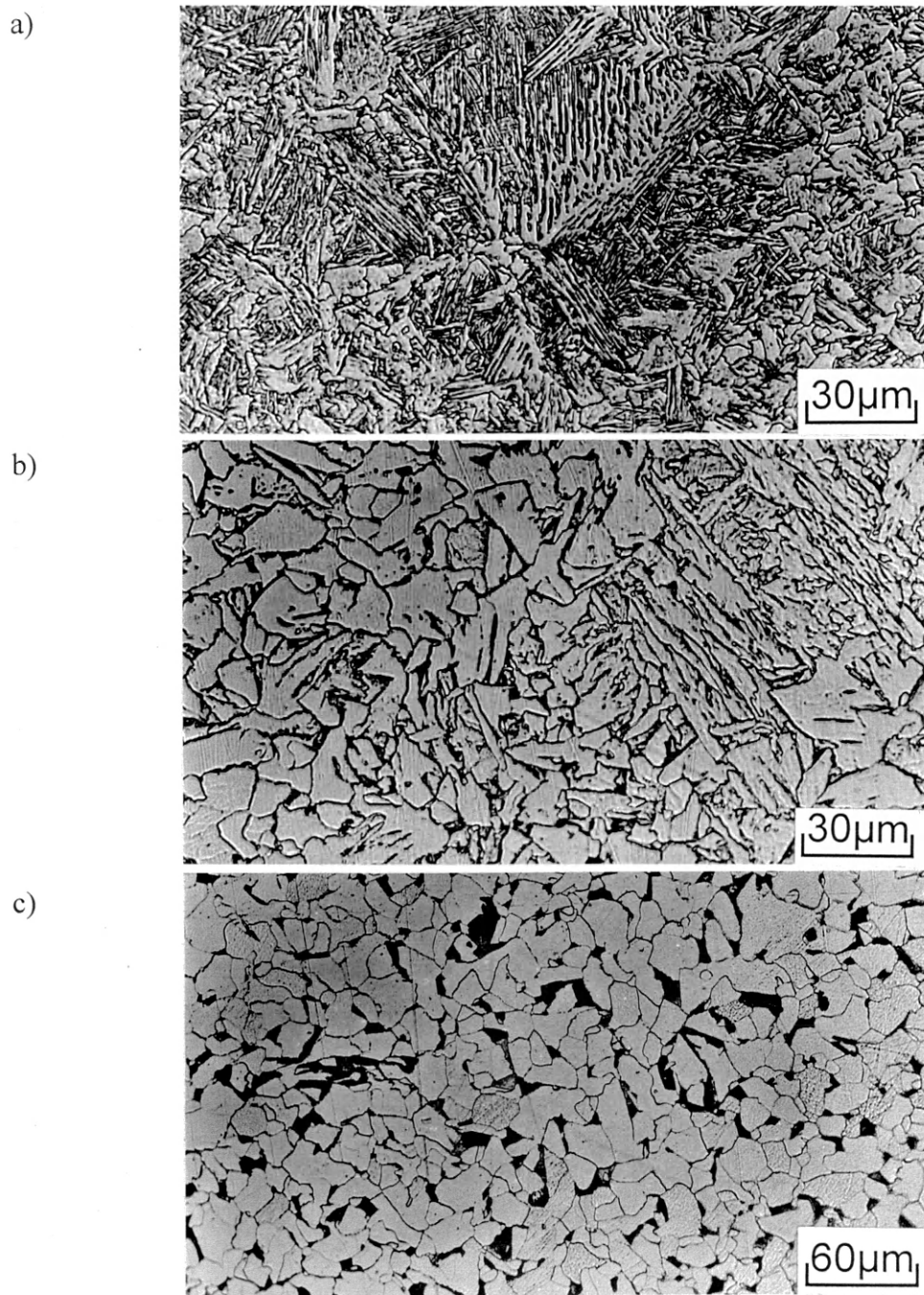
Figure 13.5. Typical microstructures of CCT specimens for alloy LNHV. 1250°C peak temperature. Δt_{8-5} times of: a) 3 seconds, b) 30 seconds, c) 300 seconds.
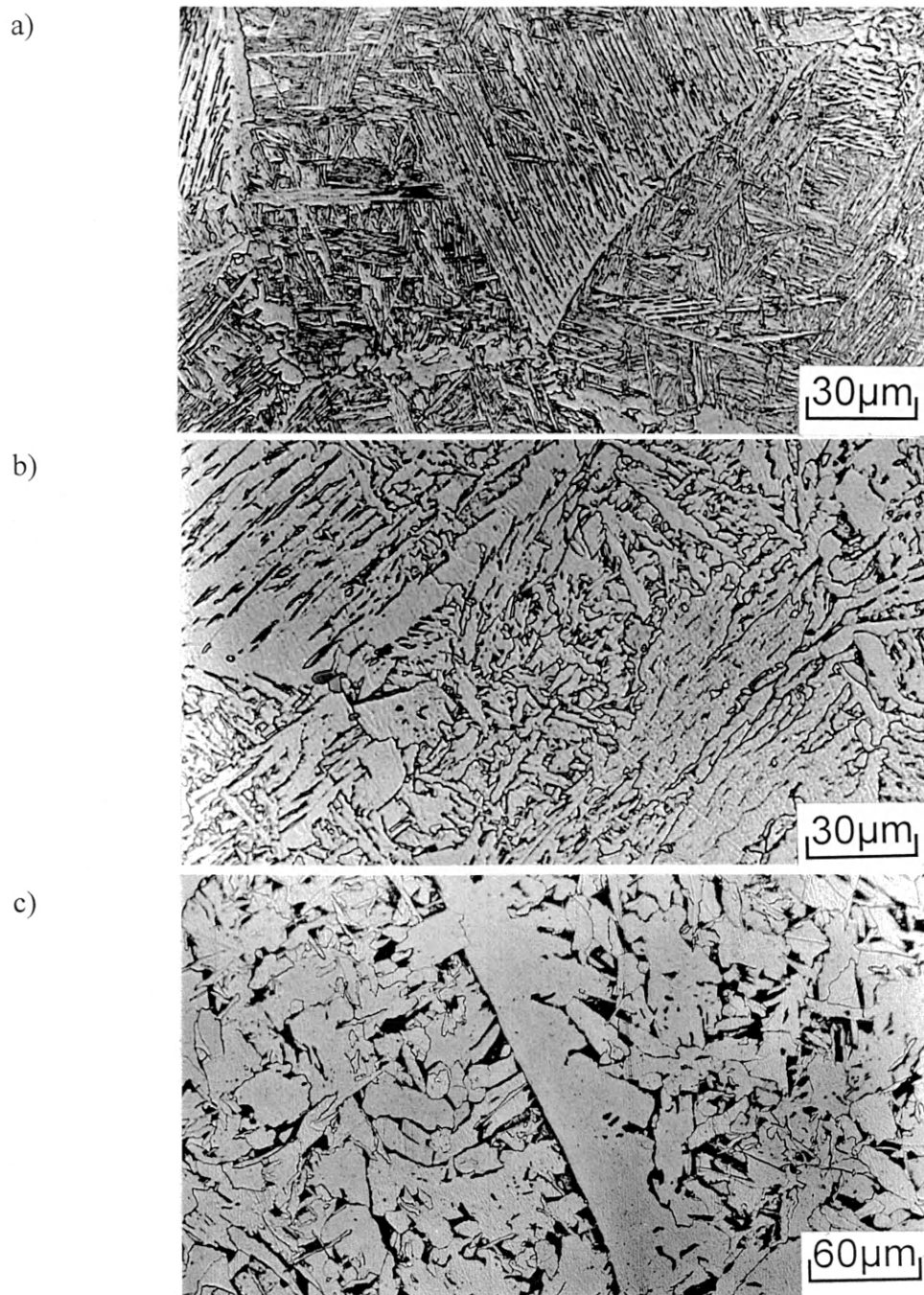
Figure 13.6. Typical microstructures of CCT specimens for alloy LNHV. 1400°C peak temperature. $\Delta t_{8\text{-}5}$ times of: a) 3 seconds, b) 30 seconds, c) 300 seconds.